Air Force Institute of Technology
AFIT Scholar

Theses and Dissertations

9-14-2017

Engineered Surfaces to Control Secondary Electron Yield for Multipactor Suppression

James M. Sattler

Follow this and additional works at: https://scholar.afit.edu/etd

Part of the Electrical and Electronics Commons

Recommended Citation

Sattler, James M., "Engineered Surfaces to Control Secondary Electron Yield for Multipactor Suppression" (2017). *Theses and Dissertations*. 770.
https://scholar.afit.edu/etd/770

This Dissertation is brought to you for free and open access by AFIT Scholar. It has been accepted for inclusion in Theses and Dissertations by an authorized administrator of AFIT Scholar. For more information, please contact richard.mansfield@afit.edu.

ENGINEERED SURFACES TO CONTROL SECONDARY ELECTRON YIELD FOR MULTIPACTOR SUPPRESSION

DISSERTATION

James M. Sattler, Lieutenant Colonel, USAF
AFIT-ENG-DS-17-S-018

DEPARTMENT OF THE AIR FORCE
AIR UNIVERSITY

AIR FORCE INSTITUTE OF TECHNOLOGY

Wright-Patterson Air Force Base, Ohio

DISTRIBUTION STATEMENT A.

APPROVED FOR PUBLIC RELEASE; DISTRIBUTION UNLIMITED.

The views expressed in this dissertation are those of the author and do not reflect the official policy or position of the United States Air Force, Department of Defense, or the United States Government. This material is declared a work of the U.S. Government and is not subject to copyright protection in the United States.

AFIT-ENG-DS-17-S-018

ENGINEERED SURFACES TO CONTROL SECONDARY ELECTRON YIELD FOR MULTIPACTOR SUPPRESSION

DISSERTATION

Presented to the Faculty

Graduate School of Engineering and Management

Air Force Institute of Technology

Air University

Air Education and Training Command

In Partial Fulfillment of the Requirements for the

Degree of Doctor of Philosophy

James M. Sattler, BSEE, MSEE

Lieutenant Colonel, USAF

September 2017

DISTRIBUTION STATEMENT A.

APPROVED FOR PUBLIC RELEASE; DISTRIBUTION UNLIMITED.

AFIT-ENG-DS-17-S-018

ENGINEERED SURFACES TO CONTROL SECONDARY ELECTRON YIELD FOR MULTIPACTOR SUPPRESSION

DISSERTATION

James M. Sattler, BSEE, MSEE
Lieutenant Colonel, USAF

Committee Membership:

Robert A. Lake, PhD
Chair

Richard G. Cobb, PhD
Member

Tod V. Laurvick, PhD
Member

ADEDEJI B. BADIRU, PhD
Dean, Graduate School of Engineering
and Management

AFIT-ENG-DS-17-S-018

Abstract

A significant problem for satellites, vacuum electron devices (VEDs), and particle accelerators is multipactor: an avalanche of vacuum electrons caused by rapidly recurring secondary electron emission (SEE) stimulated by a time-varying electric field. The consequences of a multipactor event range in severity from a temporary disruption of the affected electronic device to permanent damage if the multipactor leads to an electric discharge. Since the 1960s, when multipactor gained significant notoriety as a problem, the vast majority of multipactor suppression methods involved geometrical modifications, surface coatings, electron conditioning, electrode biasing, and applied magnetic fields. The limited success of these methods combined with the demand for higher frequency, higher power, and multicarrier systems has caused satellite engineers to impose power level restrictions as the primary multipactor suppression method.

In the past 10 years, new research into an old multipactor suppression method has shown great potential. This method relies on the principle that rough surfaces emit fewer numbers of secondary electrons than smooth surfaces of equivalent material. The secondary electron yield (SEY) – defined as the ratio of the number of electron emissions escaping the surface to the number of electrons that initially impact the surface – provides a critical parameter in the multipactor process. If the dielectric surfaces of microwave windows and the conductive surfaces of radio frequency (RF) and microwave devices can be roughened such that their SEY is less than unity, multipactor becomes impossible because there can be no growth in the vacuum electron population.

This research applies modern micro- and nano-scale design and fabrication techniques to create microporous and nanoporous surfaces to study the fundamental principles that describe how surface topography controls SEY. The primary surface feature characteristics studied are aspect ratio (the ratio of feature height to width) and distribution density (the spacing of the features). Two semi-empirical models were developed to help predict the SEY of a porous surface. The first model was based on a simple two-dimensional (2D) pore structure; the second model was based on a more accurate three-dimensional (3D) pore structure. The models were validated by comparing predictions to experimental SEY measurements made on microporous gold surfaces. All of the porous gold surfaces used for testing were designed, fabricated, and characterized at the Air Force Institute of Technology (AFIT). SEY measurements of the porous gold surfaces were made using a pre-existing SEY apparatus located at the Materials and Manufacturing Directorate of the Air Force Research Laboratory. Additionally, a new, more accurate SEY measurement apparatus was constructed for dedicated SEY measurements at AFIT.

The more accurate 3D model predicts that a porous gold surface with pore aspect ratios of 2.0 and a distribution density (porosity) of 0.5 will control the maximum SEY to unity, providing a multipactor-resistant surface. These models, along with the experimental results, also confirm an important understanding: the ability of an artificially roughened surface to control SEY is not a function of the surface feature size; rather, it is a function of surface feature aspect ratio and distribution density.

AFIT-ENG-DS-17-S-018

Soli Deo gloria

Acknowledgments

In the classical liberal arts tradition, a successful dissertation demonstrates an individual's mastery of a particular subject matter and scholarly method. Yet the road to such mastery is paved by the support of others – and the longer the road, the greater the debt of acknowledgements...

My advisor Dr. Robert Lake and my committee members, Dr. Richard Cobb and Dr. Tod Laurvick for their research guidance and mentorship, which transformed me into a more complete researcher and problem solver.

Dr. Ronald Coutu for fostering in me, the belief that I could make substantial and relevant contributions to this field.

Dr. Tyson Back, Dr. Steve Fairchild, Dr. Paul Murray, and Mr. Gregg Gruen for providing me vital opportunities to collect the data necessary for this research.

Dr. Robert Fitch, Dr. Dennis Walker, Mr. Rich Johnston, and Mr. Adam Fritzsche for their invaluable cleanroom and device fabrication support.

Dr. Christine Schubert Kabban for her expertise and teaching abilities that equipped me with the statistical methods used in this research.

Mr. Greg Smith and Mr. Chris Sheffield for their kind, selfless, and unwavering laboratory and technical equipment support.

MAJ Christina Dugan for her timely help to perform x-ray photoelectron spectroscopy.

My fellow students, for their friendship, encouragement, humor, and the continuous reminder that we are connected in our failures and successes…and that somehow, with patience and persistence, we would ultimately succeed.

My parents, for fostering in me a passion for learning and equipping me with the faith and assurance that my Creator sustains me with His eternal love.

My children, for their innocent and unconditional love and reminding me to enjoy life during the PhD marathon.

Most of all to my wife, for her patient, selfless, and faithful love…and for being the confidence and hope that kept me going when I thought I could go no further.

James M. Sattler

Table of Contents

Page

I. Introduction 1

1.1 Multipactor Overview 1
1.2 Types of Multipactor 2
1.2.1 Two-Surface (Metallic) Multipactor 2
1.2.2 Single-Surface (Dielectric) Multipactor 4
1.3 Interest in Multipactor Research 6
1.4 Multipactor Suppression 7
1.5 Research Goal, Questions and Approach 12
1.6 Summary 14

II. Background 15

2.1 Historical Review 15
2.2 Factors Affecting Two-Surface Multipactor 27
2.2.1 Analysis of the Synchronism Condition 29
2.2.2 Secondary Electron Emission 35
2.3 Porous Surfaces for SEY Suppression 45
2.4 Visual Bibliography of Multipactor Research 46
2.5 Summary 49

III. Methodology 50

3.1 Semi-Empirical SEY Modeling of Porous Surfaces 50
3.1.1 Probability of Electron Escape for a Two-Dimensional Pore Model 53
3.1.2 Probability of Electron Escape for a Three-Dimensional Pore Model 55
3.1.3 Analysis of the Porous Surface SEY Models 58
3.2 Engineered Surface Designs and Fabrication 63
3.2.1 Design Considerations 63
3.2.2 Microporous Surface Designs and Fabrication 67
3.2.3 Nanoporous Surface Designs and Fabrication 69
3.3 Surface Characterization 75
3.4 SEY Measurements 76
3.5 AFRL Materials and Manufacturing Directorate SEY Measurement System 82
3.6 AFIT SEY Measurement System 85
3.7 Thermomechanical Effects on Porous Surfaces 95
3.8 Summary 96

IV. Results 97

4.1 Fabrication Results: Microporous Surfaces 97
4.2 Fabrication Results: Nanoporous Surfaces 106
4.2.1 Extreme-Optimized Photolithography (EOP) 106
4.2.2 Electron-Beam Lithography 115
4.3 Porous Surface Materials Characterization Results 120
4.3.1 Energy Dispersive X-ray Spectroscopy 120

4.3.2 X-Ray Photoelectron Spectroscopy ... 123
4.4 SEY Measurements ... 125
4.5 New SEY Measurement Chamber ... 130
4.6 Thermomechanical Simulation Results ... 136
4.7 Summary ... 137

V. Analysis ... 139

5.1 Generalized SEY Model for Roughened Surfaces ... 139
5.2 Analysis of Measured vs. Modeled SEY Data ... 142
5.3 Engineered Surface Designs for Multipactor Suppression ... 145
5.4 Summary ... 147

VI. Conclusions and Recommendations ... 149

6.1 Answers to Research Questions ... 149
6.2 Contributions ... 152
6.2.1 Geometrically Perfect Microporous Surfaces ... 152
6.2.2 Applying Nanosphere Lithography to SEY Control ... 152
6.2.3 New 2D Semi-Empirical SEY Model for Porous Surfaces ... 153
6.2.4 New 3D Semi-Empirical SEY Model for Porous Surfaces ... 153
6.2.5 Geometrically Perfect Nanoporous Surfaces ... 153
6.2.6 Extreme Temperature Effects on Micro- and Nano-Pores ... 154
6.2.7 New SEY Measurement System ... 154
6.3 Recommendations for Future Work ... 154
6.3.1 Sample Manipulator Repair and SEY System Calibration ... 155
6.3.2 SEY Study: Microporous/Nanoporous Surfaces ... 155
6.3.3 SEY Study: Grooved Surfaces on Silicon Wafer ... 155
6.3.4 SEY Studies: Laser-Patterned Grooved Surfaces ... 156
6.3.5 Grooved Surface Waveguide Simulation Study ... 156
6.4 Summary ... 156

Appendix A. Process Followers ... 158

Appendix B. Automated Heidelberg Mask-Writing Program ... 162

Appendix C. SEY Vacuum Chamber Procedures ... 165

Appendix D. SEY Measurement Procedures ... 169

Appendix E. SEY Chamber Bakeout Procedures ... 173

Appendix F. SIMION® Tutorial ... 176

Appendix G. MATLAB® Code ... 183

Bibliography ... 193

List of Figures

Figure Page

1. Illustration of the process for a two-surface (metallic), first-order multipactor. 3

2. Illustration of the process for a single-surface (dielectric) multipactor. 5

3. Microscope images of artificially roughened surfaces fabricated in 1937 by Bruining *et al.* using carbon soot deposited by a flame of burning turpentine (a) and spraying an alcoholic suspension of soot (b) [44]. 10

4. Illustration showing how engineered surfaces can control secondary electron emission (SEE): (a) SEE from a smooth surface; (b) recapture of SEE from an engineered porous surface. 11

5. Farnsworth's 1934 radio frequency electron multiplier tube design [33]. 16

6. Multipactor experiment setup used by Hatch and Williams in 1954 [76]. 20

7. Hatch and Williams multipactor susceptibility plots developed by experimental measurement (a), theory (b), and both measurement and theory (c) [76]. 20

8. Hatch and Williams susceptibility curves showing cutoff frequencies (vertical dashed lines) for various electrode separations [76]. 21

9. Secondary electron emission data for aluminum referenced by Hatch in his 1961 paper showing a typical SEY (δ) curve (top) and typical energy distribution (bottom) [79]. 22

10. Plot of secondary emission yield (δ) versus applied voltage for various angles of incidence for lithium (0° is normal incidence) [84]. 24

11. Obliquely incident electron paths associated with cross-field multipactor [48]. 25

12. Illustration of the relationships between the two fundamental multipactor processes, the factors that influence them, and the corresponding multipactor suppression techniques. 28

13. Range of emission phases for electrons contributing to multipactor [78]. 32

14. Example plot of multipactor susceptibility curves showing the minimum and maximum voltages for 3 different emission energies: 2 eV (solid line); 5 eV (dash-dot line); 10 eV (dashed line) [8]. 34

15. Secondary electron emission and its effect on current-voltage curves of a tetrode studied by Jonker [46].................... 36

16. Distribution data for secondary electron emission measured from a Ni target using normally incident 500 eV primary electrons: (a) energy distribution data; (b) angular distribution data [94].................... 38

17. General shape of the secondary electron yield (SEY) curves for each emission type involved in secondary electron emission [99]. 40

18. General shape of the secondary electron yield (δ) curve as a function of impact energy (E_i) [14]. 41

19. Porous surface study by Ye *et al.*: (a) modeled array of cylindrical pores; (b) scanning electron microscope images of Ye's pores (created using a silver etch process) that show distinct topographies for the non-pore and pore-bottom regions [70]. 46

20. Multipactor visual bibliography I – origins of research.................... 47

21. Multipactor visual bibliography II – modern theories. 48

22. Multipactor visual bibliography III – suppression by engineered surfaces. 48

23. Porous surface geometry used for 2D and 3D secondary electron yield (SEY) models: (a) distinct SEY parameters used in the weighted average model; (b) pore cross section showing distinct parameters for $\sigma_{\text{non-pore}}$ and $\sigma_{\text{pore-bottom}}$. 51

24. Illustration of the 2D pore model showing key parameters. 53

25. Illustration of the 3D pore model showing key parameters. 56

26. Comparison of the 2D and 3D porous surface SEY models showing the total SEY of the porous surface ($\sigma_{\text{porous-surface}}$), based on $\sigma_{\text{non-pore}} = 1.7$ and $\sigma_{\text{pore-bottom}} = 1.6$. 59

27. Comparison of the mean probability of electron escape from a cylindrical pore predicted by a 2D and 3D pore model. 60

28. Illustration of the inverse linear relationship between the total SEY of the porous surface and surface porosity, based on $\sigma_{\text{non-pore}} = 1.7$ and $\sigma_{\text{pore-bottom}} = 1.6$. 62

29. Illustration of the nonlinear relationship between the total SEY of the porous surface and pore aspect ratio, based on $\sigma_{non\text{-}pore} = 1.7$ and $\sigma_{pore\text{-}bottom} = 1.6$. 62

30. Square-based porous surface layout used to calculate *Porosity*. 64

31. Relationship between pore height and spacing for a square-based porous surface layout with *Porosity* = 0.5 and $A_R = 2.0$ (practical fabrication region circled). 65

32. Maximum porosity of pore layout patterns of interest: (a) square layout; (b) close-packed layout. 66

33. Microporous surface designs to be fabricated using an electroplating process. 68

34. Process for fabricating gold microporous surfaces using electroplating. 69

35. Extreme-optimized photolithography process to pattern sub-micron features. 70

36. Process to fabricate nanoporous surfaces using extreme-optimized photolithography (useful for *Porosity* < 0.25). 71

37. Nanoporous surface designs for electron-beam lithography. 73

38. Process to fabricate nanoporous surfaces using electron-beam lithography. 74

39. Illustration of the spherical collector method for measuring total SEY. 77

40. Illustration of the two-step method for measuring total SEY using a Faraday cup. 78

41. Illustration of the two-step method for measuring total SEY without a collector or a Faraday cup. 79

42. AFRL SEY measurement chamber (left); chamber interior with sample (right). 82

43. Ultra-High Vacuum chamber before conversion to a Secondary Electron Yield measurement system. 86

44. CAD model of the 5-axis sample manipulator made by UHV Design [108]. 88

45. Kimball Physics model ELG-2 electron gun with 1 eV to 2 keV energy range (top), optional tip-mounted Faraday cup (top insert), and controller (bottom)........ 89

46. Close-up photo of the new AFIT secondary electron yield (SEY) measurement system's sample manipulator and Faraday cup. 90

47. Kimball Physics phosphor screens (left); Kimball Physics photo of illuminated phosphor screen (right). 91

48. SIMION® screenshot showing the ELG-2 and a simulated beam shape for 2000 eV electrons. 92

49. SIMION® output file showing the e-gun settings that result in a minimum spot size (circled in red). 92

50. CoventorWare® thermomechanical model of a 10µm deep, 10µm diameter gold micro-pore used to determine changes caused by thermal expansion and contraction. 95

51. Photolithography mask layout used to fabricate microporous surfaces (left) and individual sample dimensions (right). 97

52. Photograph of the final microporous photolithography mask, which took eight individual mask-write "sessions" performed over the course of 7 days. 99

53. Photograph of the first attempt to electroplate the microporous samples: wafer patterned with "AZ 9260" photoresist (left); electroplated gold delamination (right). 100

54. Photograph of the five microporous samples successfully fabricated and ready for characterization. 101

55. Scanning electron microscope images of microporous samples 1-1 (top), 2-1 (middle), and 3-1 (bottom) showing excellent pattern consistency and pore yield. 102

56. Scanning electron microscope images of microporous sample 1-1 showing minor pore sidewall breakdown. 103

57. Scanning electron microscope images of microporous sample 1-2 showing pore deformation and sidewall breakdown. 103

58. Scanning electron microscope images of microporous sample 2-1 showing excellent pattern consistency and near-perfect cylindrical pore geometry. 104

59. Scanning electron microscope images of microporous sample 3-1 showing excellent pattern consistency and near-perfect cylindrical pore geometry. 105

60. Scanning electron microscope images of microporous sample 3-2 showing excellent pattern consistency and near-perfect cylindrical pore geometry. 105

61. Mask layout designed for the Heidelberg exposure study consisting of 40 reticles of each of three designs (left); photo of the final mask (right). 107

62. Mask layout designed for the Heidelberg exposure study consisting of 40 reticles of each of three designs (left); photo of the final mask (right). 109

63. Microscope images of the nanoporous mask created by the 1-µm Heidelberg (left) and corresponding 1818 photoresist patterns created using the nanoporous mask and AFIT's EVG® UV photolithography exposure system. 110

64. Nanoporous surfaces fabricated with extreme-optimized photolithography. 111

65. SEM images of patterned 1818-SF11 photoresist layers showing undesired UV exposures in the center of the photoresist pillars caused by a diffraction pattern that is established by the mask windows (NOTE: these patterns have a 200Å cold-sputtered gold layer to facilitate SEM imaging). 113

66. SEM image of sample EOP-2 showing the undesired mask-diffraction effects that occur during UV exposure of the 1818 photoresist; the two small anomalies are gold-covered photoresist plugs that remained following the metal liftoff. 114

67. Microscope image of the highest quality test-coupon fabricated during the e-beam exposure study (left); SEM images of the highest porosity samples that were destroyed during the gold-liftoff procedure. 116

68. SEM images of nanoporous gold surface regions – taken from the highest quality test-coupon fabricated during the e-beam exposure study. 117

69. Key dimensions of nanoporous gold surface regions taken from the best e-beam lithography test-exposure coupon. 117

70. Large-area (~20×20 mm^2) pattern of sample EBL-2 before performing the gold-liftoff (left) and after performing the gold-liftoff (right). 118

71. SEM image of the ~20×20 mm^2 sized sample EBL-2 showing excellent pore shape, size, spacing, and pattern consistency. 119

72. SEM images of various locations from the large-area sample EBL-2 showing the varying degree of pore-plug residue that remained after performing the gold liftoff. 119

73. Bulk composition analysis of the sputtered (top) and electroplated (bottom) reference samples obtained using Energy Dispersive x-ray Spectroscopy (EDS). 121

74. Win X-Ray Monte Carlo simulation performed 10,000 times using 20 keV electrons at a beam current of 20 μA directed towards a gold surface. 122

75. Surface elemental composition of the sputtered and electroplated reference samples obtained using X-ray photoelectron spectroscopy with a Mg K_α x-ray source. 124

76. Secondary electron yield (SEY) measurements of microporous gold surfaces obtained using the Air Force Research Laboratory SEY measurement chamber (Error bars show 2 standard deviations above and below the sample mean) 126

77. Key regions of secondary electron yield (SEY) measurement curves: low-energy region with first SEY crossover (left); SEY-maximum region (right). 127

78. Secondary electron yield measurements of gold reference samples with error bars showing two standard deviations above and below the sample mean (left); SEM image showing differences between sputtered and electroplated gold topographies (right). 128

79. Comparison of 2D and 3D secondary electron yield (SEY) model predictions to SEY measurements of microporous gold surfaces (Error bars shows 2 standard deviations above and below the sample mean) 129

80. Mechanical drawings of the rotary feedthrough used to actuate the Faraday cup on the ELG-2 electron gun [112]. 131

81. AFIT's first dedicated secondary electron yield (SEY) measurement system. 132

82. Metallic battery enclosure designed to provide a -27 Volt DC bias to the sample with minimal current leakage. 133

83. Secondary electron yield (SEY) measurements of the microporous gold reference samples obtained with the new AFIT SEY measurement chamber. 134

84. Plots of the sample leakage currents measured while performing SEY measurements of the two gold reference samples... 135

85. Periodically patterned surface based on unspecified features used for developing a general SEY model for engineered surfaces. 140

86. Grooved surface topography for multipactor suppression, feasible with a laser ablation process. 141

87. Plot of semi-empirical 3D SEY model predictions based on the gold reference SEY data collected and the specific dimensions of the microporous samples fabricated in this effort (Note: the proposed design has *Porosity* = 0.5 and A_R = 2.0. 142

88. Plot of 3D SEY model predictions with experimentally measured maximum SEY values overlaid. 144

List of Tables

Table Page

1. Secondary electron yield data for metals arranged by atomic number [93]. 43

2. Secondary electron yield data for various materials [94]. 44

3. Effects of physical and environmental factors on secondary electron yield [37]. 45

4. Range of achievable porous surface design parameters using extreme-optimized photolithography (EOP). 72

5. Total number of 200 nm diameter pores to be individually exposed by electron-beam lithography for various surface sizes. 74

6. Equipment necessary for measuring total SEY using the Faraday cup method. 81

7. Magnitude of electron deflection in the AFRL SEY measurement system (assuming a 50 mm working distance) caused by the Earth's magnetic field. 85

8. ELG-2 settings that minimize beam spot size at a 20 mm working distance. 93

9. Magnitude of electron deflection in the AFIT SEY measurement system (assuming a 20 mm working distance) caused by the Earth's magnetic field. 94

10. Photolithography pattern-file sizes for microporous samples. 98

11. Microporous surface fabrication results. 106

12. Results of the Heidelberg mask-writing exspoure study. 108

13. Nanoporous surface fabrication results achieved with Extreme-Optimized Photolithography. 114

14. Nanoporous surface fabrication results obtained with e-beam lithography........ 120

15. Thermomechanical effects of extreme temperatures on a gold micro/nano-pore. 137

16. Design estimates for multipactor-free porous surfaces of various metals. 147

List of Abbreviations

Abbreviation Page

2D: Two-Dimensional ... 53

3D: Three-Dimensional ... 55

AFB: Air Force Base ... 85

AFIT: Air Force Institute of Technology ... 13

AFRL: Air Force Research Laboratory ... 68

CAD: Computer-Aided Design ... 87

CF: ConFlat ... 86

CNT: Carbon Nanotube ... 86

DC: Direct Current ... 17

DUV: Deep Ultraviolet ... 72

E-beam: Electron beam ... 69

EDS: Energy Dispersive x-ray Spectroscopy ... 76

E-gun: Electron gun ... 83

EOP: Extreme-Optimized Photolithography ... 70

ESA: European Space Agency ... 9

FD: Feature Density ... 139

IGRF: International Geomagnetic Reference Field ... 83

IRE: Institute of Radio Engineers ... 23

JPL: Jet Propulsion Laboratory ... 25

K.E.: Kinetic Energy ... 83

MULCOPIM: Workshop on Multipactor, Corona and Passive Intermodulation ... 27

NASA: National Aeronautics and Space Administration 9

NOAA: National Oceanic and Atmospheric Administration 83

PIC: Particle-In-Cell 27

PMTs: Photomultiplier Tubes 16

RF: Radio Frequency 1

RIE: Reactive Ion Etch 70

SEE: Secondary Electron Emission 3

SEM: Scanning Electron Microscope 45

SEY: Secondary Electron Yield 3

UHV: Ultra-High Vacuum 40

UV: Ultraviolet 109

VED: Vacuum Electron Device 9

W.D.: Working Distance 85

WMM: World Magnetic Model 83

XPS: X-ray Photoelectron Spectroscopy 76

ENGINEERED SURFACES TO CONTROL SECONDARY ELECTRON YIELD FOR MULTIPACTOR SUPPRESSION

I. Introduction

This chapter introduces the topic of multipactor and provides the scope and objectives of this research effort. The first section briefly describes multipactor, including why it is significant. The second section defines the two types of multipactor and breaks down the physical process involved in each type. The third section discusses the level of interest in multipactor research, including the industries focused on understanding and controlling this phenomenon. The fourth section presents the topic of multipactor suppression. The chapter concludes with the scope and objectives of this research effort.

1.1 Multipactor Overview

Multipactor is a complex and potentially destructive phenomenon that can occur in microwave and radio frequency (RF) circuits under high, ultra-high, and extremely high vacuum conditions. Often described as an "avalanche" of electrons, multipactor consists of a rapid growth in free electrons under the influence of a time-varying electric field [1]–[5]. The electron avalanche typically peaks at a steady-state level (referred to as saturation), within 50 to 300 RF cycles producing electron densities on the order of 10^{11} to 10^{12} cm^{-3} [5], [6]. There are numerous undesired effects caused by multipactor including

1) microwave cavity loading and detuning [7]–[10],
2) substantial RF power dissipation [7]–[11],
3) generation of harmonics [9], [10],

4) noise enhancement [8]–[10],
5) localized heating and out-gassing of exposed surfaces [7]–[11],
6) breakdown or microwave discharge [7], [8], [10], [12], [13], and
7) damage to RF windows or RF circuit components [7]–[10].

An important aspect of multipactor is the wide range of frequencies (MHz to GHz) and geometries in which it can occur [8], [14]. Consequently, multipactor is a critical problem affecting particle accelerators and space–based communication systems because of their use of microwave circuits in a vacuum environment [9], [15]–[17].

1.2 Types of Multipactor

Given the two primary requirements necessary for multipactor (vacuum and a high frequency electric field), there exist a wide variety of environments and conditions under which multipactor can occur. To better distinguish different varieties of multipactor, two distinct types are defined: two-surface (metallic) and single-surface (dielectric). The first observations of multipactor were of the two-surface type [18]. This may help explain why two-surface multipactor has been studied significantly more than single-surface multipactor [19].

1.2.1 Two-Surface (Metallic) Multipactor

Two-surface multipactor involves a metallic gap and an applied high frequency electric field while under vacuum. In his seminal paper on multipactor, Rodney Vaughan describes two-surface multipactor as “a sheet-like cloud of electrons oscillating between two surfaces, driven by and in synchronism with an RF field” [7]. Figure 1 provides an

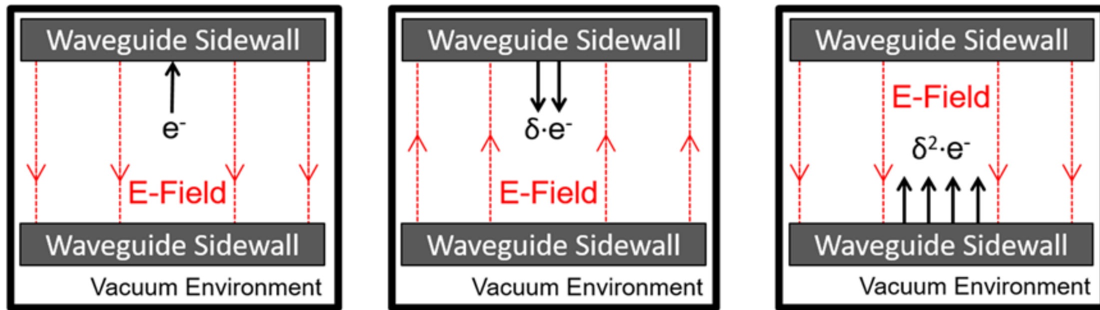

***1.** A seed electron is accelerated by a time-varying electric field (E-Field) into a sidewall.*

***2.** The impact causes the emission of δ secondary electrons, which are accelerated toward the opposite sidewall by the now-reversed E- Field.*

***3.** The impact of the δ secondaries causes δ·δ secondaries to be emitted. The process continues leading to an avalanche of electrons.*

Figure 1: Illustration of the process for a two-surface (metallic), first-order multipactor.

illustration of the two-surface multipactor process. The process initiates when one or more seed electrons (also known as *initial* or *primary* electrons) are positioned in the gap. Sources of seed electrons include:

1) field emission from a macroscopic irregularity on a sidewall [16], [20], [21],
2) electrons native to the space environment (i.e. Van Allen radiation belts or space weather events) [9],
3) electrons released via the photoelectric effect from the sidewalls of microwave components in particle accelerators [9], and
4) electron cascades produced by cosmic rays [16], [20], [21].

Once established in the gap, the seed electron is accelerated towards one of the sidewalls by the RF electric field oriented perpendicular to the sidewalls (Figure 1a). Upon impact with the sidewall, the seed electron causes secondary electrons to be emitted under a process called secondary electron emission (SEE). If the sidewall material has a secondary electron yield (SEY) that is greater than unity ($\delta > 1$), the number of secondary electrons

will be greater than the number of incident electrons (Figure 1b). If the secondary electrons are emitted in synchronism with the reversal of the RF electric field, they will be accelerated toward the opposite sidewall. Upon impact with the opposite sidewall, the secondary electrons stimulate new secondary electrons based on the SEY (δ) of the opposite sidewall (Figure 1c). If the electron transit time across the gap is equal to half the period of the RF electric field, the process will be repeated continuously leading to an avalanche of electrons. For example, a single electron in a waveguide constructed with material having an SEY = 2, would grow to $2^{50} \approx 10^{15}$ electrons after only 50 RF cycles. Because the phenomenon requires SEE to occur in resonance with an RF field, two-surface multipactor is also referred to as "secondary electron resonance" and "resonance secondary electron emission" [18], [22], [23].

1.2.2 Single-Surface (Dielectric) Multipactor

By contrast, single-surface multipactor involves a dielectric surface, a high frequency electric field oriented parallel to the dielectric surface, and high vacuum pressures or lower [19], [24]. This type of multipactor is common in high power microwave systems and linear accelerators because of the use of RF windows [8], [24]–[29]. The primary difference between two-surface and single-surface multipactor is the dielectric material. Unlike metals, which tend to be very good electrical conductors, dielectrics can possess a fixed charge distribution. Thus, when the dielectric emits secondary electrons, a net positive charge forms at the dielectric surface, which establishes a static electric field. This static electric field acts to draw electrons back to the dielectric where they can generate additional secondary electrons. Figure 2 provides an illustration of the single-surface multipactor

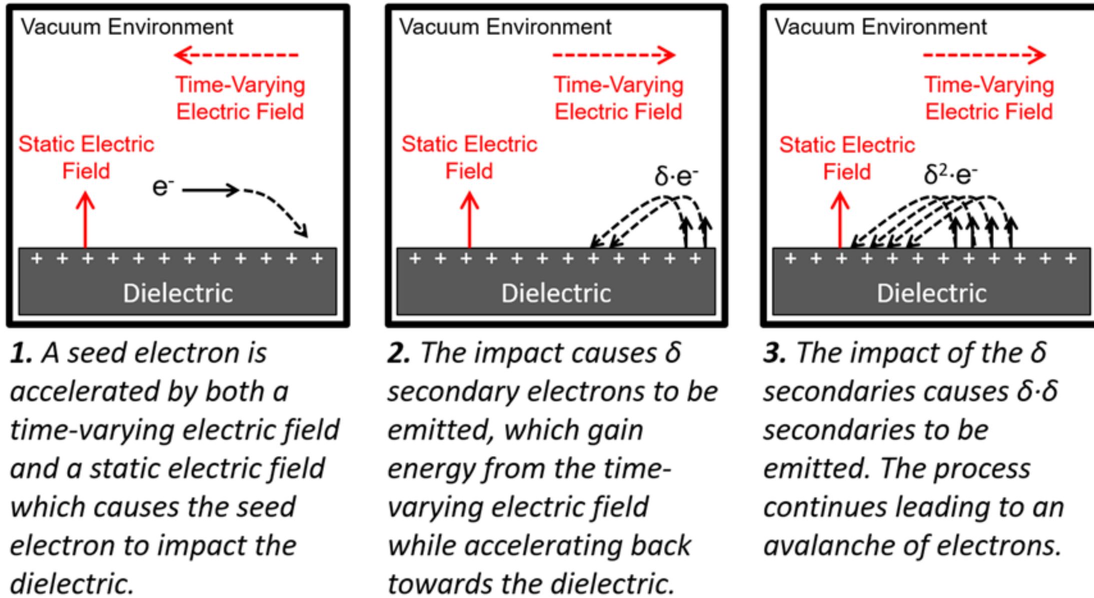

Figure 2: Illustration of the process for a single-surface (dielectric) multipactor.

process. The process initiates in a similar manner as two-surface multipactor: one or more seed electrons are positioned near the dielectric surface. The seed electron, under the influence of the time-varying electric field, gains energy as it accelerates parallel to the dielectric surface. If the dielectric contains a region of positive surface charge, the seed electron's trajectory will bend toward the surface (Figure 2a). Upon impact, the seed electron can initiate secondary electron emission. If the SEY of the dielectric material is greater than unity ($\delta > 1$), there will be more secondary electrons than incident electrons. Once emitted, the initial velocity of the δ secondary electrons moves them away from the dielectric surface. These free electrons gain energy from both the RF and static electric fields as they accelerate on a trajectory towards the positively charged dielectric (Figure 2b). Upon impact, the δ secondary electrons initiate the emission of δ^2 secondary electrons (Figure 2c). As this routine plays out, an avalanche of electrons is created which transfers

substantial energy from the RF electric field directly to the dielectric surface. This energy causes localized heating that can lead to dielectric window cracking and failure [18], [19]. Because the RF electric field runs parallel with the dielectric surface, new secondary electrons are always able to gain energy from the RF electric field, regardless of the electric field's phase angle. Thus, the resonance condition necessary for two-surface multipactor, is absent from the typical single-surface multipactor [8], [18]. It should be noted that single-surface multipactor can involve an RF electric field oriented perpendicular to the dielectric surface – an example of this is a dielectric tube [30]. In such cases, the perpendicular RF field can drive a resonance condition between the RF period and the electron trajectory duration [30]. However, most cases of single-surface multipactor do not involve such a resonance condition. Ultimately, the removal of this resonance condition in most single-surface cases tends to increase the difficulties associated with preventing multipactor damage to dielectrics used in vacuum RF systems [8], [31].

1.3 Interest in Multipactor Research

Although multipactor has been studied for nearly a century, it has received relatively little attention in the broader scientific and engineering communities, failing to even be recognized in textbooks [7], [19]. The author attributes this "limited publicity" to three primary reasons:

1) multipactor failed to gain widespread acceptance as a useful scientific or engineering application [7], [16];

2) undesired multipactor events affect a small set of unique scientific and commercial industries that range from particle accelerators and magnetically confined fusion apparatus to vacuum electronic devices and space-based systems [8], [14], [16];

3) the few commercial industries that must account for multipactor label significant portions of their research as proprietary [8], [14].

Recently, interest in multipactor research has been growing on both the application and prevention fronts. Applications that have been studied include electron gun technology, plasma display technology, and sensitive receiver protection [8], [32]. In fact, the first publication describing multipactor was an attempt to use the phenomenon to amplify low intensity television signals [33]. However, the vast majority of multipactor research has been, and continues to be, focused on prevention [7], [16]. This prevention-focused tendency may be best summarized by Rodney Vaughan, who wrote in his landmark paper, "multipactor in this sense is recognized as being far more often damaging than beneficial" [7]. Despite the historically narrow applications of multipactor research, its interest is on the rise as modern demand for better and more capable space-based communication networks have increased the need for higher power, multicarrier communications satellites which are at increased risk to multipactor [3], [16]. This increased demand has driven a growing appetite in the satellite design community, to develop better tools and solutions to suppress multipactor in satellite payloads [31], [34].

1.4 Multipactor Suppression

As Vaughan points out, the majority of multipactor research is conducted to find methods of suppression [7]. A critical factor in multipactor suppression is the type of multipactor that might occur (dielectric or metallic). Historically, multipactor suppression follows three primary approaches.

1) Conditioning – a process whereby a controlled multipactor is intentionally initiated to remove adsorbed gas and other non-native materials from the

surface which lowers the SEY and prevents the occurrence of a future multipactor [8], [18], [28], [35]–[37].

2) Surface Coatings – lowering the SEY of the exposed surface by coating the original surface with a low-SEY material can restrain the electron avalanche [7], [8], [18], [28], [35], [38], [39].

3) Geometrical Modifications – changing the physical layout of an RF system (*e.g.* electrode separation or RF window location) to impose unfavorable multipactor conditions [7], [8], [35], [38], [39].

Although conditioning can provide effective suppression, it is a lengthy and time-consuming process that requires the equipment necessary to initiate a multipactor [8], [35]. Surface coatings may be the most thoroughly researched method but cannot be applied in all situations and are often plagued by degradation over time [8]. Geometrical modifications are perhaps the most widely favored suppression method due to their simplicity and effectiveness [7], [8]. However, there are many situations where design constraints render geometrical modifications impossible, spurring the need for other effective suppression methods. Beyond the three primary suppression methods (which approach suppression passively), other more active methods have been explored. These methods include applying static electric or magnetic fields to alter electron trajectories or applying RF power abruptly to raise the electric field strength above the multipacting zone [35], [39], [40]. Another, more exotic passive method of suppression involves filling empty spaces of the discharge region to reduce the mean free path of the electrons [38].

Multipactor suppression is also pursued using a more systematic approach involving the development and refinement of design and test standards that ensure production systems are multipactor free [31], [34], [41]. This approach is essential when dealing with space-based systems where a single multipactor event can destroy a satellite with no hope

of repair. The European Space Agency (ESA), National Aeronautics and Space Administration (NASA), and many commercial organizations have developed or adopted stringent design principles and rigorous testing methods to develop multipactor-free systems [31], [34], [41]. The most proven design principle is the use of power margins which involves restricting the maximum power of a system to an acceptable margin below the multipactor threshold [31], [34], [41]. Power margins solve the problem of multipactor by limiting the electric field strength, which reduces the SEY, preventing the secondary electron avalanche. The tradeoff with power margins is the self-imposed constraint that power will be limited to below some pre-determined threshold, even though the system can provide more capability when operating above that threshold. Ultimately, this “multipactor design-and-test” approach has led to more reliable systems based on conservative power margins [31], [34], [41]. However, as more powerful and more complicated multicarrier communication satellites are designed, multipactor prevention via power margin design and test becomes more challenging and expensive and can lead to overly conservative margins [16], [42], [43].

This research investigates a promising suppression method that has historically received little attention. This method involves artificially roughening or engineering a surface to reduce the SEY of a surface. During the 1930s and 1940s, research exploring methods to control SEE in vacuum electron devices (VEDs) demonstrated the first use of this method to reduce the SEY of metallic surfaces [37], [44]–[46]. In order to artificially roughen a surface these pioneering researchers used various techniques including burning turpentine to deposit a carbon soot layer, spraying a carbon soot suspension, and depositing various metals through sublimation or evaporation [37], [44], [45]. However, these SEY

reductions were difficult to precisely control due to the crude surface engineering methods available at that time. Figure 3 shows microscope images of two of these artificially roughened surfaces, fabricated in 1937 by Bruining *et al.* (the agglomerated particles in Figure 3b were assessed to be ~100 μm in diameter) [44]. A subsequent investigation into this method was studied by R. Hayes 50 years ago as part of an effort to raise the power handling capacity of RF windows used in high-power microwave tubes [18]. According to the theory provided in their final report, grooving the surface of a dielectric RF window suppresses single-surface multipactor "if the grooves are perpendicular to the direction of the electric field" [18]. Their experiments involving 1.50, 0.75, and 0.37 mm sized grooves in alumina (Al_2O_3), beryllia (BeO), and quartz (SiO_2) windows, provided encouraging results for single-surface multipactor suppression [18]. Of note, they report better suppression results using the smallest groove size and when the grooved alumina window crests are coated with titanium suboxide (TiO_x, where $1 < x < 2$) [18].

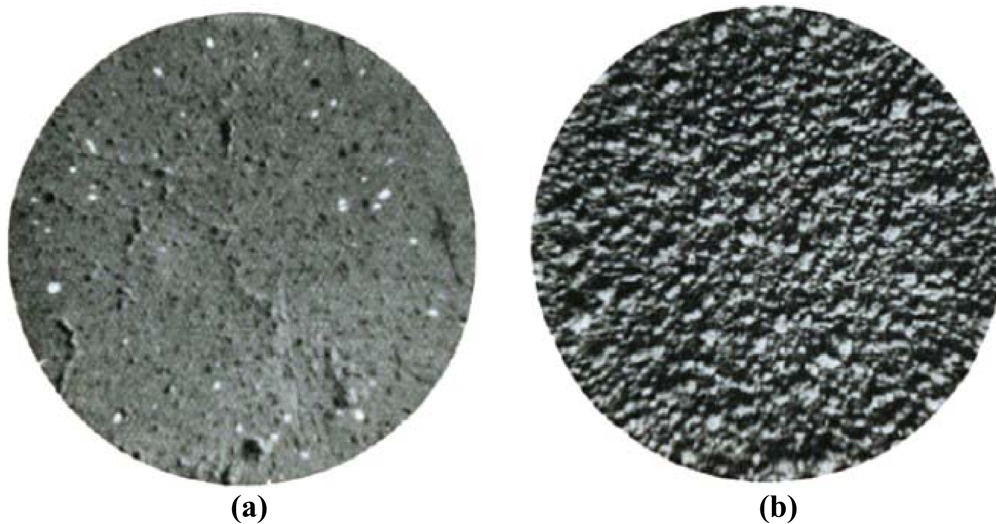

Figure 3: Microscope images of artificially roughened surfaces fabricated in 1937 by Bruining *et al.* using carbon soot deposited by a flame of burning turpentine (a) and spraying an alcoholic suspension of soot (b) [44].

Despite the obvious potential for multipactor suppression provided by the previous two research examples, the vast majority of multipactor suppression research has focused on other methods [26]–[29], [35], [36], [38], [47]–[67]. Only in the last ten years has there been a revitalization of research focused on using engineered surface topographies to control SEE for multipactor suppression [10], [39], [68]–[75]. A primary reason for this is the widespread ability to engineer the surface topography of a material down to nanometer-sized features using modern micro- and nano-structure fabrication techniques. Figure 4 illustrates how an engineered surface can control SEE by creating opportunities for the recapture of secondary electron emissions. Advantages of this approach to multipactor suppression include the relaxing power restrictions and avoiding geometrical alterations that are not always practical. Several recent research efforts involving both modeling and experiment of engineered surfaces have shown tremendous promise for reducing the SEY of both metals and dielectrics [10], [39], [70]–[75]. However, because this approach is

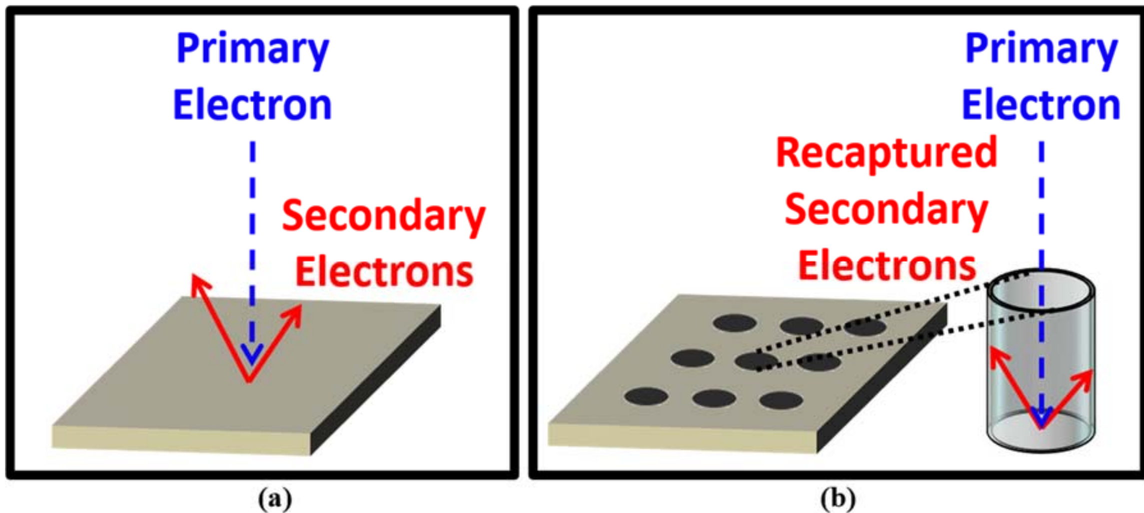

Figure 4: Illustration showing how engineered surfaces can control secondary electron emission (SEE): (a) SEE from a smooth surface; (b) recapture of SEE from an engineered porous surface.

relatively new and unstudied, additional research is necessary to prove the concept and determine optimum surface topographies. The illustration in Figure 4b indicates that the amount of SEE recapture will depend on two important parameters: (1) the surface density of pores, which is known as *porosity* (i.e. how tightly spaced are the pores) and (2) the *aspect ratio* of the pores (i.e. the ratio of pore height to pore diameter). Consequently, these two variables are hypothesized to be the critical design parameters in the development of engineered surfaces for SEY control. However, this hypothesis must be verified through a comprehensive study involving both theoretical modeling and experimental measurements.

1.5 Research Goal, Questions and Approach

When undertaking a long and difficult research effort, it is important to identify a clear and concise goal for the effort. The goal provides overarching guidance and leads to the formulation of specific questions that, when answered, achieve the goal. Those specific questions also lay out a research approach consisting of specific objectives that provide a roadmap for the researcher.

The goal of this dissertation is to determine optimal surface topographies to control the secondary electron yield for the purpose of multipactor suppression.

Below are five questions that should be answered to achieve this goal.

1) What is the relationship between total SEY and porous surface parameters of <u>aspect ratio</u> and <u>porosity</u>?

2) Does the absolute feature size of a patterned surface play a critical role in controlling SEY (i.e. how do microporous surfaces compare to nanoporous surfaces with regard to total SEY when they have equivalent feature aspect ratio and spacing)?

3) What are the research community recognized (i.e. published) SEY measurement methods and what are their tradeoffs? This question is necessary

because a significant part of this dissertation will involve designing and constructing a new SEY measurement system for the Air Force Institute of Technology (AFIT).

4) Can existing micro- and nano-fabrication techniques create large-scale topographies of consistently spaced and sized pores or other features and if so, what are these techniques?

5) How do extreme changes in temperature modify the topography of a porous surface and affect the ability of the porous surface to control SEY?

The answers to these questions will enable significant progress toward multipactor suppression through engineered surfaces. The research approach needed to answer these questions involves eight intermediate objectives.

1) Develop and analyze an SEY model for a porous surface assuming a 90° angle of incidence for the primary electrons.

2) Design microporous and nanoporous surfaces with varying aspect ratios, pore spacing, and pore sizes.

3) Develop a fabrication process and fabricate the microporous and nanoporous surfaces

4) Characterize the pore size, shape, consistency, and chemistry of the fabricated surfaces.

5) Construct an in-house SEY measurement system.

6) Perform SEY measurements of the fabricated surfaces at a 90° angle of incidence.

7) Analyze the results to validate or refine the proposed SEY model for porous surfaces.

8) Determine an optimal porous surface design for multipactor suppression.

The scope of this research is evident from the aforementioned approach and includes the design, fabrication, characterization, and testing of engineered surfaces to validate a new

SEY model in addition to designing, purchasing, constructing, and validating a new SEY measurement system. Although not explicitly included in the research questions or approach, multipactor suppression remains the overarching goal. As a new area of research for the Air Force Institute of Technology, these five questions and eight objectives provide a well-focused initial effort that can easily be expanded to include other materials (*e.g.* Ag, Cu, Al, and Stainless Steel), topographies, and non-normal angles of incidence as follow-on work.

1.6 Summary

This chapter introduced the topic of multipactor beginning with why it is a subject of interest for satellites, VEDs, and particle accelerators. The two distinct types of multipactor were described: two-surface (metallic) and single-surface (dielectric). A short discussion on multipactor research interest was provided, which provided an explanation for the historically small amount of interest in this subject. An overview of the primary multipactor suppression approaches and techniques was given along with the unique approach pursued in this effort which has until recently been largely ignored. Finally, the overarching goal of this research effort was presented, along with research questions and objectives that provide the approach and scope of this dissertation.

II. Background

This chapter provides an in-depth review of the published literature on multipactor and SEE. Section 2.1 provides a historical review of the multipactor phenomenon from its first observations to the present. Section 2.2 discusses key factors that affect two-surface multipactor including the synchronism condition necessary for two-surface multipactor and a background on the SEE phenomenon and the critical role it plays in multipactor. Finally, Section 2.3 provides background on recent efforts to use porous surfaces to suppress SEY for multipactor suppression.

2.1 Historical Review

The first known observation of the multipactor phenomenon occurred in 1924 by C. Gutton during experimental investigations into low-pressure gas breakdowns at high frequencies (1 to 100 MHz) [76]. Subsequent work by Kirschner (1925) as well as C. Gutton and H. Gutton (1928) and H. Gutton (1930) provided additional details on this new phenomenon. However, it is unclear if these pioneering experimentalists in the field of gas breakdown knew the underlying mechanism behind their observations [14]. In 1934, in an effort to design better television systems, P. T. Farnsworth published his idea for an amplifier that made use of the phenomenon observed by the Guttons and Kirschner [33]. Farnsworth reported on "a new method of amplifying very feeble electric currents by making use of secondary electron emission," a method he titled "Secondary Electron Multiplication" [33]. For accurately describing the phenomenon first reported on by C. Gutton ten years prior, Farnsworth is often credited as the first to "recognize," "identify,"

or “discover” the multipactor phenomenon [7], [8], [16]. The process described by Farnsworth involves repeated occurrences of SEE as the source of electron amplification, similar to the method of electron current amplification provided by photomultiplier tubes (PMTs). However, whereas PMTs use electrodes (called dynodes) biased with constant voltage, Farnsworth’s design used RF-biased electrodes operating at 50 MHz (see Figure 5). Although Farnsworth viewed this phenomenon as a useful signal amplification method, he also reported on the ability of these oscillations to destroy the tube [33]. Farnsworth eventually demonstrated his electron multiplication tubes in Chicago at a 1936 meeting of the Institute of Radio Engineers, referring to the devices as “Multipactors” [77]. However, by the late 1930s, researchers had identified a saturation mechanism attributed to space charge forces that ultimately limited the success of Farnsworth’s “Multipactors” for use in electron amplification [14], [78]. By the 1940s, the term “multipactor” had been transferred from Farnsworth’s devices to a term describing the phenomenon of secondary electron resonance [7].

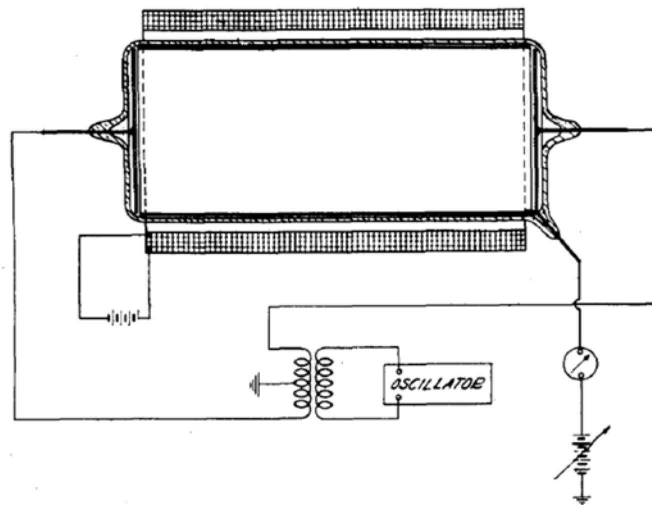

Figure 5: Farnsworth’s 1934 radio frequency electron multiplier tube design [33].

During the 1930s, while Farnsworth was attempting to use multipactor for television signal amplification, researchers exploring low-pressure discharges at high frequencies began to propose theories to describe multipactor. Henneburg, Orthuber, and Steudel published one of the earliest well-known theories in 1936. Their publication provided three important theoretical contributions for two-surface multipactor, based on the assumption that the secondary electrons are emitted with zero velocity [8], [14], [79].

1) They derived the resonance condition on the electron transit time across the two-surface gap [8].

2) They identified the RF electric field conditions necessary to support a stable multipactor [14].

3) They reported on a "phase-focusing" mechanism that leads non-resonant electron emissions toward a resonant phase over several half-cycles [8], [14], [79].

Although their emission velocity assumption was eventually refuted, their work provided an early reference for future multipactor studies. A subsequent study conducted by Danielsson in 1943 provided a theoretical analysis of previous gas breakdown experiments conducted by Backmark and Bengston [76]. In his analysis, Danielsson proposed a breakdown mechanism that closely resembles the two-surface multipactor description provided previously in Section 1.2.1. The mechanism proposed by Danielsson's was appropriately labeled "secondary-electron resonance breakdown," which provided an alternate and more descriptive term for multipactor [76].

In the late 1940s, Gill and von Engel performed a series of experiments on low-pressure (~1 mTorr) RF discharges and noted a curious property. At pressures above rough vacuum (i.e. greater than 1 mTorr), gas discharges were found to be similar for electrodes whether biased using a direct current (DC) or an RF voltage [80]. However, at rough vacuum

pressures and below, initiating a DC discharge might require thousands of volts, whereas an RF discharge could be initiated with as little as a hundred volts [80]. Gill and von Engel correctly postulated that a secondary electron resonance mechanism was enabling these low pressure RF discharges to occur at relatively low voltages [76]. Their 1948 publication is considered to be the first systematic study of multipactor and, although it supported Danielsson's broad concept of secondary electron resonance, it contained several important mathematical differences [76]. In their paper, Gill and von Engel laid out clear evidence supporting the theory that the electron growth necessary to attain a low pressure gas discharge, occurs by secondary emission and not from gas ionization [80]. They demonstrated this by showing the breakdown field for a high frequency gas discharge under low pressure is independent of the gas type and pressure [76], [80]. Furthermore, Gill and von Engel used experimental results to outline regions of multipactor susceptibility (now called susceptibility curves). Perhaps most importantly, Gill and von Engel invalidated the emission velocity assumption used by Danielsson and Henneburg *et al.* by demonstrating the sensitivity of these regions to non-zero emission velocities [8]. Rather than replace the zero velocity emission assumption with a complicated distribution of random emission velocities, Gill and von Engle introduced a constant parameter k, equal to the ratio of the secondary's impact velocity to their emission velocity [14]. Although there is no physical basis for the assumption behind this new parameter, it is a useful simplification for determining discharge conditions in terms of external parameters such as applied voltage magnitude/frequency and electrode separation [8], [76], [81]. This is because k does not depend on these external parameters, although it does depend on the secondary emission

properties of the electrode material [81]. Multipactor theory based on this assumption is now referred to as the "constant-*k*" theory [8], [81].

The next milestone in multipactor theory development came in 1954 when Hatch and Williams published follow-on results to Gill and von Engel. Hatch and Williams continued using two important assumptions from Gill and von Engel: the constant-*k* assumption and the assumption that secondary electron velocities are normal to the electrode surfaces [76]. However, using a new experimental technique, Hatch and Williams were able to measure the upper breakdown curve, which enabled the first complete plots of the multipactor susceptibility regions previously developed by Gill and von Engel [76]. Figure 6 shows the experimental setup used by Hatch and Williams in their 1954 publication. An important achievement for Hatch and Williams was the agreement attained between theory and experimental measurements, a problem that plagued Gill and von Engel [8], [81]. Figure 7 illustrates the good agreement Hatch and Williams obtained between measurement and theory. Another contribution from their paper was further demonstration of the relation between cutoff frequency and electrode separation as shown in Figure 8. In 1958, Hatch and Williams published follow-on work that expanded their theory to include higher-order modes up to 9/2-cycle. They also introduced a new parameter called the frequency-gap, or "*fd*", representing the applied voltage frequency times the electrode separation [82]. This new parameter allowed for comparisons of multipacting data over a wide range of conditions, simplifying the process to characterize a specific system for multipactor [82]. The utility of the Hatch and Williams theory for constructing multipactor susceptibility curves established their work as the cornerstone of multipactor theory for decades to come [8].

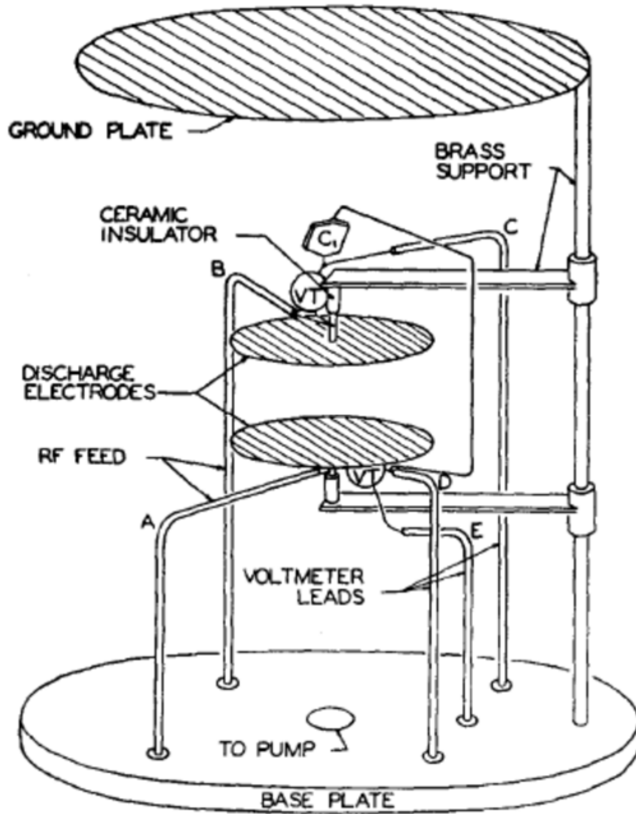

Figure 6: Multipactor experiment setup used by Hatch and Williams in 1954 [76].

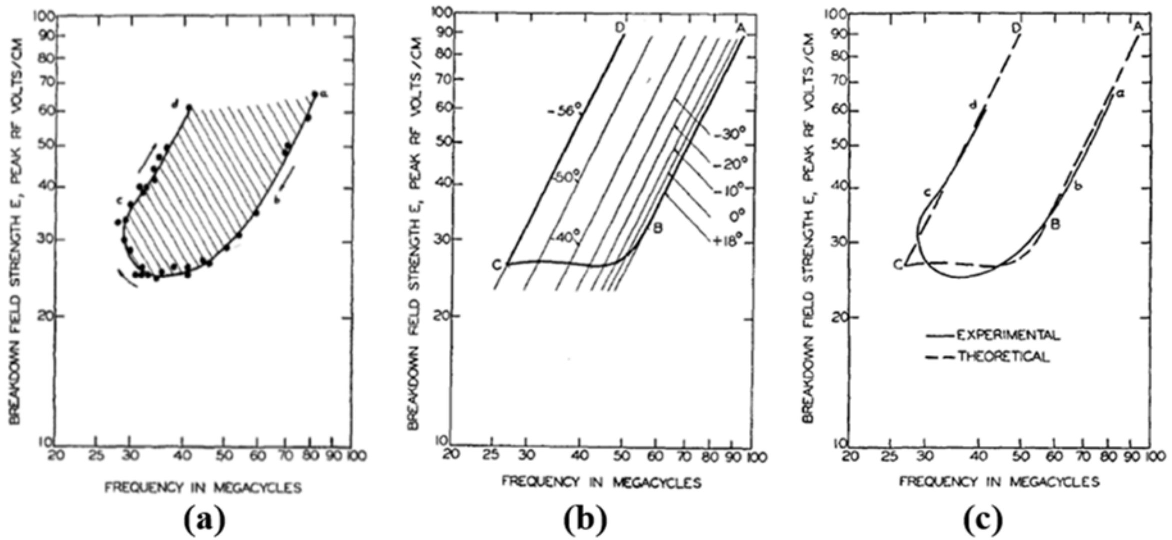

Figure 7: Hatch and Williams multipactor susceptibility plots developed by experimental measurement (a), theory (b), and both measurement and theory (c) [76].

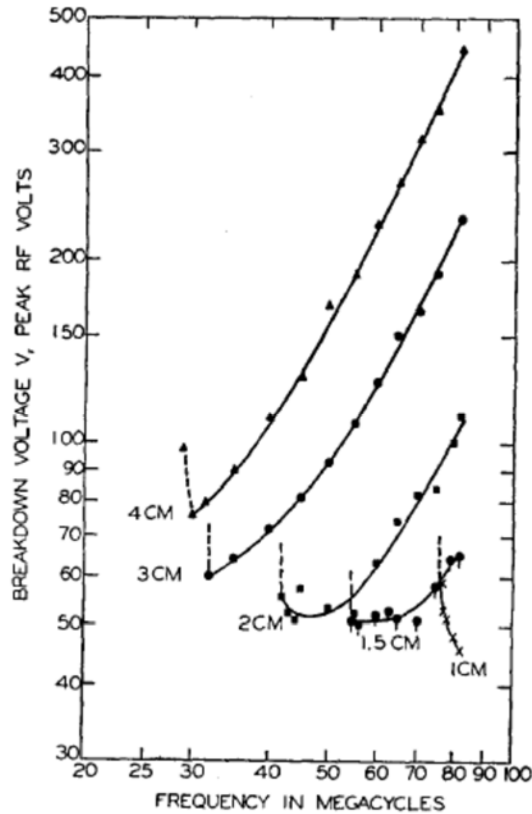

Figure 8: Hatch and Williams susceptibility curves showing cutoff frequencies (vertical dashed lines) for various electrode separations [76].

In 1961 A. J. Hatch reexamined previously developed multipactor theories (including the constant-*k* theory) that were based on the assumption that all electrons traverse the interelectrode gap in an infinitesimally thin sheet (i.e. the electron "bunching" range is zero) [79]. In his 1961 paper, Hatch replaced the zero bunching range assumption with a finite bunching range of possible electron emission velocities and phases by allowing the constant k to vary in the range $1 \leq k \leq \infty$ [14], [79]. Hatch explains the logic of this range physically by noting its requirement that electrons arrive at an electrode with an energy equal to or exceeding the emission energy [79]. Another important topic raised in Hatch's 1961 paper regards the effects of secondary-emission characteristics. Hatch declares the

two most important secondary-emission characteristics of the electrode surfaces are the SEY and the distribution of emission energies [79]. Figure 9 shows both the SEY curve and the distribution data for the emission energy referenced by Hatch. By noting the slowly varying nature of the SEY curve as a function of arrival energy (Figure 9 top), Hatch concluded there is minimal electron population enhancement due to SEY unless arrival energy varies rapidly with phase [79]. Hatch goes on to note two effects caused by the distribution of emission energies (Figure 9 bottom). The first is an electron population enhancement at phase angles where resonance occurs near 5 eV (left peak in Figure 9). The second is that electrons which do not possess half cycle transit times, broaden the range of

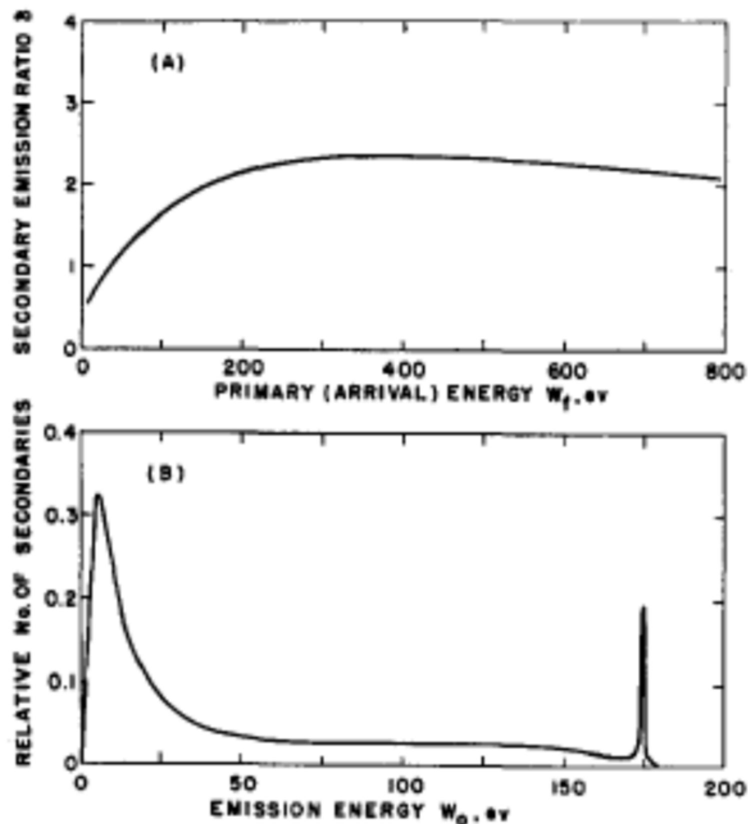

Figure 9: Secondary electron emission data for aluminum referenced by Hatch in his 1961 paper showing a typical SEY (δ) curve (top) and typical energy distribution (bottom) [79].

bunching phase angles which helps to offset the previous to effects [79]. Finally, Hatch's 1961 paper rejected the "phase-focusing mechanism" first proposed in 1936 by Henneburg, Orthuber, and Steudel as a way to describe how non-resonant electrons become resonant over several half-cycles by "phase advance or retardation" [79]. Hatch concluded that such a phase-focusing mechanism is not possible in multipacting because "a completely new crop of secondaries is emitted each half-cycle" [79].

By the 1960s, multipactor research was transitioning from a theoretical pursuit to a practical matter as engineers working on high-power microwave VEDs began encountering component failures attributed to multipactor. Over fifty years later, it is easy for us to understand the adverse impact multipactor was playing in these systems, but at that time, meticulous experiments were required to prove this fact. One of the biggest unknowns was the failure mechanism of ceramic RF windows used in high-power microwave devices. Coincidentally, in 1961, two studies seeking to understand this failure mechanism were published in the same issue of the Institute of Radio Engineers (IRE) Transactions on Electron Devices. The first paper, published by Preist and Talcott, examined damage to RF windows in klystrons caused by heating [47]. The second paper, published by Vaughan at General Electric, examined cracking and puncturing of RF windows in magnetrons [48]. Both studies found multipactor to be the underlying failure mechanism (albeit under different circumstances). Both studies also included ideas to suppress the multipactor using surface treatments or geometrical modifications. Preist and Talcott reported on a relatively new type of multipactor involving only a single surface [47]. Although S. C. Brown had previously reported on single surface multipactor in 1959, his findings required an external magnetic field to bend the electrons back to the surface [83]. By contrast, Preist & Talcott

demonstrated that a tangential RF electric field could sustain a single-surface multipactor [47]. This new type of multipactor significantly expanded the importance of multipactor research by exposing the vulnerability of dielectric surfaces in vacuum to experience multipactor. At the same time, Vaughan's study involving magnetrons, showed evidence of a "cross-field" type of two-surface multipactor involving obliquely incident electrons [48]. In discussing cross-field multipactor, Vaughan points out the increased risk they pose to microwave tubes because they involve obliquely incident electrons, which create larger yields of secondary electrons as shown in Figure 10 [48], [84]. Those increased yields result in sustained multipactor at higher voltages. Figure 11 contains an illustration of the electron paths in a cross-field multipactor. In 1968, Vaughan published results from a follow-on study of multipactor in magnetrons. In that paper, Vaughan recognized the

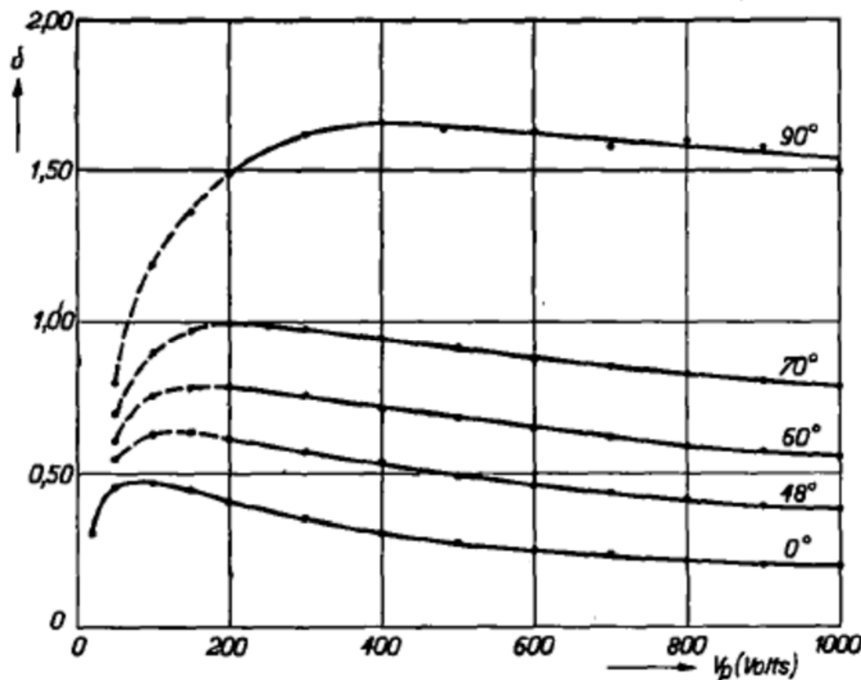

Figure 10: Plot of secondary emission yield (δ) versus applied voltage for various angles of incidence for lithium (0° is normal incidence) [84].

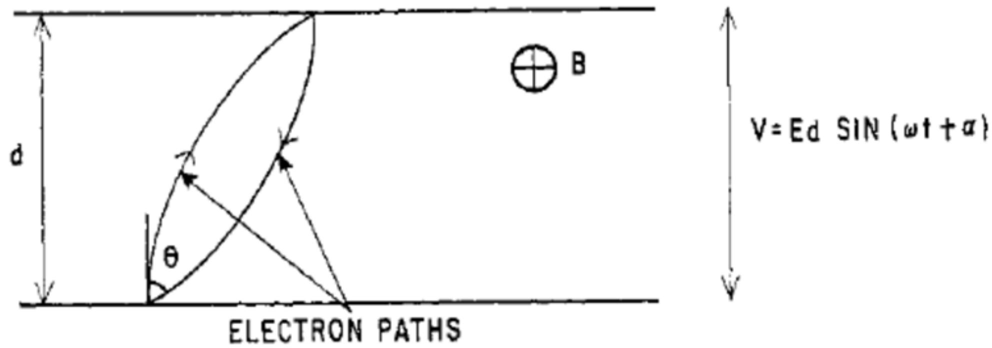

Figure 11: Obliquely incident electron paths associated with cross-field multipactor [48].

ability of magnetrons to experience the single-surface multipactor reported by Preist and Talcott, as well as the cross-field multipactor he previously reported [85]. Vaughan also recognized that other types of multipactor were possible in magnetrons, and that multipactor can occur frequently in magnetrons with effects ranging from "harmless to disastrous" [85].

Throughout the 1960s, 1970s, and 1980s numerous multipactor studies were conducted in support of governmental agencies and companies working primarily on space systems and particle accelerators. These studies examined multipactor in a variety of microwave devices including waveguides and RF windows, with the overall goal to find practical multipactor prevention techniques [18], [22], [49]. In the late 1960s, NASA's Jet Propulsion Laboratory (JPL) began sponsoring workshops on voltage breakdown at low air pressure. These workshops provided an opportunity for the community of space systems engineers to discuss knowledge gained by observations of multipactor. One of the papers presented at the second of these workshops referenced multipactor problems experienced by JPL during the Ranger program involving unmanned spacecraft sent to photograph the lunar surface [51]. The author of that paper also humbly recognized the need for more

research into multipactor power dissipation and geometry restrictions while acknowledging the necessity of a trial and error methodology for designing multipactor-free systems [51]. Other examples of this trial and error design methodology can be found years later underscoring the difficulty associated with designing multipactor-free systems [56].

Despite numerous multipactor studies taking place during that time period, the advancement of multipactor theory had essentially stalled [8]. However, advances in computing led to the development of multipactor computer simulations for use in designing systems less susceptible to multipactor [53]–[55], [57]–[59]. Although these simulations were limited to calculating single electron trajectories, they provided a tremendous improvement over the alternative trial-and-error design methodology [8].

In 1988, Vaughan published a landmark paper on multipactor in which he reviewed the field of multipactor research and presented an alternative to the constant-*k* theory for two-surface multipactor [7]. Interestingly, this new theory was based on work the 1936 publication by Henneburg, Orthuber, and Steudel [8]. Derived from first principles, Vaughan's theory included the following assumptions and simplifications:

1) the initial velocity of the secondary electrons is monoenergetic and nonzero;
2) no magnetic fields are present;
3) space-charge forces are ignored;
4) both surfaces have identical SEE characteristics [7].

Vaughan used his theory to provide the first attempt to analytically estimate the level of saturation [7]. In 1995, Riyopoulos *et al.* extended Vaughan's theory to account for orthogonal electric and magnetic fields by conducting a rigorous mathematical analysis

[86]. That same year, Kishek *et al.* proposed a simple model to analyze a multipactor discharge in an RF cavity, providing the first multipactor analysis to account for cavity loading and detuning caused by the multipactor current [15]. In 1997, Riyopoulos *et al.* accounted for random secondary electron emission velocities and delay times and showed that they are compatible with the phase-focusing mechanism, invalidating Hatch's conclusion from 1961 [1], [14].

In 1993, the first conference dedicated to multipactor took place. Held every 2-3 years in Spain or The Netherlands, the "International Workshop on Multipactor, Corona and Passive Intermodulation" (MULCOPIM) has convened 9 times, stimulating increased attention on the field of multipactor. Over this time, the number of publications relating to multipactor has skyrocketed. Current interest areas of multipactor research include multicarrier systems, 3D particle-in-cell (PIC) codes, "ping-pong" modes of multipactor involving both single-surface and two-surface, suppression through low-SEY coatings and surface engineering, non-resonant multipactor, and applying nonlinear dynamics and chaos to more accurately model multipactor [3], [10], [16], [64], [66]–[68], [70], [87]–[91].

2.2 Factors Affecting Two-Surface Multipactor

Many factors can enhance or suppress two-surface multipactor. However, almost all of these factors are distinguishable by their influence on two overarching processes involved in the vacuum region of a multipactor: electron transport and electron population growth. Electron transport is the process by which electrons move across the two-surface gap or in the region near the dielectric window. This process is influenced by factors that include (but are not limited to) geometry (*e.g.* gap distance or dielectric window orientation),

electric and magnetic field properties (strength, orientation, frequency, phase), and electron mean free path (vacuum conditions). Alternatively, electron population growth refers to the process that creates the electron avalanche. Driven exclusively by SEE, this process is heavily influenced by properties of the surfaces involved (chemistry and topography) as well as the energy of the electrons at the time they impact a surface. Figure 12 shows an illustration relating these processes to influencing factors and suppression techniques including the general suppression methods presented in Section 1.4. Figure 12 helps illustrate the versatility of surface treatments (which includes both low-SEY coatings and engineered surfaces) by showing how it can affect both the SEY and the emission angle. Although this research effort targets multipactor suppression by engineering surface topography to control SEY, it is worthy to consider the synchronism condition necessary for effective electron transport in two-surface multipactor. Thus, this section will begin with a mathematical analysis of this condition followed by an examination of the factors that influence SEE.

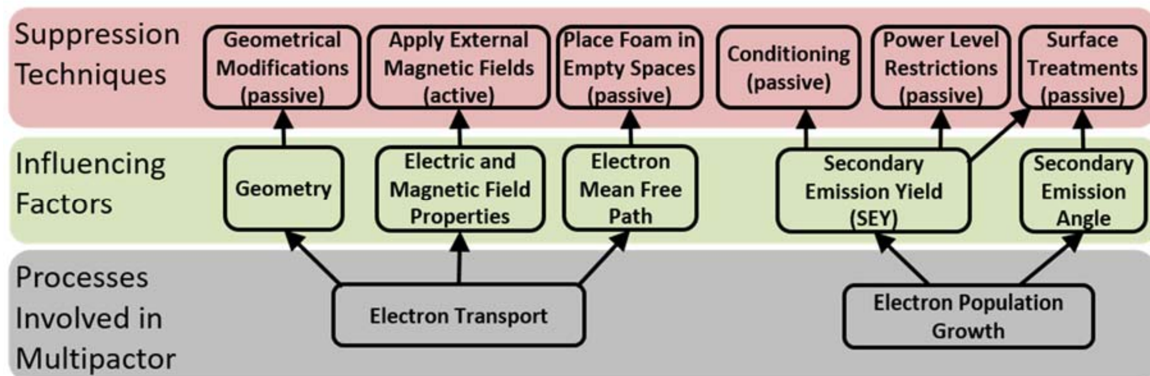

Figure 12: Illustration of the relationships between the two fundamental multipactor processes, the factors that influence them, and the corresponding multipactor suppression techniques.

2.2.1 Analysis of the Synchronism Condition

This section presents an *ab initio* mathematical analysis of two-surface multipactor under the assumptions and simplifications previously outlined and used by Vaughan. Figure 1 provides an illustration that will be helpful to keep in mind during this derivation. We begin by considering an electron that is emitted from the bottom surface at position $x = 0$ and time $t = 0$ with velocity v_o. Assuming there are no magnetic fields present and ignoring space-charge forces, this free electron is acted upon by the time-varying electric field present in the gap which has an associated time-varying gap voltage

$$V_g(t) = V_{g_o} \sin(\omega t + \theta), \tag{1}$$

where V_{g_o} is the voltage amplitude which we assume a constant (*i.e.* no loading), ω is the angular frequency of the gap voltage and θ is the phase of the gap voltage at time $t = 0$. We now apply the synchrony condition that must be satisfied for a two-surface multipactor to be sustained: the phase of the gap voltage must be in synchronism with the electron's return to the bottom surface [14]. Additionally, each time the electron impacts the top surface, the gap voltage phase must be a half-cycle different from the phase associated with impact at the bottom surface. For a given voltage, only electrons emitted from the bottom surface when the phase equals θ (or θ plus multiples of 2π) will contribute to sustaining the multipactor. These circumstances define the boundary condition

$$x(t) = d \text{ when } \omega t = N\pi, \qquad N = 1, 3, 5, \ldots \tag{2}$$

where d is the distance between the two surfaces and N is called the order of the multipactor. The order of the multipactor defines how many RF half-cycles occur during each electron transit across the gap. Thus, a first-order multipactor ($N = 1$) represents a

case where the electron transit time is equal to one half of an RF cycle. We now express the motion of this free electron using the equation

$$m\frac{d^2x}{dt^2} = \frac{e}{d}V_{g_o}\sin(\omega t + \theta), \tag{3}$$

where m is the electron mass and e is the electron charge. Rearranging and integrating Equation 3 (with respect to time) provides the electron velocity as a function of time:

$$v(t) = \frac{-eV_{g_o}\cos(\omega t + \theta)}{m\omega d} + C. \tag{4}$$

Applying the initial condition $v(t = 0) = v_o$, we can solve for the constant of integration

$$\begin{gathered} v(t = 0) = v_o = \frac{-eV_{g_o}\cos\theta}{m\omega d} + C \\ \rightarrow\ C = \frac{eV_{g_o}\cos\theta}{m\omega d} + v_o, \end{gathered} \tag{5}$$

which provides a final expression for the electron velocity as a function of time:

$$v(t) = \frac{eV_{g_o}}{m\omega d}[\cos\theta - \cos(\omega t + \theta)] + v_o. \tag{6}$$

We now integrate Equation 6 (with respect to time) to determine the electron position as a function of time:

$$x(t) = \frac{eV_{g_o}}{m\omega d}\left(t\cos\theta - \frac{\sin(\omega t + \theta)}{\omega}\right) + v_o t + C. \tag{7}$$

Applying the initial condition $x(t = 0) = 0$, we can solve for the constant of integration

$$\begin{gathered} x(t = 0) = 0 = \frac{eV_{g_o}}{m\omega d}\left(-\frac{\sin\theta}{\omega}\right) + C \\ \rightarrow\ C = \frac{eV_{g_o}\sin\theta}{m\omega^2 d}, \end{gathered} \tag{8}$$

which provides a final expression for the electron position as a function of time:

$$x(t) = \frac{eV_{g_o}}{m\omega^2 d}[\omega t\cos\theta - \sin(\omega t + \theta) + \sin\theta] + v_o t. \quad (9)$$

We now apply Equation 2 (the boundary condition necessary for multipactor) to yield

$$x\left(t = \frac{N\pi}{\omega}\right) = d = \frac{eV_{g_o}}{m\omega^2 d}[N\pi\cos\theta - \sin(N\pi + \theta) + \sin\theta] + v_o\frac{N\pi}{\omega}. \quad (10)$$

Combining sine terms and solving Equation 10 for V_{g_o} yields

$$V_{g_o} = \frac{m\omega d}{e}\left(\frac{\omega d - N\pi v_o}{N\pi\cos\theta + 2\sin\theta}\right) \text{ where } N = 1, 3, 5, \ldots . \quad (11)$$

Equation 11 is equivalent to Vaughan's Equation 3 and defines the synchronism condition relating the gap voltage to the emission or "launch" phase of the electrons. An important point made by Kishek is that this equation does not mean that electrons emitted at other phases cannot contribute to a multipactor [14]. In fact, many of these electrons will contribute in a process called "phase-focusing." Phase-focusing occurs when electrons emitted out of phase, undergo a process by which their phase converges with the fixed phase [14]. By contrast, phase de-focusing occurs when electrons emitted out of phase, undergo a process by which their phase diverges from the fixed phase [14]. The determining factor between phase-focusing and phase de-focusing is how close the launch phase is to the ideal resonance phase. Myers specified the breakpoint between phase-focusing and defocusing as 65° (see Figure 13) [78]. In other words, an electron emitted at a launch phase between 0° and 65° (before phase reversal) will "catch up" to the ideal resonance phase and contribute to the multipactor.

Having identified the requirement for phase-focusing, we revisit Equation 11 to define regions where multipactor is possible (i.e. susceptibility curves). These regions are bounded by minimum and maximum gap voltages. We will now derive these gap voltage

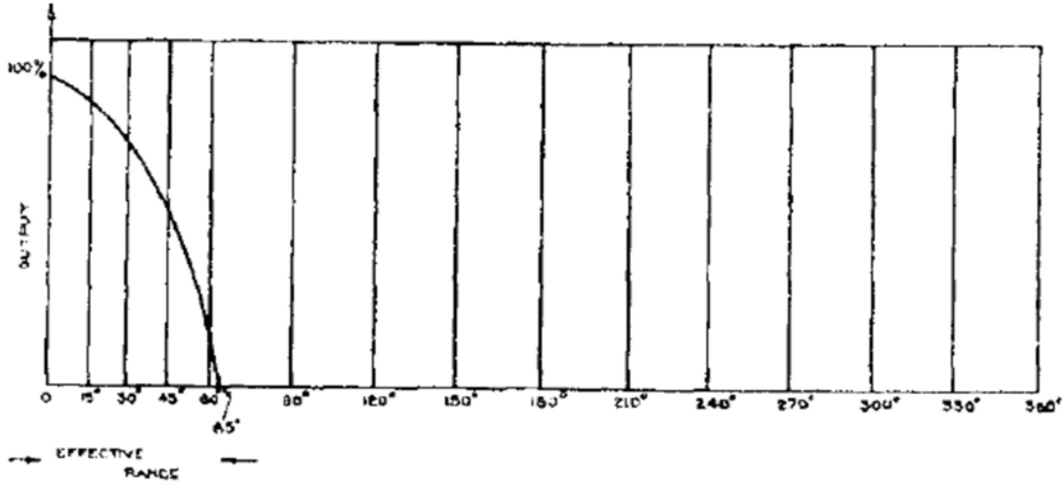

Figure 13: Range of emission phases for electrons contributing to multipactor [78].

boundaries beginning with the minimum gap voltage. For a given initial velocity, the minimum gap voltage that can sustain a multipactor ($V_{g_{min}}$) occurs when the denominator of Equation 11 is maximum, which occurs when

$$\tan\theta = \frac{2}{N\pi}. \tag{12}$$

Noting that Equation 12 describes a right triangle with legs of length of 2 and $N\pi$, we can determine $\cos\theta$ and $\sin\theta$ by finding the hypotenuse of the triangle ($\sqrt{2^2 + (N\pi)^2}$) and then applying the definitions of the cosine and sine functions to yield

$$\cos\theta = \frac{N\pi}{\sqrt{2^2 + (N\pi)^2}}, \quad \sin\theta = \frac{2}{\sqrt{2^2 + (N\pi)^2}}. \tag{13}$$

Substituting these values back into Equation 11 and simplifying yields

$$V_{g_{min}} = \frac{m\omega d}{e}\left(\frac{\omega d - N\pi v_o}{\sqrt{(N\pi)^2 + 4}}\right). \tag{14}$$

We now make substitutions for $\omega = 2\pi f$ and $v_o = \sqrt{2E_o/m}$ into Equation 14 to get

$$V_{g_{min}} = \left(\frac{1}{\sqrt{(N\pi)^2 + 4}}\right)\left(\frac{m[2\pi f d]^2}{e} - N\pi f d\sqrt{\frac{8\pi^2 m E_o}{e^2}}\right), \quad (15)$$

where f is the frequency in Hertz, d is the gap distance in meters, and E_o is secondary electron emission energy in Joules. Because typical multipactor frequencies are on the order of a gigahertz and typical gap distances are on the order of a centimeter, we will substitute $f = f_{GHz} \times 10^9$ and $d = d_{cm} \times 10^{-2}$ into Equation 15. Additionally, because the SEE energies are on the order of a few electron volts, it is customary to convert E_o to units of eV, which we do with the substitution, $E_o = E_{oeV} \times 1.602 \times 10^{-19}$. These substitutions along with values for m (9.11×10^{-31}kg) and e (1.602×10^{-19}C) yield,

$$V_{g_{min}} = \left(\frac{22450(f_{GHz}d_{cm})^2 - N\pi f_{GHz}d_{cm}\sqrt{44900E_{oeV}}}{\sqrt{(N\pi)^2 + 4}}\right). \quad (16)$$

Note that Equation 16 shows a quadratic relationship between the minimum gap voltage ($V_{g_{min}}$) and the frequency-gap product ($f_{GHz}d_{cm}$).

We now revisit Equation 11 to determine the maximum gap voltage. Kishek *et al.* remark that a closed-form solution for the maximum gap voltage (maximum V_{g_o} or $V_{g_{max}}$) does not exist for nonzero E_o although it can be solved numerically [8]. Therefore we begin with the assumption that $E_o = 0$ (i.e. $v_o = 0$) which reduces Equation 11 to

$$V_{g_o}(v_o = 0) = \frac{m}{e}\left(\frac{(\omega d)^2}{N\pi\cos\theta + 2\sin\theta}\right). \quad (17)$$

Equation 17 is maximized when the denominator is minimized with the caveat that θ must be between 0° and 65° (i.e. phase-focusing is required). This occurs when $\theta = 0°$ which simplifies Equation 17 to

$$V_{g_{max}}(v_o = 0) = \frac{m}{e}\left(\frac{(\omega d)^2}{N\pi}\right). \quad (18)$$

Making the same substitutions previously used for convenience ($\omega = 2\pi f, f = f_{GHz} \times 10^9$ and $d = d_{cm} \times 10^{-2}$) and plugging in values for *m* and *e* we arrive at

$$V_{g_{max}}(v_o = 0) = 22550\left(\frac{(f_{GHz}d_{cm})^2}{N\pi}\right). \quad (19)$$

As was the case with $V_{g_{min}}$ (Equation 16), we note that Equation 19 contains a quadratic relationship between $V_{g_{max}}$ and $f_{GHz}d_{cm}$. Thus, both $V_{g_{min}}$ and $V_{g_{max}}$ appear as straight lines with a slope of 2 on the log-log plots typically used for susceptibility curves shown in Figure 14 [8]. A final remark on the subject of multipactor calculations comes from Vaughan who notes precise calculations are "seldom justified" because the electron emission velocity (v_o) affects both $V_{g_{min}}$ and $V_{g_{max}}$ and is never known with accuracy; even worse, v_o is not single-valued but a statistical distribution [7].

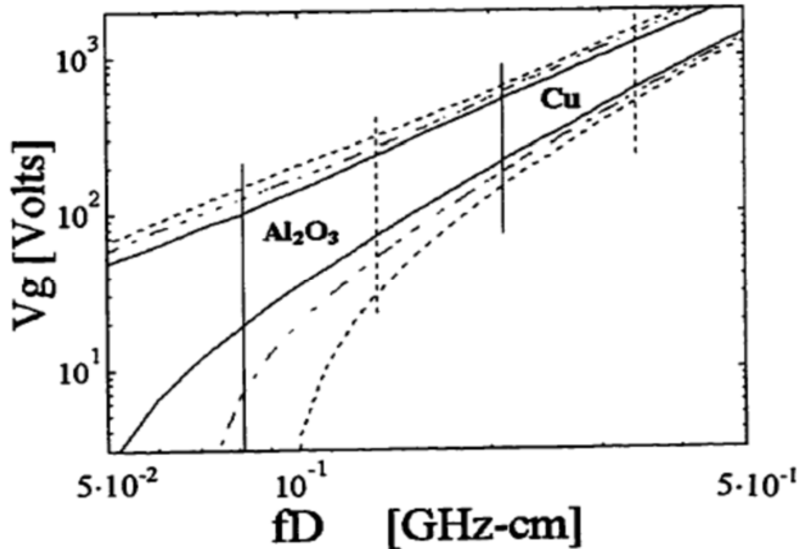

Figure 14: Example plot of multipactor susceptibility curves showing the minimum and maximum voltages for 3 different emission energies: 2 eV (solid line); 5 eV (dash-dot line); 10 eV (dashed line) [8].

2.2.2 Secondary Electron Emission

Secondary electron emission was first discovered in 1902 by Austin and Starke who were studying the reflection of electrons from metal surfaces [92]–[94]. They found metal targets that were capable of emitting more electrons than they were receiving from an external source, an indication that the primary electrons were causing additional electrons to be emitted from the metal [92]. During the 1930s, researchers at Philips' Laboratories in Eindhoven were studying SEE because of its importance to the VEDs of that period (*e.g.* diodes, triodes, tetrodes) [44]–[46]. In these devices, SEE occurring within the device generally had an unfavorable effect on the VED's performance. Examples of unfavorable SEE cited by Bruining include "secondary emission of anode and screen grid in a tetrode, the secondary emission of the glass wall, the secondary emission of the grid in a broadcasting valve." Jonker studied the effect of secondary emissions from the anode contained within a tetrode and found these emission caused severe distortions in the current-voltage curves for the device [46]. Figure 15 shows the effect SEE had on the tetrode's operation: the solid curve shows the ideal anode current in the absence of SEE; the dashed curve shows the distorted anode current caused by SEE, and the dash-dot curve shows the anode current when the anode is modified to suppress SEE. Thus, these researchers began the first-known attempts to suppress SEE and their efforts provide great insight to achieve this goal. For example, in 1937, Bruining *et al.* write,

"*The capability to emit secondary electrons of a soot-covered surface is small, if it is struck by primary electrons. Soot is composed of very small particles and has a surface which is rich in labyrinths. If a primary electron falls into such a labyrinth it is almost*

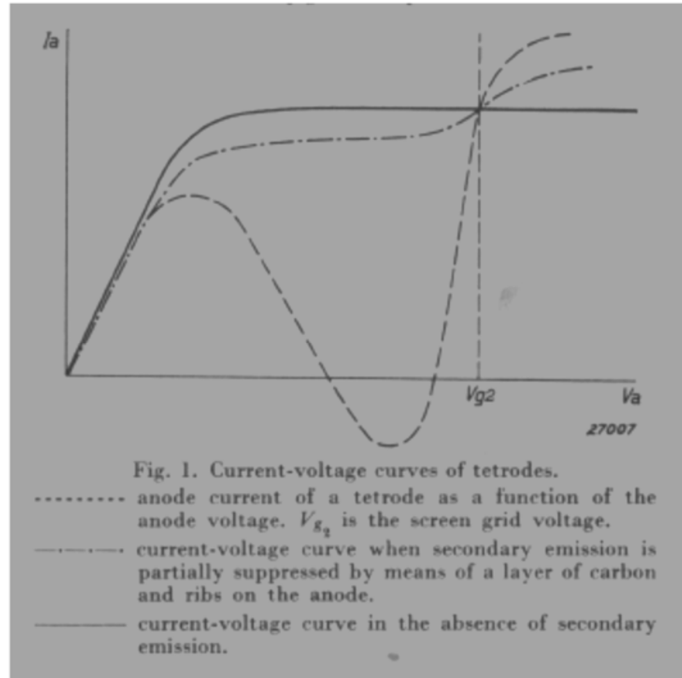

Fig. 1. Current-voltage curves of tetrodes.
- - - - - - - - - anode current of a tetrode as a function of the anode voltage. V_{g_2} is the screen grid voltage.
—·—·—· current-voltage curve when secondary emission is partially suppressed by means of a layer of carbon and ribs on the anode.
———— current-voltage curve in the absence of secondary emission.

Figure 15: Secondary electron emission and its effect on current-voltage curves of a tetrode studied by Jonker [46].

impossible for the secondaries to escape. In this case the secondary emission is low compared with a smooth and coherent surface of the same material" [44].

Additionally, in 1938, Jonker writes,

"The lowest secondary emission is obtained from a layer of carbon which is deposited in such a way that the surface is rough or flaky, so that the secondary electrons are for the most part captured in the cavities between the grains of carbon and cannot be drawn away" [46].

Unfortunately, the techniques available to these researchers, to create these labyrinths or cavities, were limited by the technology of that era. These techniques included using a flame of burning turpentine to deposit a layer of carbon soot, directly spraying a suspension of carbon soot, or depositing various metals using sublimation or evaporation [44]–[46].

By the 1940s and 1950s, decades of experimental research into SEE provided the necessary data for comprehensive reviews to be conducted by McKay (1948), Bruining (1954), Dekker (1958), and Hachenberg & Brauer (1959) [92]–[94]. While these, and other efforts provided increased consensus on the processes involved in SEE, the only universal agreement was that a complete and accurate theory of SEE was lacking, owing to its complex nature [92]–[98]. Simon and Williams describe SEE as involving three physical processes:

1) generation/excitation of secondary electrons;
2) electron transport through the solid to the surface;
3) electron transport through the vacuum-solid interface [98] [71].

Close consideration of each of these processes illuminates why a complete and accurate theory of SEE is difficult to attain. Lye and Dekker, who provided a well-known empirical model for SEY in 1957, expand on the first two processes listed above. First, they note that a true understanding of the first process "requires a detailed knowledge of the band structure of the solid, and of the electronic transition probabilities" [96]. Regarding the second process, they emphasize the behavior of the excited lattice electrons is "complicated by their interaction with other lattice electrons and by scattering due to phonons and lattice defects" [96]. Thus, it quickly becomes clear that a complete understanding of SEE theory is beyond the scope of this research effort. However, it is nonetheless prudent to understand key properties of SEE and the relationships between SEE and other important factors involved in multipactor including primary impact energy and material properties.

Regardless of the type of material, there are two remarkable consistencies for SEE: the emission energy distribution and emission angular distribution as shown in Figure 16. The

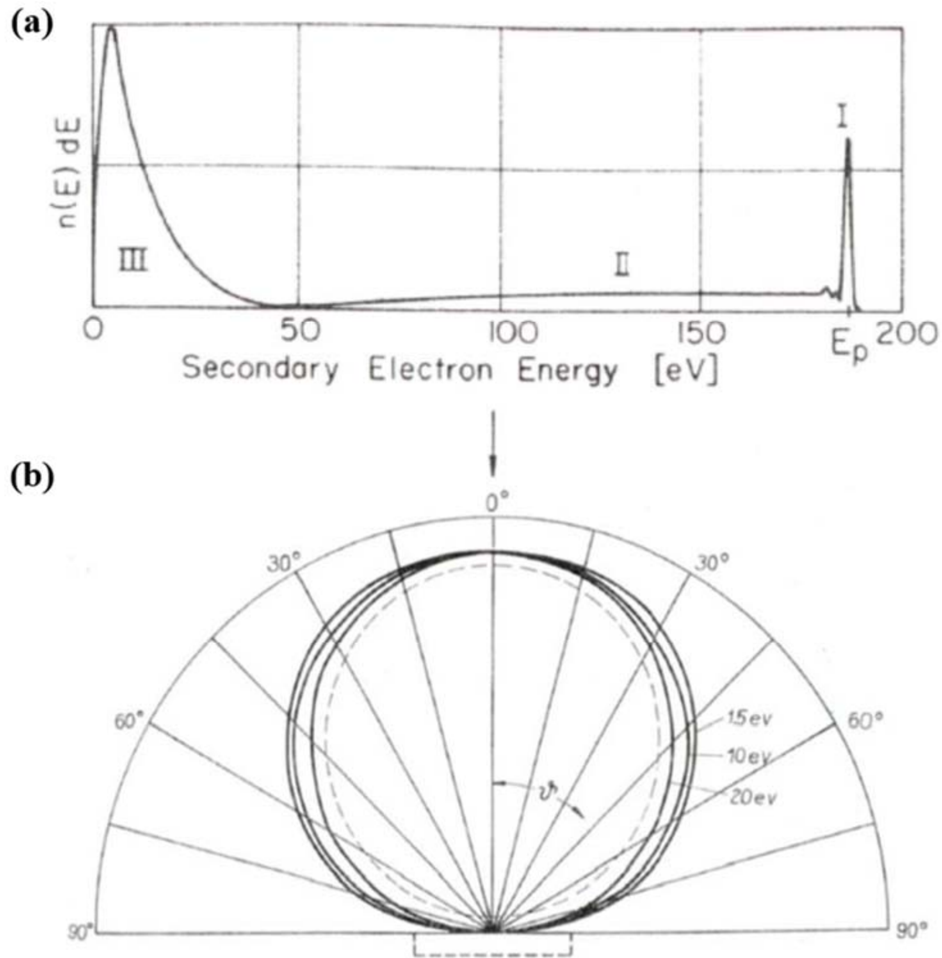

Figure 16: Distribution data for secondary electron emission measured from a Ni target using normally incident 500 eV primary electrons: (a) energy distribution data; (b) angular distribution data [94].

energy distribution is divided into three groups (Figure 16a). Group I consists of elastically reflected primary electrons with energy equal to the primary electron energy, E_p (sometimes referred to as the impact or incident energy, E_i). Group II consists of inelastically backscattered primaries (also known as rediffused primaries) which are primary electrons that were backscattered after undergoing one or more inelastic collisions within the bulk material. These collisions cause the Group II electrons to lose energy prior to their emission, thus their emission energies range from 50 eV to E_p as shown in Figure

16a. Group III consists of the true secondaries with energies below 50 eV [97]. As Figure 16a shows, the total number of reflected and backscattered electrons (area under the Group I and II curves) is typically small compared to the number of true secondaries (area under the Group III curve). This trend has led to an accepted convention of including all three groups of emitted electrons under the overarching label “secondaries” [93]. Birdsall and Bridges note that the shape of the true secondary distribution curves are remarkably similar for all the metals with the peak occurring between 1.2 eV and 2.5 eV [97]. They also note that the shape is “essentially independent of the primary energy, E_p, for $20 \text{ eV} < E_p < 1000 \text{ eV}$” [97]. Figure 16b shows the angular distribution of secondary electrons, which follows the cosine function (i.e. the largest portion of electron emission are emitted normal to the surface and there are no electrons emitted parallel to the surface).

The most important and useful SEE parameter is the yield of electrons that are emitted when a single primary electron strikes the surface. This parameter is known as the SEY or SEE coefficient. However, because there are three categories of secondary electrons, there are different ways to define and measure SEY, which can lead to significant confusion if not clearly communicated. The four types of secondary electron yields predominately used in the literature are the *true SEY*,

$$\delta = \frac{\text{number of true secondaries}}{\text{total number of primaries}}, \tag{20}$$

the *elastically reflected electron yield*,

$$\varepsilon = \frac{\text{number of elastically reflected primaries}}{\text{total number of primaries}}, \tag{21}$$

the *inelastically backscattered electron yield*,

$$\eta = \frac{\text{number of inelastically backscattered primaries}}{\text{total number of primaries}} \tag{22}$$

and the *total SEY*,

$$\sigma = \delta + \varepsilon + \eta \,. \tag{23}$$

Although each of these yields are distinct, their symbols have only recently become widely standardized, thus, older publications sometimes refer to them differently [37], [52], [92]–[94], [97]. To minimize confusion, this dissertation will use the yields and symbols defined in Equations 20-22. Figure 17 shows a generalized plot of each of these yields [99].

The simplest method for measuring SEY is to measure the electron currents going in and out of a sample bombarded by an electron beam (e-beam) under ultra-high vacuum (UHV) pressures ($\leq 10^{-9}$ Torr). Under this method, the total SEY is often measured as

$$\sigma = \frac{I_\sigma}{I_p}, \tag{24}$$

where I_σ is the total electron emission current (consisting of elastically reflected,

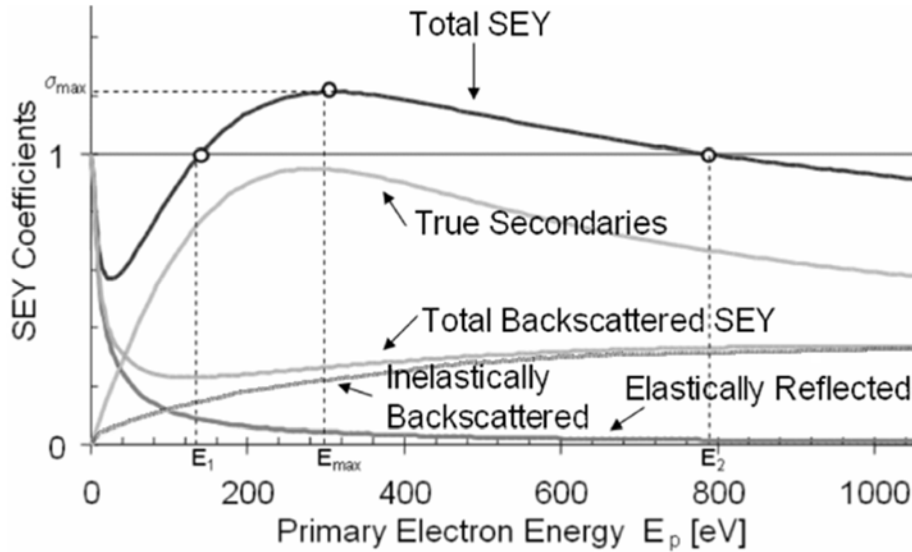

Figure 17: General shape of the secondary electron yield (SEY) curves for each emission type involved in secondary electron emission [99].

inelastically backscattered, and true secondary electrons) and I_p is the e-beam current [94]. For a given material, two external parameters that greatly affect the SEY are the impact energy, E_i, and the impact angle [14]. In 1989, Vaughan published a new, empirical formula for SEY, which he intended to replace Lye and Dekker's 1957 empirical model for low impact energies [100]. Vaughan's SEY formula is

$$\delta(E_i) = \delta_{max}(ve^{1-v})^k, \tag{25}$$

where E_i is the impact energy, δ_{max} is the maximum yield for the material under consideration, $v = E_i/E_{max}$, E_{max} is the impact energy that causes δ_{max}, and $k = 0.62$ for $v < 1$, and $k = 0.25$ for $v > 1$ [100]. In 1993, Vaughan's formula was experimentally verified by Shih and Hor using molybdenum [101]. Figure 18 contains a generalized plot of Equation 25 showing the salient features used in Vaughan's formula (δ_{max} and E_{max}). The two incident energies for which the yield is unity (E_1 and E_2) are commonly referred to as the first and second crossover points [8]. Kishek provides a simple explanation for the shape of the SEY curve noting that low-energy primary electrons are not capable of

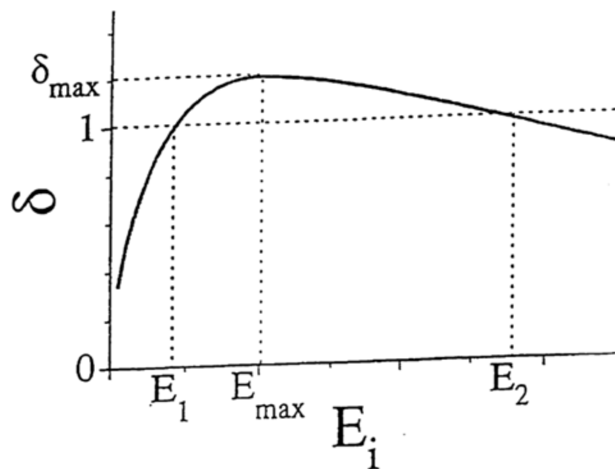

Figure 18: General shape of the secondary electron yield (δ) curve as a function of impact energy (E_i) [14].

liberating many secondaries, and high-energy primary electrons will penetrate too deeply into the material for the secondaries to escape [14]. Figure 18 also illustrates an important requirement for multipactor: the impact energy must be between E_1 and E_2 the SEY to be greater than one (i.e. $\delta > 1$), which is necessary to sustain a multipactor. For metals, E_{max} is ranges from 85 eV to 900 eV with δ_{max} ranging between 0.5 and 1.7 (see Table 1). By contrast insulators can have E_{max} up to several thousand electron volts with δ_{max} as high as 15 (see Table 2 below). A general explanation for the difference in SEYs between metals and insulators is provided by Dekker [93]. He notes the strong tendency for internal secondaries in metals (those that have not yet been emitted), to interact with conduction-band electrons, causing a rapid loss of energy that leaves the secondaries with insufficient energy to overcome the barrier and escape [93]. By contrast, internal secondaries created in insulators do not transfer much energy to conduction band electrons (which rarely exist) and thus are able to migrate over relatively large distances, giving them greater chance of escape [93]. Finally, there are several important trends to note regarding the effect that different environmental or material conditions have on SEY. McKay provides a nice summary of these factors, which are provided in Table 3 below.

Table 1. Secondary electron yield data for metals arranged by atomic number [93].

Atomic number	Element symbol	δ_m	E_{pm}°	E_{pI}°	E_{pII}°	References
3	Li	0.5	85	—	—	Kollath[a]
4	Be	0.5	200	—	—	Kollath[a]
11	Na	0.82	300	—	—	Woods[b]
12	Mg	0.95	300	—	—	Kollath[a]
13	Al	0.95	300	—	—	Kollath[a]
19	K	0.7	200	—	—	Kollath[a]
22	Ti	0.9	280	—	—	Kollath[a]
26	Fe	1.3	(400)	120	1,400	Kollath[a]
27	Co	1.2	(500)	200	—	Kollath[a]
28	Ni	1.35	550	150	1,750	Kollath[a]
29	Cu	1.3	600	200	1,500	Kollath[a]
37	Rb	0.9	350	—	—	Kollath[a]
40	Zr	1.1	350	175	(600)	Kollath[a]
41	Cb	1.2	375	175	1,100	Kollath[a]
42	Mo	1.25	375	150	1,300	Kollath[a]
46	Pd	>1.3	>250	120	—	Kollath[a]
47	Ag	1.47	800	150	>2,000	Kollath[a]
48	Cd	1.14	450	300	700	Kollath[a]
50	Sn	1.35	500	—	—	Kollath,[a] Woods[b]
51	Sb	1.3	600	250	2,000	Kollath,[a] Appelt[c]
55	Cs	0.72	400	—	—	Kollath,[a]
56	Ba	0.82	400	—	—	Kollath,[a]
73	Ta	1.3	600	250	>2,000	Kollath,[a]
74	W	1.35	650	250	1,500	Kollath[a]
78	Pt	1.5	750	350	3,000	Kollath,[a] Appelt[d]
79	Au	1.45	800	150	>2,000	Kollath,[a]
80	Hg	1.3	600	350	>1,200	Kollath,[a]
81	Tl	1.7	650	70	>1,500	Kollath,[a]
82	Pb	1.1	500	250	1,000	Kollath,[a]
83	Bi	1.5	900	80	>2,000	Kollath,[a] Appelt[c]
90	Ta	1.1	800	—	—	Kollath[a]

NOTE: δ_{max} is shown as δ_m, E_{max} is shown as E_{pm}, and the first and second crossover points are shown as E_{pI} and E_{pII}.

Table 2. Secondary electron yield data for various materials [94].

Group	Substance	δ_m	E_{pm}°
Semiconductive elements	Ge (single crystal)	1.2–1.4	400
	Si (single crystal)	1.1	250
	Se (amorphous)	1.3	400
	Se (crystal)	1.35–1.40	400
	C (diamond)	2.8	750
	C (graphite)	1	250
	B	1.2	150
Semiconductive compounds	Cu_2O	1.19–1.25	400
	PbS	1.2	500
	MoS_2	1.10	
	MoO_2	1.09–1.33	
	WS_2	0.96–1.04	
	Ag_2O	0.98–1.18	
	ZnS	1.8	350
Intermetallic compounds	$SbCs_3$	5–6.4	700
	SbCs	1.9	550
	$BiCs_3$	6–7	1,000
	Bi_2Cs	1.9	1,000
	GeCs	7	700
	Rb_3Sb	7.1	450
Insulators	LiF (evaporated layer)	5.6	
	NaF (layer)	5.7	
	NaCl (layer)	6–6.8	600
	NaCl (single crystal)	14	1,200
	NaBr (layer)	6.2–6.5	
	NaBr (single crystal)	24	1,800
	NaJ (layer)	5.5	
	KCl (layer)	7.5	1,200
	KCl (single crystal)	12	
	KJ (layer)	5.5	
	KJ (single crystal)	10.5	1,600
	RbCl (layer)	5.8	
	KBr (single crystal)	12–14.7	1,800
	BeO	3.4	2,000
	MgO (layer)	4	400
	MgO (single crystal)	23	1,200
	BaO (layer)	4.8	400
	BaO—SrO (layer)	5–12	1,400
	Al_2O_3 (layer)	1.5–9	350–1,300
	SiO_2 (quartz)	2.4	400
	Mica	2.4	300–384

NOTE: δ_{max} is shown as δ_m and E_{max} is shown as E_{pm}.

Table 3. Effects of physical and environmental factors on secondary electron yield [37].

FACTOR	EFFECT ON SEY	REASON
Material Work Function	Higher work functions reduce SEY	High work functions present high vacuum-energy barriers
Crystal Structure	Crystal structure is known to affect SEY but with no clear trends	N/A
Temperature	No direct effect*	N/A
Electron Angle of Incidence	Larger incident angles (moving away from normal incidence) increase SEY	As incident angle increases electron penetration depth decreases
Primary Current	No direct effect**	N/A
Surface Topography	Rough surfaces reduce SEY	Rough surfaces increase occurrences of electron recapture
Adsorbed Gas	Typically increases SEY - depends on gas type, thickness, and chemical interaction with the surface	Adsorbed layers can yield an appreciable number of secondaries

*indirect effects exist because temperature alters crystal structure and surface chemistry.

**indirect effects exist because large currents cause surface conditioning [34].

2.3 Porous Surfaces for SEY Suppression

In 2013, Ye *et al.* published a paper that considered the use of a porous surface for controlling the SEY of a material [70]. Figure 19 shows an illustration of the array of cylindrical pores modeled by Ye, as well as Scanning Electron Microscope (SEM) images of a silver porous surface they fabricated and tested. In their paper, Ye demonstrated that a weighted average, which combines the SEY of the pore regions with the SEY of the non-pore regions, can be used to model the SEY of the entire porous surface [70]. This weighted average model will provide the foundation for the SEY models developed in Chapter III. The porous surface shown in Figure 19b was fabricated using photolithography combined with an aqueous chemical etch to pattern the pores. The aqueous etch results in pores that have a cavernous nature (see Figure 19b). This provides an important takeaway that must be considered when creating a porous surface SEY model – namely, the process used to

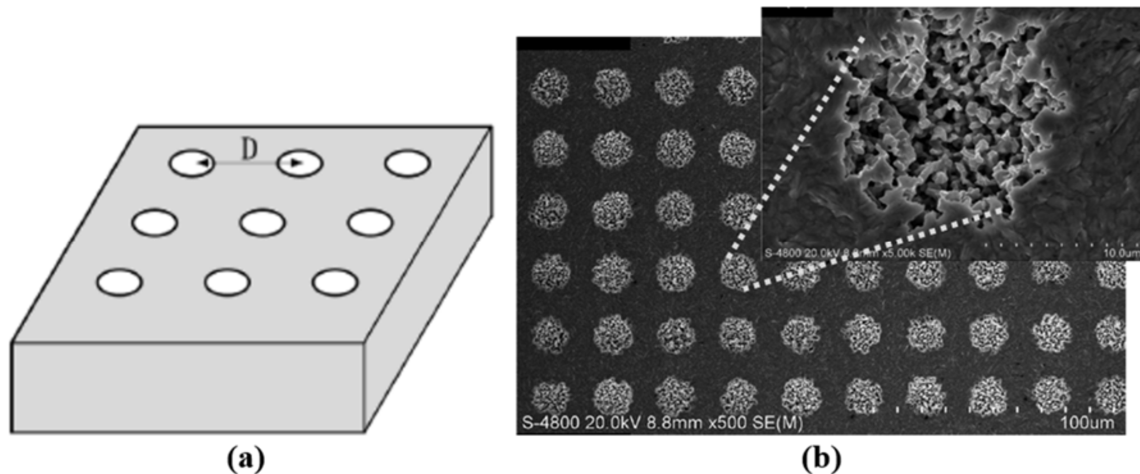

Figure 19: Porous surface study by Ye *et al.*: (a) modeled array of cylindrical pores; (b) scanning electron microscope images of Ye's pores (created using a silver etch process) that show distinct topographies for the non-pore and pore-bottom regions [70].

fabricate the pores (chemical etching, laser ablation, electroplating, etc.) will likely result in distinct surfaces for the non-pore regions and the pore regions. These surfaces can be distinct in both their topography and chemistry, either of which would result in a distinct SEY. Thus, the porous surface SEY models developed in Chapter III, must incorporate distinct SEY parameters for the distinct pore and non-pore regions of a porous surface.

2.4 Visual Bibliography of Multipactor Research

In an effort to connect together, the previously presented background information, this section provides three visual bibliographies that show how various research efforts were used to conduct follow-on work in the field of multipactor. The three visual bibliographies are presented chronologically from oldest to newest. Figure 20 shows the major research efforts conducted during the early years of multipactor research. Figure 21 shows some of the major theoretical contributions and advancements made during the resurgence of multipactor research that took place in the 1980s and 1990s. The gray boxes in Figure 21

highlight efforts previously recognized in Figure 20. Figure 22 shows recently conducted theoretical and experimental research into multipactor suppression by surface coatings and surface structures. The gray boxes in Figure 22 highlight a combination of recurring conferences, community best practices, and previously recognized efforts from Figure 21.

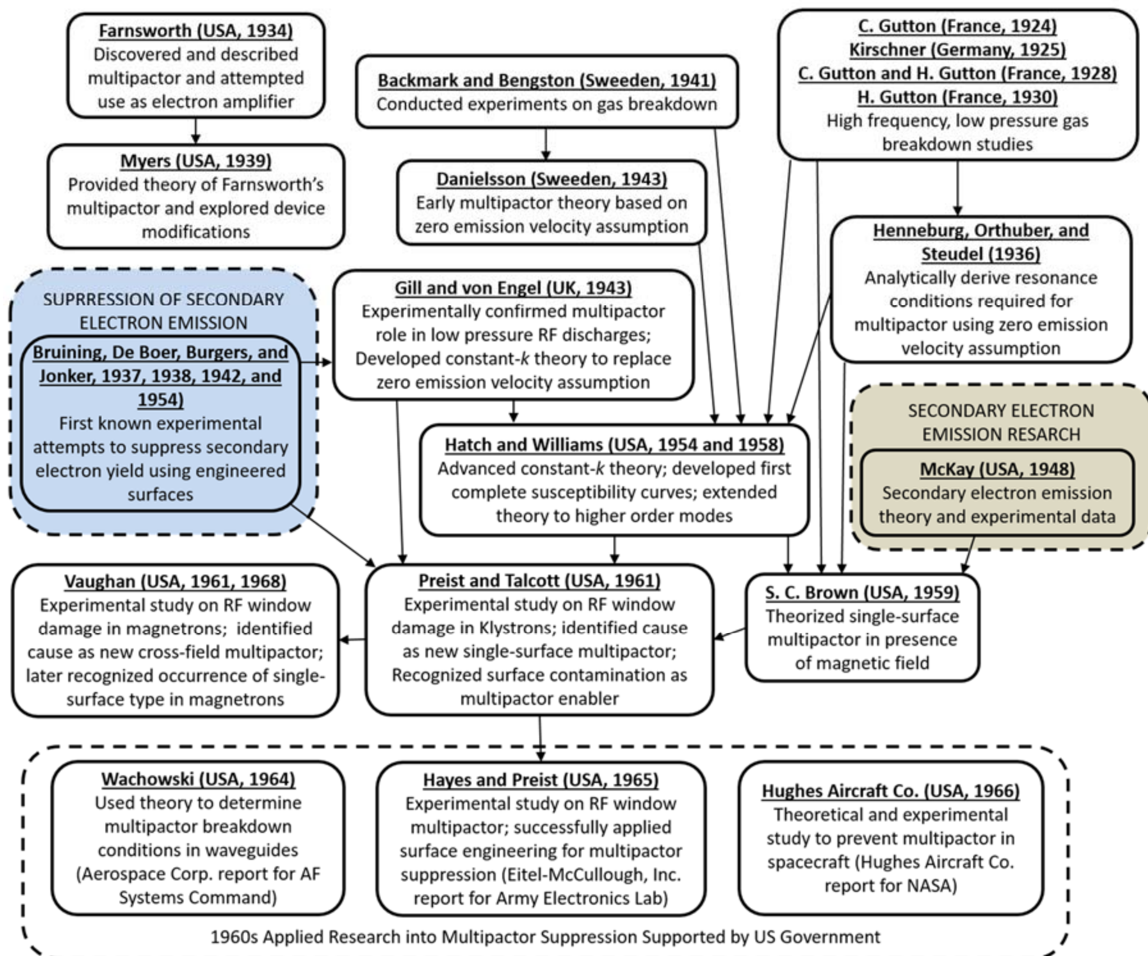

Figure 20: Multipactor visual bibliography I – origins of research.

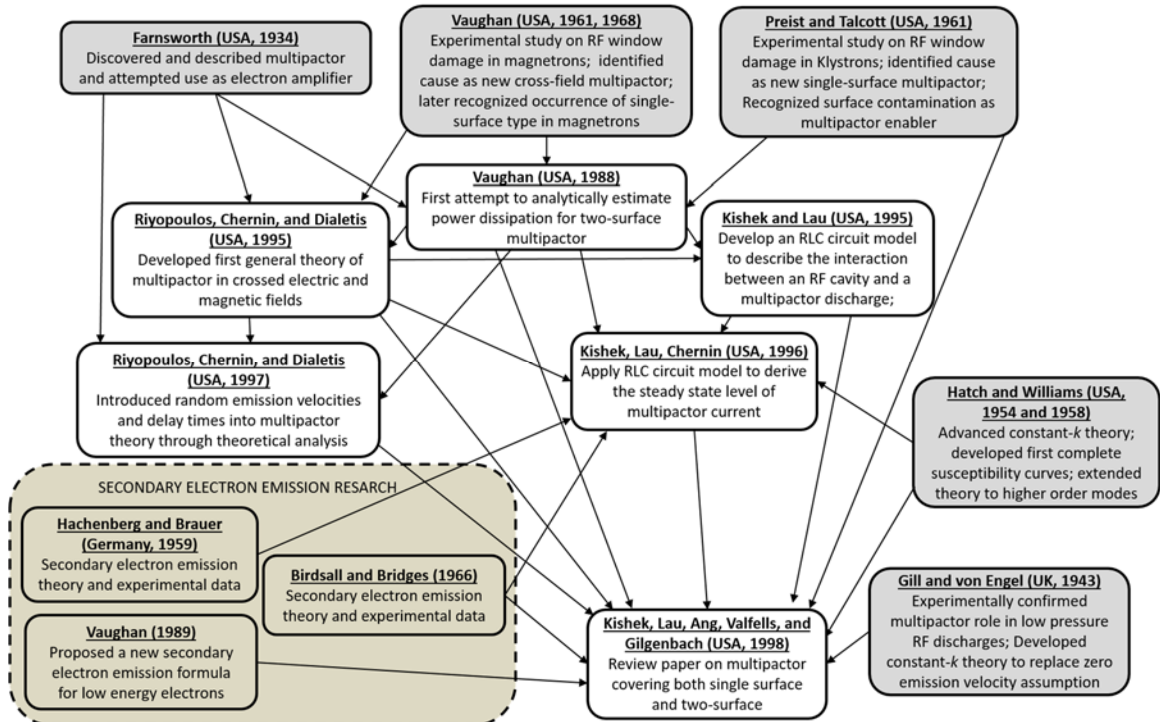

Figure 21: Multipactor visual bibliography II – modern theories.

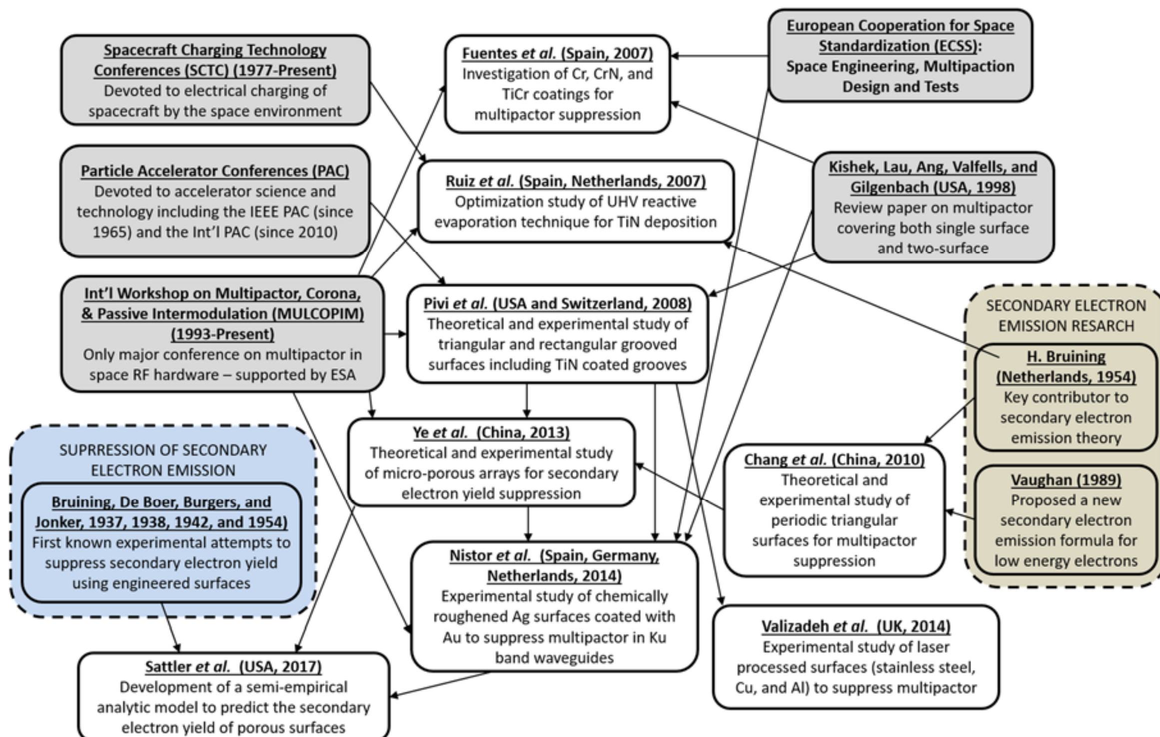

Figure 22: Multipactor visual bibliography III – suppression by engineered surfaces.

2.5 Summary

This chapter provided a chronological review of previously conducted multipactor research from its first observations to the present. Noteworthy publications were highlighted and, where appropriate, attention was focused on published results that have implications for this research effort. Additionally, a topical presentation was made describing the two overarching processes involved in multipactor: electron transport and SEE. Factors that influence these processes were presented and tied to specific multipactor suppression techniques. A detailed analysis of the synchronism condition required for two-surface multipactor was presented and used to show how susceptibility curves are defined. Finally, a fundamental description of SEE was provided including a discussion of the key parameter, SEY, as well as the environmental and material factors that influence it.

III. Methodology

This chapter outlines and explains the methods used to answer the questions presented in Section 1.5. The results of these methods are presented in Chapter IV and analyzed in Chapter V. Section 3.1 presents the methodology used to develop SEY models for porous surfaces. Section 3.2 provides the engineered surface designs and processes to fabricate porous surfaces for experimental SEY measurements in support of model validation. Section 3.3 lays out the various methods used to characterize the surfaces (i.e. topography and chemistry) of the fabricated designs. Section 3.4 explores a variety of methodologies used to measure SEY and discusses their advantages and disadvantages. Section 3.5 lays out the SEY measurement system used by the Air Force Research Laboratory Materials and Manufacturing Directorate, which was used to collect the relevant SEY data for this research. Section 3.6 describes the new, dedicated SEY measurement system, which was designed, constructed, and tested as part of this dissertation. Finally, Section 3.7 describes the thermomechanical modeling used to understand how extreme temperature changes affect the ability of the engineered surface to control SEY.

3.1 Semi-Empirical SEY Modeling of Porous Surfaces

Determining optimal surface topographies to control SEE requires an accurate model to predict the SEY of an engineered surface. The models developed are based on porous surfaces with cylindrical pores because such surfaces can be fabricated for model validation through experimental SEY measurements. All models presented are semi-empirical in nature due to the complex nature of SEE. However, the empirically measured

parameters contained in these models could be replaced by an accurate analytic model for the specific parameter.

Figure 23a provides an illustration of the porous surface geometry with two distinct *total SEY* parameters σ_{pore} and $\sigma_{\text{non-pore}}$, which account for all possible secondary contributions as defined in Equation 23. As mentioned in Section 2.3, Ye *et al.* have previously shown that a weighted average of σ_{pore} and $\sigma_{\text{non-pore}}$ can be used to determine an effective SEY for the entire porous surface by using the pore spacing density (i.e. porosity) as the weight [70]. This weighted average method provides the fundamental equation for determining the total SEY of the porous surface:

$$\sigma_{\text{porous-surface}} = \sigma_{\text{pore}}\left(Porosity\right) + \sigma_{\text{non-pore}}\left(1 - Porosity\right), \tag{26}$$

where *Porosity* is defined as

$$Porosity = \frac{\text{Surface Area of Pores}}{\text{Total Surface Area}}. \tag{27}$$

The parameter $\sigma_{\text{non-pore}}$ can be determined by directly measuring the total SEY of an

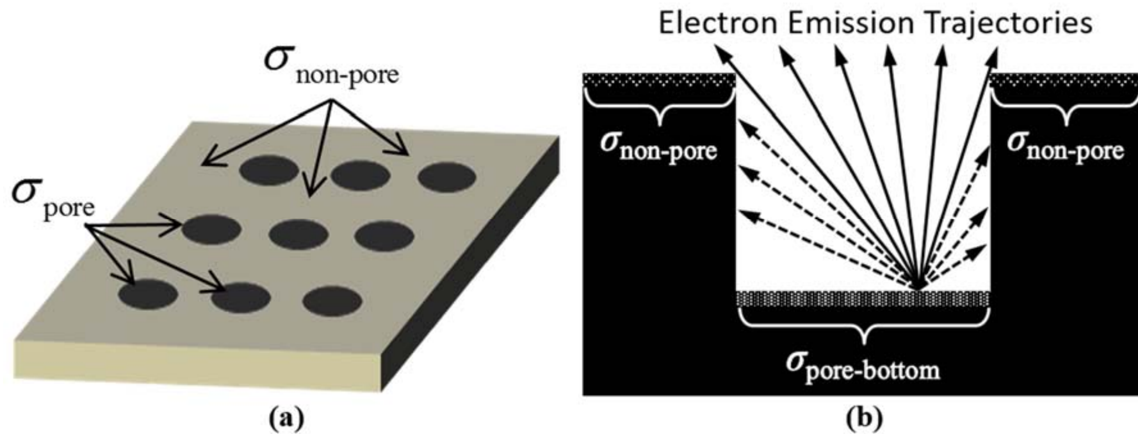

Figure 23: Porous surface geometry used for 2D and 3D secondary electron yield (SEY) models: (a) distinct SEY parameters used in the weighted average model; (b) pore cross section showing distinct parameters for $\sigma_{\text{non-pore}}$ and $\sigma_{\text{pore-bottom}}$.

unpatterned region of the non-pore surface. However, the parameter σ_{pore} must account for both the SEY of the surface at the bottom of the pore and the probability that an electron will escape the pore as shown in Figure 23b. As discussed in Section 2.3, it is necessary to maintain distinct SEY parameters for the distinct pore and non-pore regions. Figure 23b shows how this distinction is made by establishing unique parameters for $\sigma_{non\text{-}pore}$ and $\sigma_{pore\text{-}bottom}$. With this distinction, the parameter σ_{pore} can be defined mathematically as

$$\sigma_{pore} = \sigma_{pore\text{-}bottom}\left(P_{escape}\right), \quad (28)$$

where P_{escape} is the probably of an electron emitted from the bottom surface of a pore to escape the pore and contribute to $\sigma_{porous\text{-}surface}$. The parameter $\sigma_{pore\text{-}bottom}$ can be determined by directly measuring the total SEY of an unpatterned region of the pore-bottom surface. The parameter P_{escape} can be determined using probability theory and the cylindrical geometry of the pores. Several assumptions are made during this development:

1) primary electrons impact the sample at normal incidence,
2) electron emissions follow linear trajectories,
3) electrons that impact the pore sidewall are recaptured,
4) the electron emission polar angle (θ) is a cosine-distributed random variable with a range 0 to $\pi/2$ (see Figure 16b),
5) the electron emission azimuthal angle (ϕ) is a uniformly-distributed random variable with range 0 to 2π,
6) the location of an electron emission originating at the bottom of a pore is a uniformly-distributed random variable (r), and
7) all three aforementioned random variables are independent.

To determine P_{escape} we first consider a 2D pore and then a more complicated 3D pore.

3.1.1 Probability of Electron Escape for a Two-Dimensional Pore Model

Figure 21 illustrates the geometrical layout and parameters involved in the derivation of P_{escape} for the two-dimensional (2D) pore model, which we refer to as $P_{\text{escape-2D}}$. The maximum polar emission angles that permit electron emission are

$$\theta_1 = \arctan\left(\frac{R+r}{H}\right) \quad \text{and} \quad \theta_2 = \arctan\left(\frac{R-r}{H}\right), \tag{29}$$

where R is the pore radius, H is the pore height, and r is the uniformly distributed random variable that provides the position of the electron emission as the distance from the pore center to the emission site. We now apply the cosine distribution for the polar angle of electron emission (assumption 4 from Section 3.1) and sum (i.e. integrate) over all polar angles that permit electron escape. This provides the following conditional probability of escape ($P_{\text{escape-2D}}$) that depends on the azimuthal angle of emission, ϕ (i.e. emission towards the left sidewall represents $\phi = \pi$; emission towards the right sidewall represents $\phi = 0$):

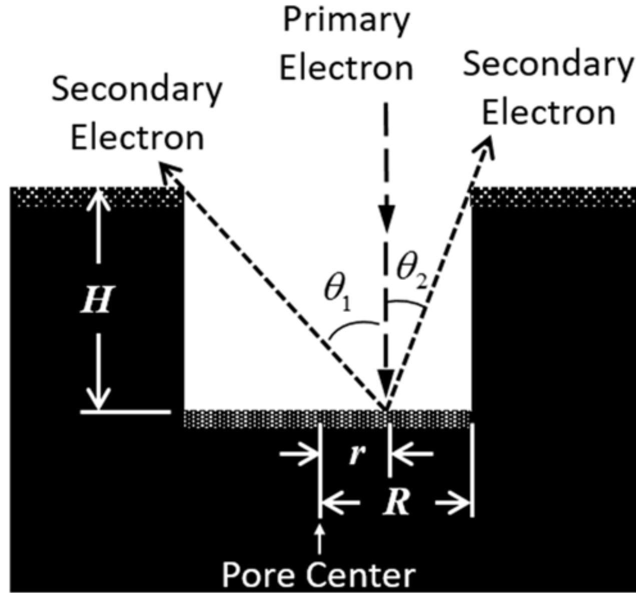

Figure 24: Illustration of the 2D pore model showing key parameters.

$$P_{\text{escape-2D}} = \begin{cases} \int_0^{\theta_1} \cos(\theta)\, d\theta = \sin(\theta_1) = \sin\left[\arctan\left(\frac{R+r}{H}\right)\right], & \text{for } \phi = \pi \\ \int_0^{\theta_2} \cos(\theta)\, d\theta = \sin(\theta_2) = \sin\left[\arctan\left(\frac{R-r}{H}\right)\right], & \text{for } \phi = 0 \end{cases}. \tag{30}$$

The two conditional probabilities in Equation 31 can be combined according to their probability of occurrence (i.e. the probability that $\phi = \pi$ and the probability that $\phi = 0$) to determine a mean probability of escape:

$$\overline{P}_{\text{escape-2D}} = \left(P_{\phi=\pi}\right)\sin\left[\arctan\left(\frac{R+r}{H}\right)\right] + \left(P_{\phi=0}\right)\sin\left[\arctan\left(\frac{R-r}{H}\right)\right]. \tag{31}$$

Applying assumption 5 above and noting that ϕ is a discrete random variable for the 2D model with only two outcomes ($\phi = 0$ or $\phi = \pi$) provides

$$P_{\phi=\pi} = P_{\phi=0} = \frac{1}{2}. \tag{32}$$

Substituting the probabilities in Equation 32 into Equation 31 yields,

$$\overline{P}_{\text{escape-2D}} = \frac{1}{2}\sin\left[\arctan\left(\frac{R+r}{H}\right)\right] + \frac{1}{2}\sin\left[\arctan\left(\frac{R-r}{H}\right)\right]. \tag{33}$$

Equation 33 provides a mathematical expression for the mean probability of escape from a 2D rectangular pore given the pore's shape (height and radius) and a specific location, r, on the bottom of the pore. Unfortunately, this is not useful from a practical standpoint because the objective with this probability model is to determine a single-valued probability of electron escape, given the dimensions of the pore. Achieving that objective requires us to select a specific value for the random variable r, denoted r_{specific}, that best represents this random variable over its range, $0 < r < R$. We define r_{specific} as the value of r at which the probability of an electron emission for the region defined by $0 < r < r_{\text{specific}}$,

equals the probability of an electron emission for the region defined by $r_{\text{specific}} < r < R$. This value represents the median of r, denoted r_{med}, and can be determined by solving the following equation for r_{med}:

$$\int_{0}^{r_{\text{med}}} f_r dr = \int_{r_{\text{med}}}^{R} f_r dr \,. \tag{34}$$

For the 2D model, since r maps directly to the emission location it is uniformly distributed with a probability density function, $f_r = 1/R$. Solving Equation 34 provides $r_{\text{med}} = R/2$. Substituting this value of r into Equation 33 and replacing the variables R and H in Equation 33 with an aspect ratio defined as,

$$A_R = \frac{H}{2R}, \tag{35}$$

we arrive at the final model describing the probability of escape for a 2D pore:

$$\overline{P}_{\text{escape-2D}}\left(r = \tfrac{R}{2}\right) = \frac{1}{2}\sin\left[\arctan\left(\frac{3}{4A_R}\right)\right] + \frac{1}{2}\sin\left[\arctan\left(\frac{1}{4A_R}\right)\right]. \tag{36}$$

Combining Equations 26, 28, and 36 provides a complete SEY model for a porous surface based on a 2D pore geometry.

3.1.2 Probability of Electron Escape for a Three-Dimensional Pore Model

Figure 25 illustrates the geometrical layout and parameters involved in the derivation of P_{escape} for the three-dimensional (3D) pore model, which we refer to as $P_{\text{escape-3D}}$. Determining the maximum polar emission angles for the 3D case requires finding an expression for D, the distance between the emission location and the circle at the base of

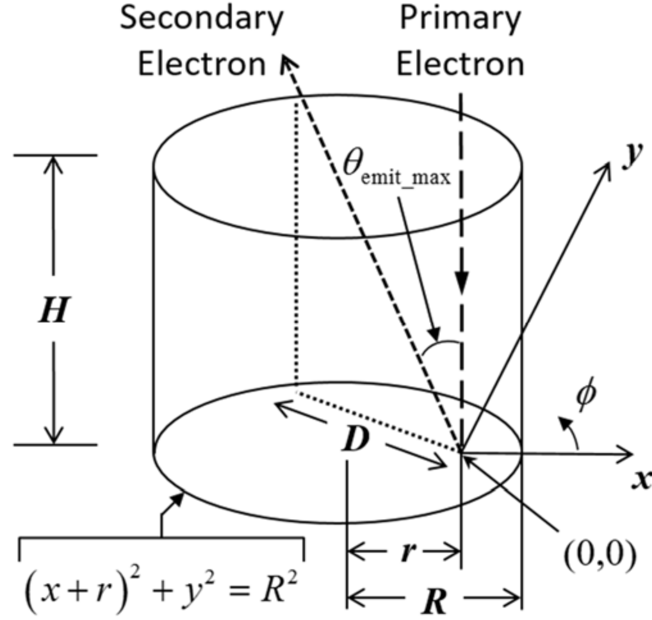

Figure 25: Illustration of the 3D pore model showing key parameters.

the pore that outlines the pore sidewalls (see Figure 25). This circle is given by the equation,

$$(x+r)^2 + y^2 = R^2 . \tag{37}$$

Converting Equation 37 to cylindrical coordinates by substituting $x = D\cos(\phi)$ and $y = D\sin(\phi)$ and then rearranging terms yields the quadratic equation,

$$D^2 + (2r\cos\phi)D + (r^2 - R^2) = 0 . \tag{38}$$

Solving Equation 38 for D provides,

$$D = \sqrt{R^2 - r^2\sin^2\phi} - r\cos\phi . \tag{39}$$

Therefore, the maximum polar emission angle, θ_{emit_max}, is given by,

$$\theta_{emit_max} = \arctan\left[\frac{D}{H}\right] = \arctan\left[\frac{\sqrt{R^2 - r^2\sin^2\phi} - r\cos\phi}{H}\right]. \tag{40}$$

Applying the cosine distribution for the polar angle of electron emission (assumption 4) and summing over all polar angles that permit electron escape provides a conditional probability for $P_{\text{escape-3D}}$ that depends on the azimuthal angle of emission, ϕ:

$$P_{\text{escape-3D}} = \int_0^{\theta_{\text{emit_max}}} \cos(\theta)\,d\theta = \sin(\theta_{\text{emit_max}}) = \sin\left(\arctan\left[\frac{\sqrt{R^2 - r^2\sin^2\phi} - r\cos\phi}{H}\right]\right). \tag{41}$$

For the 2D model, ϕ was a discrete (binary) random variable; however, for the 3D model, ϕ is a continuous random variable over the range $0 \le \phi \le 2\pi$. Therefore, determining a mean probability of escape (by applying assumption 5 above) must account for the infinite number of equally likely probabilities for electron emission at a given azimuth in the range $0 \le \phi \le 2\pi$. Summing these infinite conditional probabilities results in the mean probability,

$$\overline{P}_{\text{escape-3D}} = \frac{1}{2\pi}\int_0^{2\pi} \sin\left(\arctan\left[\frac{\sqrt{R^2 - r^2\sin^2\phi} - r\cos\phi}{H}\right]\right) d\phi. \tag{42}$$

Unfortunately, the integral in Equation 42 cannot be solved in closed form. However, a numerical evaluation will provide useful results for the purposes of this research. We now return to the random variable r, to determine the value, r_{specific}, at which the probability of an electron emission for the region defined by $0 < r < r_{\text{specific}}$, equals the probability of an electron emission for the region defined by $r_{\text{specific}} < r < R$. As in the 2D case, this value represents the median of r and can be determined by solving Equation 34 for r_{med}. However, whereas in the 2D case, r maps directly to the emission location and thus has $f_r = 1/R$, in the 3D case, r maps to a radius of infinite emission locations and thus has a different (non-uniform) distribution. This distribution equals the ratio of the circumference of the circle described by r to the area of the entire region of the bottom of the pore:

$$f_r(r) = \frac{2\pi r}{\pi R^2} = \frac{2r}{R^2}. \quad (43)$$

Substituting Equation 43 into Equation 34 and solving for r_{med} (under the condition, that r_{med} must be non-negative) provides:

$$\int_0^{r_{\mathrm{med}}} \frac{2r}{R^2} dr = \int_{r_{\mathrm{med}}}^{R} \frac{2r}{R^2} dr \;\rightarrow\; \frac{r_{\mathrm{med}}^2}{R^2} = \frac{R^2}{R^2} - \frac{r_{\mathrm{med}}^2}{R^2} \;\rightarrow\; r_{\mathrm{med}} = \frac{R}{\sqrt{2}}. \quad (44)$$

Substituting this median value of r back into Equation 42 and simplifying yields,

$$\overline{P}_{\text{escape-3D}} = \frac{1}{2\pi} \int_0^{2\pi} \sin\left(\arctan\left[\frac{R}{H\sqrt{2}} \left(\sqrt{1+\cos^2\phi} - \cos\phi \right) \right] \right) d\phi. \quad (45)$$

Finally, replacing the variables R and H in Equation 45 with aspect ratio (Equation 35) provides a final model for the probability of escape for a 3D pore:

$$\overline{P}_{\text{escape-3D}}\left(r = \tfrac{R}{\sqrt{2}} \right) = \frac{1}{2\pi} \int_0^{2\pi} \sin\left[\arctan\left(\frac{\sqrt{1+\cos^2\phi} \;-\; \cos\phi}{2A_R\sqrt{2}} \right) \right] d\phi. \quad (46)$$

Combining Equations 26, 28, and 46 provides a complete SEY model for a porous surface based on a 3D pore geometry.

3.1.3 Analysis of the Porous Surface SEY Models

Although Chapter V will provide additional analysis of the 2D and 3D porous surface SEY models, a preliminary analysis is provided here to inform and guide the design of engineered surfaces to be fabricated and tested for model validation. To begin, a comparison of the 2D and 3D models was performed to assess whether the much simpler 2D model, provided sufficient accuracy to be used instead of the 3D model. Figure 26 shows total SEY predictions for a variety of porous surfaces ranging in porosity and aspect

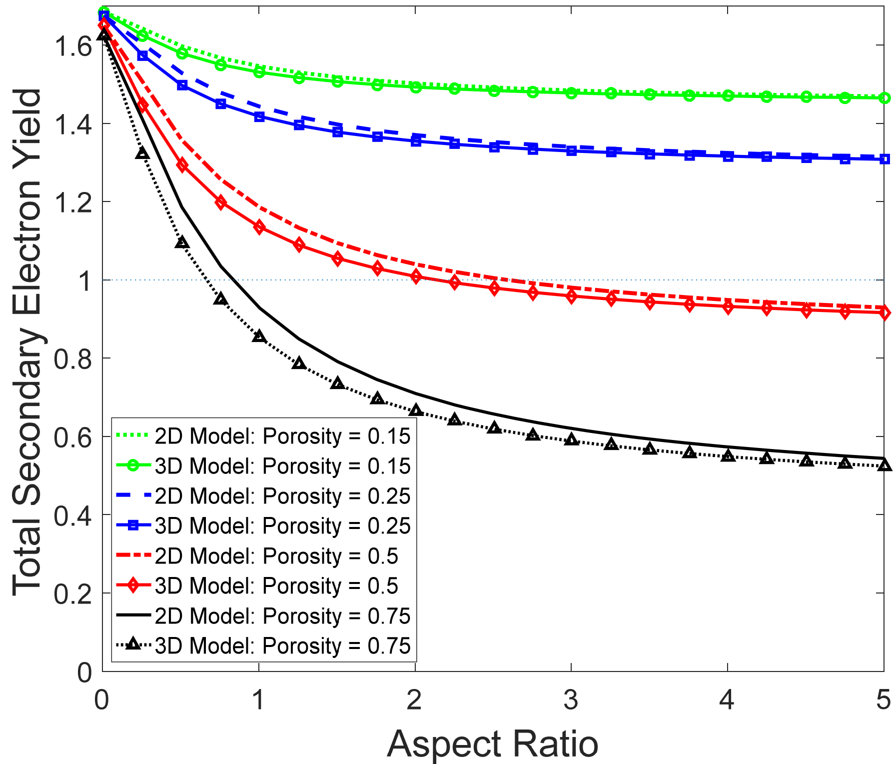

Figure 26: Comparison of the 2D and 3D porous surface SEY models showing the total SEY of the porous surface ($\sigma_{porous\text{-}surface}$), based on $\sigma_{non\text{-}pore}$ = 1.7 and $\sigma_{pore\text{-}bottom}$ = 1.6.

ratio. These plots, and the subsequent plots of total SEY predictions in this chapter, were based on $\sigma_{non\text{-}pore}$ = 1.7 and $\sigma_{pore\text{-}bottom}$ = 1.6. These seemingly arbitrary values were selected because they are in the range of measured maximum total SEY values for gold provided in a database of SEY measurements compiled and published by D.C. Joy [102]. The value for $\sigma_{non\text{-}pore}$ was chosen to be slightly larger than $\sigma_{pore\text{-}bottom}$ to reflect the prediction that most surface engineering fabrication processes (wet chemical etching, laser ablation, electroplating) will provide lower SEY surfaces at the bottoms of the pores as shown in Figure 19. The plots in Figure 26 clearly indicate that the 3D model predicts lower total SEY values than the 2D model over the range of values for porosity and aspect ratio. This difference is linked directly to the inaccuracies of the 2D model, which are

attributed to the 2D simplification of the azimuthal angle of emission (ϕ) being restricted to only two values (0 and π). The inaccuracies of this simplification accumulate in Equation 36. To better explore the 2D and 3D model differences, a plot of each model's probability of escape (Equations 36 and 46) are provided in Figure 27 along with a plot of the absolute difference between the two formulae. The difference between the P_{escape} models peaks at 0.068 (at $A_R = 0.44$) and stays above 0.05 over the range $0.18 < A_R < 1.17$. This is important because of the role aspect ratio plays in any engineered surface for controlling SEE. Although higher aspect ratios improve electron recapture (thus reducing SEY), they also negatively affect the performance characteristics of the RF or microwave device in which the engineered surface is incorporated. Additionally, high aspect ratio surface features are

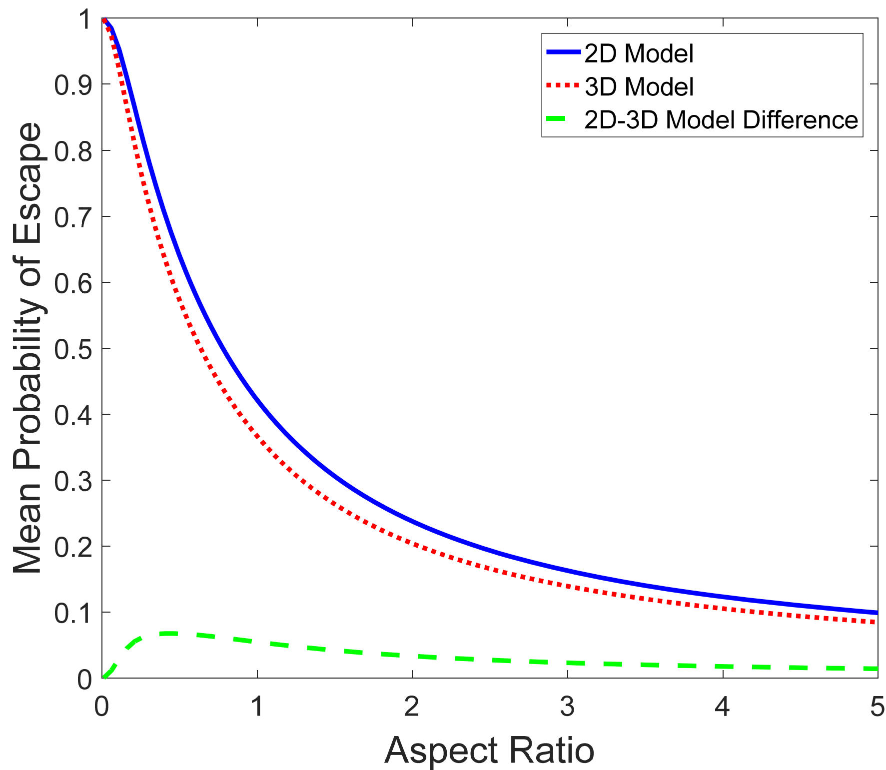

Figure 27: Comparison of the mean probability of electron escape from a cylindrical pore predicted by a 2D and 3D pore model.

extremely challenging to fabricate with consistency over large areas. Therefore, it is likely that engineered surface solutions for multipactor suppression will involve aspect ratios that are less than two. From this reason, it becomes essential that any SEY model for an engineered surface be accurate over the range $0 < A_R < 2$. Consequently, the 3D model was chosen as the best model to achieve the research goal.

The second half of this analysis was to use the model "to inform and guide the design of engineered surfaces…for model validation." An examination of the role that surface chemistry plays in the 3D model requires understanding the relationship between $\sigma_{\text{porous-surface}}$ and the surface chemistry parameters $\sigma_{\text{non-pore}}$ and $\sigma_{\text{pore-bottom}}$. Equations 26 and 28 show these relationships to be positive and linear. Consequently, it is important to employ low-SEY materials in any engineered surface used for multipactor suppression. Another consequence of these relationships is that any engineered surface used for SEY control remains susceptible to changes in surface chemistry (adsorption, oxidation, etc.), which alter both $\sigma_{\text{non-pore}}$ and $\sigma_{\text{pore-bottom}}$. An examination of the role surface topography plays in these models requires understanding the relationship between $\sigma_{\text{porous-surface}}$ and the topography parameters *Porosity* and A_R. Let us first consider the "$\sigma_{\text{porous-surface}}$-*Porosity*" relationship. Equation 26 shows an inverse linear relationship between these parameters (assuming pore-regions emit fewer electrons per area than the non-pore regions). Figure 28 shows this relationship over a variety of plots covering a range of feasible aspect ratios and using the same values of $\sigma_{\text{non-pore}} = 1.7$ and $\sigma_{\text{pore-bottom}} = 1.6$. Let us now consider the $\sigma_{\text{porous-surface}}$-$A_R$ relationship. Equation 46 reveals a nonlinear relationship between these parameters which is illustrated in Figure 29 for a variety of plots covering a range of feasible *Porosity* values and using the same values of $\sigma_{\text{non-pore}} = 1.7$ and $\sigma_{\text{pore-bottom}} = 1.6$.

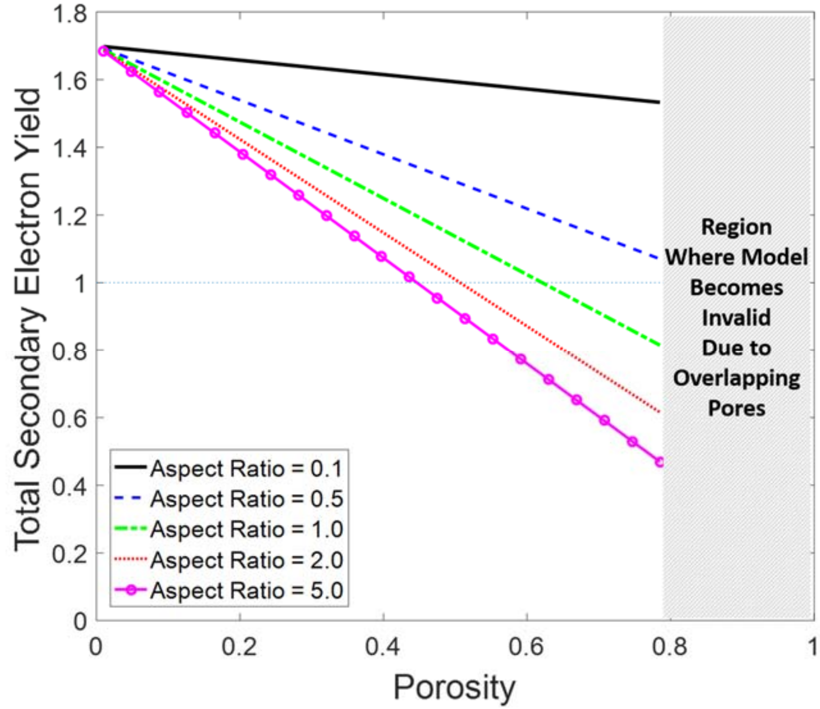

Figure 28: Illustration of the inverse linear relationship between the total SEY of the porous surface and surface porosity, based on $\sigma_{\text{non-pore}} = 1.7$ and $\sigma_{\text{pore-bottom}} = 1.6$.

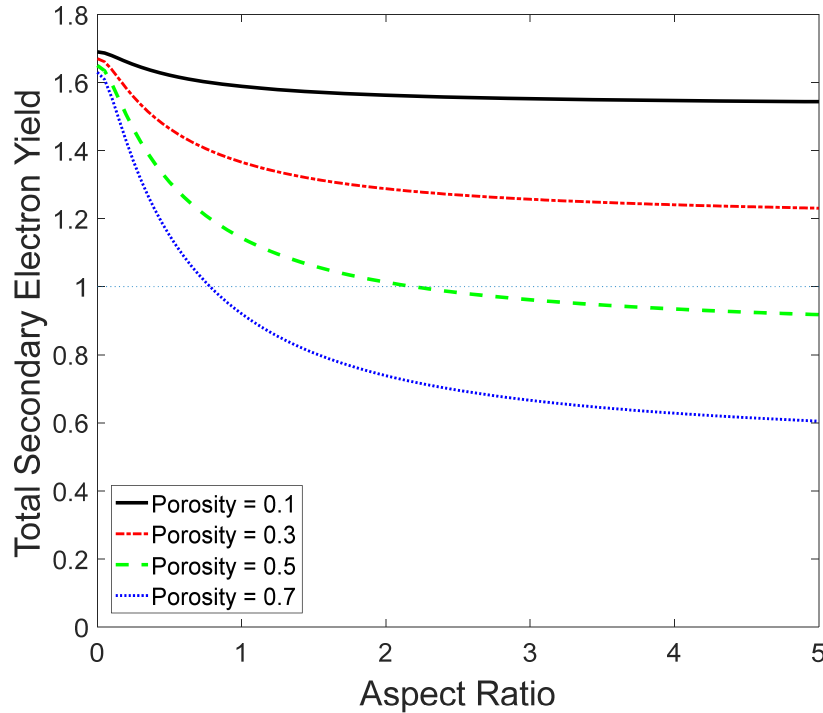

Figure 29: Illustration of the nonlinear relationship between the total SEY of the porous surface and pore aspect ratio, based on $\sigma_{\text{non-pore}} = 1.7$ and $\sigma_{\text{pore-bottom}} = 1.6$.

Remembering the overarching goal of this dissertation is, "to determine optimal surface topographies to control secondary electron emission," it should be noted that both Figure 28 and Figure 29 indicate a surface design for multipactor suppression when *Porosity* = 0.5 and A_R = 2.0. This provides a design target for the next section.

3.2 Engineered Surface Designs and Fabrication

3.2.1 Design Considerations

The previous modeling effort helped confirm two design hypotheses: (1) increasing pore height (i.e. aspect ratio) will decrease SEY (greater chance for electron recapture), and (2) increasing pore density (i.e. *Porosity*) will decrease SEY (greater chance for an electron to fall within a pore). The curves provided in Figure 28 illustrates the importance of maximizing *Porosity* in order to minimize total SEY. The linear relationship is important because it means changes in *Porosity* will yield consistent changes in total SEY…in other words, this relationship does not exhibit any "diminishing return" behavior. By contrast, the curves provided in Figure 29 show the inverse nonlinear relationship between total SEY and aspect ratio. In contrast to the five curves shown in Figure 28, the convergence and flattening slope of the four curves in Figure 29 indicate a "diminishing return" behavior for reducing SEY by increasing aspect ratio. This important trend provides useful information for the designer: pursuing higher and higher aspect ratios to reduce SEY is a misguided objective. This conclusion fits nicely with two other noteworthy design trends: (1) as aspect ratio increases, surface fabrication difficulty increases; (2) increasing the aspect ratio of surface features inside a waveguide or other RF/microwave device can negatively affect the device's ability to propagate RF/microwave waves.

The primary challenge to achieving the previously mentioned porous surface design for multipactor suppression (*Porosity* = 0.5 and A_R = 2.0) is the tradeoff between aspect ratio and *Porosity*. To better illustrate this, let us consider how to achieve an A_R = 2.0. For practical fabrication purposes, the pore height will be limited to 6 µm. Thus, according to Equation 35, achieving an A_R = 2.0 would require a pore radius of 1.5 µm. Given these design constraints, we can now consider how to achieve a *Porosity* = 0.5. Figure 30 shows the geometry of a simple pore pattern based on a square-layout. The *Porosity* of the pore layout shown in Figure 30 is,

$$Porosity = \frac{\pi R^2}{\left(2R+S\right)^2}. \tag{47}$$

Therefore, achieving a *Porosity* = 0.5, given the 1.5 µm pore radius necessary for A_R = 2.0, requires a pore spacing of 0.76 µm. Figure 31 helps illustrate the challenge of fabricating porous surfaces with *Porosity* = 0.5 and A_R = 2.0 by showing the relationship between pore height and pore spacing necessary to achieve *Porosity* = 0.5 and A_R = 2.0. The practical region for achieving such a surface is circled in red.

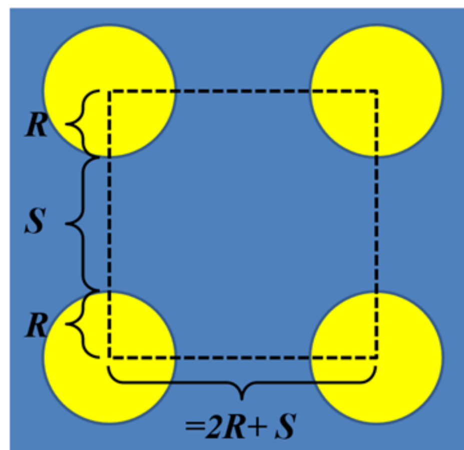

Figure 30: Square-based porous surface layout used to calculate *Porosity*.

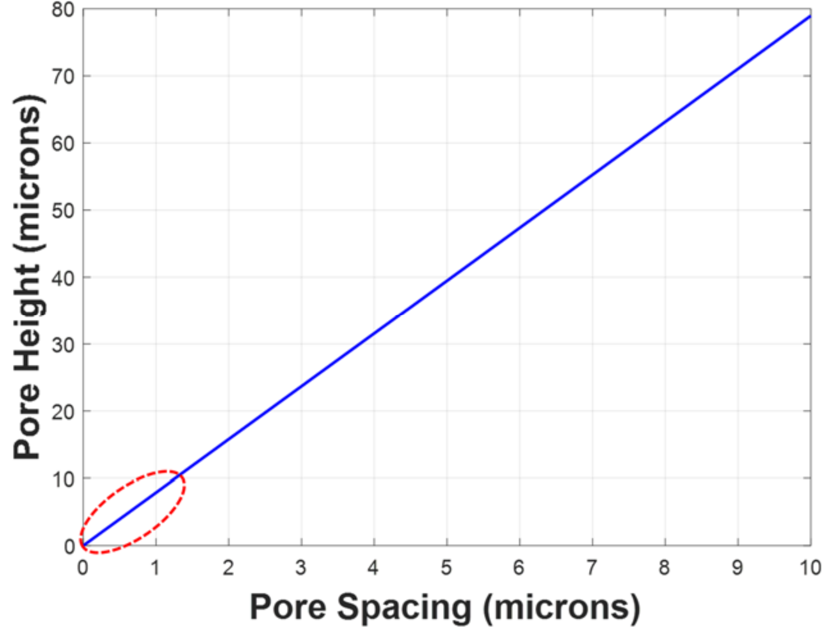

Figure 31: Relationship between pore height and spacing for a square-based porous surface layout with *Porosity* = 0.5 and A_R = 2.0 (practical fabrication region circled).

A limitation of Equation 26 is that it assumes the ideal pore geometry shown in Figure 23. However, as *Porosity* → 1, the ideal pore geometry breaks down because the pores begin to overlap, erasing segments of the pore sidewalls. The upper limit of *Porosity* can be determined by considering the specific arrangement of pores. Figure 32 shows the maximum valid porosity for two pore layout patterns of interest. From Equation 27, the porosity for the square layout (Figure 32a) is

$$Porosity = \frac{\pi R^2}{4R^2} = 0.785, \tag{48}$$

which leads to the defined range: $0 \le Porosity \le 0.785$. The porosity for the close-packed layout (Figure 32b) is

$$Porosity = \frac{\pi R^2}{2R^2\sqrt{3}} = 0.907, \tag{49}$$

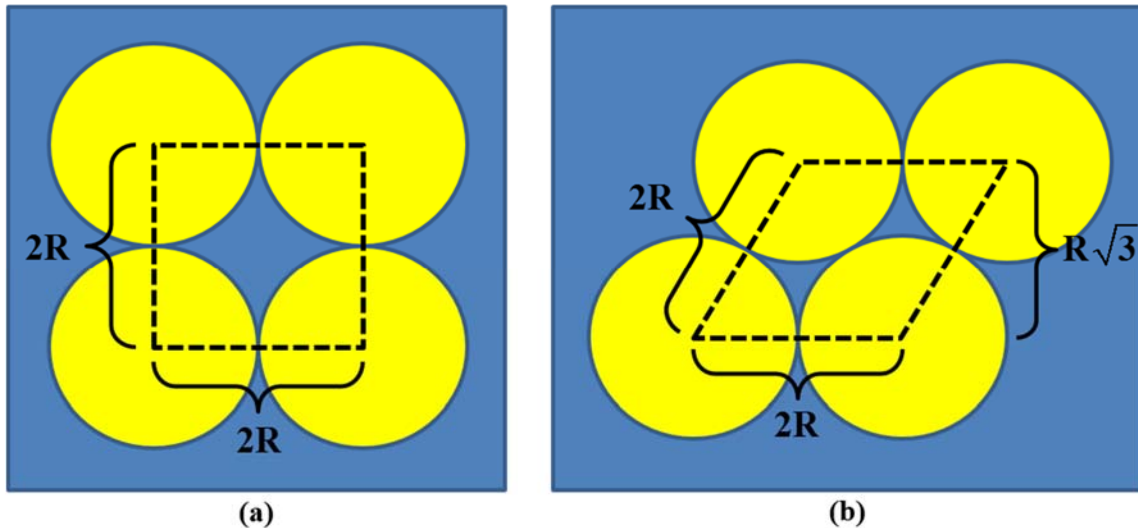

Figure 32: Maximum porosity of pore layout patterns of interest: (a) square layout; (b) close-packed layout.

which leads to the defined range: $0 \leq Porosity \leq 0.907$. These ranges must be considered when designing engineered surfaces. The following list provides a summary of noteworthy design rules taken from the preceding analysis for engineering porous surfaces.

1) Maximize *Porosity* to minimize $\sigma_{\text{porous-surface}}$.

2) *Porosity* must be limited to values below 0.785 for square layouts and below 0.907 for close-packed layouts to avoid overlapping pores.

3) There is a "diminishing return" benefit to increasing aspect ratio to lower SEY.

4) There are tradeoffs that accompany larger aspect ratios including fabrication difficulty and increased insertion losses for RF/microwave devices.

Although these design rules are believed to be accurate for engineering the most effective surfaces for reducing SEY, they must be proven with experimental validation.

3.2.2 Microporous Surface Designs and Fabrication

As previously discussed, the target porous surface designs (i.e. surfaces with a large *Porosity* and aspect ratio) are constrained by several practical fabrication realities. A fabrication decision that was made early on in this effort was to use an additive metal process instead of a subtractive metal process. An additive metal process would avoid the imperfect pore shapes demonstrated by Ye *et al.* using a metal etch process (see Figure 19). Additive metal processes include metal sputtering, evaporation, and electroplating (also known as electrodeposition). To achieve the larger pore sizes needed for microporous samples, an electroplating process was selected for its ability to deposit thick metal layers (~6 µm). By contrast, metal sputtering and evaporation are best suited for layer thicknesses less than 1.0 µm. Furthermore, electroplating provides smooth pore sidewalls by depositing gold around a pattern of photoresist pillars that act as a mold. The only requirement for an electroplating fabrication process is a photoresist layer that is thicker than the electroplated metal thickness. The AZ® 9260 photoresist, manufactured by MicroChemicals®, provides thicknesses ranging from 5 µm to 20 µm and was available for use in AFIT's cleanroom. Appendix A-1 contains the steps to pattern a 9-µm thick layer of the AZ® 9260 photoresist.

Figure 33 shows a matrix of six microporous designs that will be fabricated to validate the 3D porous surface SEY model (Equations 26, 28, and 46) using experimental methods. The range of sample porosity (0.13 to 0.91) provides a large contrast for the designed experiment. The range of aspect ratio for micron-sized pores is limited by the 6-µm gold thickness associated with electroplating. Although it is possible to achieve an aspect ratio of 2.0 with a 6-µm thick layer of gold, this would require shrinking the pore diameter to 3 µm and the pore spacing to 0.76 µm. Such a pore spacing is smaller than the feature

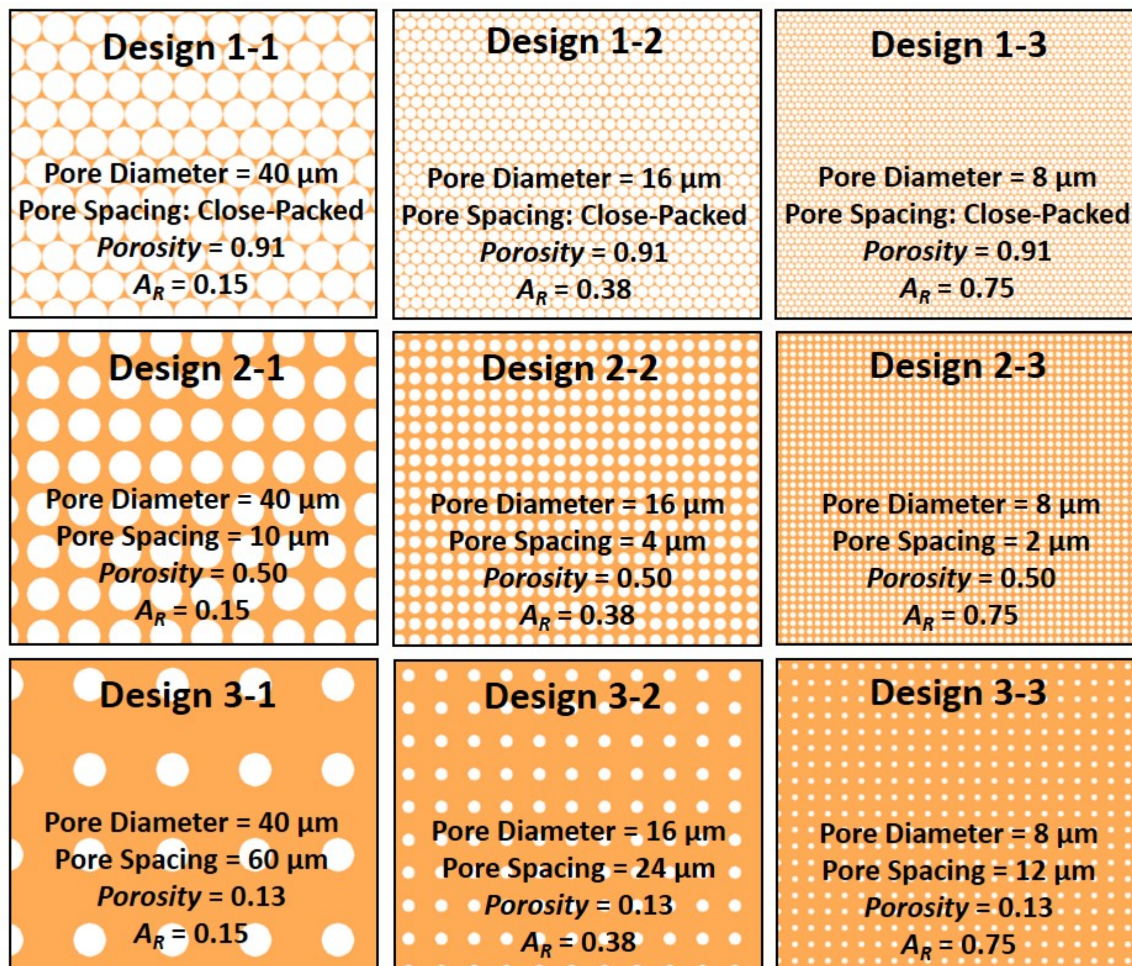

Figure 33: Microporous surface designs to be fabricated using an electroplating process.

resolution of the patterning equipment available at AFIT. Ultimately, a maximum aspect ratio of 0.75 was selected to balance fabrication difficulty and the ideal design parameters.

Figure 34 illustrates the process for fabricating microporous gold surfaces using photolithography and electroplating. Gold was selected as the porous surface material for three reasons: (1) it is readily available for electroplating at AFIT and the Air Force Research Laboratory (AFRL), Sensors Directorate; (2) it has well-documented SEY curves; (3) it is considered a viable material for multipactor suppression treatments in RF

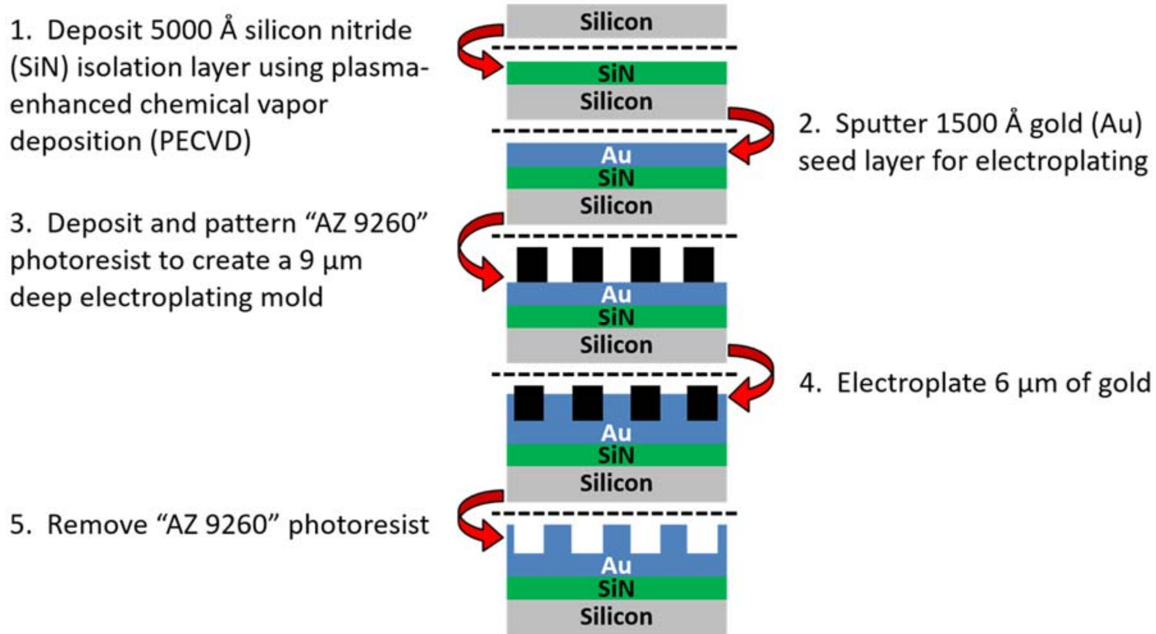

Figure 34: Process for fabricating gold microporous surfaces using electroplating.

systems because of its resistance to oxidation [10]. However, future studies of other metals (silver, copper, nickel, stainless steel, etc.) are possible by acquiring different electroplating solutions or contracting with an outside electroplating agency.

3.2.3 Nanoporous Surface Designs and Fabrication

To help answer the first, second and fourth research questions posed in Section 1.5, samples of nanoporous surfaces are needed. Unfortunately, standard photolithography methods are not effective at nanometer scales. Thus, more innovative and modern fabrication methods are necessary to create these nanoporous surfaces. Ultimately, two fabrication methods were intensively explored for this research: extreme-optimized photolithography and electron-beam (e-beam) lithography.

Extreme-Optimized Photolithography (EOP)

The mask-writing lithography systems available at AFIT are two Heidelberg model µPG 101 Tabletop Micro Pattern Generators. The more capable of AFIT's two systems can laser-write feature sizes down to 1 µm with an alignment accuracy of 400 nm. This means the laser position is controllable down to 400 nm. Figure 35 shows a two-step exposure process that could use this system to pattern pillars of photoresist as small as 400×400 nm^2. These pillars of photoresist could then be used as a mold around which a metal could be evaporated to create a porous surface. The size of the pillars can be controlled by varying the spacing of the laser-exposed paths (between 400 nm and 500 nm). For pores smaller than 400 nm, the pillars can be shrunk using reactive ion etching (RIE). Although the pillars would have a square shape (as shown on the right side of Figure 35), a pre-metallization clean of the surface using an oxygen plasma ash would provide some rounding of the pillars to provide a more cylindrical pore shape. Figure 36 illustrates the process for fabricating nanoporous surfaces using this form of extreme-optimized photolithography (EOP). Unfortunately, this process has a critical design limitation – pore spacing is fixed to the

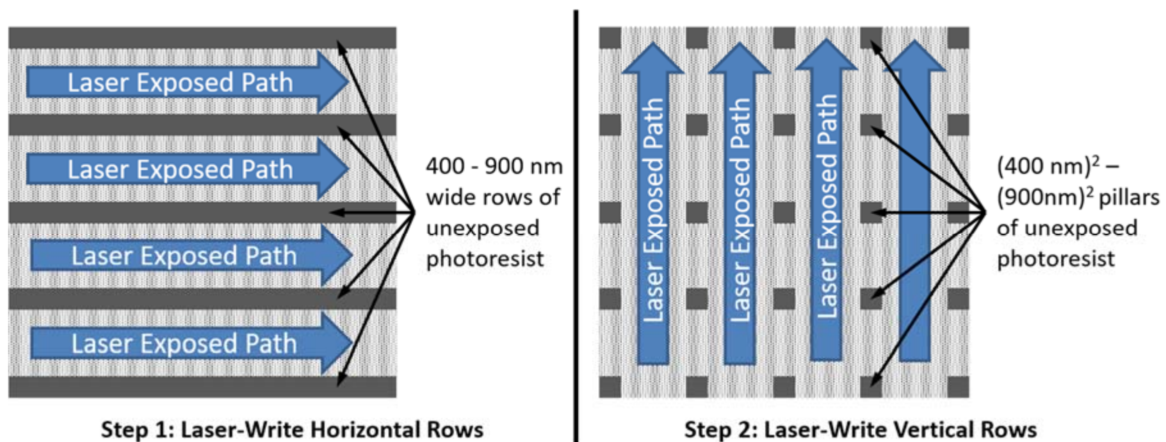

Figure 35: Extreme-optimized photolithography process to pattern sub-micron features.

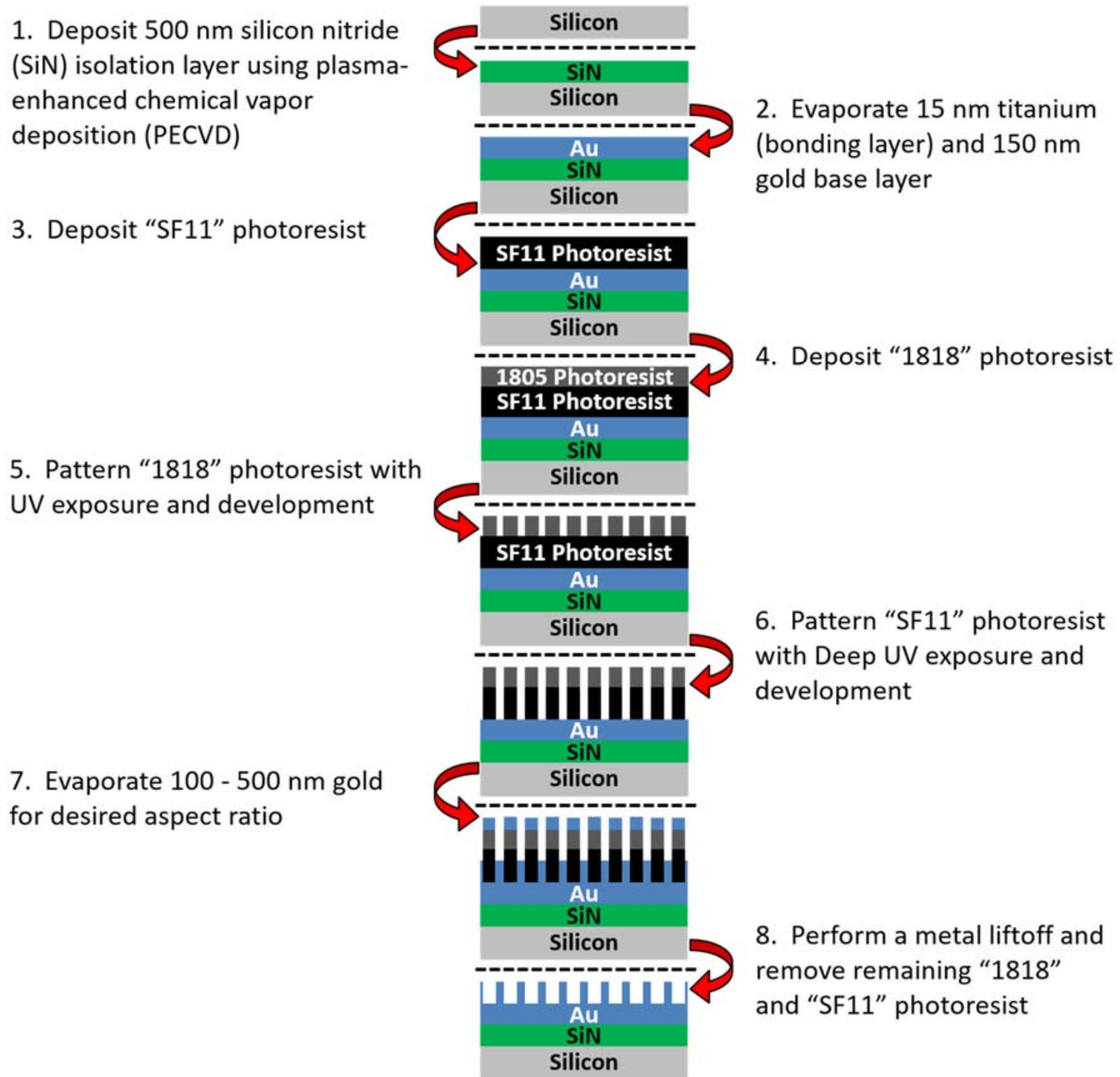

Figure 36: Process to fabricate nanoporous surfaces using extreme-optimized photolithography (useful for *Porosity* < 0.25).

spot size of the laser (1000 nm). For example, the *Porosity* of a surface with $400\times400\ \text{nm}^2$ pores would be (using Equation 27),

$$Porosity = \frac{(400\text{nm})^2}{(400\text{nm}+1000\text{nm})^2} = 0.0816\,. \tag{50}$$

In order to reach a *Porosity* of 0.5 the pore size would have to be 2.4×2.4 μm^2, which is not ideal because this pore size is in the transition region between nanoporous and microporous surfaces. The challenge with this process will likely be performing the deep ultraviolet (DUV) exposure of the bottom resist layer (SF11). This is because the pillars of 1818 photoresist will be extremely small which may result in complete exposure of the SF11 from diffraction of the DUV waves. Ultimately, this process may prove useful for fabricating nanoporous surfaces with aspect ratios as large as one, but only for designs with *Porosity* ≤ 0.25. Table 4 shows the range of porous surface design parameters that are possible using this process.

Table 4. Range of achievable porous surface design parameters using extreme-optimized photolithography (EOP).

Process Type	**Pore Footprint (nm^2)**	***Porosity***	**Aspect Ratio (assume gold layer ≤ 500 nm)**
Original EOP with RIE	200×200	0.02	≤ 2.50
Original EOP with RIE	300×300	0.05	≤ 1.67
Original EOP	400×400	0.08	≤ 1.25
Original EOP	500×500	0.11	≤ 1.00
Original EOP	600×600	0.14	≤ 0.83
Original EOP	700×700	0.17	≤ 0.71
Original EOP	800×800	0.20	≤ 0.63
Original EOP	900×900	0.22	≤ 0.56
Original EOP	1000×1000	0.25	≤ 0.50

E-beam Lithography

An alternative to the previous, unproven approach is to use e-beam lithography, which uses a focused beam of electrons to expose an electron-sensitive resist for patterning. The AFRL Sensors Directorate has the capability to pattern features as small as tens of nanometers using e-beam lithography. Their system is a JEOL model JBX-6300FS e-beam

lithography system capable of writing features as small as 5 nm. Figure 37 shows five nanoporous surface designs that would be realistic to pattern using the JBX-6300FS e-beam lithography system. The designs are based on a 200nm pore diameter with the pores written as octagons to reduce the size of the pattern file that must be loaded on the e-beam system. However, because of the electron backscattering that occurs during e-beam lithography which causes additional and undesired photoresist exposure, these octagons will ultimately round off to give the photoresist pillar a cylindrical shape after the e-beam exposure and development is complete. Because of the size and spacing of the pores combined with the use of a metal liftoff technique, a negative-tone photoresist, “ma-N 2403,” will be used for e-beam lithography. Additionally, an e-beam exposure study is required to determine the optimal e-beam dose/intensity to make the patterns in Figure 37. Figure 38 illustrates the fabrication process that will be used to create the nanoporous

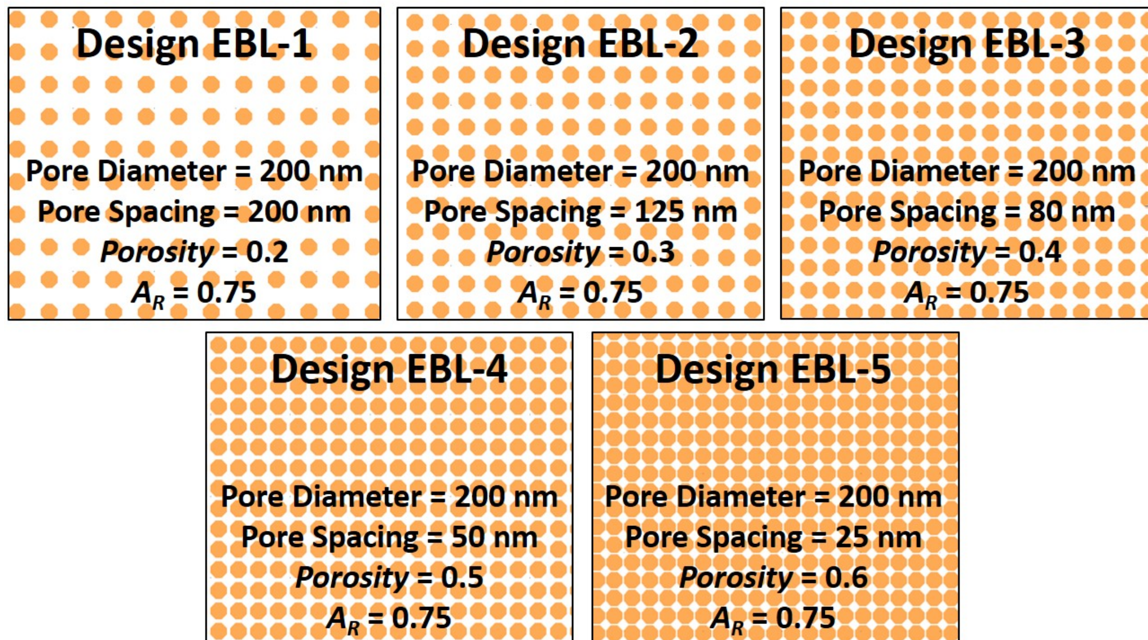

Figure 37: Nanoporous surface designs for electron-beam lithography.

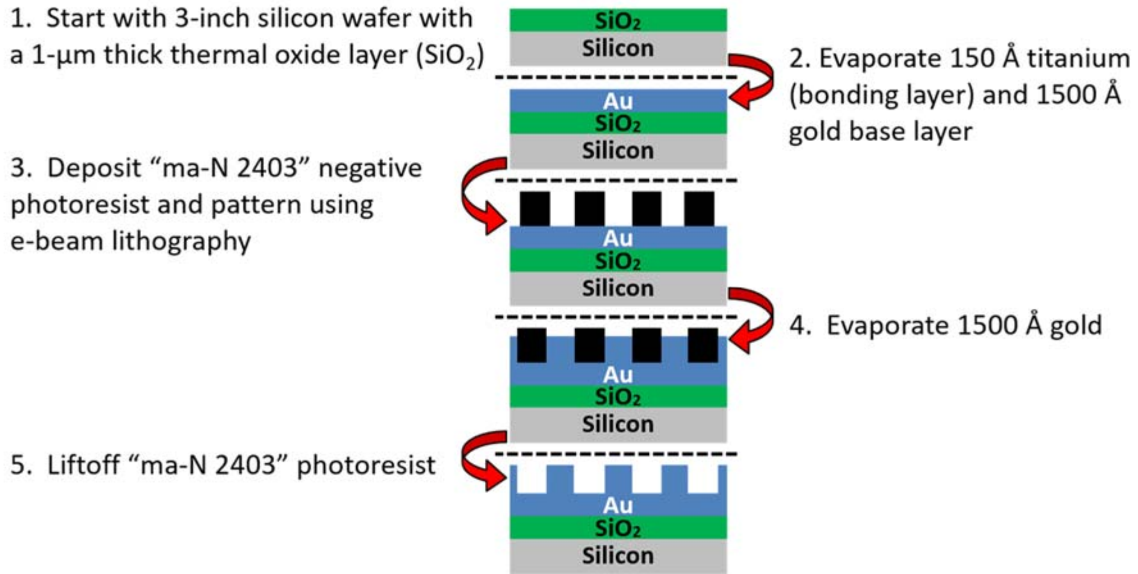

Figure 38: Process to fabricate nanoporous surfaces using electron-beam lithography.

surface designs shown in Figure 37 using e-beam lithography. The isolation layer was changed from silicon nitride to silicon dioxide because wavers were readily available that already contained a 1-µm SiO_2 layer. The primary challenge to fabricating nanoporous surfaces using e-beam lithography will likely be patterning surfaces large enough to allow SEY measurements to be performed. This challenge relates back to the fourth research question posed in Section 1.5. Table 5 shows the total number of pores (200 nm diameter) that must be individually exposed to create surfaces large enough to test using an SEY

Table 5. Total number of 200 nm diameter pores to be individually exposed by electron-beam lithography for various surface sizes.

Design	Pore Spacing (nm)	Total Number of 200nm-Diameter Pores		
		5×5 mm^2	7.5×7.5 mm^2	10×10 mm^2
EBL-1	200	156,250,000	351,562,500	625,000,000
EBL-2	125	236,686,390	532,544,378	946,745,562
EBL-3	80	318,877,551	717,474,489	1,275,510,204
EBL-4	50	400,000,000	900,000,000	1,600,000,000
EBL-5	25	493,827,160	1,111,111,111	1,975,308,642

measurement system. For example, if it takes 1 second to expose a pattern of 10 pores, exposing a surface area 5×5 mm^2 of these pores, spaced 200 nm apart, would take 180 days! Fortunately, a 100×100 μm^2 test coupon of these pores spaced 200 nm apart was written in about 1 minute, which implies that a 5×5 mm^2 surface could be written in less than 2 days.

3.3 Surface Characterization

Following the fabrication of the various engineered porous surfaces, a surface characterization must be performed. This characterization is important for two reasons:

1) the topography of the fabricated surfaces will not perfectly match the initial designs and it will be essential to know the *Porosity* and aspect ratio of each sample prior to SEY testing;

2) the chemistry of the gold surface will be altered by random surface processes (e.g. adsorption and oxidation) and these chemistries must be known to better interpret and explain the SEY data that will ultimately be measured.

Various methods will be used to characterize the topography of the microporous and nanoporous surfaces including optical microscopy, profilometry and scanning electron microscopy. Optical microscopy will be used to confirm the overall size of the pattern and ensure a high degree of consistency and yield are achieved across the entire pattern. A profilometer, capable of measuring surface feature heights as small as ~200 nm, will be used to determine the average pore height associated with each microporous surface. The height of the nano-pores (designed to be 150 nm) will be determined by the precision equipment used in the metal evaporation process, which is accurate to within 10 angstroms (i.e. 150 nm ± 1 nm). Finally, the SEM located in AFIT's cleanroom will be used to measure the pore diameter and spacing for both microporous and nanoporous samples.

Two methods will be used to characterize the chemistry of the gold samples. Energy Dispersive x-ray Spectroscopy (EDS) will be used to characterize the chemistry of the bulk gold material. X-ray Photoelectron Spectroscopy (XPS) will be used to characterize the chemistry of the gold surface.

3.4 SEY Measurements

The general approach for measuring SEY (as discussed in Section 2.2.2) is relatively simple; however, in practice, obtaining accurate SEY measurements can be quite difficult. A variety of factors can dramatically affect these measurements including sample conductivity, sample surface chemistry, vacuum chamber pressure, and numerous parameters related to the primary e-beam (beam current, total dose, spot size, working distance, angle of incidence, and energy spread). Further complicating SEY measurements is the fact that secondary emissions consist of true secondaries, elastically reflected primaries, and inelastically backscattered primaries. Most SEY measurements do not attempt to distinguish between these categories and therefore provide the total SEY (σ) previously defined in Equation 23 and Equation 24.

Since Austin and Starke first discovered SEE in 1902, a variety of measurement approaches have been developed. Today, there are three widely accepted approaches for measuring the SEY of conductive samples. All three methods involve directing a beam of monoenergetic electrons at the sample of interest inside a UHV chamber. As implied in Equation 24, the general principle behind any SEY measurement is the determination of the number of electron emissions from the sample caused by a known number of primary electrons incident upon the sample.

The first SEY measurement method uses a shaped collector (sometimes referred to a Faraday cup) that surrounds the target and captures any secondaries emitted by the target (see Figure 39) [34], [71], [73], [74]. The collector is biased +10-50 volts (relative to the grounded sample) to help capture electrons emitted from the sample and ensure that any true secondary or backscattered electrons that might be emitted from the shaped collector are recaptured by the collector. The total electron emission current (I_σ) is then measured using an electrometer or picoammeter connected between the collector and ground. A second electrometer is used to measure the sample current (I_s) flowing the sample and ground. Whereas I_σ is always measured negative, I_s can be positive or negative depending on the SEY of the sample at the primary electron energy. When I_s is positive, the SEY > 1; when I_s is negative the SEY < 1. The total SEY is then found by substituting $I_p = I_\sigma + I_s$ into Equation 24, which provides

$$\sigma = \frac{I_\sigma}{I_\sigma + I_s}. \tag{51}$$

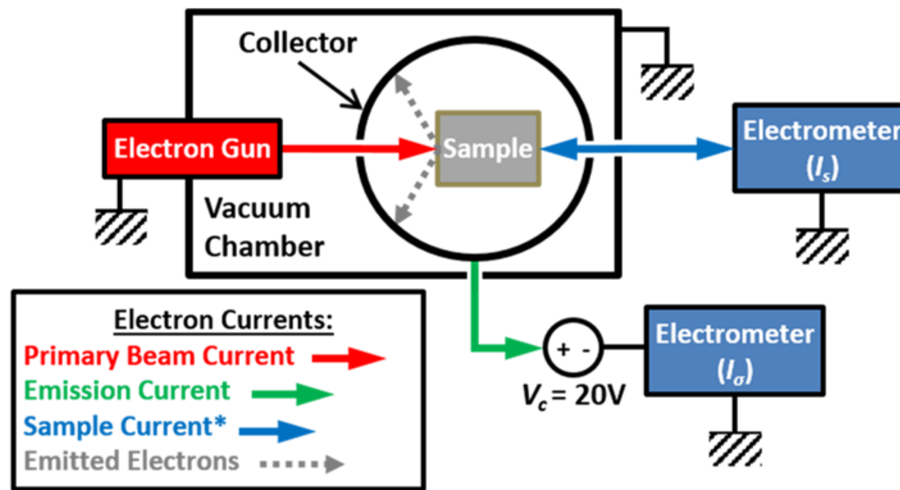

Figure 39: Illustration of the spherical collector method for measuring total SEY.

The shaped collector method neglects SEE from the collector and captured by the sample, which is a reasonable approximation for a positively biased collector [34].

The second widely accepted SEY measurement method eliminates the need for a spherical collector by measuring the primary beam current with a Faraday cup or reference sample and the sample current [10], [34], [65]. Figure 40 illustrates this method using a retractable Faraday cup. Returning to Equation 24 and substituting $I_\sigma = |I_p| + I_s$, we get

$$\sigma = \frac{|I_p| + I_s}{|I_p|} = 1 + \frac{I_s}{|I_p|}, \tag{52}$$

where I_p is always negative. To ensure all emitted electrons are repelled from the sample, the sample is biased to -20 volts (relative to the vacuum chamber, which is grounded). Similar to the first method when I_s is positive, the total SEY < 1; when I_s is negative, the total SEY > 1.

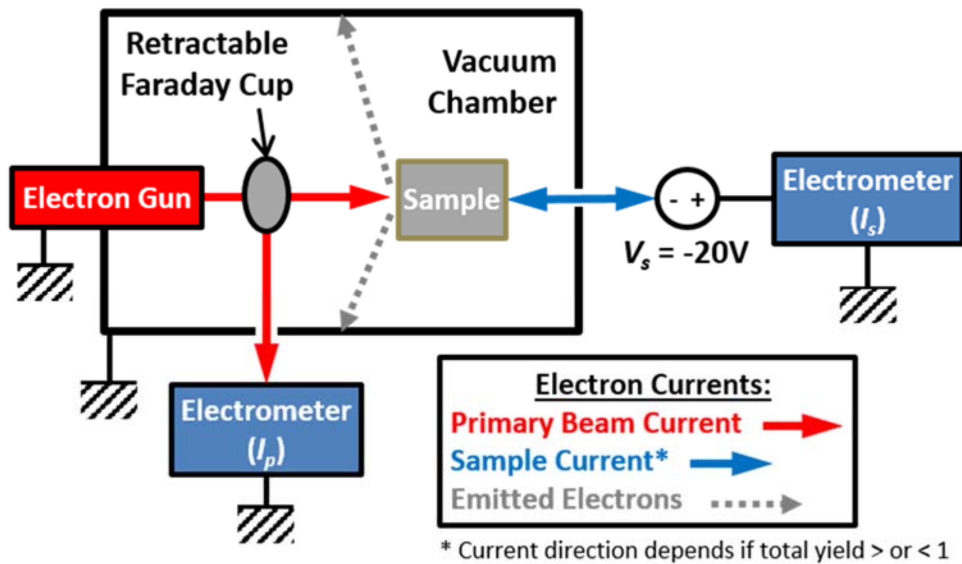

Figure 40: Illustration of the two-step method for measuring total SEY using a Faraday cup.

The third method eliminates the need for a spherical collector and a Faraday cup by measuring the sample current twice: first with the sample biased to +100-500 volts and again with the sample unbiased [68], [72], [103], [104]. Figure 41 illustrates the two steps of this method. With the sample biased +100-500 V, any backscattered or secondary electrons emitted from the sample are recaptured by the sample and accounted for in the sample-to-ground current measurement. Thus, the sample current provides an approximate measurement of the primary beam current ($I_{s1} \approx I_p$). Next, the sample bias is removed and the sample current is re-measured to determine the difference between the primary beam current and the electron emission current ($I_{s2} = I_p - I_\sigma$). Using these two measurements the total SEY of the surface can be determined according to,

$$\sigma = \frac{I_{s1} - I_{s2}}{I_{s1}} = \frac{I_p - \left(I_p - I_\sigma\right)}{I_p} = \frac{I_\sigma}{I_p}. \tag{53}$$

The method that is most likely to produce the most accurate results is the shaped collector method [34]. This is for two primary reasons: (1) it is the only method where the

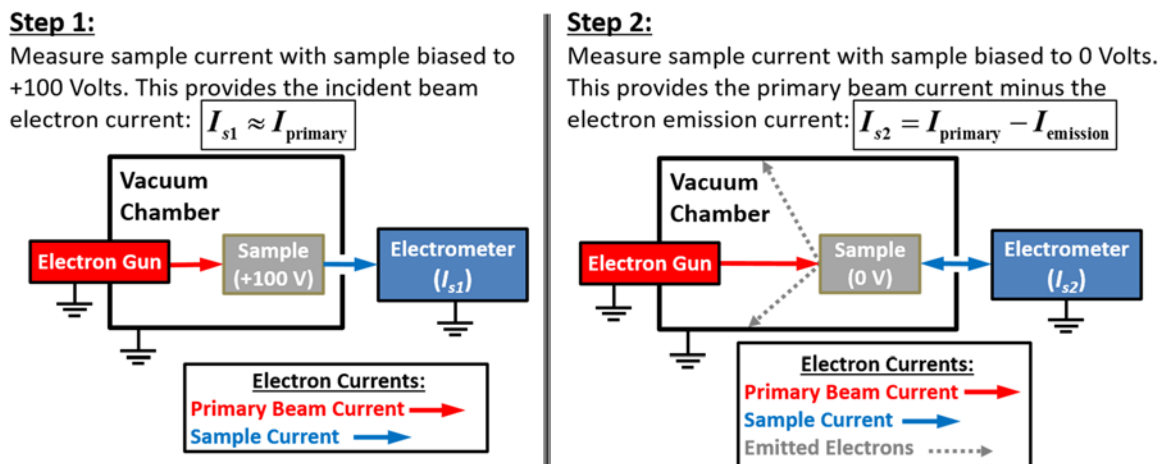

Figure 41: Illustration of the two-step method for measuring total SEY without a collector or a Faraday cup.

secondary emission current is directly measured; (2) the sample is not biased (sample biasing can distort results by influencing the trajectory of incident electrons). Additionally, a properly positioned, spherically-shaped collector that is biased will provide neutral electric field conditions along the path of incident electrons minimizing the undesired effects of e-beam deflection [34]. The next preferred method is the retractable Faraday cup method because it directly measures the primary beam current using a Faraday cup. Least preferred is the two-step sample current measurement method because it requires large sample biases to provide an indirect measurement of the primary beam current. These large biases will also increase the electron beam energy, a change that must also be accounted for in the SEY calculations.

There are several additional considerations for measuring SEY, all of which relate to the primary e-beam. Because multipactor involves low-energy electrons impacting the surfaces, most multipactor studies involving SEY use primary electron energies between zero and 2 keV [10], [36], [68], [70]. Another important factor is the primary e-beam current, which should be minimized (on the order of tens of nanoAmps) to avoid conditioning (i.e. measuring a reduced SEY due to the primary electrons altering the surface chemistry) [34], [36], [74]. Another critical factor is the distance the beam has to travel. This distance should be minimized to avert undesired beam deflections due to ambient magnetic fields present which can greatly influence low energy electrons (< 500 eV). Finally, the vacuum chamber pressure will greatly influence SEY measurements and consequently, UHV is typically recommend [34].

For this research effort, the two-step sample current measurement method shown in Figure 41 will be used because a measurement system based on this method is available at

the AFRL Materials and Manufacturing Directorate. However, a major contribution of this dissertation will include the design, equipment requisition, construction and testing of a new, AFIT SEY measurement chamber based on the retractable Faraday cup method shown in Figure 40. This system will provide numerous measurement advancements over the AFRL system, including the ability to perform temperature-dependent SEY studies, angle of incidence SEY studies, and crystallographic orientation SEY studies. The new system will also provide a much more accurate low-energy electron gun (1eV – 2keV) and provide a pulsed mode for the electron gun that will allow SEY measurements of insulators. Table 6 provides a list of the key pieces of equipment needed to construct the new AFIT SEY measurement system. At the onset of this research effort (summer 2015), only the UHV chamber was on-hand at AFIT, although it was in a non-operational status and location.

Table 6. Equipment necessary for measuring total SEY using the Faraday cup method.

Equipment	Purpose
Ultra-High Vacuum (UHV) chamber with sample exchange load lock and transfer arm	Minimize undesired particle interactions; provide ability to load/unload samples without venting main chamber
Sample Manipulator (5-axis control plus sample heating/cooling)	Control sample position and orientation with respect to primary beam; control temperature of sample during testing
Low Energy Electron Gun (1 eV to 2 keV)	Provide controlled source of monoenergetic primary electrons
Faraday Cup	Collects primary electrons to measure the beam current
2x Electrometers	Measure both the primary electron beam current and the sample current

3.5 AFRL Materials and Manufacturing Directorate SEY Measurement System

The bulk of the SEY measurements will be made using the SEY measurement system located at the AFRL Materials and Manufacturing Directorate. Figure 42 shows a photo of the vacuum chamber system and a close-up image of the sample mount and electron gun. The AFRL system uses a UHV chamber with a base pressure around 10^{-10} Torr. The electron gun is contained in a STAIB Instruments DESA 150 energy analyzer and can provide electrons with energies up to 5 keV. The system is set up with a ~50 mm working distance between the electron gun and the sample (shown in Figure 42, right photo). The electron gun is in a horizontal configuration with the sample manipulator positioned vertically. The sample manipulator is capable of spinning 360° around the vertical axis allowing two samples to be loaded on opposite sides of the sample mount. This speeds up the testing process when multiple samples must be tested. The electron gun parameters (energy, current, and beam width) are controlled using rack mounted controllers. The sample bias is supplied by a Stanford Research Systems, model PS325 high voltage power supply. Sample currents are measured using a Keithley electrometer, Model 6517A

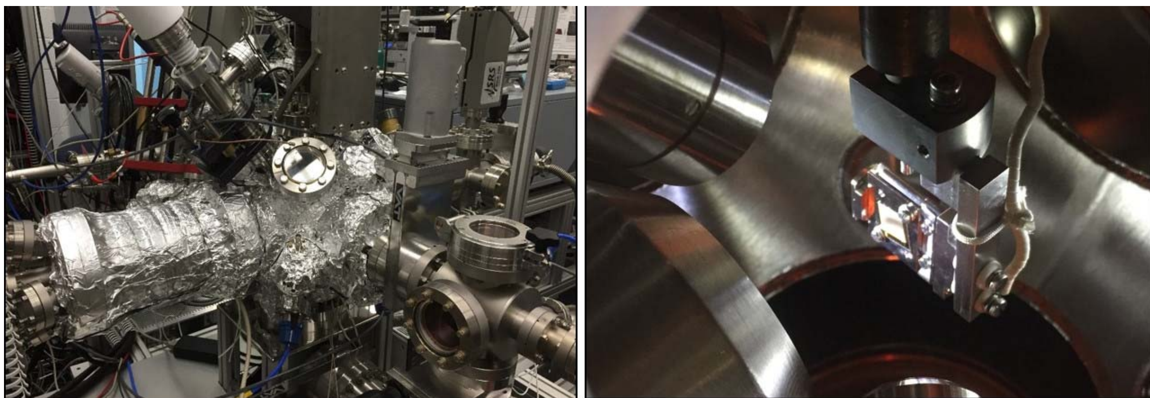

Figure 42: AFRL SEY measurement chamber (left); chamber interior with sample (right).

connected to a computer running a custom LabVIEW® program that saves the data to a text file. Testing one sample over the energy range of interest (0 to 2 keV) requires about 2 hours after the sample is loaded and the chamber is pumped down to UHV overnight.

A final experimental concern worth investigating regards the amount of magnetic field-induced deflection that electrons will undergo between the time they exit the electron gun (e-gun) and arrive at the sample. The Earth's magnetic field provides the primary magnetic field presence in the laboratory. Using the orientation and working distance of the AFRL SEY measurement system along with the magnetic field components at the latitude and longitude of the laboratory, a deflection distance can be determined. The magnitude of force on an electron moving in a magnetic field is given by,

$$F_B = qvB\sin\theta, \tag{54}$$

where q is the charge of one electron (1.6×10^{-19} C), v is the velocity of the electron in meters per second, B is the magnetic field intensity (in Tesla), and θ is the angle between the magnetic field lines and the electron's velocity vector. The velocity of an electron can be determined from its kinetic energy (in Joules) using the equation

$$v_{e^-} = \sqrt{\frac{2(\text{K.E.})}{m_e}}, \tag{55}$$

where the kinetic energy (K.E.) in Joules is determined by multiplying the e-gun energy (given in eV) by 1.6×10^{-19} J/eV and m_e is the rest mass of an electron (9.11×10^{-31} kg). The National Oceanic and Atmospheric Administration (NOAA) provides a convenient web-based magnetic field calculator. This calculator can use either the World Magnetic Model (WMM) or the International Geomagnetic Reference Field (IGRF). Using the US

Geological Survey Earth Explorer to estimate the laboratory's latitude (39.78°N) and longitude (84.08°W), and the "mapcoordinates.net" website to estimate altitude (290 meters), the magnetic field strength was determined to be 20,116.5 nT north, 2,211.3 nT west, and 48,409.2 nT down using the WMM [105]–[107]. Conveniently, the AFRL e-gun-to-sample path is oriented along a north-south trajectory, which means that magnetic field component can be ignored. The remaining two components can be combined into a single magnetic field component that is perpendicular to the electron velocity vector:

$$B_{\perp} = \sqrt{2211.3^2 + 48409.2^2} = 48459.7\,\text{nT}\,. \tag{56}$$

Finally, the angle θ = 90° because only the perpendicular magnetic field component was used. Applying this angle and substituting Equation 55 into Equation 54 provides,

$$F = qB_{\perp}\sqrt{\frac{2(\text{K.E.})}{m_e}}\,. \tag{57}$$

We can now apply Newton's Second Law to Equation 57 and rearrange terms to arrive at,

$$a = \frac{qB_{\perp}}{m_e}\sqrt{\frac{2(\text{K.E.})}{m_e}} = \frac{qB_{\perp}}{m_e^{3/2}}\sqrt{2(\text{K.E.})}\,, \tag{58}$$

where a is the acceleration of the electron. The magnetic deflection distance traveled by an electron (with no initial velocity in the direction of F_B) is given by the kinematic equation,

$$d_B = \frac{1}{2}at^2, \tag{59}$$

where t is the period of time, during which acceleration occurs. The value of t can be determined from the equation,

$$t = \frac{\text{distance}}{\text{velocity}} = \frac{\text{W.D.}}{v_{e^-}} = \text{W.D.}\sqrt{\frac{m_e}{2(\text{K.E.})}}\,, \tag{60}$$

where W.D. is the working distance between the e-gun tip and the sample. Substituting Equations 58 and 60 into Equation 59 provides,

$$d_B = \frac{1}{2}\left(\frac{qB_\perp}{m_e^{3/2}}\sqrt{2(\text{K.E.})}\right)\left(\text{W.D.}\sqrt{\frac{m_e}{2(\text{K.E.})}}\right)^2 = \frac{qB_\perp(\text{W.D.})^2}{2\sqrt{2m_e(\text{K.E.})}}. \tag{61}$$

Table 7 provides electron deflection distances for various e-gun energies, calculated using Equation 61. These results emphasize the importance of minimizing working distance and maximizing sample area to ensure the e-beam does not deflect off the intended target.

Table 7. Magnitude of electron deflection in the AFRL SEY measurement system (assuming a 50 mm working distance) caused by the Earth's magnetic field.

Electron (E-gun) Energy (eV)	Deflection Distance (mm)
50	2.54
70	2.15
100	1.80
150	1.47
200	1.27

3.6 AFIT SEY Measurement System

A significant contribution of this research has been the construction of a new dedicated SEY measurement system at AFIT. This system provides the first SEY measurement capability at AFIT, and the most accurate SEY measurement capability at Wright-Patterson AFB. Because of the lengthy process involved in constructing this system (writing proposals, purchasing expensive custom scientific equipment, installing equipment, and troubleshooting unanticipated equipment problems), this work was performed in parallel with the primary SEY modeling and experimental research efforts.

The UHV vacuum chamber, previously used for carbon nanotube (CNT) research, provided the cornerstone for this new SEY system. Figure 43 shows a photo of the UHV chamber before conversion to an SEY measurement apparatus. All structural vacuum components of the original system were purchased from the Kurt J. Lesker Company and rated for UHV. The chamber consists of a 12-inch diameter spherical main chamber with 11 ConFlat (CF) ports (four 8” ports, two 6” ports, one 4.5” port, and four 2.75” ports). The sample transfer arm is a linear rack-and-pinion system, with 24-inch range, that is was outfitted with a new sample transfer fork, capable of transporting a molybdenum puck on which test samples are mounted. The sample transfer arm is connected to a planar load-lock vessel with a horizontally hinged rectangular access door for loading and unloading samples. The door contains a rubber O-ring that self-seals under vacuum. The system uses two Pfeiffer turbomolecular pumps (models TMU262PN and TMH071YPN) each backed

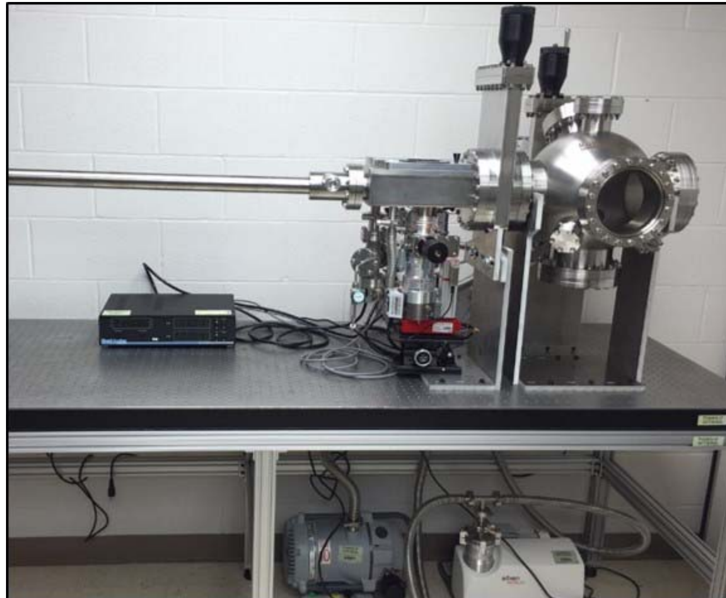

Figure 43: Ultra-High Vacuum chamber before conversion to a Secondary Electron Yield measurement system.

by a separate roughing pump. These four pumps allow the system to reach a base pressure of 6×10^{-8} Torr without performing a high-temperature bake-out. Following a 5-day 200°C bake-out, the base pressure drops to 5×10^{-9} Torr. Pressure is measured using two convection gauges for low vacuum (atmosphere to 10^{-3} Torr) and two ionization gauges for high vacuum (9.9×10^{-4} Torr to 10^{-9} Torr). The gauges are controlled by a rack-mountable box that displays the pressure in units of Torr and is capable of remote operation using an RS-232 connection. The entire system is elevated above a standard optics table using three custom aluminum support brackets mounted directly to the table (see Figure 43). Fabricated by the AFIT model shop, the support brackets provide 9.5 inches of clearance between the 8-inch bottom flange and the top of the support bracket.

The sample manipulator is custom-made by UHV-Design and provides 5-axes of manipulation, sample heating to 800°C, sample cooling to -150°C, and an electrically isolated sample puck that allows sample currents to be measured [108]. Figure 44 shows a 3D Computer-Aided Design (CAD) rendering of the sample manipulator with a detailed drawing of the nest that will hold the sample puck. Using the center of the spherical vacuum chamber as a reference point, the sample manipulator will be manually adjustable in the X-direction (± 25 mm), Y-direction (± 12 mm), and Z-direction (± 12 mm) as well as rotation in azimuth (full 360°) and elevation (+/-180°). These features will allow the operator to have complete control over the e-beam-to-sample geometry. This precise positional control will allow for enhanced SEY studies that incorporate impact angle, crystallographic orientation, and other variables of interest. The manipulator will also be capable of flash heating a sample to 900°C, continuous sample heating to 800°C and continuous cooling to -150°C (cooling requires a liquid nitrogen supply). Controlled

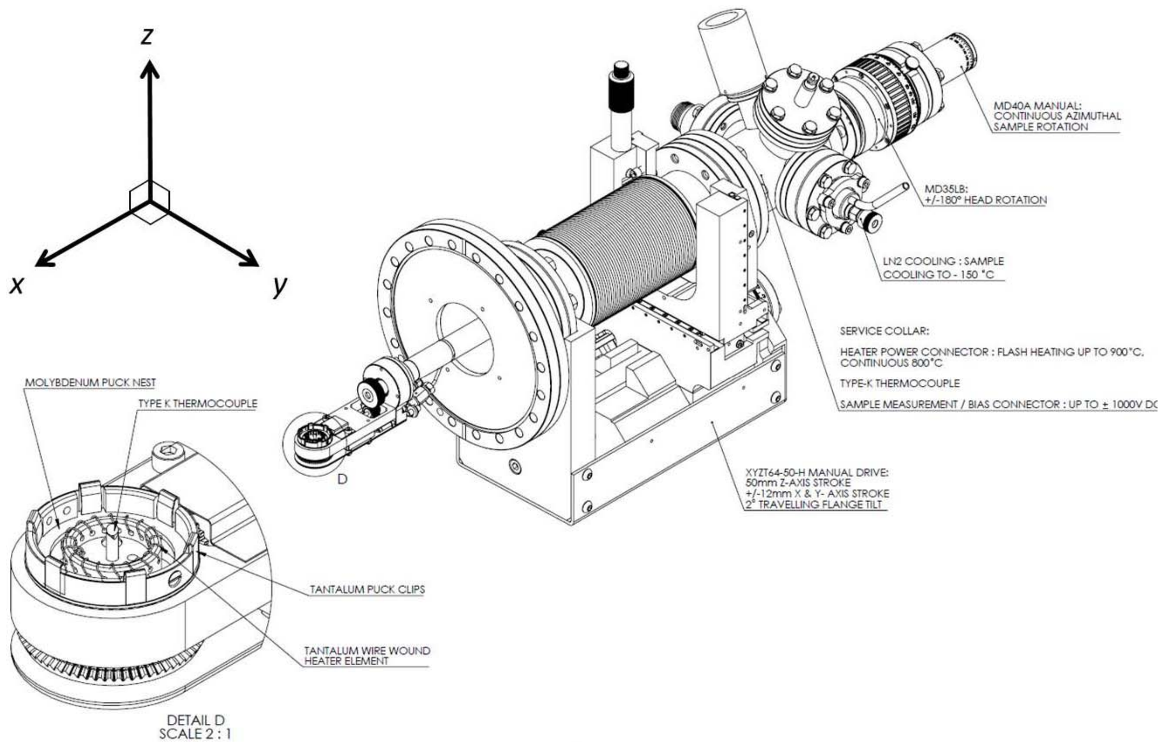

Figure 44: CAD model of the 5-axis sample manipulator made by UHV Design [108].

heating is accomplished using a type-K thermocouple installed in the puck nest (see Detail D in Figure 44) and displayed on a rack-mountable power supply with programmable temperature controller. Samples will be mounted to a 35.6 mm diameter 99.95% pure molybdenum puck that can accommodate samples up to 25 mm in length and width.

The electron gun is a Kimball Physics model ELG-2 with model EGPSS-1022E power supply and controller, shown in Figure 45. The model ELG-2 is ideal for SEY studies because it has the capability to provide low-energy electrons from 1 eV to 2 keV while maintaining a constant beam current of 1 nA to 10 μA. Because of this, it is the electron gun of choice for many SEY researchers [10], [71], [73], [103]. As previously stated in Section 3.4, it is imperative to minimize the working distance between the electron gun and the sample. This is because the low energy electrons involved in SEY measurements

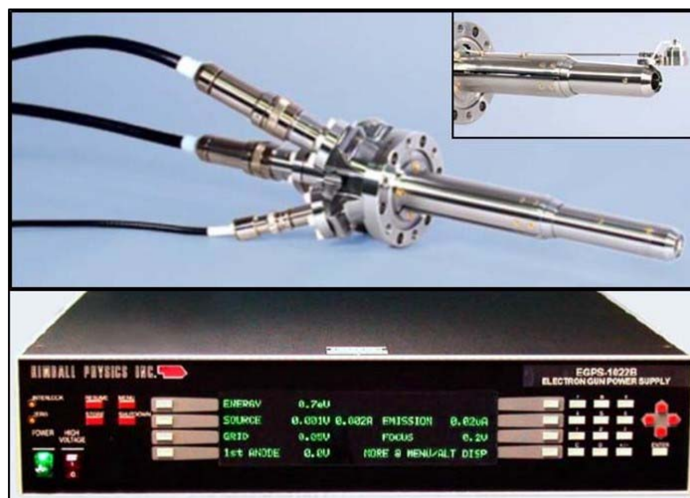

Figure 45: Kimball Physics model ELG-2 electron gun with 1 eV to 2 keV energy range (top), optional tip-mounted Faraday cup (top insert), and controller (bottom).

are heavily influenced by ambient magnetic fields, including the Earth's magnetic field. Kimball Physics recommends a 20 mm working distance between the e-gun tip and the sample for very low energy operation and can tailor the e-gun insertion length to the customer's specification. Using the spherical vacuum chamber schematics, the insertion length for the electron gun was determined to be 191 mm. This length provides 33.5 mm +/-12 mm of working distance between the electron gun tip and the sample (Note: the tip-mounted Faraday cup requires 21.5 mm of clearance from the gun tip in order to actuate). The e-gun system also includes a tip-mounted Faraday cup capable of measuring the primary electron beam current with the addition of an external electrometer or picoammeter. Because the sample transfer arm-manipulator system is arranged horizontally, the electron gun will be positioned vertically, using the 4.5-inch flange located at the top of the spherical vacuum chamber (refer to the right side of Figure 43). In this configuration, the primary e-beam will be directed down toward the sample supported by the 5-axis manipulator arm. The ELG-2 electron gun was also configured to allow for

beam rastering and pulsing. The pulsed mode will allow future SEY studies to be performed on non-conductive samples. Figure 46 shows a close-up photo of the fully installed and tested SEY measurement chamber.

When conducting SEY measurements, it is important to ensure the e-beam illuminates only the surface of interest; otherwise, the results will be skewed. There are two primary requirements to ensure only the target surface is illuminated: (1) shaping and focusing the e-beam so that the spot size is smaller than the target area; (2) detecting the invisible e-beam during illumination. Fortunately, the ELG-2 e-gun and EGPS-1022 power supply are capable of fine-tuning the e-beam spot size by adjusting the grid voltage, 1st anode voltage,

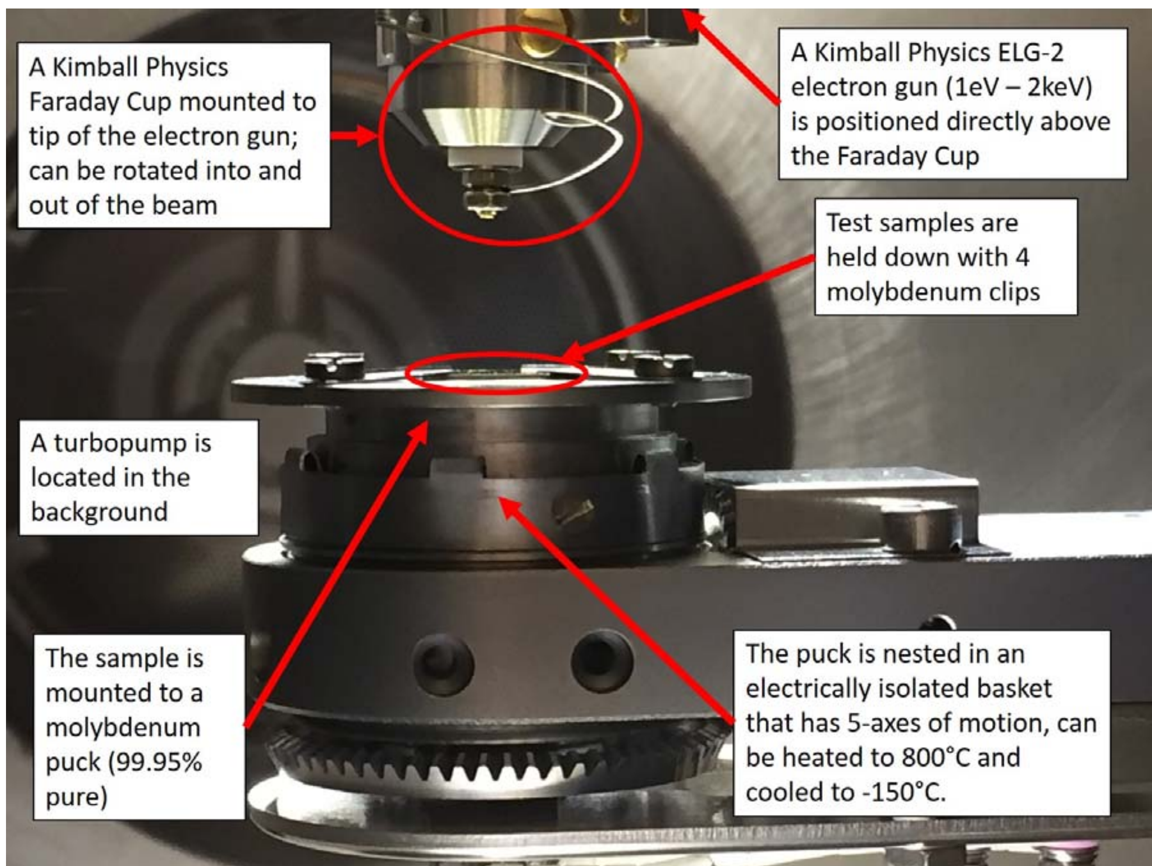

Figure 46: Close-up photo of the new AFIT secondary electron yield (SEY) measurement system’s sample manipulator and Faraday cup.

and focus voltage settings on the power supply. A phosphor screen provides a simple method to view the beam shape at the target. Figure 47 shows photos of commercially available phosphor screens and their appearance during e-beam illumination. The primary drawback to this method is that the phosphor screen requires electron energies great than ~500 eV in order to provide sufficient illumination for the human eye to see. However, the beam shape for energies below ~500 eV, is of critical importance because lower energy electrons are subject to greater trajectory deflection caused by ambient magnetic fields and electrostatic repulsion. Thus, a method is needed to determine the e-beam spot size at energies below 500 eV. To help their customers with this problem, Kimball Physics has developed a model of the ELG-2 that runs on SIMION®, a field and particle trajectory simulator. Figure 48 shows a screenshot of this ELG-2 model in SIMION® which was used to determine the e-gun settings that minimize e-beam spot size. A helpful feature available in SIMION® is the ability to sweep the focus voltage over a defined range while holding the other e-gun settings constant. This provides the user with a quick assessment of the focus setting that minimize spot size. Figure 49 shows an example of a SIMION® output file used to determine the e-gun settings minimizing the e-beam spot size. Because the

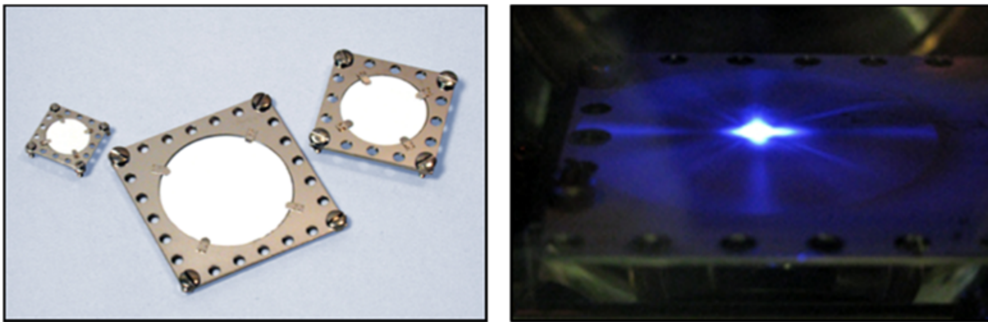

Figure 47: Kimball Physics phosphor screens (left); Kimball Physics photo of illuminated phosphor screen (right).

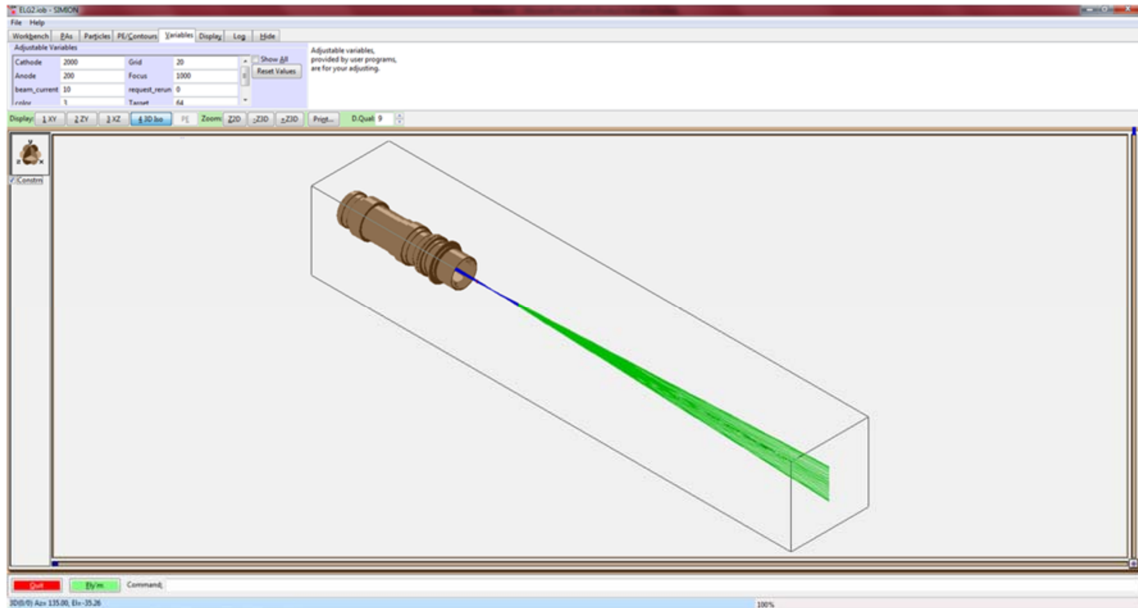
Figure 48: SIMION® screenshot showing the ELG-2 and a simulated beam shape for 2000 eV electrons.

porous surface samples to be fabricated will likely be small as shown in Table 5 (between 5 mm^2 and 10 mm^2), the objective is to determine e-gun settings that maintain a beam spot diameter under 1 mm. This will ensure that the entire e-beam illuminates only the intended surface of a properly centered sample. Table 8 shows the ELG-2 e-gun settings that

Energy	Grid	Anode	Focus	Target Current (uA)	Spot Dia.(mm)
2000	20	200	0	0.017326732673267	21.392022671911
2000	20	200	100	0.017326732673267	10.519814780292
2000	20	200	200	0.017326732673267	5.0942732009992
2000	20	200	300	0.017326732673267	2.4743871196342
2000	20	200	400	0.017326732673267	1.1430645857858
2000	20	200	500	0.017326732673267	0.49554791353613
2000	20	200	600	0.017326732673267	0.24143253175493
2000	20	200	700	0.017326732673267	0.22790077345512
2000	20	200	800	0.017326732673267	0.36190478208994
2000	20	200	900	0.017326732673267	0.58883550926234
2000	20	200	1000	0.017326732673267	0.87745280372875
2000	20	200	1100	0.017326732673267	1.2033616039675
2000	20	200	1200	0.017326732673267	1.5510319909477
2000	20	200	1300	0.017326732673267	1.9103154762574
2000	20	200	1400	0.017326732673267	2.2738576620593
2000	20	200	1500	0.017326732673267	2.6366364286242
2000	20	200	1600	0.017326732673267	2.9919485086785
2000	20	200	1700	0.017326732673267	3.3439441025851
2000	20	200	1800	0.017326732673267	3.68790311398
2000	20	200	1900	0.017326732673267	4.0189573724694

Figure 49: SIMION® output file showing the e-gun settings that result in a minimum spot size (circled in red).

minimize spot size for each energy of interest. The grid voltages shown in Table 8 are specified to be 10% of the 1st anode voltage based on a recommendation from Kimball Physics. Table 8 gives high confidence that a properly configured e-beam will illuminate only a small portion of a properly centered sample with a porous surface area greater than 0.5 mm^2. Appendix F contains a SIMION® tutorial for simulating the ELG-2 electron gun.

Table 8. ELG-2 settings that minimize beam spot size at a 20 mm working distance.

Energy (eV)	Grid (V)	1st Anode (V)	Focus (V)	Beam Diameter (mm)
2000	20	200	700	0.228
1500	17.5	175	700	0.320
1200	15	150	700	0.224
1000	12.5	125	600	0.425
900	12.5	125	600	0.284
800	12.5	125	600	0.427
700	12.5	125	650	0.358
600	12.5	125	650	0.348
500	12.5	125	650	0.361
400	12.5	125	625	0.468
350	12.5	125	625	0.388
300	12.5	125	600	0.413
275	12.5	125	575	0.541
250	12.5	125	575	0.408
225	12.5	125	550	0.451
200	12.5	125	525	0.485
180	12.5	125	500	0.541
160	12.5	125	475	0.549
140	12.5	125	450	0.498
120	9.0	90	350	0.595
100	8.0	80	300	0.703
90	7.5	75	275	0.804
80	7.5	75	250	0.896
70	7.0	70	225	0.921
60	6.0	60	190	1.045
50	5.0	50	160	0.964
40	4.0	40	130	0.960
30	3.0	30	100	0.922

As previously discussed in Section 3.5, the amount of perpendicular deflection that electrons will undergo during transit from the e-gun tip to the sample should be determined based on the layout of the AFIT SEY measurement system. In this context, the AFIT SEY system demonstrates an improvement over the AFRL SEY system because the vertical orientation of the AFIT e-gun removes the largest magnetic field component from causing electron deflection. A re-determination of the perpendicular magnetic field component for the AFIT SEY system using Equation 56 yields,

$$B_{\perp} = \sqrt{2211.3^2 + 20116.5^2} = 20237.7\,\text{nT}\,, \tag{62}$$

which is only 42% of the equivalent magnetic field strength in the AFRL SEY system. With this perpendicular magnetic field component, we can apply Equation 61 to determine deflection distances for the AFIT SEY system. Table 9 provides a summary of these deflection distances for low energy electrons and further illustrates the improved (i.e. reduced) deflection distances achieved by AFIT's new SEY system when compare to the AFRL SEY system.

Table 9. Magnitude of electron deflection in the AFIT SEY measurement system (assuming a 20 mm working distance) caused by the Earth's magnetic field.

Electron Energy (eV)	Deflection Distance (mm)
30	0.22
40	0.19
50	0.17
100	0.12
200	0.08

3.7 Thermomechanical Effects on Porous Surfaces

Acquiring an answer to the fifth research question in Section 1.5 requires exploring the relationship between temperature and the topography of microporous and nanoporous surfaces. This question is important because multipactor is a problem for space-based systems that are susceptible to extreme changes in temperature. Ideally, this question should be answered with an experimental study using the new AFIT SEY measurement chamber and its ability to heat and cool samples. However, because all planned test samples will be fabricated using a silicon wafer as the mechanical substrate, an experimental thermomechanical study would likely provide unreliable results. While this experimental study should be performed in follow-on work, the question can still be answered using a thermomechanical simulation such as CoventorWare®. Figure 50 shows a 3D model of a single micro-pore that was created using CoventorWare®. This simulation allows temperature boundary conditions to be specified, from which material displacement vectors can be obtained based on the given material. Specific locations can be selected for

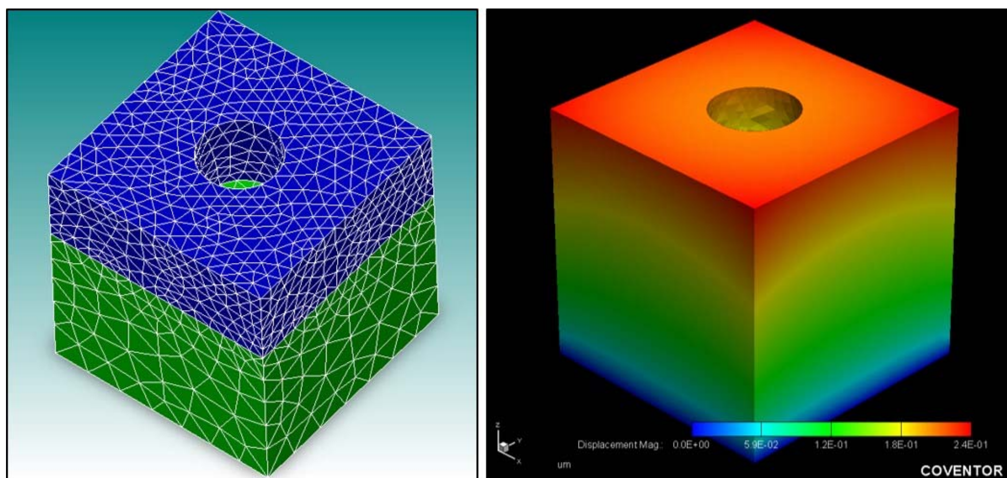

Figure 50: CoventorWare® thermomechanical model of a 10μm deep, 10μm diameter gold micro-pore used to determine changes caused by thermal expansion and contraction.

which the displacement vectors are provided. The method of simulation will be to set the temperature boundary condition for the bottom surface of the model (as oriented in Figure 50) and then select three displacement locations: (1) the center of the pore-bottom, (2) the sidewall of the pore-bottom, and (3) the sidewall of the top of the pore. Displacement data from these three locations will provide sufficient information to recalculate the pore diameter and pore height and determine the significance of the thermomechanical effects. The results from the thermomechanical simulations are provided in Chapter IV.

3.8 Summary

This chapter laid out the methodology used to answer the five research questions posed in Chapter I. Two mathematical models for determining the total SEY of a porous surface were derived and compared to select the best model. The selected model, based on a 3D pore geometry, was then used to predict total SEY values for porous surfaces and develop specific design considerations for studying how porous surfaces effect total SEY. The chosen designs of both microporous and nanoporous samples were presented along with the methods available to fabricate these surfaces. Methods for performing surface characterization, including both topography and chemistry, were presented. Three methods for measuring total SEY of conductive surfaces were detailed. The specifics and methodology of the AFRL Materials and Manufacturing Directorate SEY measurement system were discussed. The design, key pieces of equipment, and construction of the new AFIT SEY measurement system were provided along with methods to determine beam spot size. Finally, a method was provided to determine the dimensional effects that extreme temperature changes will have on an engineered surface.

IV. Results

This chapter provides the results obtained by this research effort. A detailed analysis of these results will follow in Chapter V. Sections 4.1 and 4.2 present the results obtained during fabrication of the microporous and nanoporous surfaces respectively. Section 4.3 provides the results of the materials characterization performed on different samples. Section 4.4 covers the results of the SEY measurements. Section 4.5 describes the newly completed AFIT SEY measurement chamber including preliminary results. Finally, Section 4.6 describes the results obtained from the thermomechanical simulations performed to assess the effects of extreme heating and cooling on pore size and shape.

4.1 Fabrication Results: Microporous Surfaces

The gold microporous surface designs shown in Figure 33 were laid out using the computer aided design software, L-Edit. Figure 51 shows the 3-inch photolithography

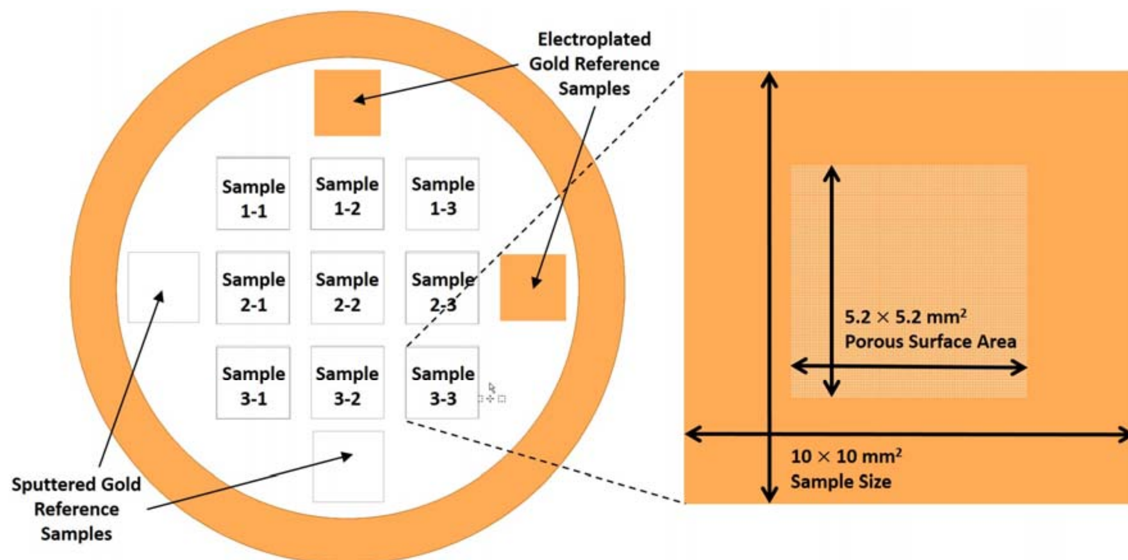

Figure 51: Photolithography mask layout used to fabricate microporous surfaces (left) and individual sample dimensions (right).

mask layout used to provide adequate sample-to-sample spacing for patterning and dicing. Ideally, the entire mask layout shown in Figure 51 would have been written to a mask in one Heidelberg "session". However, because the smallest feature size for samples 1-1, 1-2, 1-3, and 2-3 is less than 3 μm, the mask for these samples must be patterned using the "1-μm Heidelberg", which is not capable of writing the pattern for a 3-inch wafer in one session. Thus, the plan was altered to write samples 2-1, 2-2, 3-1, 3-2, 3-3, and the reference samples on the "3-μm Heidelberg" and then write the remaining four sample patterns with four individual sessions on the 1-μm Heidelberg. This plan was further complicated when it was discovered that the Heidelbergs were not capable of loading large pattern files (the limit was assessed to be ~60 MB). This was important because the ".cif" files for each individual sample get exponentially large as the pore spacing decreases (i.e. porosity increases). Table 10 shows the total number of pores in each sample and the corresponding ".cif" file size. Initially, the samples were designed to have 10×10 mm^2 porous surface areas. However, because the file sizes were too large, the porous surface areas were reduced to 5.2×5.2 mm^2. Even at that size, samples 1-2, 1-3 and 2-3 would not be achievable

Table 10. Photolithography pattern-file sizes for microporous samples.

Sample	Required Heidelberg Resolution	Pore Diameter (μm)	Pore Spacing (μm)	Number of Pores in 5.2×5.2 mm^2 Pattern	.cif File Size (MB)
1-1	1 μm	40	<1 (close packed)	20,328	14.8
1-2	1 μm	16	<1 (close packed)	123,984	73.4
1-3	1 μm	8	<1 (close packed)	491,808	223.9
2-1	3 μm	40	10	10,816	8.2
2-2	3 μm	16	4	67,600	41.4
2-3	1 μm	8	2	270,400	127.7
3-1	3 μm	40	60	2,704	2.1
3-2	3 μm	16	24	16,900	10.4
3-3	3 μm	8	12	67,600	32.0

because of the Heidelberg's ~60MB file-size restriction. The plan was further refined to divide the Heidelberg pattern file for samples 1-2, 1-3, and 2-3 into two sub-patterns of the original pattern. These sub-patterns would reduce the ".cif" file size to allow each of these samples to be written as two individual sessions on the 1-μm Heidelberg and "stitched" together using the Heidelberg's aligning accuracy. However, because the pattern-file size for sample 1-3 was so large, it was ultimately abandoned after several failed attempts to load its sub-patterns. Additionally, during mask fabrication, the pattern for sample 3-3 only partially transferred to the mask, causing sample 3-3 to be abandoned as a test article. Figure 52 shows the final photolithography mask fabricated on both the 1-μm and 3-μm Heidelberg machines over the course of a week.

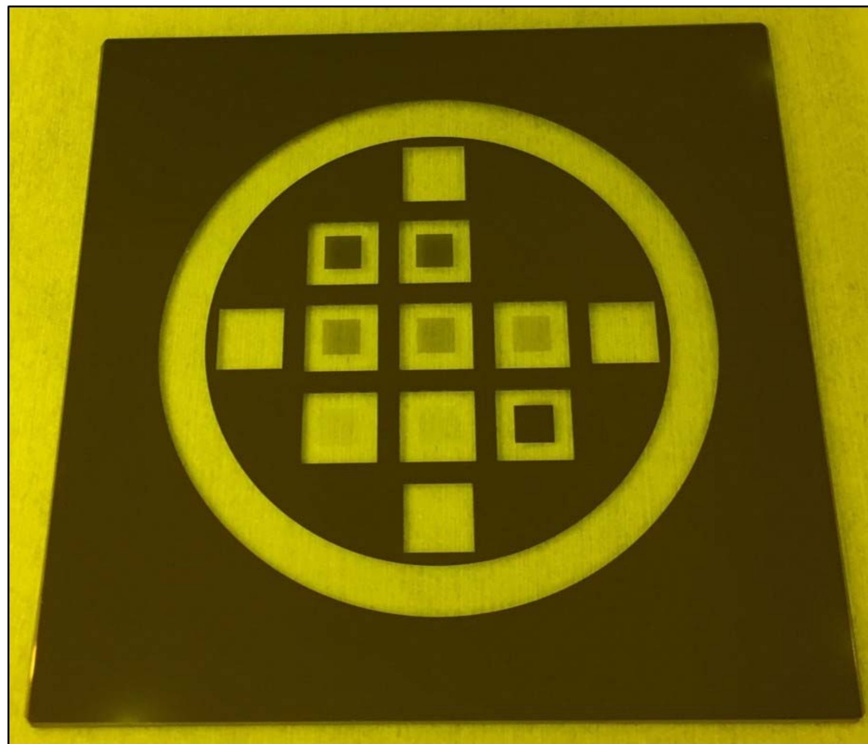

Figure 52: Photograph of the final microporous photolithography mask, which took eight individual mask-write "sessions" performed over the course of 7 days.

Upon completion of the mask, work began to complete the fabrication process outlined in Figure 34. The process was performed with minimal difficulty until the electroplating step. Numerous attempts were made to perform the electroplating using AFIT’s new and untested electroplating system. Figure 53 shows the recurring gold delamination problem that was encountered on each attempt. Microscope images of the microporous surfaces immediately after electroplating showed excellent pore formation and consistency across the sample. However, any attempt at a liftoff of the undesired photoresist-gold layer would result in delamination of both the electroplated and sputtered gold layer as shown in Figure 53 (right). Ultimately, successful electroplating was performed at the AFRL, Sensors Directorate which has a more advanced and vetted electroplating system with experienced practitioners. Unfortunately, samples 2-2 and 2-3 delaminated during the electroplating process. The total electroplating layer thickness was measured 18 times using AFIT’s

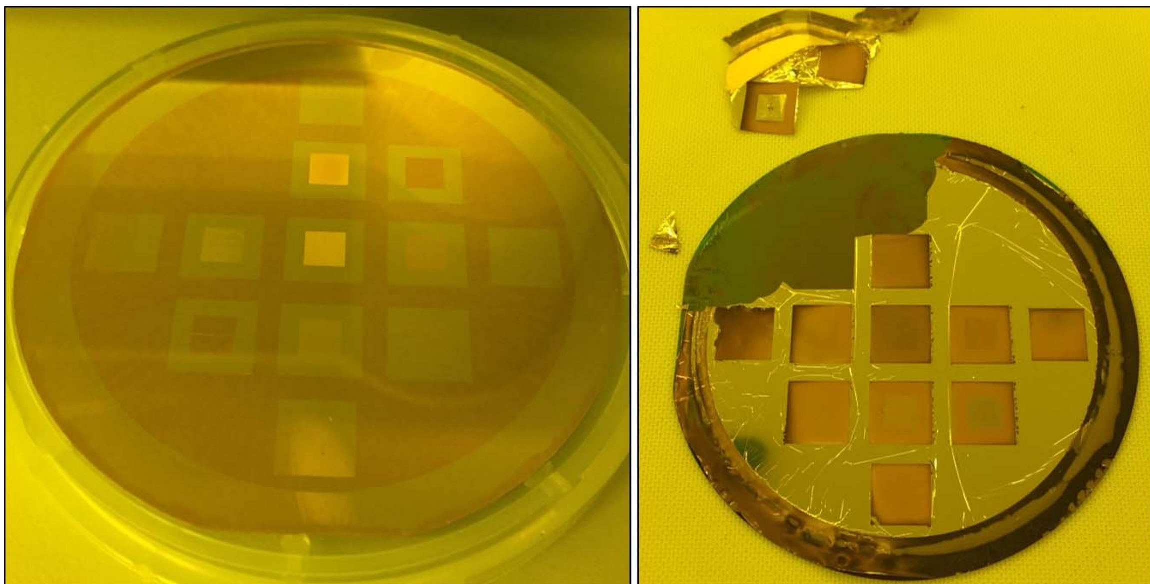

Figure 53: Photograph of the first attempt to electroplate the microporous samples: wafer patterned with “AZ 9260” photoresist (left); electroplated gold delamination (right).

profilometer and the average thickness determined to be 5.6 μm. Figure 54 shows a photo of the five microporous samples that were successfully fabricated using the electroplating process illustrated in Figure 34.

All five samples were imaged using the SEM to assess pattern consistency and yield, along with pore size and spacing. Figure 55 shows SEM-images of the entire porous surface region for samples 1-1, 2-1, and 3-1 – these images show the high degree of pattern consistency and yield that was achieved during fabrication. Figure 56 shows close-up SEM-images of the close-packed pores patterned in sample 1-1. Unfortunately, the close-packed pores of sample 1-1 experienced some minor pore sidewall breakdown that occurred during the photolithography pattern-transfer step in the fabrication process.

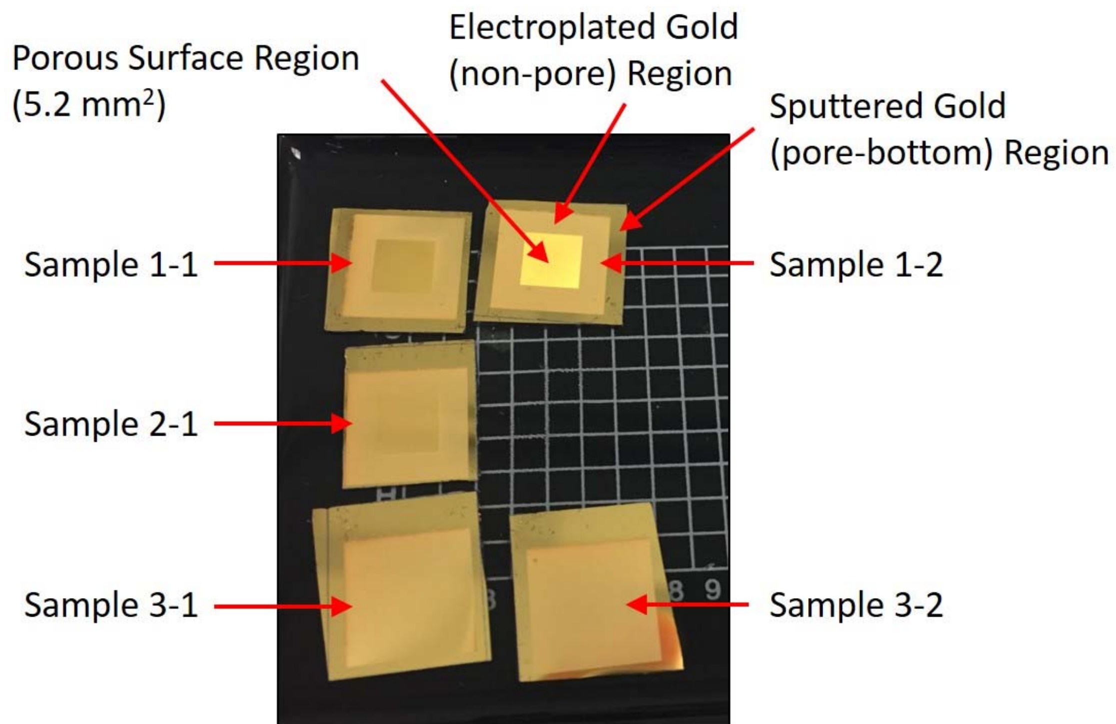

Figure 54: Photograph of the five microporous samples successfully fabricated and ready for characterization.

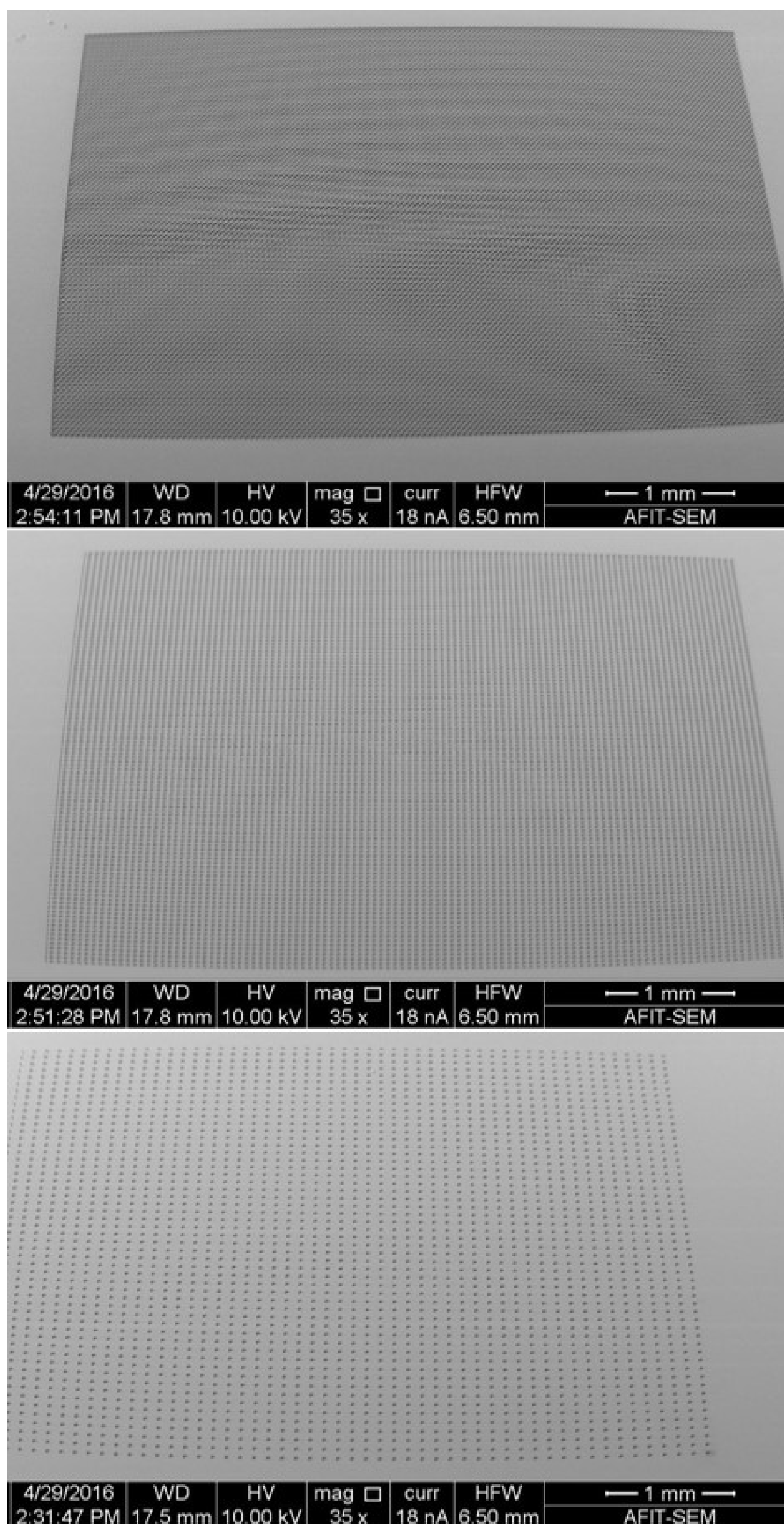

Figure 55: Scanning electron microscope images of microporous samples 1-1 (top), 2-1 (middle), and 3-1 (bottom) showing excellent pattern consistency and pore yield.

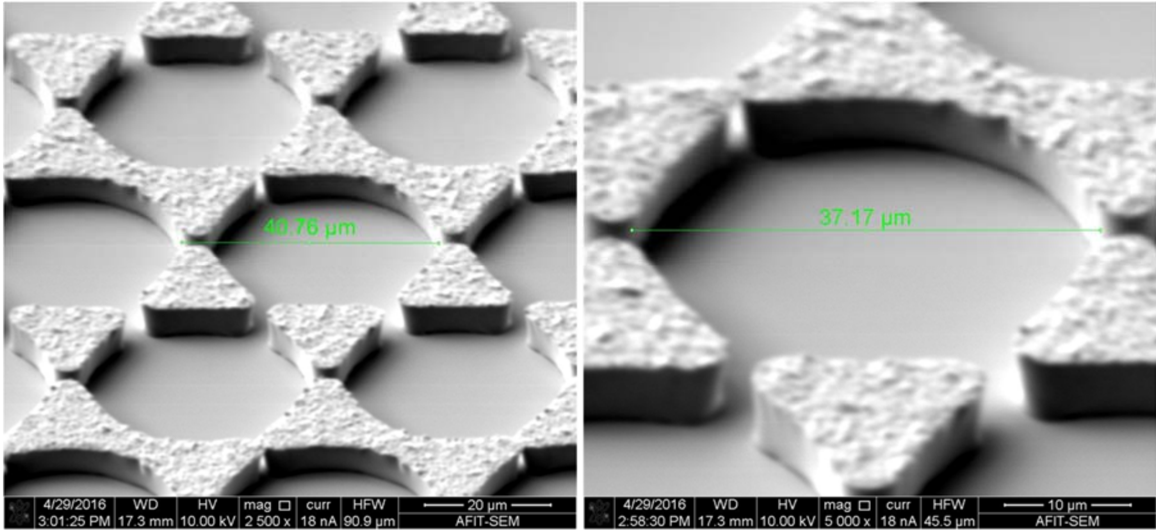

Figure 56: Scanning electron microscope images of microporous sample 1-1 showing minor pore sidewall breakdown.

Despite this, the pore sidewalls are consistently smooth and vertical with a nearly perfect cylindrical pore shape. Figure 57 shows close-up SEM-images of the close-packed pores patterned in sample 1-2. As was the case in sample 1-1, the close-packed pores experienced

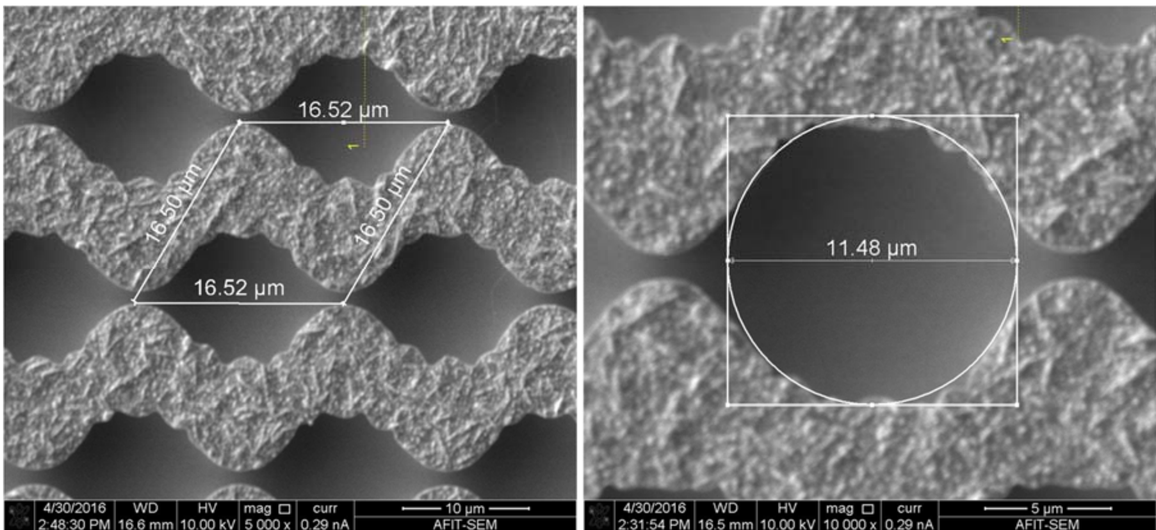

Figure 57: Scanning electron microscope images of microporous sample 1-2 showing pore deformation and sidewall breakdown.

some pore sidewall breakdown as well as cylindrical deformation that occurred during photolithography. However, the pore sidewalls for sample 1-2 are also consistently smooth and vertical. Figure 58 shows SEM-images of the pores patterned in sample 2-1 and illustrates a perfectly fabricated microporous surface. Similarly, Figure 59 shows SEM-images of the pores patterned in sample 3-1, illustrating another perfectly fabricated microporous surface. Finally, Figure 60 shows SEM-images of the pores patterned in sample 3-2, which also showed perfect pattern consistency and cylindrical pore shape. The dimensions shown in Figure 56 through Figure 60 were used in conjunction with the previously determined electroplating thickness (i.e. pore height) to determine aspect ratio and porosity for each of the five microporous samples. Table 11 provides a summary of the results compared to the original design parameters.

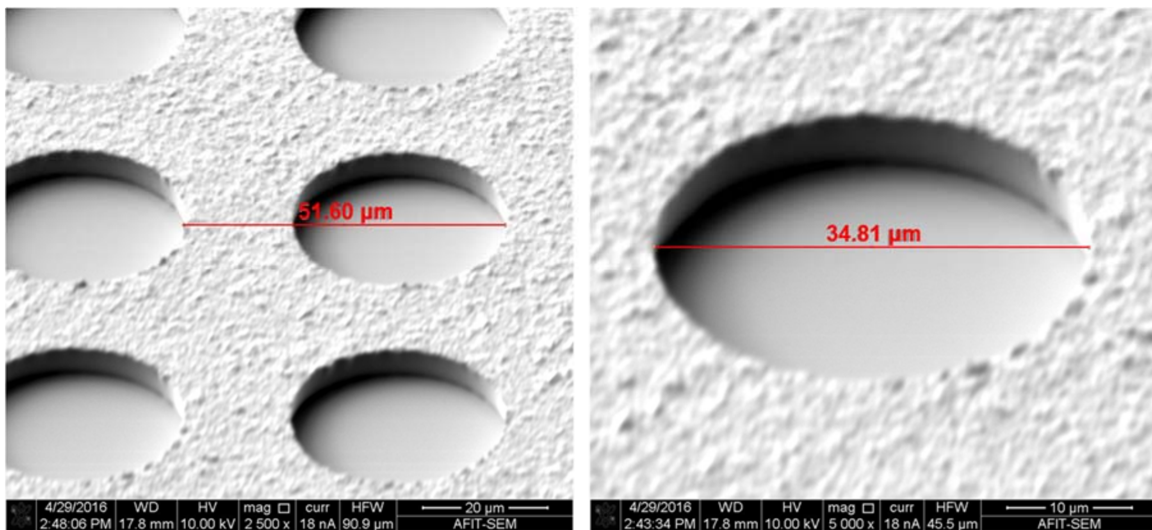

Figure 58: Scanning electron microscope images of microporous sample 2-1 showing excellent pattern consistency and near-perfect cylindrical pore geometry.

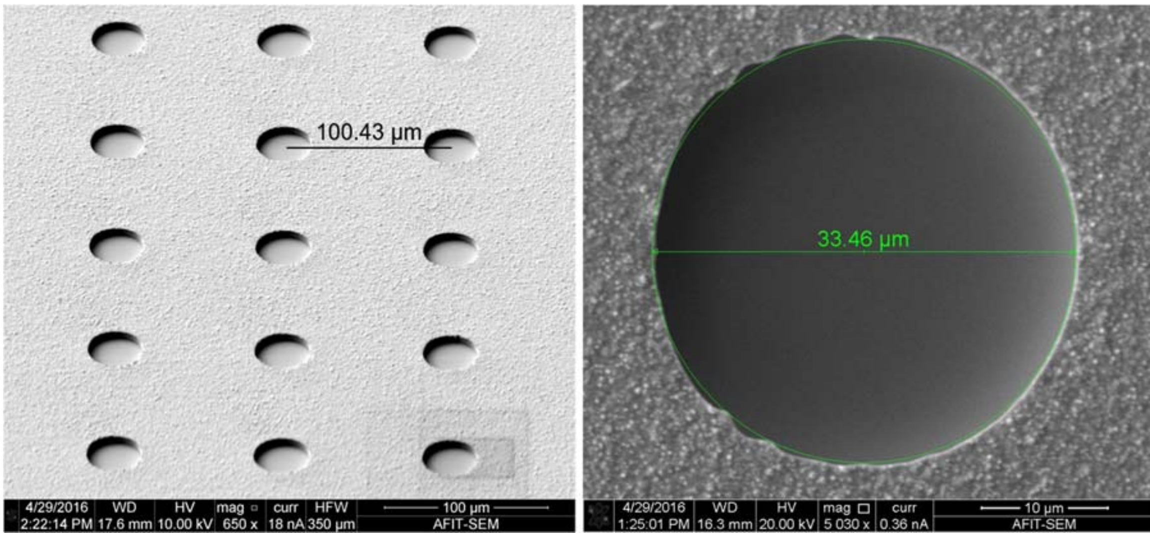

Figure 59: Scanning electron microscope images of microporous sample 3-1 showing excellent pattern consistency and near-perfect cylindrical pore geometry.

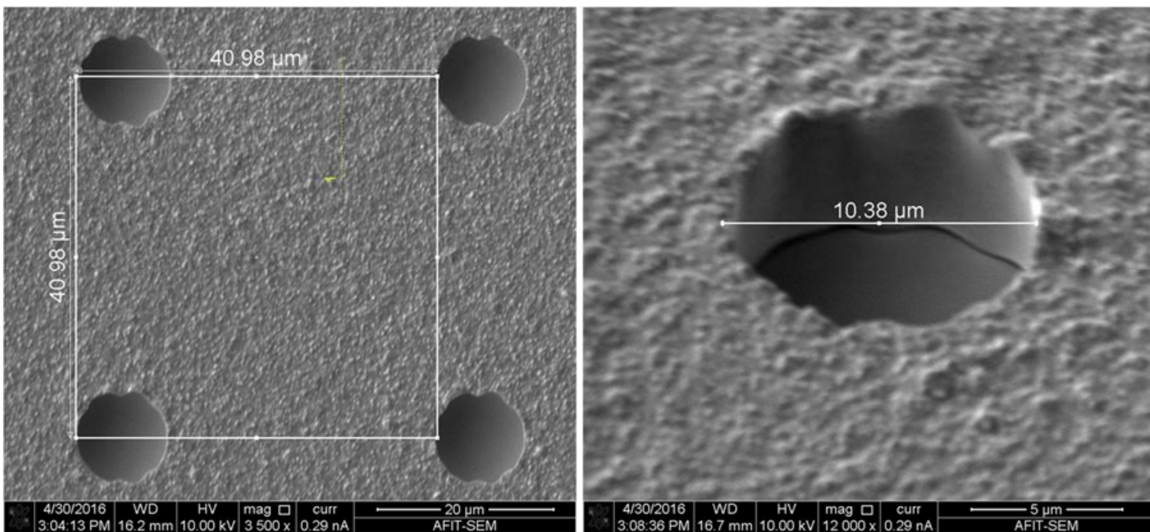

Figure 60: Scanning electron microscope images of microporous sample 3-2 showing excellent pattern consistency and near-perfect cylindrical pore geometry.

Table 11. Microporous surface fabrication results.

Sample	Designed Diameter (μm)	Fabricated Diameter (μm)	Designed Porosity	Fabricated Porosity	Designed Aspect Ratio	Fabricated Aspect Ratio
1-1	40	37.2 (-7%)	0.91	0.75 (-18%)	0.15	0.15 (-1%)
1-2	16	11.5 (-28%)	0.91	0.44 (-52%)	0.38	0.49 (+29%)
1-3*	8	N/A	0.91	N/A	0.75	N/A
2-1	40	34.8 (-13%)	0.50	0.36 (-28%)	0.15	0.16 (+5%)
2-2*	16	N/A	0.50	N/A	0.38	N/A
2-3*	8	N/A	0.50	N/A	0.75	N/A
3-1	40	33.5 (-16%)	0.13	0.09 (-31%)	0.15	0.17 (+12%)
3-2	16	10.4 (-35%)	0.13	0.05 (-62%)	0.38	0.54 (+43%)
3-3*	8	N/A	0.13	N/A	0.75	N/A

*These samples were not fabricated successfully.

4.2 Fabrication Results: Nanoporous Surfaces

Nanoporous fabrication began with a barrage of fabrication attempts based on the Extreme-Optimized Photolithography process laid out in Section 3.2.3. Significant time, process refinement, process experimentation, and porous surface redesign ultimately failed to achieve nanoporous surfaces that maintained pattern consistency and matched a cylindrical pore geometry. However, subsequent nanoporous surface fabrication attempts using e-beam lithography proved to be highly successful in both areas of pattern consistency and cylindrical pore geometry. The primary challenge with e-beam lithography was complete removal of the hundreds of millions of undesired gold plugs that were lifted off from the nano-sized gold pores for large porous surface areas (≥ 5×5 mm^2).

4.2.1 Extreme-Optimized Photolithography (EOP)

Initial attempts to create the nanoporous surface designs outlined in Table 4 were simplified to understand better, the capability of the 1-μm Heidelberg. The initial designs consisted of patterning 1-μm wide horizontal and vertical intersecting lines (which become

windows in the photolithography mask), spaced apart by 2, 3, 4, or 5 µm depending on the specific design. These 1-µm wide windows define the regions on the wafer where the 1818 photoresist (and subsequently the SF11 photoresist) is exposed and developed. As shown in step 8 of Figure 36, when the metal liftoff is performed, the square-shaped plugs of the remaining photoresist (which become rounded due to diffraction during exposure) are removed along with the metal deposited on top of the plugs. The result is a pattern of metal pores ranging in diameter from 2 to 5 µm and spaced apart by 1 µm. Two important settings for the Heidelberg are the laser power and duty cycle. The laser power can be adjusted from 1 mW to 20 mW in 1 mW increments and the duty cycle from 5% to 100% in 5% increments. After four initial mask-writing efforts failed to produce a useable mask, it was determined that a Heidelberg exposure study was needed to determine optimal Heidelberg laser settings. Figure 61 shows the mask layout used to conduct this designed experiment.

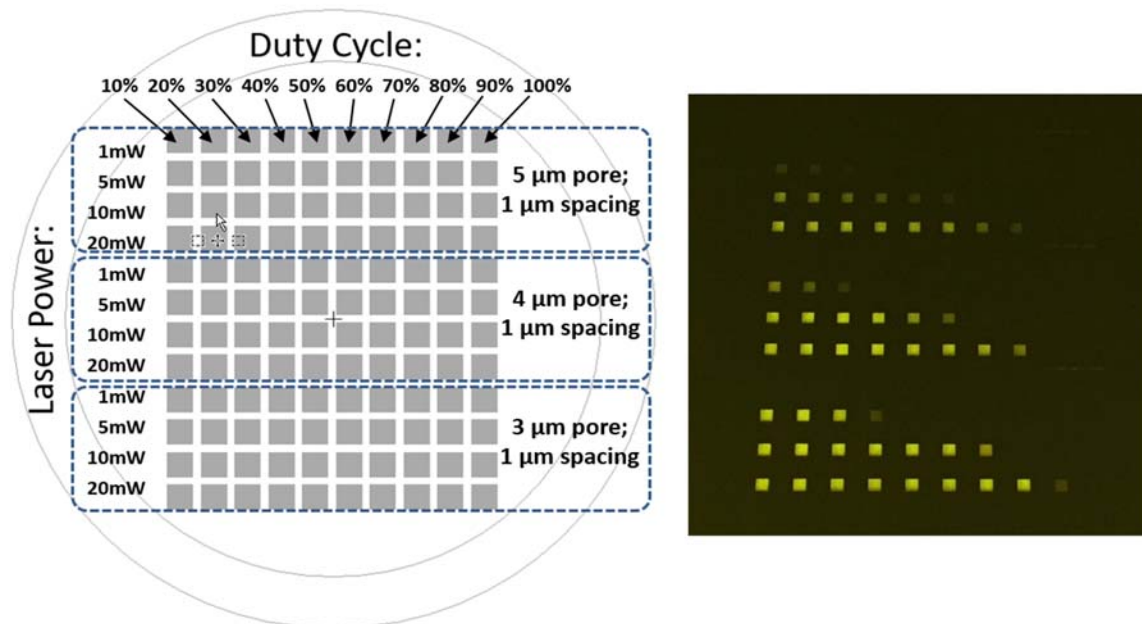

Figure 61: Mask layout designed for the Heidelberg exposure study consisting of 40 reticles of each of three designs (left); photo of the final mask (right).

The mask contained 40 replicated patterns (reticles) for each of the larger porous surface designs (5-μm, 4-μm, and 3-μm pores). Each of the 40 reticles was written at a unique laser power and duty cycle. The entire mask-writing session, involving 120 unique "pattern-exposure" combinations, was automated using a novel computer program developed by Laurvick (see Appendix B). Table 12 provides the results of the exposure study.

With the optimal laser settings determined, the 1-μm Heidelberg was used to write a final mask providing 6×6 mm^2 porous surface patterns for each of the four designs shown in Table 12. Figure 62 shows the mask layout and a photo of the fabricated mask. An additional remark about the mask shown in Figure 62 is that it was made using only horizontal lines patterned in L-Edit. This is because during the iterative mask-writing process, it was determined that the Heidelberg's laser accuracy was significantly better when writing horizontal lines vice vertical lines. Thus, the mask shown in Figure 62 required two horizontal line-writing sessions in between which, the mask was physically rotated 90 degrees to ensure the second set of horizontal lines were patterned perpendicular to the first set. This is why there are small regions of horizontal and vertical lines offset from the porous surface pattern (see right side of Figure 62). These regions of non-intersecting horizontal and vertical lines will be more clearly visible in Figure 63 through Figure 65. The left side of Figure 63 provides microscope images of the mask patterns and

Table 12. Results of the Heidelberg mask-writing exspoure study.

Design	Pore Diameter (nm)	Pore Spacing (nm)	Optimum Laser Power (mW)	Optimum Laser Duty Cycle
EOP-1	5000	1000	20	55%
EOP-2	4000	1000	20	55%
EOP-3	3000	1000	10	60%
EOP-4	2000	1000	10	60%

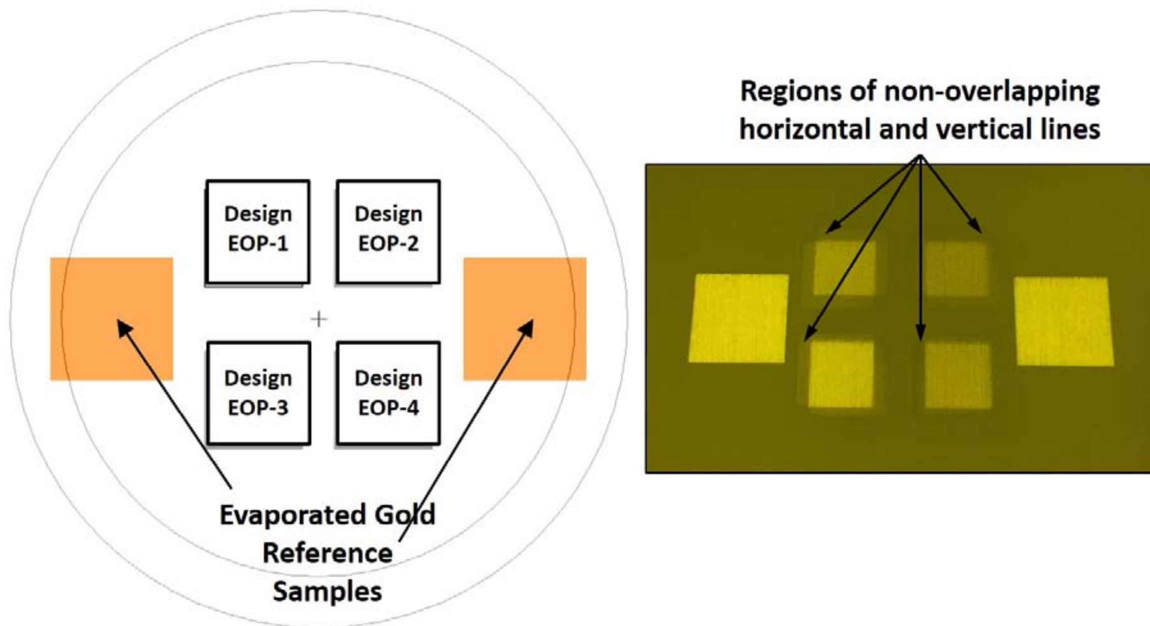

Figure 62: Mask layout designed for the Heidelberg exposure study consisting of 40 reticles of each of three designs (left); photo of the final mask (right).

demonstrates excellent pattern uniformity and pore-spacing consistency across both horizontal and vertical directions. The right side of Figure 63 provides microscope images of a test exposure of 1818 photoresist to determine how well the mask pattern would transfer to a wafer coated in photoresist. Visible in the top three patterns shown in Figure 63 is the desired effect that mask-diffraction has on converting the square mask features (Figure 63, left) to rounded pillars of photoresist (Figure 63, right). Unfortunately, the smallest pore-design pattern (bottom of Figure 63) was not successfully transferred to the photoresist because of the same mask-diffraction effects. These mask-diffraction effects are set up because the "pore-pattern" region of the mask creates an effective diffraction pattern for the 365 nm ultraviolet (UV) light that is used to expose the 1818 photoresist. Thus, when the photoresist is exposed, the ensuing diffraction pattern exposes regions of the photoresist that are obscured by the mask. Figure 64 shows SEM images of the final

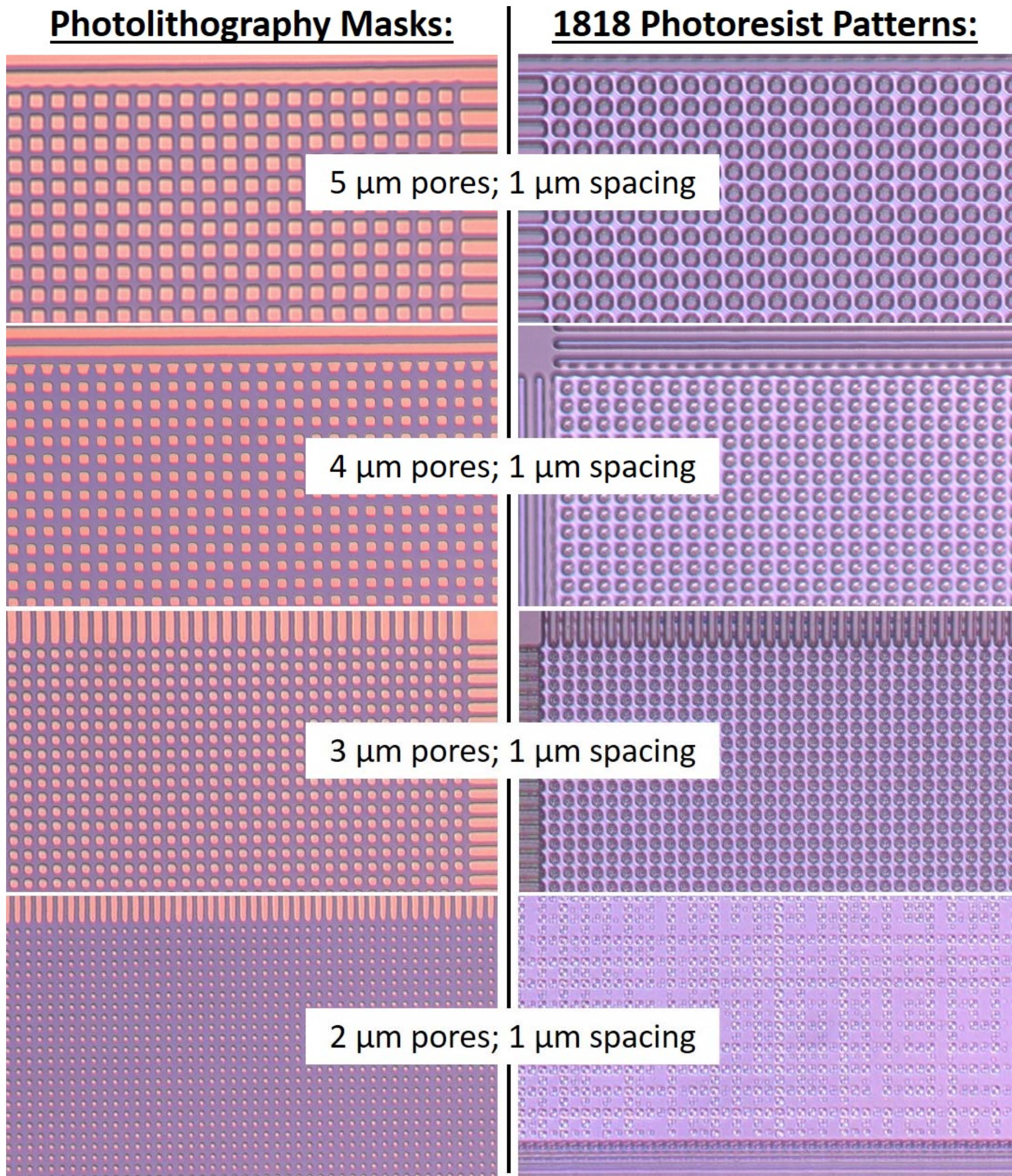

Figure 63: Microscope images of the nanoporous mask created by the 1-µm Heidelberg (left) and corresponding 1818 photoresist patterns created using the nanoporous mask and AFIT's EVG® UV photolithography exposure system.

porous gold samples fabricated using EOP. An additional undesired mask-diffraction effect is visible in the images for samples EOP-2 and EOP-3 shown in Figure 64. In this case, the

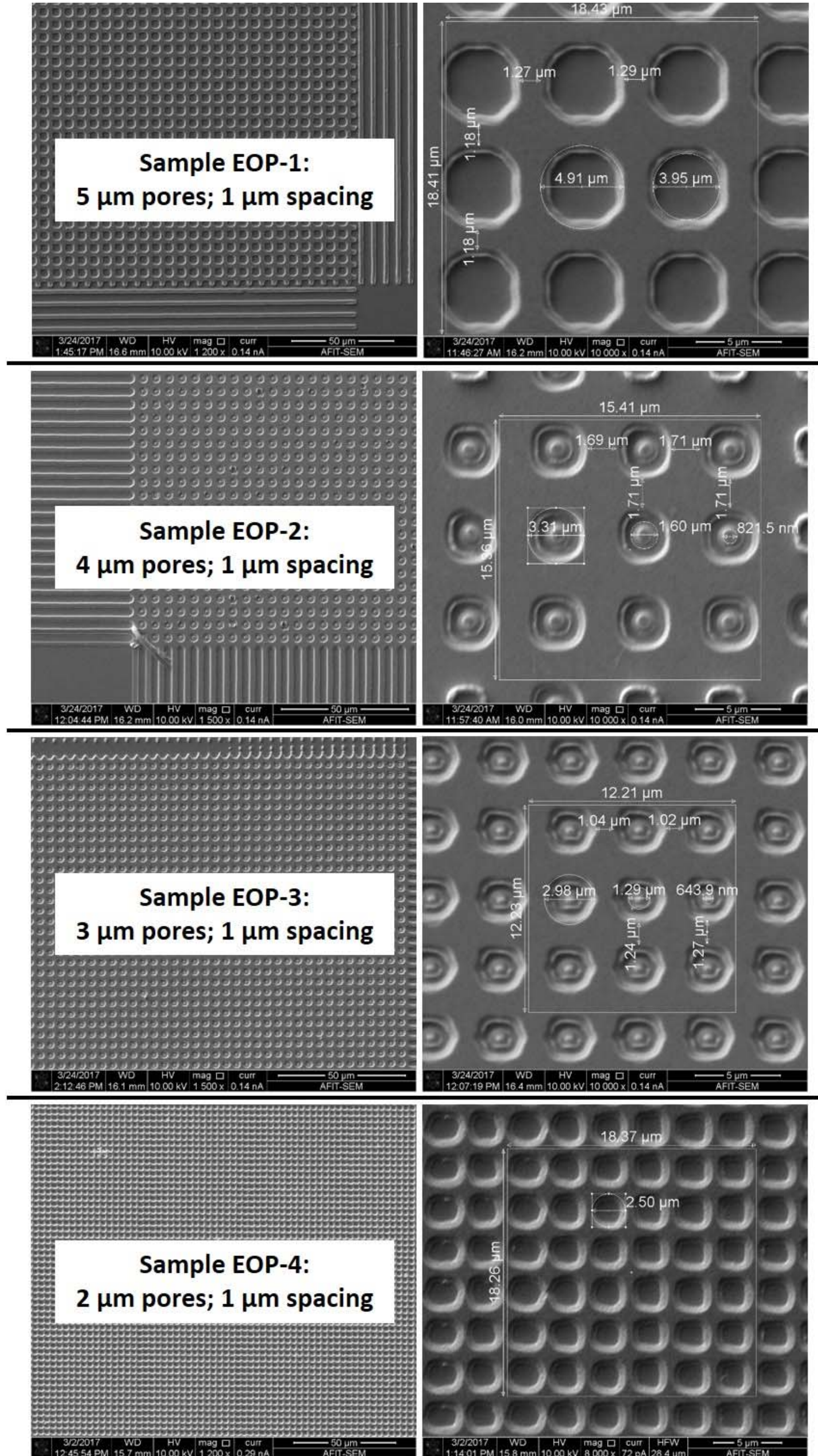

Figure 64: Nanoporous surfaces fabricated with extreme-optimized photolithography.

mask-diffraction exposed small regions of photoresist in the centers of the pores, which resulted in tiny gold protrusions in the centers of the pores. These protrusions were not consistent throughout the 6×6 mm^2 porous surface patterns because of minor variations in mask-to-sample gap during UV exposure. Additionally, these protrusions were never observed in the pores for sample EOP-1 because the feature sizes are large enough to prevent the mask diffraction pattern from exposing the photoresist pillars. Figure 65 further illustrate this diffraction effect by showing SEM images of samples that we patterned by both the EVG® UV exposure and the follow-on DUV exposure which patterns the underlying SF11 photoresist. Evident in Figure 65 is the increasing consistency of exposed photoresist in the center of the photoresist pillars as the pore size gets smaller ("black dots" on the left-side images for EOP-2 and EOP-3). Additionally, it is worth noting the existence of these "black dots" at the ends of the horizontal and vertical lines shown in the bottom right SEM image in Figure 65. This provides additional evidence that the gold protrusions forming in the pore centers are caused by a mask-diffraction pattern – because the diffraction pattern exposure areas (i.e. "black dots") cease to exist for areas of the mask that do not contain intersection lines. Figure 66 provides another image that supports this conclusion. The two anomalies visible in Figure 66 are photoresist pillars that were not removed from the surface during the metal liftoff step. The photoresist pillar positioned toward the bottom of Figure 66 clearly shows a hole in its center which corresponds to the size of the gold protrusion. Table 13 provides a summary of the nanoporous surface fabrication results achieved using EOP. However, these results are imperfect because of the existence of the gold protrusions in many of the pores for samples EOP-2, EOP-3, and EOP-4.

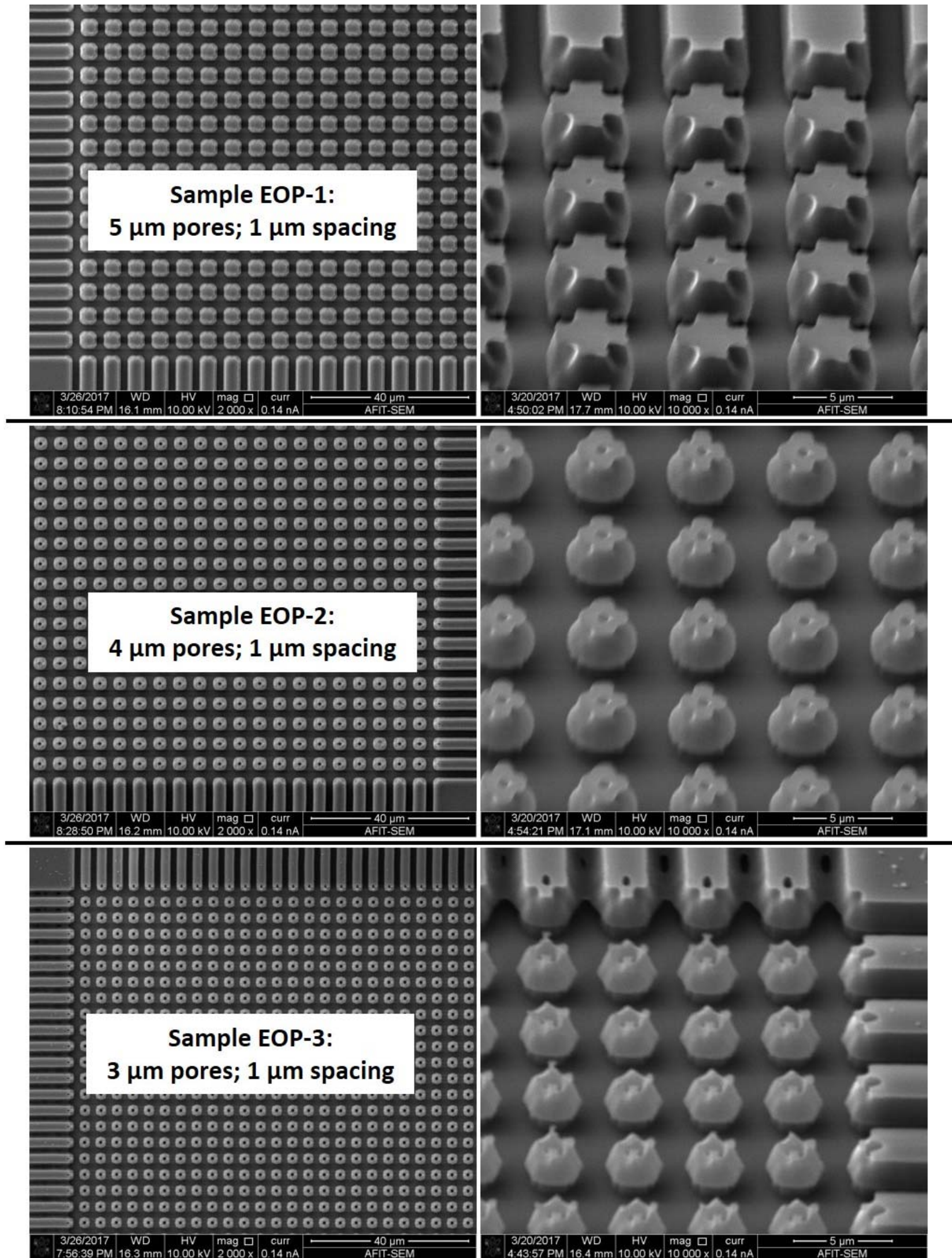

Figure 65: SEM images of patterned 1818-SF11 photoresist layers showing undesired UV exposures in the center of the photoresist pillars caused by a diffraction pattern that is established by the mask windows (NOTE: these patterns have a 200Å cold-sputtered gold layer to facilitate SEM imaging).

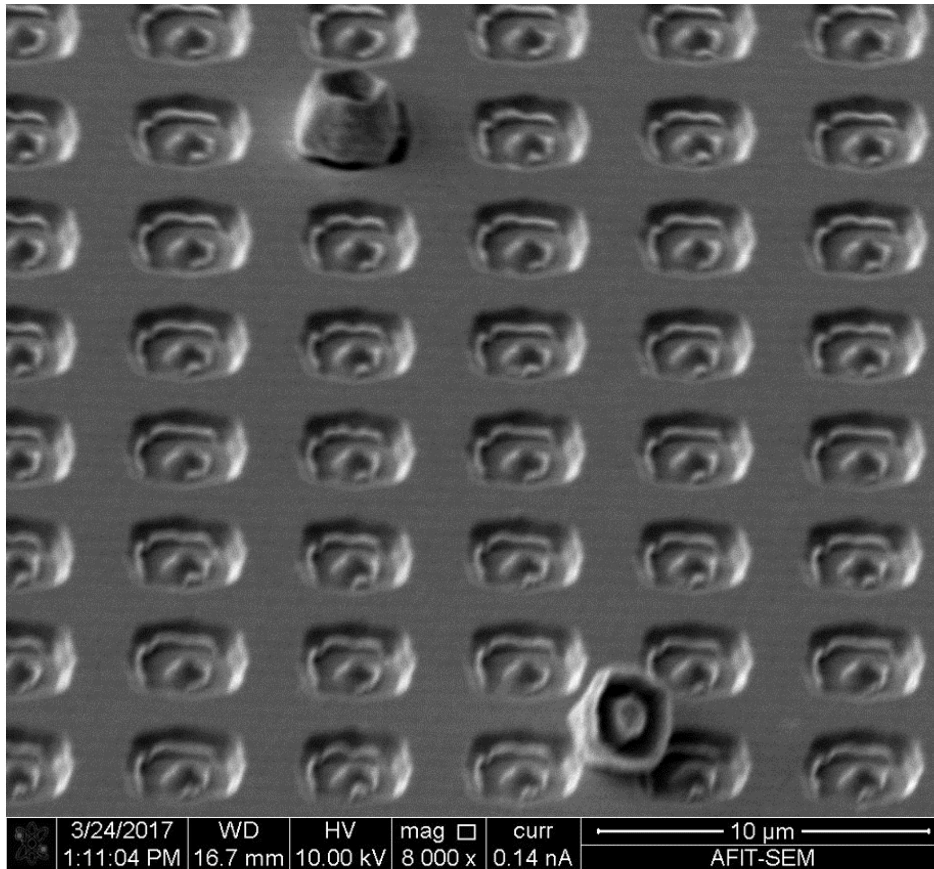

Figure 66: SEM image of sample EOP-2 showing the undesired mask-diffraction effects that occur during UV exposure of the 1818 photoresist; the two small anomalies are gold-covered photoresist plugs that remained following the metal liftoff.

Table 13. Nanoporous surface fabrication results achieved with Extreme-Optimized Photolithography.

Sample	Designed Diameter (nm)	Fabricated Diameter (nm)	Designed Porosity	Fabricated Porosity	Designed Aspect Ratio	Fabricated Aspect Ratio
EOP-1	5000	4400	0.55	0.42	0.10	0.14
EOP-2*	4000	3300	0.50	0.34	0.13	0.19
EOP-3*	3000	2800	0.44	0.39	0.17	0.22
EOP-4*	2000	2500	0.35	0.55	0.25	0.24

*sample contains regions of significant pattern deformation caused by mask-diffraction effects

4.2.2 Electron-Beam Lithography

The gold nanoporous surfaces shown in Figure 37 were laid out in L-Edit for patterning with AFRL's electron-beam lithography system. Because the e-beam patterning process involves using a negative-tone photoresist ("ma-N 2403") that has not previously been used at AFRL, an e-beam exposure study was performed to determine optimal e-beam exposure settings. To perform this study, L-Edit was used to layout a test-coupon containing $100 \times 100\ \mu m^2$ nanoporous patterns of each of the five designs shown in Figure 37. The e-beam system was used to pattern six copies of this test-coupon on a silicon wafer piece containing a 150 nm evaporated gold layer and a layer of "ma-N 2403" photoresist. Each of the six test coupon copies were written at unique e-beam settings to determine the optimal settings. Figure 67 shows images of the highest quality test-coupon that was fabricated during the e-beam exposure study. This test-coupon corresponded to an e-beam exposure of 150 $\mu C/cm^2$. Unfortunately, the highest porosity nanoporous designs did not survive the gold-liftoff process as shown by the bottom two designs of the test-coupon shown in Figure 67. However, a detailed inspection of the nanoporous surfaces that did survive showed a remarkably high-quality pattern of 200 nm diameter pores. Figure 68 shows SEM images of these patterns. Although the pattern for EBL-4 did not survive the gold-liftoff, regions of undisturbed nano-pores were visible and enabled the SEM image for EBL-4. Thus, it may be possible to fabricate a sample of EBL-4 by using a more delicate gold-liftoff procedure. Figure 69 further illustrates the quality of these nanoporous surfaces by showing near-perfect dimensions for pore diameter and pore spacing.

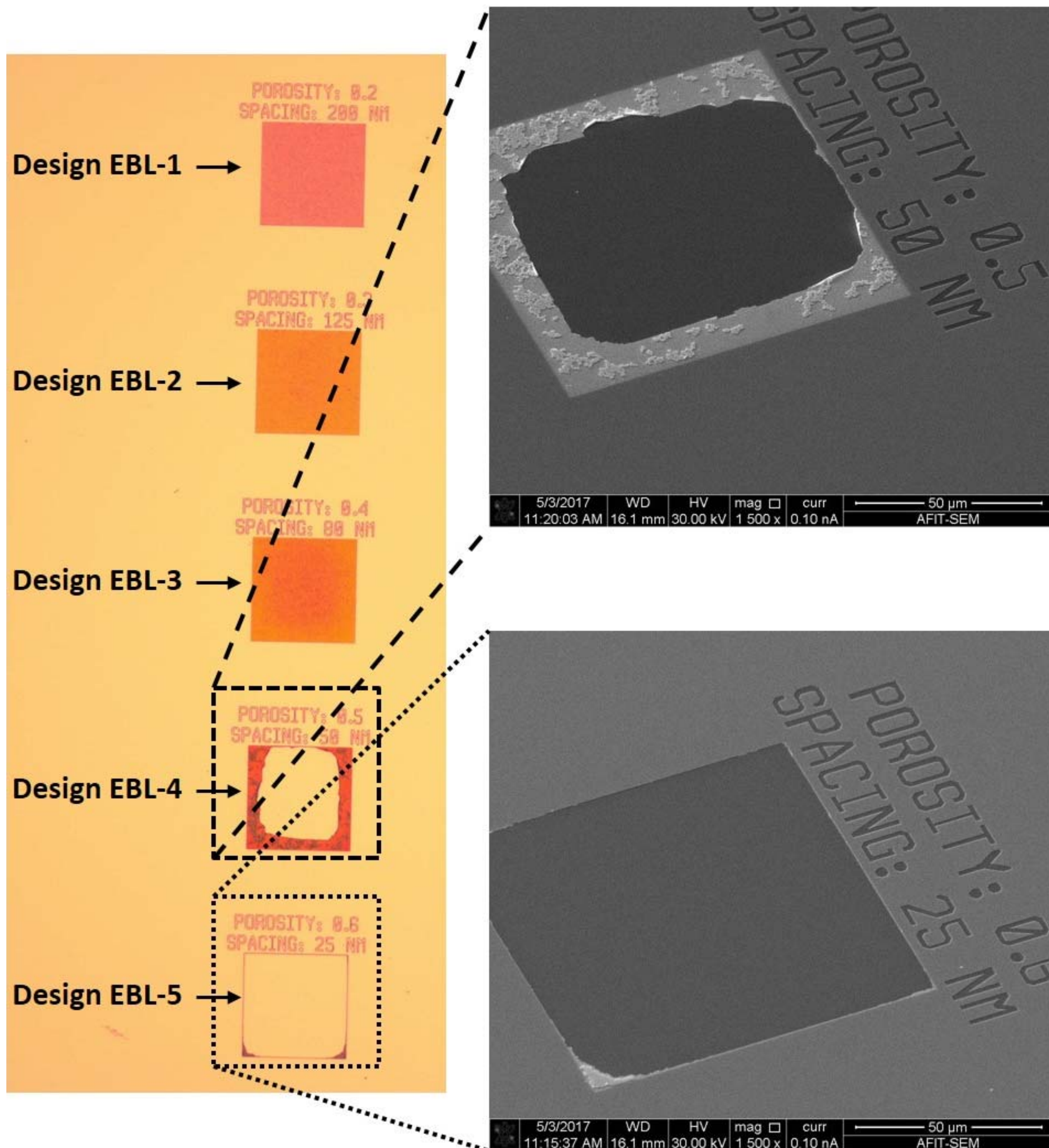

Figure 67: Microscope image of the highest quality test-coupon fabricated during the e-beam exposure study (left); SEM images of the highest porosity samples that were destroyed during the gold-liftoff procedure.

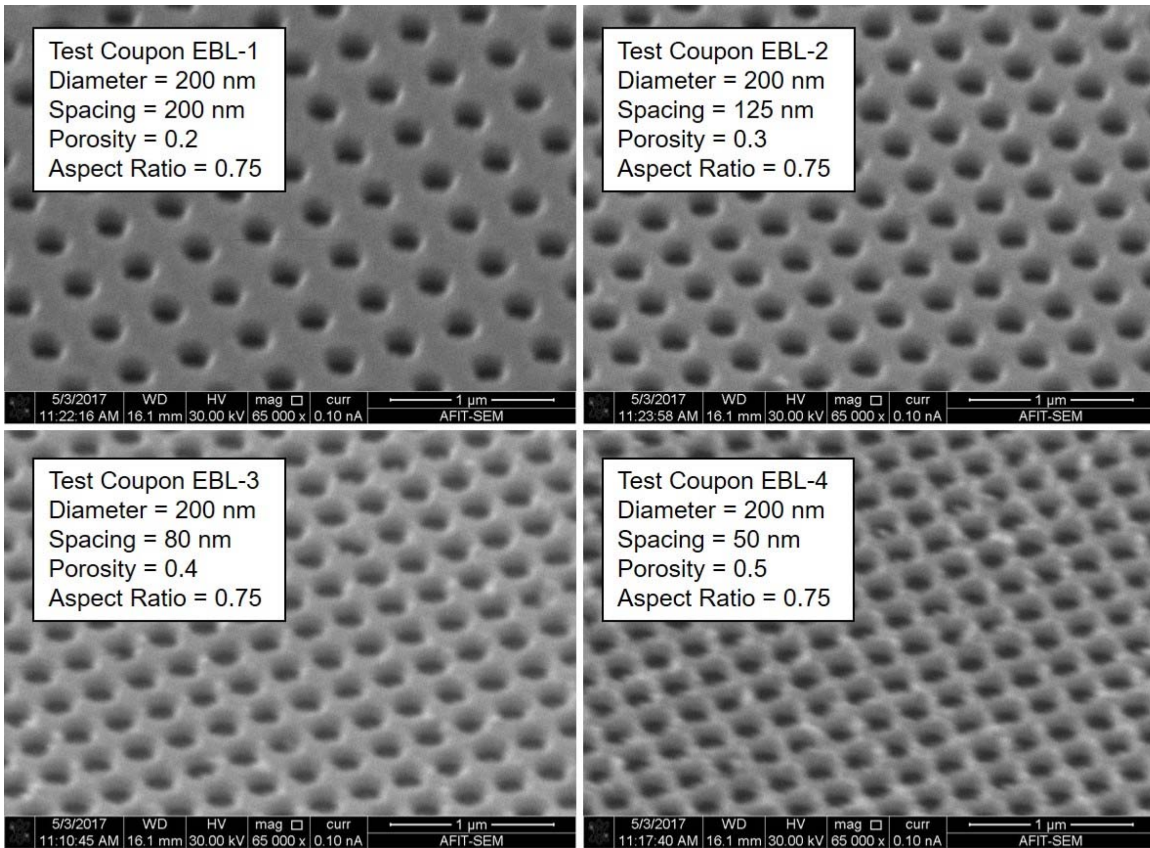

Figure 68: SEM images of nanoporous gold surface regions – taken from the highest quality test-coupon fabricated during the e-beam exposure study.

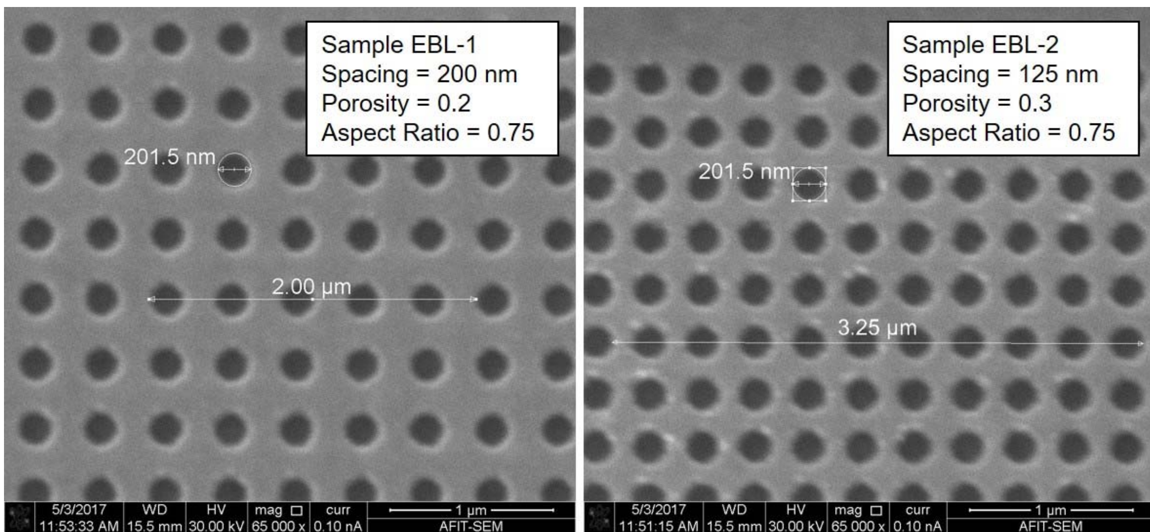

Figure 69: Key dimensions of nanoporous gold surface regions taken from the best e-beam lithography test-exposure coupon.

Having determined the optimal e-beam exposure settings and demonstrated successful fabrication of high quality nanoporous surfaces, the focus shifted to making nanoporous sample sizes large enough to allow SEY testing. To do this, design EBL-2 was used to create a 500×500 μm^2 nanoporous pattern in L-Edit that was loaded in the e-beam lithography system. The e-beam system was then used to write the 500×500 μm^2 pattern and repeat the process approximately 40 times to create a ~20×20 mm^2 sample of design EBL-2. Because of the number of individual octagons (pores) that had to be patterned (nearly 2 billion), the e-beam exposure took several days to complete. Figure 70 shows a "before and after" photo of sample EBL-2. The upper left quadrant of the pattern that is missing from the post-liftoff photo was due to an over-exposure of the e-beam resist for that region. Figure 71 shows a close-up SEM image of the nano-pores in sample EBL-2, which match the high quality pores obtained during the test-coupon fabrication. Figure 72 shows four SEM images captured from different regions of sample EBL-2. These images

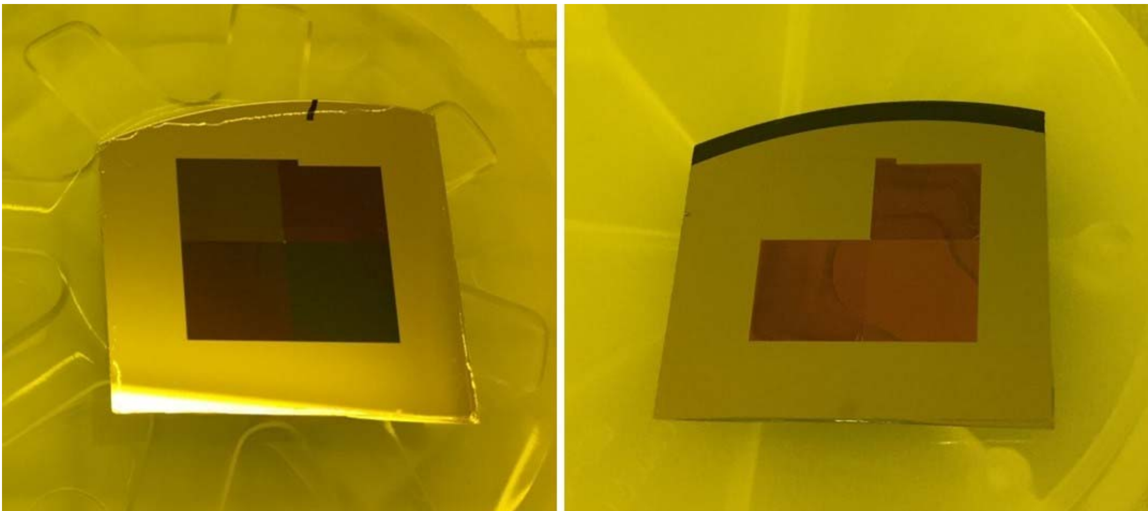

Figure 70: Large-area (~20×20 mm^2) pattern of sample EBL-2 before performing the gold-liftoff (left) and after performing the gold-liftoff (right).

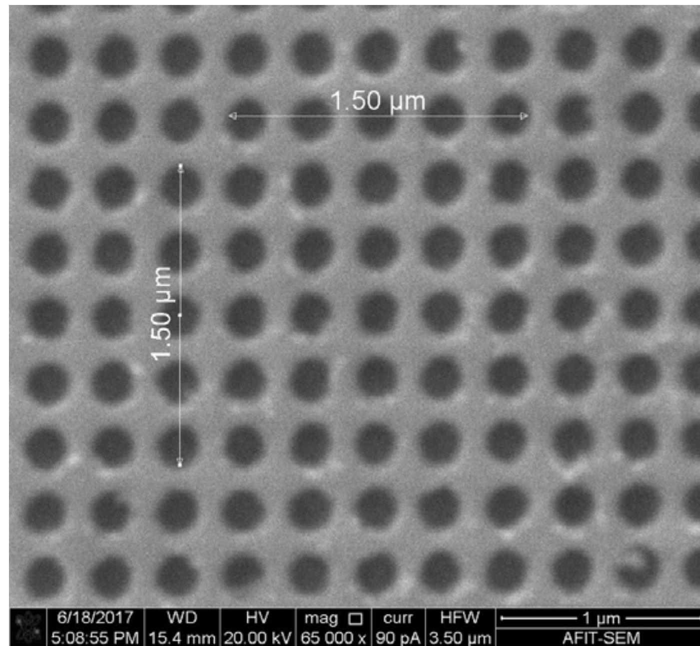

Figure 71: SEM image of the ~20×20 mm^2 sized sample EBL-2 showing excellent pore shape, size, spacing, and pattern consistency.

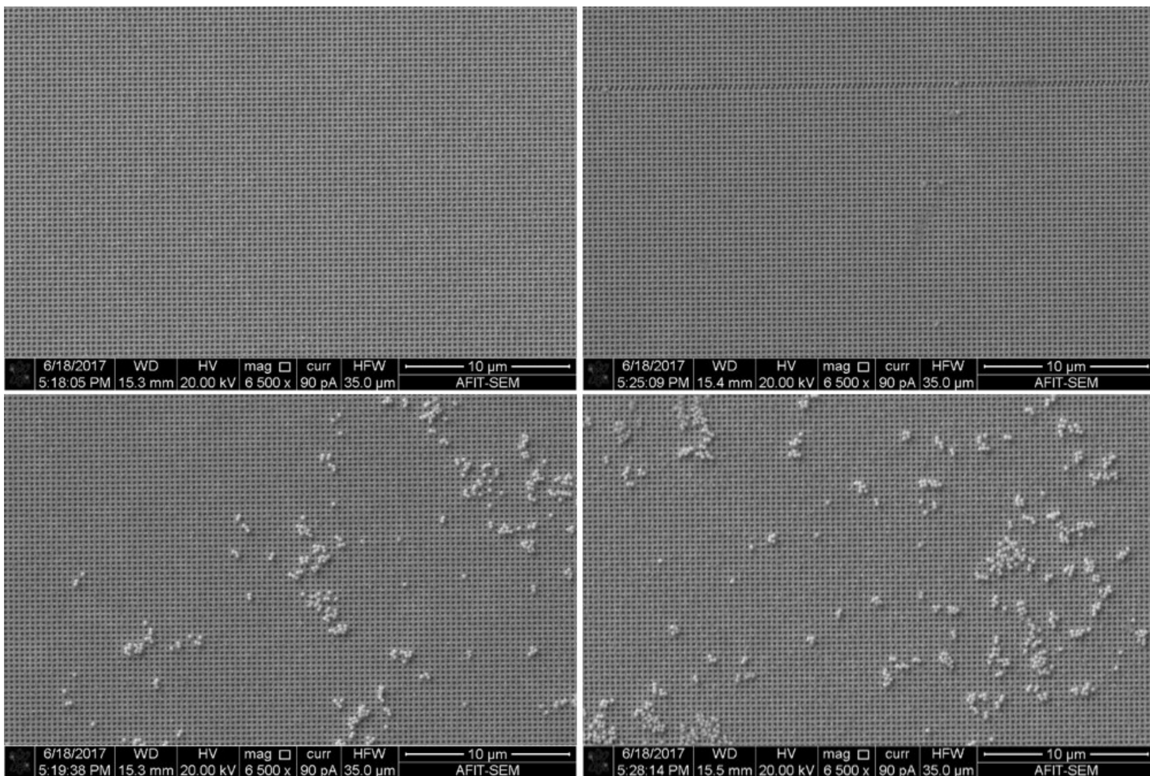

Figure 72: SEM images of various locations from the large-area sample EBL-2 showing the varying degree of pore-plug residue that remained after performing the gold liftoff.

illustrate a new fabrication challenge when making large-area patterns: it is very difficult to remove all of the gold nano-pore plugs that are created during gold-liftoff. This challenge was partially overcome by submerging the sample upside-down in acetone during additional ultrasonic cleaning attempts. However, some of the pore-plug residue remained and therefore must be accounted for during SEY measurements. Based on SEM images of sample EBL-2, it is estimated that less than 5% of the surface area is contaminated with pore-plug residue. Table 14 provides a summary of the fabrication results obtained using e-beam lithography in conjunction with gold evaporation and a gold-liftoff.

Table 14. Nanoporous surface fabrication results obtained with e-beam lithography.

Sample	Designed Diameter (nm)	Fabricated Diameter (nm)	Designed Porosity	Fabricated Porosity	Designed Aspect Ratio	Fabricated Aspect Ratio
EBL-1*	200	201.5	0.20	0.20	0.75	0.74
EBL-2*	200	201.5	0.30	0.30	0.75	0.74
EBL-3*	200	194	0.40	0.36	0.75	0.77
EBL-4**	200	201.5	0.50	0.51	0.75	0.74
EBL-5***	200	Unknown	0.60	Unknown	0.75	Unknown

*7x7 mm^2 samples contain regions of pore-plug residue

**largest sample was 100×100 μm^2 and was partially destroyed during gold liftoff

***largest sample was 100×100 μm^2 sample was completely destroyed during gold liftoff

4.3 Porous Surface Materials Characterization Results

4.3.1 Energy Dispersive X-ray Spectroscopy

Due to the small size of pores involved in these surfaces (which could foster the trapping of contaminants) and the various fabrication chemicals and processes involved, an EDS study was performed to better characterize the samples. Figure 73 shows the EDS results for both the sputtered gold reference sample and the electroplated gold reference

sample. The EDS was performed using a 20-μA electron beam current of 20 keV electrons directed at the gold samples. These 20 keV electrons penetrate deep into the target where they interact with atoms in the bulk material. Some of these interactions will cause inner-shell electrons to be ejected, creating an electron hole, which can be filled by an electron from an outer orbital. When such an electron fills the hole, the difference in electron energy

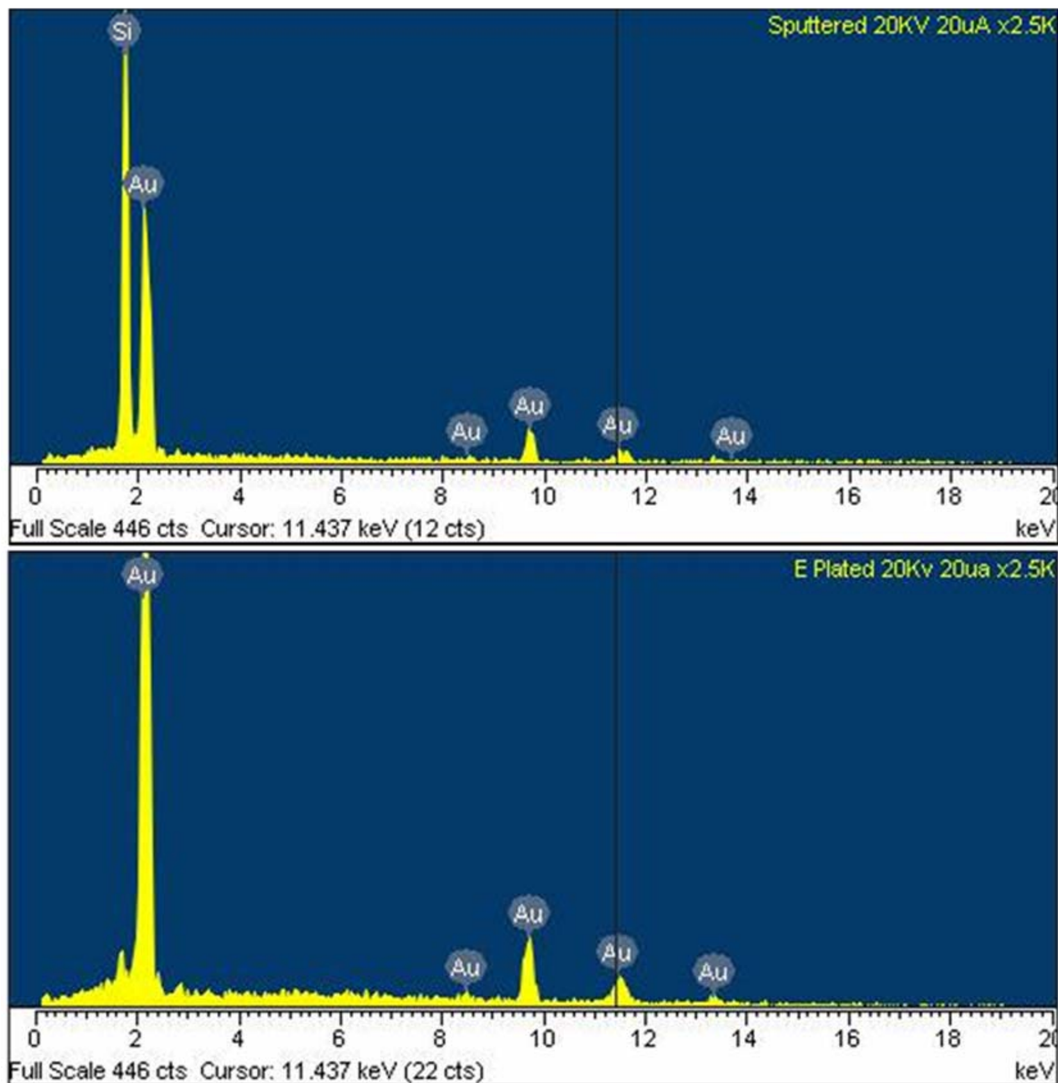

Figure 73: Bulk composition analysis of the sputtered (top) and electroplated (bottom) reference samples obtained using Energy Dispersive x-ray Spectroscopy (EDS).

can be given off as an x-ray that is characteristic of the atomic structure of the emitting element. In this way, EDS allows the elemental composition of the bulk material to be determined. The only anomaly detected with EDS was the strong indication of a silicon presence in the sputtered gold reference sample (see top left of Figure 73). A secondary analysis of the penetration depth of the 20 keV EDS electrons determined that the silicon peak is present because the electrons are penetrating through the 150 nm gold layer and into the silicon substrate. This secondary analysis was done computationally using Win X-Ray to perform 10,000 Monte Carlo simulations of 20 keV electrons penetrating into a gold surface. Figure 74 shows a cross-sectional view of the resulting electron paths determined by Win X-Ray (blue lines represent absorbed electrons; red lines represent back-scattered

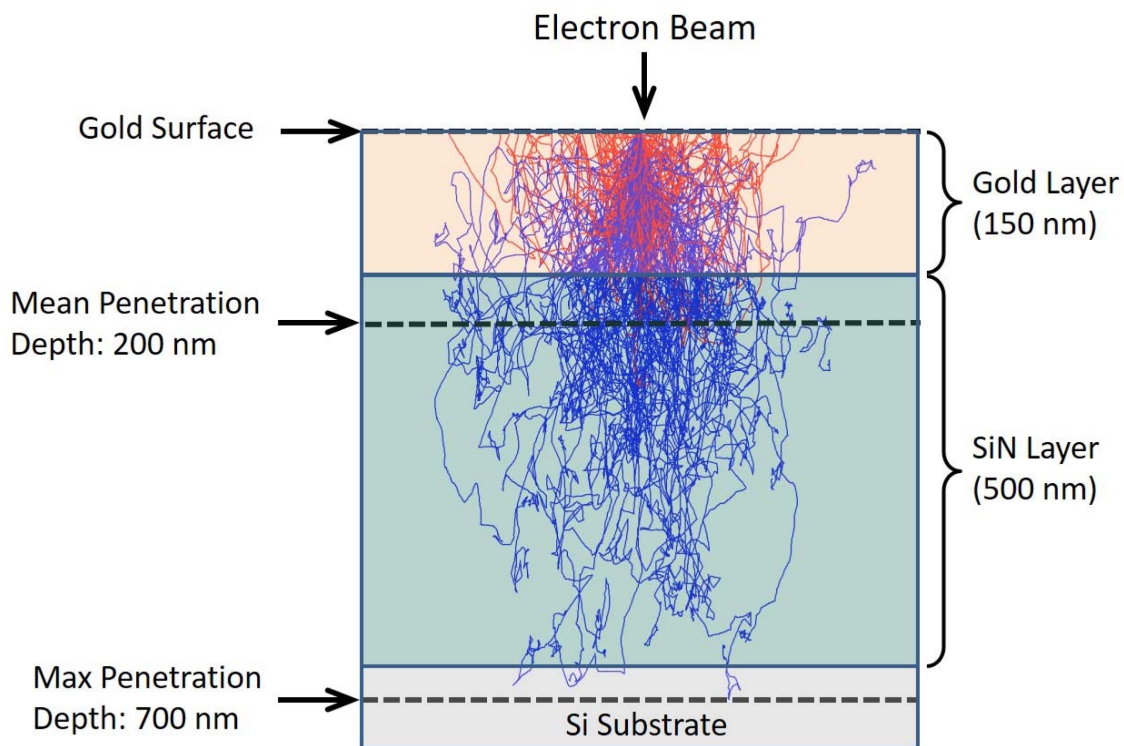

Figure 74: Win X-Ray Monte Carlo simulation performed 10,000 times using 20 keV electrons at a beam current of 20 μA directed towards a gold surface.

electrons). Figure 74 confirms the fact that numerous EDS electrons penetrated beyond the 150 nm gold layer and into the silicon nitride layer and silicon substrate causing the silicon peak in the EDS plot for the sputtered gold. There is no corresponding silicon peak in the EDS plot for electroplated gold because the electroplating process deposited 5.6 μm of gold. An additional EDS was performed on microporous sample 2-1 to ensure there were no residual photoresist contaminants (i.e. carbon-containing organic compounds) in the pores. The EDS plots from this study showed no such contaminants and looked remarkably similar to the plots shown in Figure 73.

4.3.2 X-Ray Photoelectron Spectroscopy

A surface chemical analysis was performed on both the sputtered and electroplated reference samples using XPS. Incident x-rays were provided by a Magnesium K_α source emitting at 1253.6 eV. A "VG Scienta R3000" hemispherical analyzer was used to detect escaping electrons and characterize their energies. In this setup, the x-rays bombard the gold sample causing electrons to be ejected from different orbital shells. Because these electrons will have a small mean free path within the material, only electrons generated near the surface (~10 nm) will escape the material, allowing for detection by the analyzer. In this way, XPS is a surface characterization technique. Figure 75 shows the wide-scan XPS results for both the sputtered and electroplated gold reference samples. Both the sputtered and electroplated gold XPS results are in reasonable agreement with other published XPS results for sputtered and electroplated gold [109]–[111]. The primary difference shown by the XPS characterization is a change in the carbon-oxygen atomic concentrations at the surface, with the percentage of gold concentration relatively

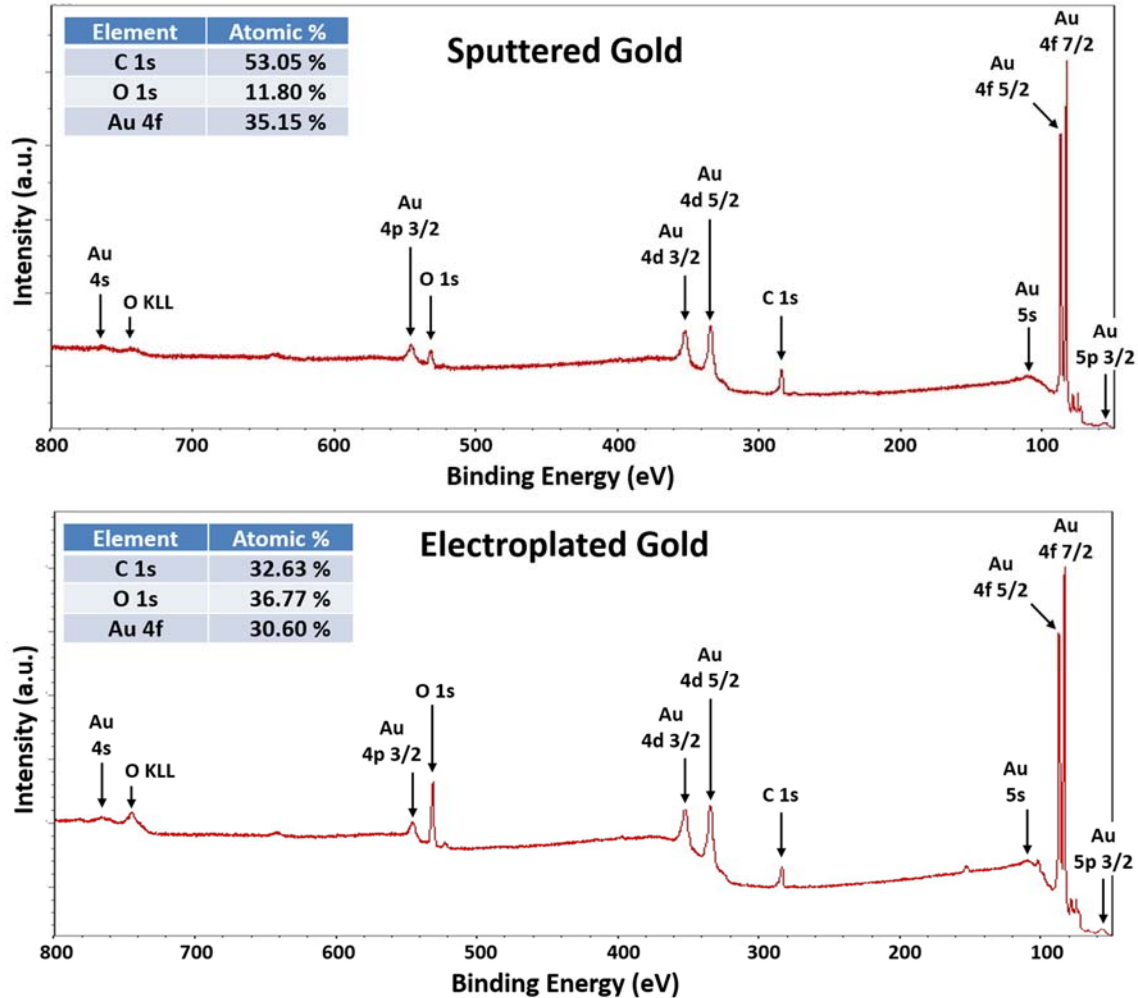

Figure 75: Surface elemental composition of the sputtered and electroplated reference samples obtained using X-ray photoelectron spectroscopy with a Mg K_{α} x-ray source.

unchanged. Although not predicted, this compositional difference is not unexpected when comparing the sputtering process (involving UHV conditions and a gold target that is 99.999% pure) to the electroplating process (involving gold in aqueous solution containing other proprietary chemicals). The difference in topography of these gold depositions (visible in Figure 60) will also play a role in the type of and concentration of non-native species that adsorb to the surface. These differences in surface atomic concentration will also be evident in the SEY measurements shown in the next section.

4.4 SEY Measurements

SEY measurements were performed on two non-porous gold reference samples (sputtered and electroplated gold) and the five microporous gold surfaces presented in Section 4.1. These SEY measurements were performed over the course of three months (August – September 2016) at the AFRL Materials and Manufacturing Directorate. Numerous previous SEY measurement attempts were conducted to refine the techniques used during data collection. Specific attention was given to performing all measurements using identical methods to ensure parity between the measurements. Samples were loaded into the vacuum chamber load-lock one day and allowed to pump down for at least 4 hours before transferring to the main chamber. Once loaded in the main chamber, samples were pumped down at least 12 hours (overnight) before measurements were recorded – this ensured the measurements were conducted under UHV conditions ($< 5\times10^{-9}$ Torr). Prior to data recording, the STAIB Instruments DESA 150 energy analyzer was used to provide an image of the porous surface (equivalent to an SEM). This image was used to align the porous surface with the e-gun and to focus the e-gun to ensure that only the porous surface was exposed to the e-beam. The vertical sample manipulator shown in Figure 42 was used for alignment adjustments. The e-gun filament current was adjusted between 1.18 and 1.19 amps to provide a ~20 nA sample current with the +100V bias applied. This ~20 nA sample current (corresponding to the e-beam current) was chosen to minimize electron conditioning of the sample surface (i.e. chemical alterations to the surface).

Figure 76 shows the measured SEY for all microporous samples as well as the two gold reference samples. The error bars bound two standard deviations above and below the sample mean, providing a 95% confidence interval that the true mean is within the bars

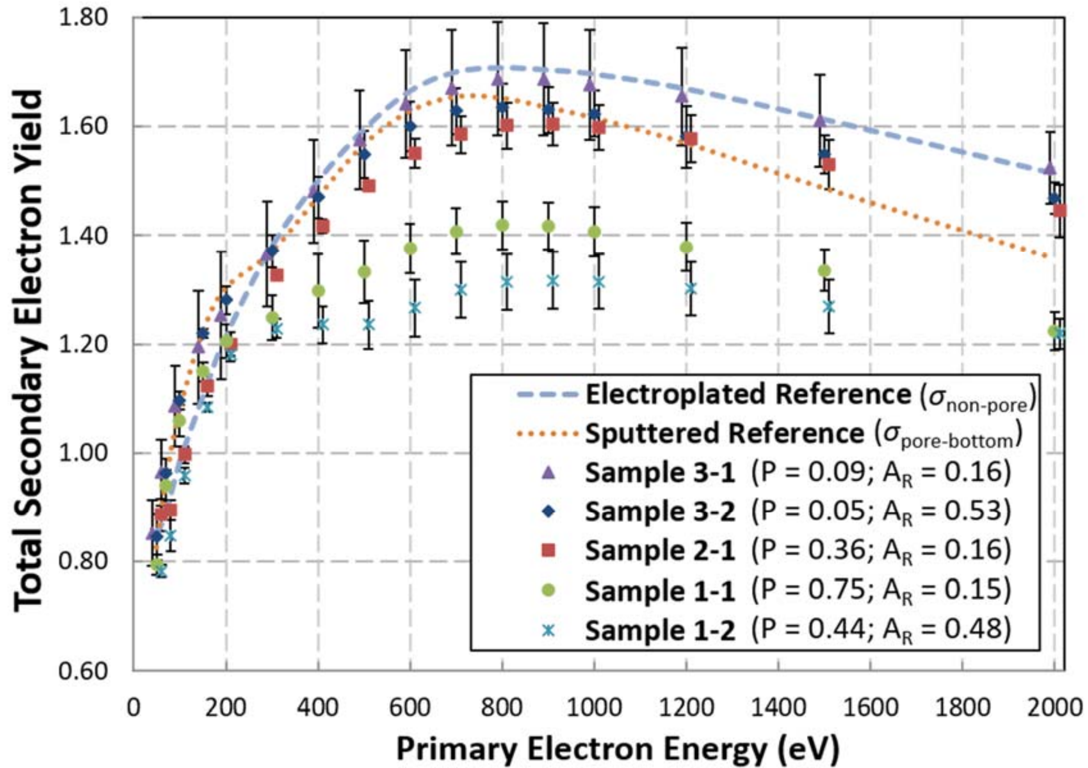

Figure 76: Secondary electron yield (SEY) measurements of microporous gold surfaces obtained using the Air Force Research Laboratory SEY measurement chamber (Error bars show 2 standard deviations above and below the sample mean).

(Note: error bars are not shown for the reference samples). When considering how to suppress multipactor by reducing SEY, there are two key parameters of interest on the SEY curves: (1) the first crossover energy, E_1, and (2) the maximum total SEY, σ_{max} (see Figure 17). Any surface modification method that increases E_1 will reduce the multipactor susceptibility region (see Figure 7) because lower-energy electrons will no longer contribute to SEE. Similarly, any surface modification method that lowers σ_{max} will reduce the multipactor susceptibility region because fewer electrons will be generated by SEE events. Figure 77 provides a closer look at these SEY-curve regions. The effect modifying surface topography has on E_1 is somewhat evident in Figure 77 (left) by the rightward

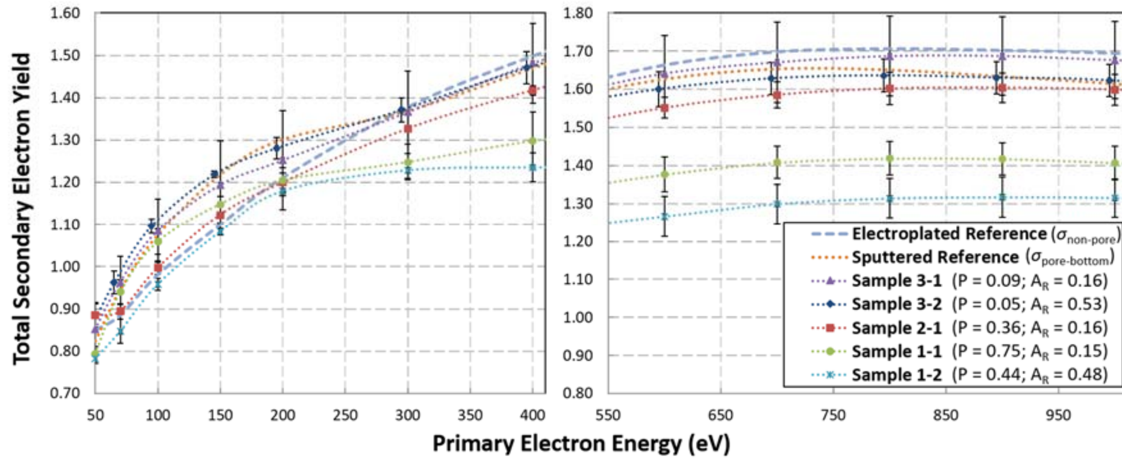

Figure 77: Key regions of secondary electron yield (SEY) measurement curves: low-energy region with first SEY crossover (left); SEY-maximum region (right).

shifting of the curves with increasing porosity and aspect ratio. More impressively, the effect modifying surface topography has on lowering σ_{max} is clearly visible in Figure 77 (right) by the lowering of the curves with increasing *Porosity* and aspect ratio.

Because these porous samples consist of two regions: mesas of electroplated gold and valleys of sputtered gold, the SEY curves for reference samples of those regions becomes important to understanding the results. Figure 78 provides a closer look at the exclusive SEY curves for these non-porous regions alongside an SEM image of both regions. For consistency, the error bars bound two standard deviations above and below the sample mean. A surprising result shown in Figure 78 is that the smoother sputtered gold surface has a lower σ_{max}. This is attributed to the different chemistries these surfaces have, as previously identified by the XPS study discussed in Section 4.3.2. The differences in the reference sample SEY curves must be considered for when analyzing the results provided in Figure 76 because they will account for some of the changes to the SEY curves. Fortunately, the 2D and 3D porous surface SEY models, previously developed in Section

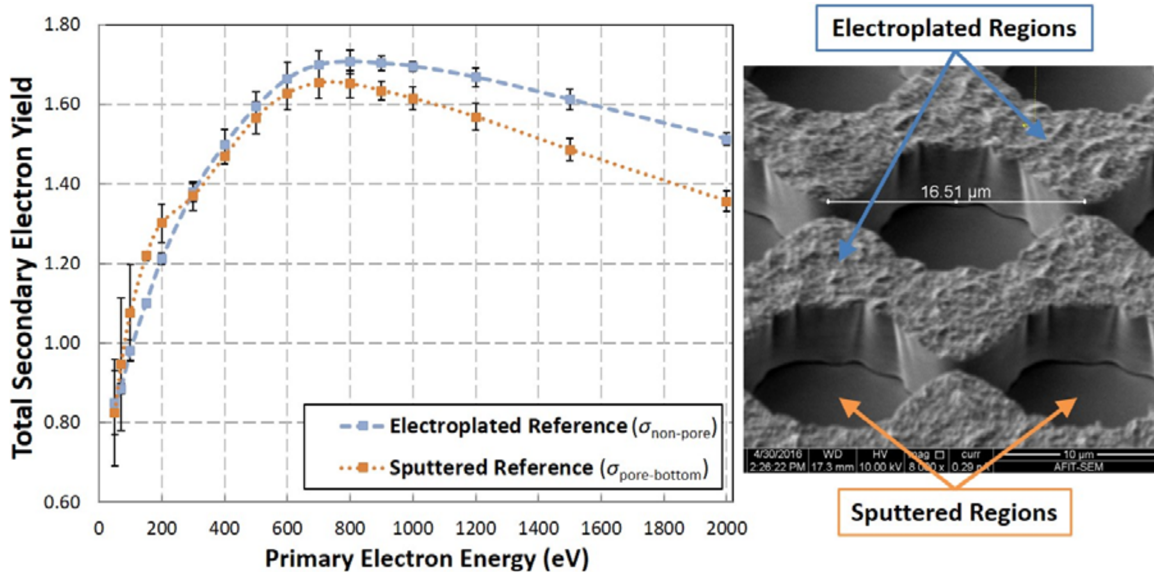

Figure 78: Secondary electron yield measurements of gold reference samples with error bars showing two standard deviations above and below the sample mean (left); SEM image showing differences between sputtered and electroplated gold topographies (right).

3.1, account for these differences in the parameters $\sigma_{\text{non-pore}}$ and $\sigma_{\text{pore-bottom}}$. Therefore, we can now use the data shown in Figure 78, along with the microporous surface fabrication data provided Table 11, to predict SEY curves for microporous gold samples.

Figure 79 shows plots of SEY predictions for both the 2D and 3D models, alongside the relevant experimentally measured SEY curves from Figure 76. The data for all samples in Figure 79, over the range 400 eV to 1200 eV, shows the improved prediction capability provided by the 3D SEY model. For samples 1-1 and 1-2, the vertical separation between the predicted curves and the measured curves is attributed to the pore deformation that occurred for these close-packed samples (see Figure 56 and Figure 57). By contrast, the near-perfect overlap of the predicted and measured curves for samples 2-1, 3-1, and 3-2 helps validate both the 2D and 3D models because these samples had near-perfect cylindrical pores (see Figure 58, Figure 59, and Figure 60).

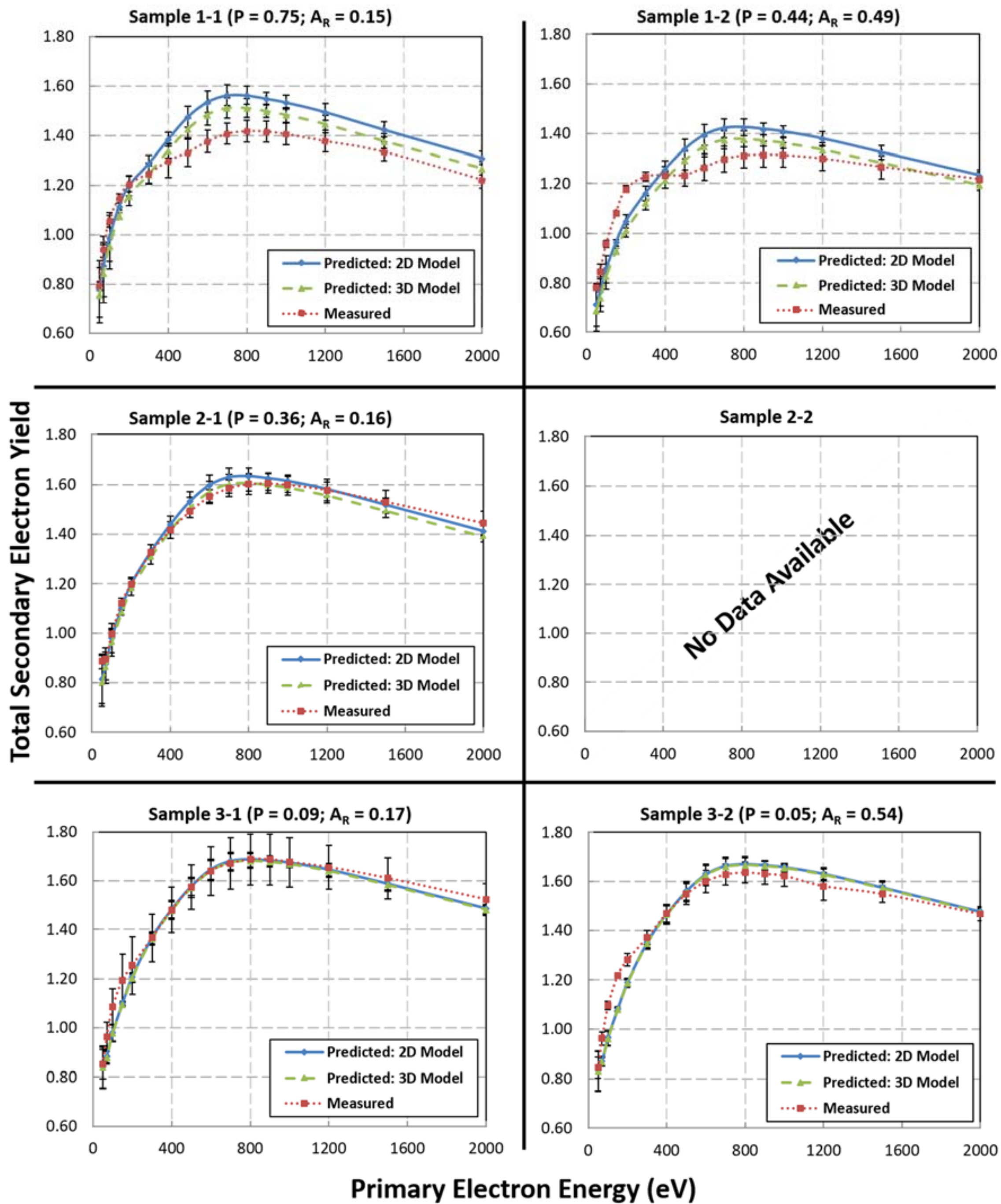

Figure 79: Comparison of 2D and 3D secondary electron yield (SEY) model predictions to SEY measurements of microporous gold surfaces (Error bars shows 2 standard deviations above and below the sample mean).

4.5 New SEY Measurement Chamber

A major part of this research effort was the construction of AFIT's first SEY measurement chamber, which was completed 1 December 2016. However, after 1 day of initial operation, the Faraday cup attached to the ELG-2 became inoperable because of mechanical binding in the manual rotator knob that prevented the Faraday cup to fully open and close. After consultation with Kimball Physics, the ELG-2 was removed and shipped to Kimball Physics for repair. The repaired e-gun was received 9 December and reinstalled but the same problem returned in February 2017, resulting in a second removal and return to Kimball Physics for further repairs. Since then, the Faraday cup has performed with no further problems. However, because this was now a recurring problem, an inquiry was made into the source of the problem and the repair. The technical representative from Kimball Physics stated that they, "found that the actuator was rubbing the end of the Cu block" and that this is this is "usually not a problem, but…maybe during the initial machining process the Cu got too hot and is now softer than usual." The manufacture's repair involved filing the copper block down and applying some Mo lubricant. When asked if the user could cause the problem, Kimball Physics insisted that scenario is unlikely. Furthermore, the Kimball Physics technical representative expressed great confidence in the reliability of the rotary-actuated Faraday cup design because they have performed extremely reliably in the past. The technical representative did reiterate the importance of limiting bakeout temperature to 200°C or below as a restriction provided by the manufacturer of the rotary feedthrough, Huntington Mechanical Labs, Inc. Figure 80 shows the mechanical drawings of the rotary feedthrough including the bakeout specification [112].

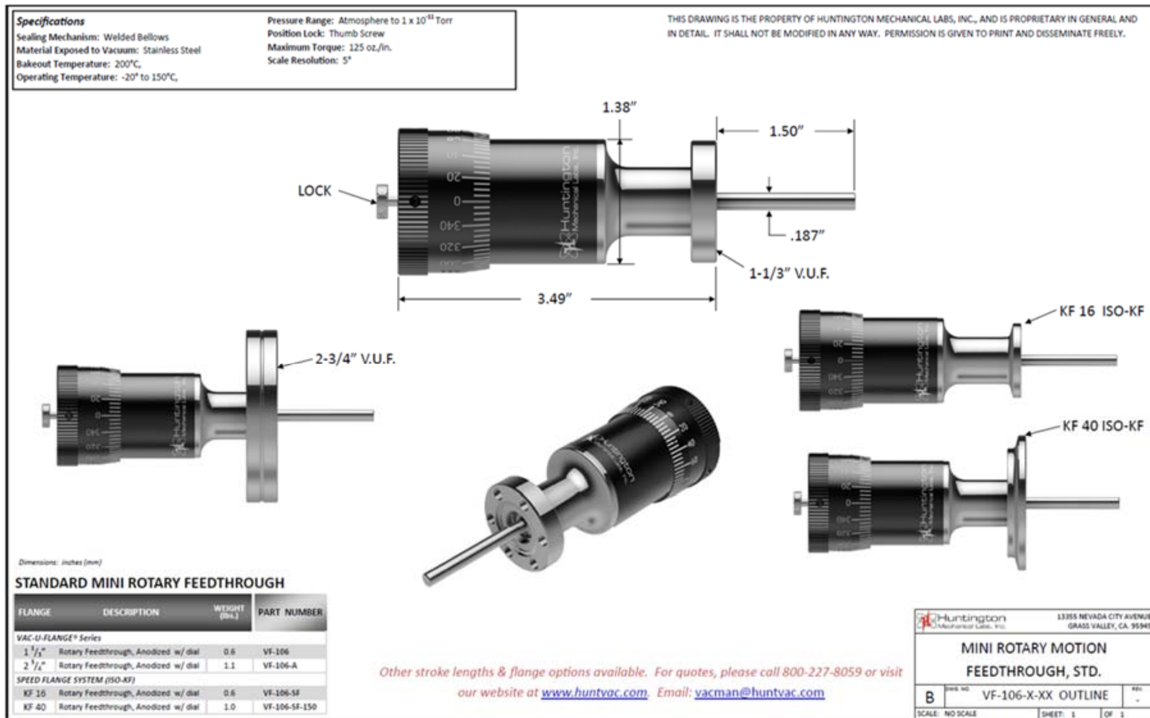

FLANGE	DESCRIPTION	WEIGHT (lbs.)	PART NUMBER
VAC-U-FLANGE® Series			
1 1/3"	Rotary Feedthrough, Anodized w/ dial	0.6	VF-106
2 3/4"	Rotary Feedthrough, Anodized w/ dial	1.1	VF-106-A
SPEED FLANGE SYSTEM (ISO-KF)			
KF 16	Rotary Feedthrough, Anodized w/ dial	0.6	VF-106-SF
KF 40	Rotary Feedthrough, Anodized w/ dial	1.0	VF-106-SF-150

Figure 80: Mechanical drawings of the rotary feedthrough used to actuate the Faraday cup on the ELG-2 electron gun [112].

Figure 81 shows the final SEY measurement system. The system consisted of the original Kurt Lesker UHV chamber, Kimball Physics ELG-2 e-gun and EGPS-1022 power supply, UHV-Designs 5-axis sample manipulator, two Keithley model 6514 electrometers, a custom-made 27V battery enclosure, and a custom-made LabVIEW® data collection program. The custom LabVIEW® program was designed to control both Keithley electrometers and record their respective currents (one for the Faraday cup and one for the sample). The program allows the user to control the e-beam settings using the EGPS-1022 power supply while manually entering the e-beam energy in a prompt provided by the LabVIEW® program.

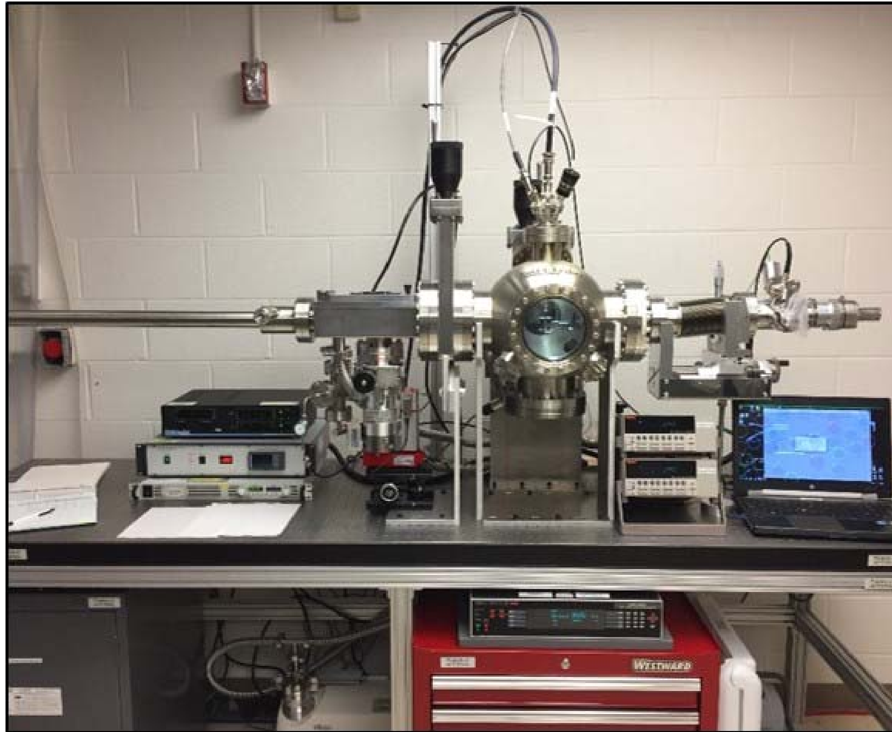

Figure 81: AFIT's first dedicated secondary electron yield (SEY) measurement system.

Figure 82 shows the custom-made 27V battery enclosure that was incorporated instead of a programmable DC supply to minimize sample-to-ground current leakage. This technique was learned as a best practice from Professor I. Monterro during discussions at the 2017 International Workshop on Multipactor, Corona, and Passive Intermodulation. Unfortunately, subsequent testing of the SEY system consistently revealed a 3-nA leakage current measured between the sample and ground with no e-beam illumination. Evidence gathered from additional troubleshooting has revealed the existence of a low-resistance sample-to-ground path somewhere within the sample manipulator. This leakage current was determined to be extremely stable, with a total variation less than 0.1% over 62 sample current measurements recorded at different e-beam energies. Given the existence of this

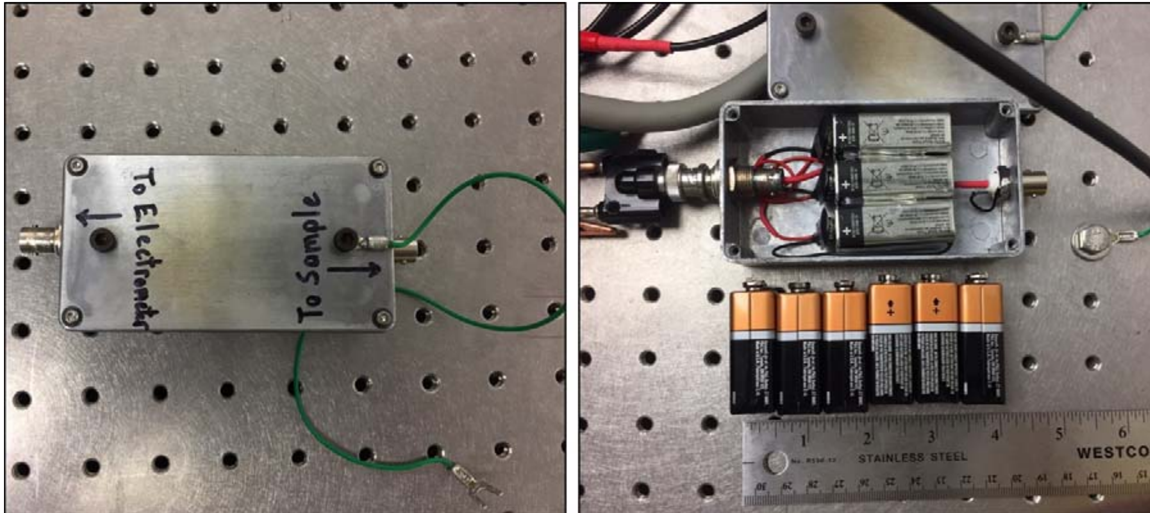

Figure 82: Metallic battery enclosure designed to provide a -27 Volt DC bias to the sample with minimal current leakage.

leakage current, the SEY measurement methodology was modified by adding a step to measure the sample leakage current. The new procedure followed a 3-step process:

1) measure the e-beam current using the Faraday cup;

2) measure the sample leakage current by recording the sample current with the Faraday cup covering the e-gun (new);

3) measure the sample current with the Faraday cup open and the e-beam illuminating the sample.

The leakage current measured in step 2 would be subtracted from the sample current during post-measurement data processing.

Using this procedure, SEY measurements were performed on both the sputtered gold and electroplated gold reference samples. Figure 83 shows the results from these measurements. The data shown in Figure 83 contains three noteworthy features: two of these add credibility to this measurement system while the third raises a concern about the

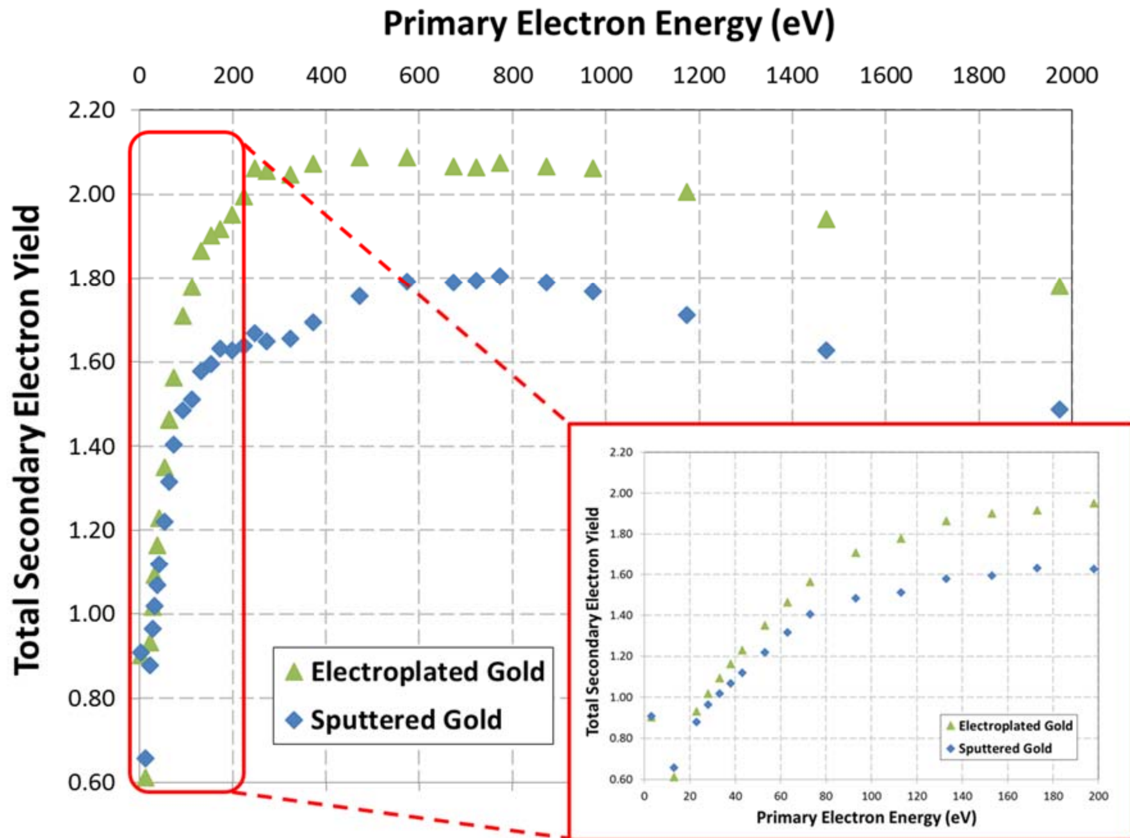

Figure 83: Secondary electron yield (SEY) measurements of the microporous gold reference samples obtained with the new AFIT SEY measurement chamber.

accuracy of the system. First, the SEY of the electroplated gold is higher than the SEY of the sputtered gold, which is consistent with the AFRL SEY measurements (Figure 78) and adds credibility to the system. Second, the SEY curves for both samples "rebound" at extremely low primary energy, which is consistent with the shape of these curves as shown in Figure 17. This "rebound" effect results from the inability of extremely low-energy electrons to create true secondary electrons that have sufficient energy to overcome the material's work function and escape. Thus, the only electron emissions from the surface are elastically backscattered electrons, which become the dominant electron-surface interaction as the primary energy decreases to zero. The observation of this SEY "rebound

effect" adds additional credibility to the SEY measurement system. The third noteworthy feature is the unusually high SEY values that were measured for both gold reference samples. The SEY data compiled by D.C. Joy does not show gold SEY values above 1.8 [102]. While it is possible that many of the measurements compiled by Joy were sputter-cleaned prior to SEY measurements (a process that would lower the SEY), the fact that SEY measurements of these samples performed at AFRL showed values in line with the data compiled by Joy, raises a concern. One explanation is that the sample leakage currents change when the e-beam illuminates the sample, which would render the new measurement methodology invalid. Figure 84 shows the sample leakage currents recorded while performing the SEY measurements shown in Figure 83. Although the magnitude of the leakage current shifted between the measurements of the two samples, the consistency of the currents for each sample is remarkable. The shift in leakage current from 3 nA for the

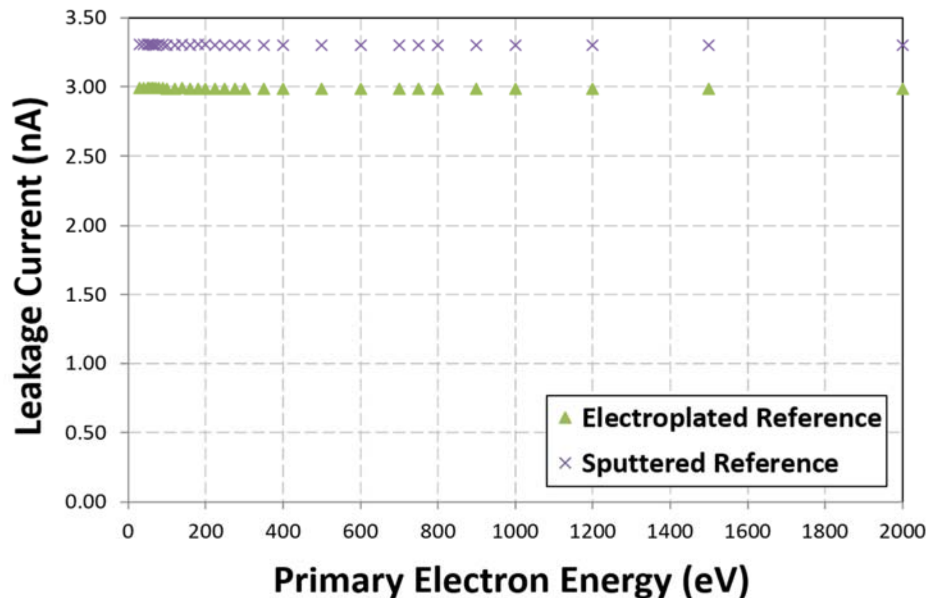

Figure 84: Plots of the sample leakage currents measured while performing SEY measurements of the two gold reference samples.

electroplated gold to 3.3 nA for the sputtered gold is attributed to the sample puck loading procedure. Because the sample manipulator was previously shown to have a low-resistance path between the sample and ground, the process of transferring the puck into the manipulator basket is believed to have caused enough physical jarring to change the low-resistance path. Unfortunately, subsequent SEY measurements, which involved additional sample loading and unloading, demonstrated an ever-increasing and inconsistent leakage current (over 10 nA) from measurement to measurement. This indicates the need to have the sample manipulator examined for repair. Eliminating the sample-to-ground leakage current should be considered a high priority because it would increase confidence in the accuracy of the system. Finally, the ability of the sample manipulator to heat and cool samples provides an exciting capability for future research. The ability to conduct temperature-dependent SEY studies is extremely rare in the SEY research community and makes the new AFIT SEY measurement system stand out as a unique experimental measurement capability.

4.6 Thermomechanical Simulation Results

Table 15 shows the results from the thermomechanical simulations that were performed using CoventorWare®. Because the second research question in Chapter I was concerned with examining the differences between microporous and nanoporous surfaces, the simulations were performed for two pore sizes: a 10-μm diameter pore with an aspect ratio of 1.0 and a 200 nm diameter pore with an aspect ratio of 1.0. Positional displacement measurements were made of each simulated pore during steady state high and low temperature exposures of 400°C and -200°C. As Table 15 shows, the amount of pore

expansion and contraction is extremely small relative to the pore's dimensions. Furthermore, these changes result in negligible effects to the aspect ratio, *Porosity*, and the overall SEY of an equivalent engineered surface. Additionally, this data indicates that equivalent thermomechanical effects can be expected for porous surfaces made from other multipactor suppression metals of interest (e.g. Ag, Cu, stainless steel). This is because the linear thermal expansion coefficients are similar for all of these metals (α_L = 14.2 ppm/°C for Au; α_L = 19.68 ppm/°C for Ag, α_L = 16.5 ppm/°C for Cu, and α_L ranges 9.9 – 17.3 ppm/°C for stainless steel).

Table 15. Thermomechanical effects of extreme temperatures on a gold micro/nano-pore.

	Temp. (°C)	Height (µm)	Diameter (µm)	A_R	$\overline{P}_{escape\text{-}3D}$	Change to *Porosity*	Change to $\sigma_{porous\text{-}surface}$*
Micro-Pore	23	10.000	10.000	1.000	0.366	0.00%	0.00%
	400	10.052	10.068	0.998	0.367	1.37%	-0.67%
	-200	9.976	9.969	0.001	0.366	-0.62%	0.30%
Nano-Pore	23	0.200	0.200	1.000	0.366	0.00%	0.00%
	400	0.201	0.201	0.999	0.367	1.38%	-0.67%
	-200	0.199	0.199	1.000	0.366	-0.62%	0.31%

*Assumes *Porosity* = 0.5; $\sigma_{non\text{-}pore}$ = 1.7; $\sigma_{pore\text{-}bottom}$ = 1.6

4.7 Summary

This chapter provided the results obtained by this research effort. These results included the successful fabrication of five of the nine microporous surface designs and successful fabrication of three of the five nanoporous surface designs. Optical lithography in conjunction with electroplating was shown to provide high quality microporous surfaces. However, the fabrication of nanoporous surfaces using optical lithography was proven to be extremely challenging and ultimately, unsuccessful. However, e-beam lithography

combined with metal evaporation provided high quality nanoporous surfaces. The results from two different materials characterization studies (EDS and XPS) were presented showing high purity gold samples in both the bulk material and at the surface. Surface contamination consisted of carbon and oxygen, which was expected. SEY measurement data for the microporous surfaces was presented showing the dramatic effect that surface topography can have on SEY. Preliminary SEY data measured using the new AFIT SEY measurement system was presented to demonstrate a functional system. Finally, the results of the thermomechanical analysis were presented which showed the negligible effect that extreme temperatures would have on a microporous or nanoporous surface and its ability to control SEY.

V. Analysis

This chapter provides an in-depth analysis of the results obtained during this research effort. Section 5.1 revisits the semi-empirical porous surface SEY models that were presented in Section 3.1 in order to develop a more generalized semi-empirical SEY model for a roughened surface. Section 5.2 provides a detailed analysis of the experimentally measured SEY data for the microporous samples along with a comparison of this data to the semi-empirical SEY model predictions. Finally, Section 5.3 provides an overarching analysis of this effort resulting in the proposal of specific engineered surface topographies for multipactor suppression.

5.1 Generalized SEY Model for Roughened Surfaces

Section 3.1 developed two semi-empirical SEY models for a porous surface. However, there are limitless non-porous patterns that could be used for SEY control. Returning to the general equations for the porous surface SEY model (Equations 26 and 28), they can be combined to provide,

$$\sigma_{\text{porous-surface}} = \sigma_{\text{pore-bottom}} \left(P_{\text{escape}}\right)\left(Porosity\right) + \sigma_{\text{non-pore}} \left(1 - Porosity\right). \tag{63}$$

Let us now consider a periodically patterned surface containing unspecified features such as the one shown in Figure 85. For such a surface, Equation 63 now becomes,

$$\sigma_{\text{rough-surface}} = \sigma_{\text{bottom-surface}} \left(P_{\text{escape}}\right)\left(FD\right) + \sigma_{\text{top-surface}} \left(1 - FD\right), \tag{64}$$

where *FD* is the surface density of unspecified features (similar to *Porosity*) defined,

$$FD = \frac{\text{Surface Area of Features}}{\text{Total Surface Area}}. \tag{65}$$

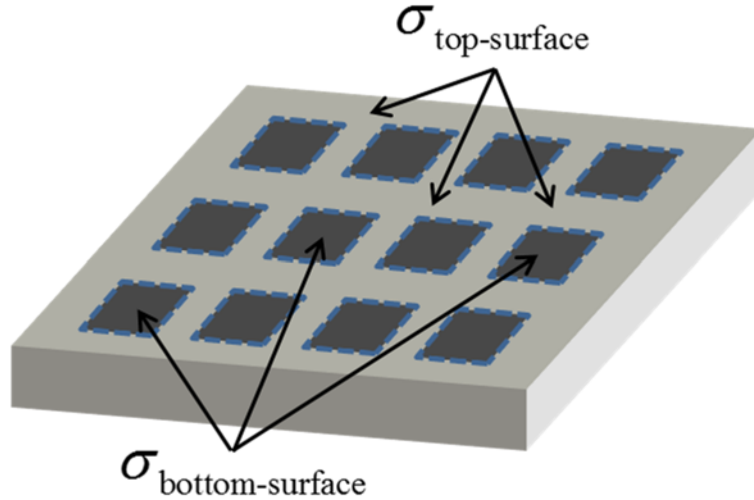

Figure 85: Periodically patterned surface based on unspecified features used for developing a general SEY model for engineered surfaces.

Equation 64 provides a generalized model for the SEY of a periodically patterned surface of unspecified features. The P_{escape} term depends on the specific geometry of the features while the *FD* term depends on the feature-to-feature spacing. Considering *FD* as the independent variable, Equation 64 can be rearranged into a general "$y = mx + b$" format:

$$\sigma_{\text{rough-surface}} = \left[\sigma_{\text{bottom-surface}}\left(P_{\text{escape}}\right) - \sigma_{\text{top-surface}}\right] FD + \sigma_{\text{top-surface}} . \quad (66)$$

Equation 66 indicates the importance of selecting a low-SEY material for the top surface because it is the y-intercept of the model. Because $\sigma_{\text{bottom-surface}}$ will always be less than or equal to $\sigma_{\text{top-surface}}$ the slope of Equation 66 will always be negative (ignoring the case of an unpatterned surface). Consequently, in order to minimize $\sigma_{\text{rough-surface}}$, both the feature density and aspect ratio should be maximized.

A more specific periodically patterned rough surface that shows promise for multipactor suppression is a grooved or trenched surface. Figure 86 shows an illustration of a grooved surface. These surfaces are advantageous for multipactor suppression for two

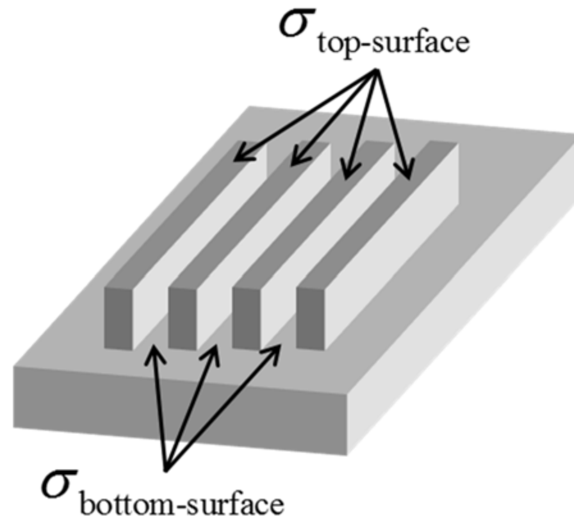

Figure 86: Grooved surface topography for multipactor suppression, feasible with a laser ablation process.

reasons: (1) grooves can be orientated in the direction of electromagnetic wave propagation to minimize insertion loss in a microwave or RF device; (2) grooved surfaces can be fabricated using a laser ablation process that would be significantly easier to implement in a production-scale manufacturing process [73]. Equation 64 could be used to develop a semi-empirical model for a grooved surface. The only term that would need to be derived is P_{escape}, which would require a 3D trench model to account for the lack of symmetry in the plane of the surface (unlike the case of a cylindrical pore, which has this symmetry). The obvious drawback to using a grooved surface for secondary electron recapture (instead of a porous surface) is the inability of the grooves to recapture electrons emitted parallel to the grooves. Thus, we would expect a grooved surface to be slightly less efficient than a porous surface for the purpose of recapturing electrons. Fully developing this SEY model and experimentally verifying are considered top priorities for follow-on work.

5.2 Analysis of Measured vs. Modeled SEY Data

The data shown in Figure 76 contains several noteworthy features to analyze more closely. First, the error bars, indicating two 2 standard deviations above and below the mean, provide high confidence that the experimentally-observed trend of reducing σ_{max} values as *Porosity* and A_R are increased is real. This trend was also observed through modeling as shown in Figure 87, which provides SEY-modeled curves that correspond to the experimental curves shown in Figure 76. The curve for a proposed design was generated using the 3D model (Equations 26, 28, and 46) and illustrates the predicted SEY curve of a porous sample with *Porosity* = 0.5 and A_R = 2.

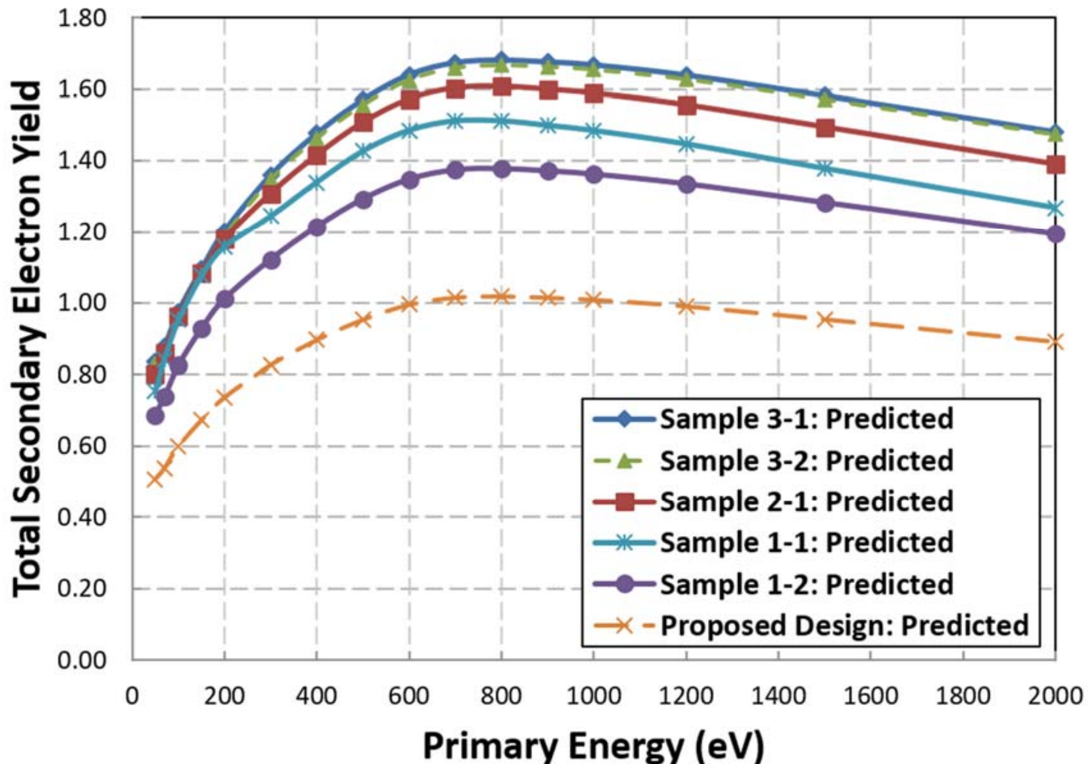

Figure 87: Plot of semi-empirical 3D SEY model predictions based on the gold reference SEY data collected and the specific dimensions of the microporous samples fabricated in this effort (Note: the proposed design has *Porosity* = 0.5 and A_R = 2.0.

Another noteworthy feature of the curves in Figure 76 is the small degree of upward concavity in the range 200 – 600 eV for the sputtered reference, sample 1-1 and sample 1-2 curves. This concavity has previously been observed and reported by Nistor *et al.* for gold surfaces, referring to the anomaly as a “shoulder” [10]. Nistor proposes that this shoulder is a transitioning of the gold SEY curve to a modified SEY curve that represents the SEY of the chemically altered surface, which contains both carbon-based adsorbates and oxygen-based condensates. The shoulder fades with increasing primary energy because higher energy electrons penetrate through the layer of non-native adsorbates and condensates and into the pure bulk gold. Thus, at higher primary energies, the measured SEY curve reflects the SEY of pure gold, while at lower primary energies the measured SEY curve reflects the SEY of a chemical mixture of the non-native species at the surface. Figure 78 shows this shouldering in the sputtered gold reference but not the electroplated gold reference. This is likely attributable to the increase in atomic concentration of carbon in the sputtered gold, detected using XPS and shown in Figure 75. Interestingly, the predicted curves for the close-packed samples (1-1 and 1-2) do not accurately predict the SEY shoulder that was measured for these samples (see top of Figure 79). It is likely that the pore sidewall breakdown observed in both of these samples combined with the pore deformation observed in sample 1-2 is responsible for this curve mismatch. For example, the measured curve for sample 1-2 contains a larger influence from the sputtered gold region because the pores were deformed with sidewall breakdown. However, the predicted results for sample 1-2 do not account for this increased influence. Since the sputtered gold reference showed an increase in the shoulder effect, this explains the failure of the predicted curves to account for this phenomenon accurately in samples 1-1 and 1-2.

Another way to analyze the measured and predicted data is to consider only the maximum value of the SEY curves (σ_{max}). Figure 88 shows predicted σ_{max} curves (determined using the semi-empirical 3D porous surface SEY model) plotted against *Porosity* for a variety of aspect ratios of interest. Overlaid on this plot are the measured values of σ_{max} for each microporous sample, to provide perspective on how accurately the model predicts the σ_{max} values. The failure of the model to predict the SEY for samples 1-1 and 1-2 (attributed to their pore sidewall breakdown and imperfect cylindrical shape) is evident in the rightmost two data points. The construct of the graph in Figure 88 is helpful to determine the design of future porous surface test samples for the purpose of model validation. For example, a future porous surface design should have *Porosity* = 0.5 and A_R = 2. Two additional porous surface designs that would help validate the model would have *Porosity* = 0.65 and A_R = 1 and *Porosity* = 0.7 and A_R = 0.5.

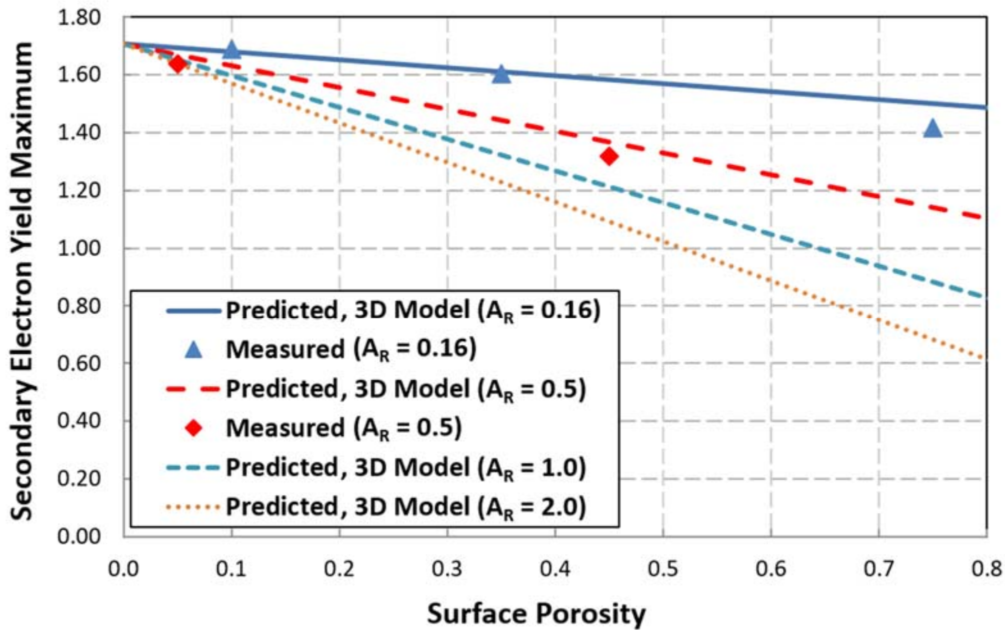

Figure 88: Plot of 3D SEY model predictions with experimentally measured maximum SEY values overlaid.

5.3 Engineered Surface Designs for Multipactor Suppression

As stated in Section 1.5, the goal of this dissertation is to determine optimal surface topographies to control the secondary electron yield for the purpose of multipactor suppression. However, because the scope of this research was limited to modeling and testing cylindrical porous surfaces, the explicit achievement of this goal is limited to these cylindrically porous topographies. Fortunately, the model developed and experimentally validated, provides the capability to consider other types of patterned surfaces (i.e. grooved surfaces) in addition to other types of materials such as silver, copper, or stainless steel.

According to the semi-empirical SEY modeled data shown in Figure 87, the topography that would achieve a multipactor-free gold surface based on cylindrical pores must have *Porosity* ≥ 0.5 and $A_R \geq 2.0$. According to the semi-empirical 3D SEY model (Equations 26, 28, and 46) and measured values of $\sigma_{non\text{-}pore} = 1.7$ and $\sigma_{pore\text{-}bottom} = 1.65$, an engineered surface based on that topography will constrain the entire SEY curve to values at or below unity. However, it is vital to recognize the role played by the empirically measured parameters, $\sigma_{non\text{-}pore}$ and $\sigma_{pore\text{-}bottom}$ (i.e. the SEY of the two gold reference samples), in this multipactor-free surface. To illustrate the point, we can use the semi-empirical 3D SEY model to recalculate the σ_{max} value of the proposed design curve shown in Figure 87 using 10% larger values of $\sigma_{non\text{-}pore}$ and $\sigma_{pore\text{-}bottom}$. Such an increase in these parameters would cause the same engineered surface (i.e. *Porosity* ≥ 0.5 and $A_R \geq 2.0$) to have $\sigma_{max} = 1.125$, a 10% increase that jeopardizes the ability of the surface to fully suppress a multipactor. This caveat becomes more significant when considering the large range of SEY data that has been measured for different elements. In 2005, Lin and Joy studied this SEY-measurement-variation problem by examining over 80 years of published SEY data from

more than one hundred different groups of authors [113]. The following quote from their paper provides a useful summary of the situation:

"An examination of this data is discouraging, because it is evident that even for common elements (such as Al or Au) for which there are often a dozen or more independent sets of data available, the level of agreement is rarely better than 25% and often shows relative divergences of 100% or more. The result of this situation is that anyone seeking yield data to explain an observation or to validate a model can usually find multiple values spanning a large enough range to support or disprove any assertion" [113].

In their paper, Lin and Joy propose a Monte Carlo simulation method for generating "…an optimized SE yield profile for each element for which an adequate supply of experimental results is available [113]." Using this method Lin and Joy determined δ_{max}(Au) = 1.28, which is reasonably lower value than the σ_{max} gold reference values measured in this research: σ_{max}(electroplated Au) = 1.7 and σ_{max}(sputtered Au) = 1.65). This difference is reasonable because the Lin and Joy value is the true SEY (no backscattered electrons), while the values measured in this effort are the total SEY which includes backscattered electrons. However, referring to the general shape of the SEE distribution (Figure 16a) and the general shape of the SEY curves (Figure 17) we note that δ_{max} is a fraction of σ_{max}. Thus, we can create a simple correction factor and expression for estimating σ_{max} of different metals according to the following,

$$\sigma_{\text{max-metal}} = \frac{\sigma_{\text{max-gold}}}{\delta_{\text{max-gold}}} \delta_{\text{max-metal}}, \quad (67)$$

where $\sigma_{max\text{-}gold}$ = 1.7 (the measured SEY of electroplated gold in this research) and $\delta_{max\text{-}gold}$ = 1.28 (the value determined by Lin and Joy) and $\delta_{max\text{-}metal}$ is the true SEY listed in the Lin

and Joy database [113]. Equation 67 allows us to calculate estimates of the porous surface design parameters needed to suppress multipactor. Table 16 provides a summary of these design parameters for a multipactor-free porous surface based on cylindrical pores. If we consider the Table 16 data in reference to a grooved surface (which would have a lower P_{escape} than a surface of cylindrical pores because electron-emission trajectories that parallel the grooves would have an escape probability close to 1), we would expect grooved surfaces for multipactor suppression to have $A_R > 2$. It should be re-emphasized that Table 16 is providing estimates to guide future SEY control studies using porous surfaces. The SEY database published by Joy provides a reasonable cross-check and validation of the "Estimate of σ_{max}" data provided in Table 16 [102].

Table 16. Design estimates for multipactor-free porous surfaces of various metals.

Material	δ_{max} from Lin and Joy [113]	$\frac{\sigma_{\text{max-gold}}}{\delta_{\text{max-gold}}}$	Estimate of σ_{max}	Porous Surface Design Parameter Estimates that Reduce $\sigma_{\text{max}} \approx 1$*	
				A_R	*Porosity*
Al	2.00	1.328	2.66	2.0	0.78
Cr	1.80	1.328	2.39	2.0	0.73
Ni	1.19	1.328	1.58	2.0	0.46
Cu	1.53	1.328	2.03	2.0	0.63
Ag	1.43	1.328	1.90	2.0	0.59
Au	1.28	1.328	1.70	2.0	0.51

*Assumes $\sigma_{\text{non-pore}} = \sigma_{\text{pore-bottom}}$ = estimate of σ_{max}

5.4 Summary

This chapter provided a detailed analysis of the results obtained by this research effort. The semi-empirical SEY model for a porous surface that was proposed in Section 3.1 was revisited, analyzed, and generalized for use with any periodically patterned rough surface.

A semi-empirical SEY model framework for a grooved surface was proposed and analyzed for its ability to recapture secondary electron emissions. The advantages of using grooved surfaces for multipactor suppression were also provided. The experimentally measured SEY data for microporous surfaces was revisited and explored in detail to explain various noteworthy features in the data. A related analysis was provided, which examined the semi-empirical SEY model predictions and how they compared to measurement. Finally, the critical topography parameters necessary for controlling SEY were summarized and used to propose engineered surface designs for multipactor suppression.

VI. Conclusions and Recommendations

This chapter summarizes the results and impact of this research effort by providing conclusions and making recommendations for future work. Section 6.1 recaps the five research questions presented in Section 1.5, providing the answers obtained by this effort. Section 6.2 lays out the specific contributions realized through this dissertation. Finally, Section 6.3 provides specific recommendations for future work that should be performed to make further advances by building on the contributions of this effort.

6.1 Answers to Research Questions

Any scientific endeavor begins with questions aimed at understanding the unknown. This dissertation began with five research questions that guided the approach and methods used throughout this effort. Revisiting these questions provides a succinct method to summarize the results of this effort.

1) What is the relationship between total SEY and the surface topography parameters of <u>aspect ratio</u> and <u>spacing</u> (i.e. porosity)?

For a surface of patterned cylindrical pores, there is an inverse nonlinear relationship between total SEY ($\sigma_{\text{porous-surface}}$) and aspect ratio ($A_R$) as defined by the combination of Equations 26, 28, and 46 and shown graphically in Figure 26. The relationship is driven by the inverse nonlinear relationship between P_{escape} and A_R in Equation 46 and shown graphically in Figure 27. The same surface has an inverse linear relationship between $\sigma_{\text{porous-surface}}$ and *Porosity* as defined in Equation 26 and shown graphically in Figure 28. Extrapolating these results to the generalized SEY model for a roughened surface (Equation 64) provides the same inverse linear relationship between $\sigma_{\text{porous-surface}}$ and *FD* (feature density). Defining the specific relationship between $\sigma_{\text{porous-surface}}$ and A_R requires

knowing the formula for P_{escape}, which requires a specific feature geometry (i.e. cylindrical pores, rectangular cuboid pores, cylindrical protrusions, trenches, etc.). However, this relationship can confidently be assessed as an inverse one because larger aspect ratios (i.e. taller surface features) will decrease the range of electron emission elevation angles that allow electron escape to occur.

2) Does the absolute feature size of a patterned surface play a critical role in controlling SEY (i.e. how do microporous surfaces compare to nanoporous surfaces with regard to total SEY when they have equivalent feature aspect ratio and spacing)?

For an engineered surface of cylinders, the absolute feature size plays no direct role in controlling SEY. This is evident in both the 2D and 3D semi-empirical SEY models by the absence of a term representing the cylinder diameter or height. This is logical because the range of polar emission angles that allow electrons to escape is the same for both a small pore and a large pore if those pores have the same aspect ratio. However, the answer to this question was only theoretically proven with the 2D and 3D SEY models. Consequently, experimental measurements of nanoporous surfaces are still necessary in order to have complete confidence in this answer. Extrapolating these results to the generalized SEY model for a roughened surface (Equation 64) will yield the same answer. This is because a regular pattern of surface features of any size and shape, will limit the polar emission angles that allow electrons to escape based exclusively on the ratio of feature height to feature width.

3) What are the research community recognized (i.e. published) SEY measurement methods and what are their tradeoffs?

Section 3.4 laid out the three widely accepted SEY measurement methods in detail and explained why the shaped collector method is recognized as the best practice. This is

because a shaped collector captures all secondary electron emissions, which are directly measured as a current. Additionally, the shaped collector can be positively biased to draw electron emissions away from the sample, eliminating the need negatively bias the sample to achieve the same effect [34]. This is a significant improvement for two reasons: (1) an applied sample bias modifies the impact energy of the primary electrons; (2) an applied sample bias would create strong electric field potentials around surface features causing unintended electrodynamic effects on both the primary and secondary electrons.

4) Can existing micro- and nano-fabrication techniques create large-scale topographies of consistently spaced and sized pores or other features and if so, what are these techniques?

The fabrication results presented in Sections 4.1 and 4.2 confirmed that both photolithography and e-beam lithography can be used to create surfaces of consistently spaced and sized pores. However, neither method was able to create large-scale samples containing these patterns – both methods were limited to surface patterns of 7×7 mm^2 or smaller. Although not explored in this dissertation, the use of wet and dry chemical etches or the use of lasers to modify surfaces are clearly understood to be the viable fabrication techniques capable of creating large-scale topographies of roughened surfaces. However, for performing basic research to understand the mathematical relationship between $\sigma_{porous\text{-}surface}$ and surface feature shape/size/density, lithographic techniques provide an outstanding method for fabricating near-perfect cylindrical pore structures.

5) How do extreme changes in temperature modify the topography of a gold porous surface and affect the ability of the porous surface to control SEY?

Extreme temperature changes were shown to have an insignificant effect on the ability of a porous surface to control SEY. However, this conclusion was only supported with

modeling and simulation that considered thermomechanical effects. Therefore, an experimental study is warranted to confirm this conclusion. Such a study is important because SEY is affected by surface chemistry, crystal structure, and quantum mechanical band structure – all of which are altered by temperature changes (see Table 3).

6.2 Contributions

This research effort has resulted in several important contributions to the field of engineered surfaces for SEY control and multipactor suppression.

6.2.1 Geometrically Perfect Microporous Surfaces

Previously published research on microporous surfaces for SEY control relied on subtractive metal etch processes to pattern the cylindrical pores. However, the chaotic nature of the wet etch process resulted in pore geometries that were inconsistent with the cylindrical shape used to develop an SEY model of the surface. This dissertation applied an additive metal deposition process (electroplating) to create perfectly-shaped cylindrical pores that match the cylindrical shape used to develop an SEY model of the surface [114]. These perfectly shaped cylindrical micro-pores ensure both the modeling results and the experimental SEY measurements are based on the same pore geometry.

6.2.2 Applying Nanosphere Lithography to SEY Control

In collaboration with another AFIT PhD student who studied the application of nanospheres to create improved micro-contacts, we explored the application of nanospheres to pattern surfaces for SEY control. This work is believed to be the first time nanosphere lithography has been considered and explored as a surface engineering method for controlling SEY [115].

6.2.3 New 2D Semi-Empirical SEY Model for Porous Surfaces

A new semi-empirical SEY model for an engineered surface of cylindrical pores was developed based on a 2D pore model (Equations 26, 28, and 36). Predictions from this model were compared to experimental measurements of microporous surfaces containing near-perfect cylindrical pores showing reasonable agreement. This is the first known SEY model that accounts for both the top and bottom surface SEY using empirical measurements [116].

6.2.4 New 3D Semi-Empirical SEY Model for Porous Surfaces

A new semi-empirical SEY model for an engineered surface of cylindrical pores was developed based on a 3D pore model (Equations 26, 28, and 46). A comparative analysis was performed on the results obtained by both the 2D and 3D pore SEY models, which demonstrated the improved accuracy of the 3D model. Scenarios were identified for which the 2D and 3D model differences are insignificant resulting in a preference for the closed-form 2D model over the more complicated 3D model that must be solved using numerical integration methods. Predictions using both the 2D and 3D models were compared to experimental measurements of microporous surfaces containing near-perfect cylindrical pores. These comparisons illustrated the improved accuracy of the 3D SEY model over the 2D SEY model. Additionally, the 3D model was used to determine an optimal topography for multipactor suppression using gold porous surfaces ($A_R = 2.0$, $Porosity = 0.5$) [117].

6.2.5 Geometrically Perfect Nanoporous Surfaces

A fabrication process was developed using electron beam lithography to produce a patterned surface of near-perfect gold cylindrical pores 200 nm in diameter. This effort also

explored and rejected the use of UV lithography for patterning engineered surfaces consisting of pore diameters on the order of a micron or less because of pattern diffraction effects associated with the UV exposure [118].

6.2.6 Extreme Temperature Effects on Micro- and Nano-Pores

A thermomechanical simulation study was performed to explore the effect extreme temperature changes would have on the physical size and shape of a gold micro-pore and nano-pore. The study, believed to be the first of its kind, demonstrated the insignificant effect extreme temperatures have on the shape and dimensions of gold micro-pores and nano-pores. The study also examined how the minor thermomechanical changes to pore size and shape would affect the ability of the porous surface to recapture SEE and concluded the effect to be insignificant [118].

6.2.7 New SEY Measurement System

A new, dedicated $120K SEY measurement system was constructed from scratch, providing a first-of-kind measurement capability for AFIT. The system was designed to provide a wide range of SEY measurement capabilities including sample heating, cooling, azimuthal rotation, and elevation rotation. The system was also designed to be able to perform SEY measurements on both conductive and non-conductive samples by using the electron gun in a pulsed mode of operation.

6.3 Recommendations for Future Work

The experimental nature of this research provides numerous opportunities for meaningful follow-on studies. These opportunities are further amplified by the fact that this was a new field of research for AFIT and consequently, required significant time and

resources to establish the new measurement capability. However, now that the capability exists, there are nearly limitless opportunities for future studies to be performed that would bear great impact on the field of multipactor suppression.

6.3.1 Sample Manipulator Repair and SEY System Calibration

Before attempting SEY studies using the new system, the proper time and attention should be paid to eliminating the sample leakage current that is intrinsic to the sample manipulator. Additionally, a system calibration should be performed by acquiring and measuring the SEY of a calibration sample for which the total SEY is well known. This will be an important step to reference in future publications involving results from experimental AFIT SEY studies.

6.3.2 SEY Study: Microporous/Nanoporous Surfaces

Once the SEY system has been calibrated, SEY measurements should be performed on the gold nanoporous samples and re-performed on the gold microporous samples to ensure parity between the results. Those results should be analyzed, compared to the SEY models provided in this dissertation and the results should be published.

6.3.3 SEY Study: Grooved Surfaces on Silicon Wafer

Design and fabricate a variety of grooved surfaces (vary aspect ratio and feature density) using internal AFIT capabilities (i.e. L-Edit, Heidelberg Mask Writer, silicon wafers, UV lithography, RIE, and gold sputtering). The grooves could be patterned into a 3-inch silicon wafer using the EVG® UV lithography system and etched with an RIE process. A gold sputtering process could then be used to coat the grooves with a 500Å layer of gold that conforms to the groove surfaces. These surfaces could then be tested for SEY

control and results compared to unmodified gold surfaces to validate an SEY model for grooved surfaces. This work could be expanded to include an angle of incidence SEY study using the grooved surfaces and the elevation angle variability of the AFIT SEY system.

6.3.4 SEY Studies: Laser-Patterned Grooved Surfaces

Work with a laser research lab or laser ablation company to determine the feasibility of patterning grooved surfaces with large aspect ratios (i.e. $A_R \geq 2$). Use a laser patterning process to create grooved surfaces of pure metallic samples of specific RF device materials of interest. Perform an experimental study to compare SEY measurements of unmodified metal samples with laser-modified metal samples. This work could be expanded by conducting a temperature-dependent SEY study of the unmodified and laser-modified surfaces using the heating and cooling capability of the AFIT SEY system. An angle of incidence SEY study could also be performed using the unmodified and laser-modified surfaces using the elevation angle variability of the AFIT SEY system.

6.3.5 Grooved Surface Waveguide Simulation Study

Perform a simulation study on the electromagnetic effects of grooved surfaces implemented in a waveguide. Consider factors such as groove aspect ratio, density, and orientation as well as transmission frequency/wavelength and analyze how these factors effect waveguide operation.

6.4 Summary

This chapter provided a summary of the overarching results of this research effort as well as concluding remarks about the direction in which future work should proceed. The original research questions that fueled this dissertation were revisited and answered. A

summary of this effort's key research contributions was provided. Finally, a detailed list was provided, outlining future research questions and studies that should be performed to build on the foundation laid by this dissertation…AFIT's first experimental research effort studying multipactor suppression.

Appendix A. Process Followers

A-1 Microporous Gold Fabrication Process Follower

PROCESS STEPS	NOTES	DATE (TIME)
CLEAN SILICON WAFER: □ Rinse in acetone, methanol, IPA, and DIW for 30 sec at 500 rpm □ Dry with nitrogen on spinner at 500 rpm and on Texwipes		
DEPOSIT SIN ISOLATION LAYER (PECVD): □ Perform 90 sec plasma clean at 100W □ Deposit 500nm SiN with settings: 10min, 20 sec, using standard recipe at 300 °C **NOTE: Deposition rate is approx. 100nm/124sec**		
SPUTTER Ti/Au SEED LAYER: □ Sputter 200 Å Ti (Jason Hickey, AFRL/RY) □ Sputter 1,500 Å Au (Jason Hickey, AFRL/RY)		
AZ 9260 COAT: □ Clean wafer with acetone, methanol, IPS, and DIW (if needed) □ Bake 60 sec 110°C hot plate □ Dispense AZ 9260 - Cover 75% of wafer then spin on/off briefly to achieve 100% coverage □ Spin Settings: 4 sec spread at 300 rpm; 60 sec spin at 2,400 rpm - Use cotton swab stick to "cotton candy" the resist flying off the wafer) □ 5 min 110°C hot plate bake		
UV EXPOSURE: □ Expose wafer using Porous Mask 1 and EVG (100 sec)		
AZ 9260 DEVELOP: □ Mix AZ® 400K Developer 100 mL : 400 mL DI water □ Spin Wafer at 300 rpm and dispense developer for 180 sec □ Rinse with DI: 300 rpm, 20 sec □ Dry: 300 rpm, 30 sec. □ Inspect photoresist under microscope (develop longer if necessary)		
CLEAR PLATING CLIP AREAS: □ Use cotton swab w/acetone to ensure all photoresist is removed from the outer diameter of the wafer		
POST-BAKE: □ Bake in Oven for 20 min at 100 C		
ASHER DESCUM: □ 2 min, 75 W, O2 Asher:		
INSPECT AND MEASURE RESIST: □ Inspect/photograph photoresist under microscope □ Measure photoresist step height		
ELECTROPLATE: □ Plating conditions* □ Bath temp: 58.5°C □ Paddle Spacing: 0.25 in between flat surface of paddle handles □ Duty cycle: 40-on/60-off □ Average DC current: ______A □ Electroplate for ______A·min □ Rinse paddle in DIW for 10 min		
REMOVE AZ 9260: □ Rinse in acetone, methanol, IPA, and DIW for 30 sec at 500 rpm □ Dry with nitrogen at 500 rpm		
MEASURE ELECTROPLATING STEP HEIGHT: 3 O'clock Square: _____, _____, _____, _____, _____, _____, _____, _____ 6 O'clock Square: _____, _____, _____, _____, _____, _____, _____, _____ 9 O'clock Square: _____, _____, _____, _____, _____, _____, _____, _____ 12 O'clock Square: _____, _____, _____, _____, _____, _____, _____, _____		

A-2 Nanoporous Gold Fabrication Process Follower – Extreme Optimized Lithography

PROCESS STEPS	NOTES	DATE (TIME)
CLEAN SILICON WAFER WITH 1 μm SiO2: □ Rinse in acetone, methanol, IPA, and DIW for 30 sec at 500 rpm □ Dry with nitrogen on spinner at 500 rpm and on Texwipes		
EVAPORATE Ti/Au LAYER: □ Sputter 150 Å Ti (Jason Hickey, AFRL/RY) □ Sputter 1,500 Å Au (Jason Hickey, AFRL/RY)		
SF11 COAT: □ Clean wafer with acetone, methanol, IPA, and DIW (30 seconds each) □ Bake 60 sec 115°C hot plate □ Flood wafer with SF11 □ 30 sec spin at 4,000 rpm (Use cotton swab stick to "cotton candy" the resist flying off the wafer) □ 2 min 200°C hot plate bake		
1818 RESIST COAT □ Flood wafer with 1818 □ 4 sec spread at 500 rpm; 30 sec spin at 4,000 rpm (ramp = 200) □ 75 sec, 115°C hot plate bake		
1818 MASK OR DIRECT WRITE EXPOSURE □ Use EVG 1818 recipe with Mask 6 (N-1/N-2/N-3/N-4) and V+H Contact (7 second exposure, 1 μm separation, 1.53 mm thick mask, 500 μm thick wafer, 3 μm thick resist)		
1818 RESIST DEVELOP: □ 45 sec develop with 351:DI (1:5); submerge in petri dish with developer and agitate slightly; CAREFULLY SPRAY FRESH DEVELOPER ON PATTERNS! □ 30 sec DI water rinse at 500 rpm □ Dry with nitrogen at 500 rpm		
INSPECT RESIST: □ Inspect photoresist under microscope: Make sure pattern is correct		
SF-11 DUV EXPOSURE □ Place wafer in center of circle □ 300 sec DUV exposure		
SF-11 DEVELOP: □ 60 sec develop with SAL 101, submerge in petri dish with developer and agitate slightly; DO NOT SPRAY FRESH DEVELOPER DIRECTLY ON PATTERNS! □ 30 sec DI rinse at 500 rpm □ Dry with nitrogen at 500 rpm		
INSPECT SF11 PATTERN: □ Inspect photoresist under microscope □ Ensure complete removal of SF11 in non-pore areas (look for gray, spotty areas of residual SF11) □ If necessary repeat DUV exposure & development (100 sec exp / 60 sec dev)		
MEASURE RESIST STEP HEIGHT: Left-most Reticle: ________, ________, ________, ________ Right-Most Reticle: ________, ________, ________, ________		
PLASMA ASHER DESCUM: □ 4 min, 75 Watts		
METAL EVAPORATION: □ Evaporate 5,000 Å Au (Rich)		
LIFT-OFF METAL: □ Heat 1165 remover to 90°C (set hot plate to 140°C for 10 minutes) □ Use scotch tape to lift off evaporated Au □ 15 min soak in 1165 at 90°C □ Clean wafer with acetone, methanol, IPA, and DIW (30 seconds each) and dry with nitrogen		
PLASMA ASHER DESCUM: □ 4 min, 150 Watts		
MEASURE GOLD STEP HEIGHT: Left Evap Gold Cell: _____, _____, _____, _____, _____, _____, _____, _____ Right Evap Gold Cell: _____, _____, _____, _____, _____, _____, _____, _____		
INSPECT AND DICE WAFER: □ Inspect wafer using SEM □ Dice wafer into 1xEOP-1, 1xEOP-2, 1xEOP-3, 2xEvaporated, and 2xSputtered Samples		

A-3 Nanoporous Gold Fabrication Process Follower – Electron Beam Lithography

PROCESS STEPS	NOTES	DATE (TIME)
CLEAN SILICON WAFER WITH 1 μm SiO2: □ Rinse in acetone, methanol, IPA, and DIW for 30 sec at 500 rpm □ Dry with nitrogen on spinner at 500 rpm and on Texwipes		
EVAPORATE Ti/Au LAYER: □ Evaporate 150 Å Ti (Jason Hickey, AFRL/RY) □ Evaporate 1,500 Å Au (Jason Hickey, AFRL/RY)		
CLEAVE WAFER INTO SAMPLES: □ Use scribe to cleave wafer into 16 pieces □ Clean samples with acetone, methanol, IPA, and DIW for 30 sec at 500 rpm		
E-BEAM LITHOGRAPHY – DR. DENNIS WALKER (AFRL/RYDD) □ Spin-coat wafer piece with 300nm thick layer of "ma-N 2403" (negative-tone photoresist) using 4K rpm spin-speed □ Provide GDS design file to Dr. Walker □ Perform e-beam exposure with does setting of 150 μC/cm2 □ Develop "ma-N 2403" using Dr. Walker's procedures		
EVAPORATE Top Au LAYER: □ Evaporate 1,500 Å Au (Jason Hickey, AFRL/RY)		
LIFT-OFF METAL: □ Heat 1165 remover to 90°C (set hot plate to 140°C for 10 minutes) □ Immerse sample upside down in petri dish of acetone floating in ultrasonic bath for 1 minute □ While keeping wafer "wet" with acetone, place sample right-side up on wafer spinner; use acetone gun to spray wafer while sample is spinning at 500 rpm □ Place sample in 1165 at 90°C for 2 minutes □ Clean wafer with acetone, methanol, IPA, and DIW (30 seconds each) □ Dry with nitrogen at 500 rpm		
PLASMA ASHER DESCUM: □ 4 min, 150 Watts		
INSPECT/MEASURE NANOPORES: □ Inspect nano-pores using SEM □ Measure Pore Diameter: _________ □ Measure Pore Spacing: _________ □ Calculate Aspect Ratio (150nm/Diameter): _________ □ Calculate Porosity: _________ □ Assess pore pattern consistency: _________________________________ □ Assess pore shape: _________________________________		

A-4 Photolithography Mask Fabrication Process Follower

PROCESS STEPS	NOTES	DATE (TIME)
LOAD MASK DESIGN: □ Turn on the nitrogen supply line to the Heidelberg to be used □ Transfer the mask design (.cif) file to the appropriate Heidelberg (1-μm or 3-μm) computer If using the Automated Heidelberg Mask-Writing Program transfer all of the design (.cif) files and the automated program (.mcr) file to the appropriate file folder □ Verify the design is correct in Layout Editor □ Open the Heidelberg program and load the design (.cif) file (if using the Automated Heidelberg Mask-Writing Program load the first design (.cif) file to be written) □ Set mask writer to 8mW power with 90% duty cycle □ Load a mask blank (photoresist side up) and activate the mask-chuck vacuum □ If using the Automated Heidelberg Mask-Writing Program double click the .mcr file to being mask-writing; otherwise, check all settings and begin writing the mask file		
DEVELOP THE MASK: □ When program is complete, carefully remove the mask □ Shut down the Heidelberg software if no additional masks will be written □ Turn off the nitrogen supply line to the Heidelberg □ Submerge mask in develop solution (3:1 DI Water:351 Developer) with agitation for 30 sec) □ Rinse with DI Water for 30 sec □ Inspect for proper development using microscope		
ETCH THE MASK CHROME LAYER: □ Submerge the mask in CR44 chrome etchant for 80 sec with agitation □ Rinse with DI Water for 30 sec □ Inspect mask for etch completeness using microscope		
REMOVE MASK PHOTORESIST AND CLEAN □ Spray the mask with acetone for 30 sec □ Spray the mask with methanol for 30 sec □ Spray the mask with isoprpyl for 30 sec □ Spray the mask with DI Water for 30 sec □ Dry mask with nitrogen □ Perform a 5 min Oxygen plasma ash at 75W to remove any remaining photoresist residue		

Appendix B. Automated Heidelberg Mask-Writing Program

The need to pattern large areas of closely-space micro- and nano-pores drove the use of a previously developed Automated Heidelberg Mask-Writing program. This program was developed by Tod Laurvick and is discussed in Appendix E of his dissertation [119]. The following description is intended to provide the reader with an overview of how to use this program.

The first step is to lay out the individual pattern files so that the coordinate location of each pattern file can be determined. These coordinate locations are then entered into an Excel® file that contains the specific Heidelberg laser settings to be used during mask writing. Figure B-1 shows the layout of this Excel® file and how it maps to the layout of a 3-inch mask. Figure B-2 provides additional details on the specific input parameters of the Excel® file.

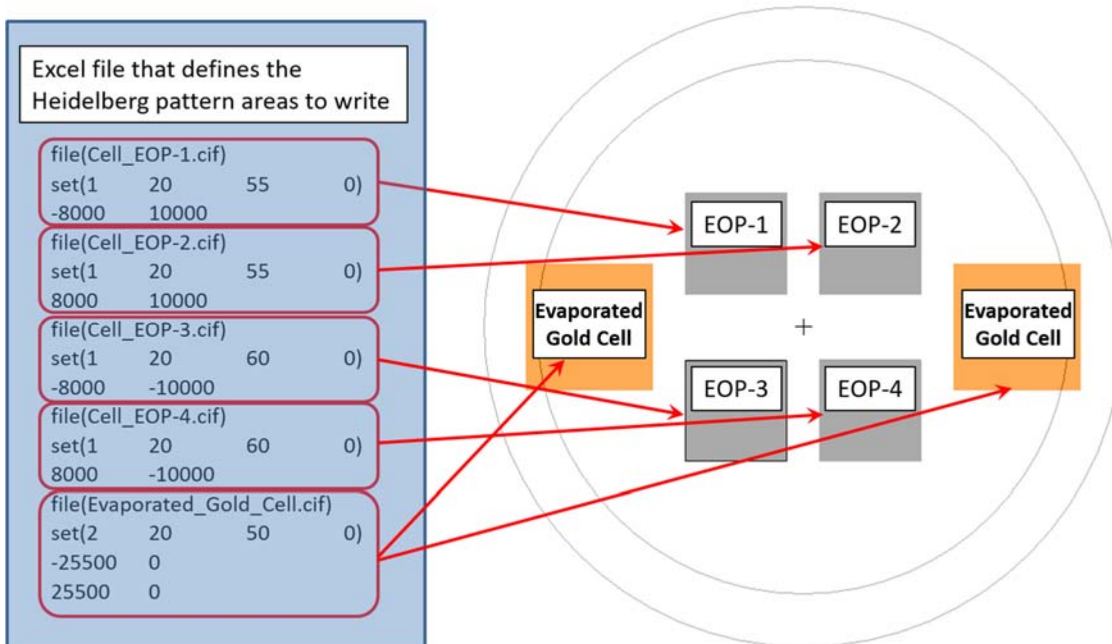

Figure B-1: Automated Heidelberg Mask-Writing Program Excel® file macro-layout.

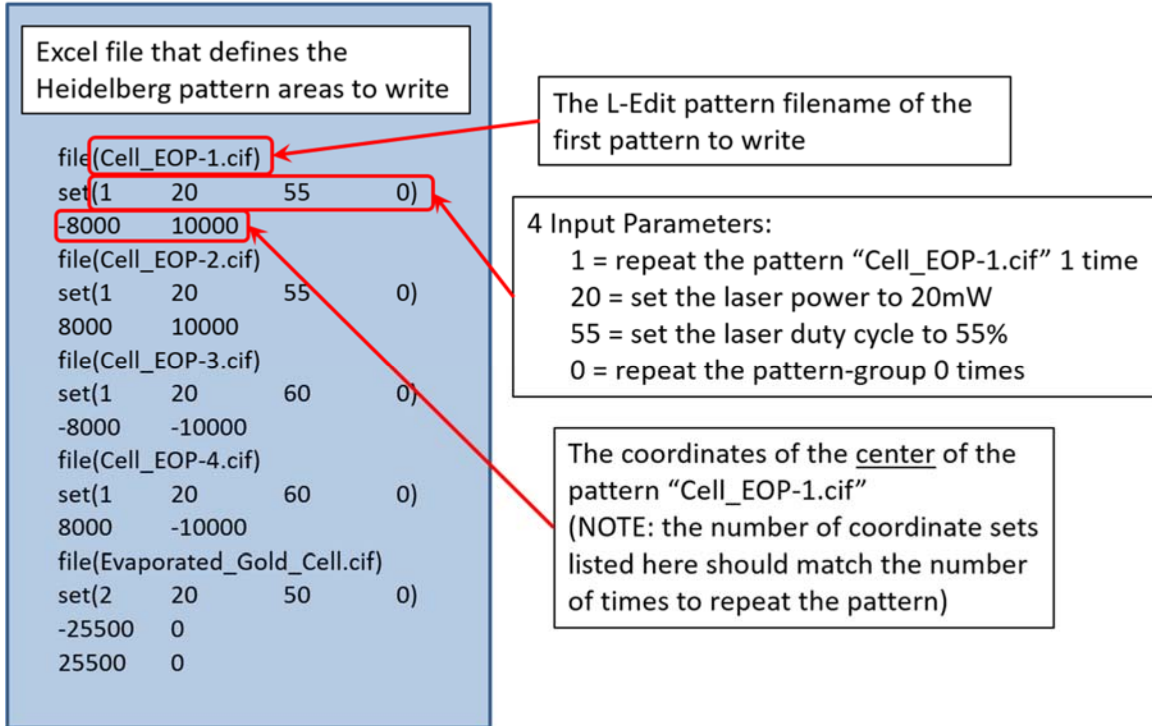

Figure B-2: Automated Heidelberg Mask-Writing Program Excel® file micro-layout.

Once the Excel® file has been created, it must be saved as a ".csv" file for use in a MATLAB® script that ultimately generates the Automated Heidelberg Mask-Writing program execution file. Once saved as a ".csv" file, the file should (1) be opened, (2) any commas that appear at the end of a line of text should be deleted, and (3) the file resaved. The MATLAB® script "ScriptBuild_From_file_v01.m" should then be run which will produce the input window shown in Figure B-3. The file locations should be set according to the appropriate locations on either the local computer running the MATLAB® script or the Heidelberg computer (see Figure B-3). After the MATLAB® script is run a new ".mcr" file is generated which is the command file that executes the Automated Heidelberg Mask-Writing program. The ".mcr" file and all of the ".cif" design files should be transferred to

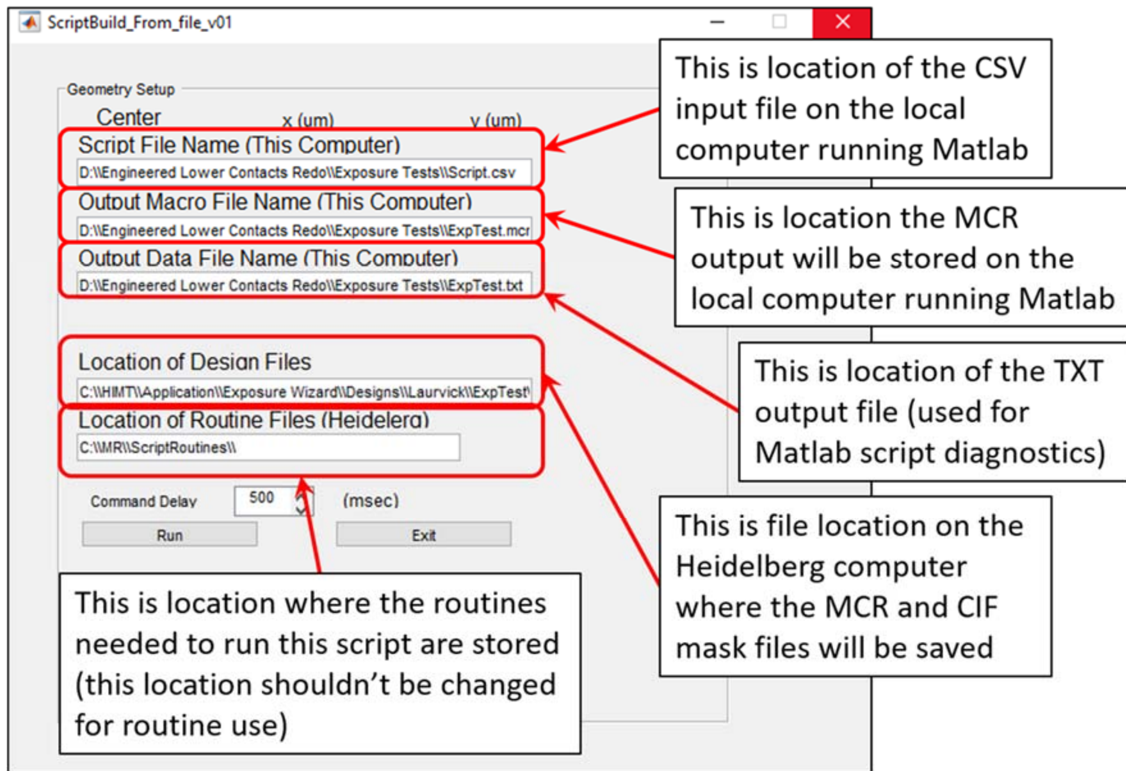

Figure B-3: Automated Heidelberg Mask-Writing Program MATLAB® input window.

the Heidelberg computer and saved in the appropriate file folder. The Heidelberg software should then be opened and one of the design ".cif" files loaded. A blank mask should then be placed on the vacuum chuck. The mask-writing process is initiated by double-clicking the ".mcr" file.

Appendix C. SEY Vacuum Chamber Procedures

NOTE: This chamber is best suited to remain under vacuum during non-use periods

<u>Day-to-Day Configuration:</u>

- Vacuum Pumps:
  - Sample Exchange Roughing Pump: **ON**
  - Main Chamber Roughing Pump: **ON**
  - Sample Exchange Turbo Pump: **ON**
  - Main Chamber Turbo Pump: **ON**

- Gate Valves:
  - Main Chamber Turbo Pump Gate Valve: **OPEN**
  - Sample Exchange Turbo Pump Gate Valve: **OPEN**
  - Sample Exchange/Main Chamber Gate Valve: **CLOSED**

- Roughing and Turbo-Backing Valves:
  - Sample Exchange Roughing Valve: **CLOSED**
  - Sample Exchange Turbo-Backing Valve: **OPEN**
  - Main Chamber Turbo-Backing Valve: **OPEN**

- Instrumentation:
  - Ion Gauges: **ON**
  - Electrometers: **OFF**
  - Electron Gun: **OFF**
  - Sample Manipulator Thermal Controller: **OFF**
  - Laptop/USB Camera: **OFF**
  - Vacuum Chamber LED Light: **OFF**

+++

<u>Sample Loading Procedures:</u>

1. Isolate Sample Exchange Chamber:
   a. Retract sample transfer arm from main chamber
   b. Close sample exchange/main chamber gate valve
   c. Close sample exchange turbo pump gate valve
      i. Leave sample exchange turbo-backing valve open
      ii. Leave sample exchange roughing valve closed

DO NOT PROCEED UNLESS SAMPLE EXCHANGE TURBO PUMP GATE IS CLOSED

2. Vent Sample Exchange Chamber:
    a. Turn off IG1 ion gauge
    b. Turn on main N_2 supply line located on the wall opposite SEY measurement stand
    c. Slowly open green N_2 knob connected to sample exchange chamber
    d. Wait 10-20 seconds until sample exchange chamber lid is rattling
    e. Reduce N_2 to a trickle

3. Load Sample:
    a. Remove sample puck from sample transfer arm fork using a **CLEAN** gloved hand
    b. Place sample on puck and secure using tabs
    c. Re-load sample puck into transfer arm fork using a **CLEAN** gloved hand
    d. Close sample exchange chamber lid
    e. Turn off main N_2 supply line located on the wall opposite SEY measurement stand
    f. Close green N_2 knob

4. Pump Down Sample Exchange Chamber:
    a. Close sample exchange turbo-backing valve
    b. Open sample exchange roughing valve
    c. Wait for sample exchange to pump down to $1x10^{-3}$ Torr (IG1 readout will go blank because the pressure dropped below the convection gauge's capability)
    d. Close sample exchange roughing valve
    e. Open sample exchange turbo-backing valve
    f. Wait 2-3 minutes
    g. Open sample exchange turbo pump gate valve
    h. Turn on IG1 ion gauge
    i. Wait for sample exchange chamber pressure to be within an order of magnitude of the main chamber (~30 min)

5. Transfer Sample Puck to Main Chamber Sample Manipulator:
    a. Open sample exchange/main chamber gate valve
    b. Carefully extend transfer arm into main chamber and align directly over sample manipulator basket
    c. Slowly raise the sample manipulator basket until puck is seated in basket (see photos on next page)
    d. Slowly retract transfer arm/fork making sure sample puck remains seated in manipulator basket
    e. Close sample exchange/main chamber gate valve

++

Sample Unloading Procedures:

1. Retract Sample Puck:
    a. Ensure sample exchange chamber pressure is within an order of magnitude of the main chamber
    b. Open sample exchange/main chamber gate valve
    c. Carefully extend transfer arm into main chamber to capture the sample puck in the manipulator basket
    d. Slowly lower the sample manipulator basket until the puck is no longer seated in basket
    e. Carefully retract sample transfer arm/fork/puck from main chamber

2. Isolate Sample Exchange Chamber:
    a. Close sample exchange/main chamber gate valve
    b. Close sample exchange turbo pump gate valve
        i. Leave sample exchange turbo-backing valve open
        ii. Leave sample exchange roughing valve closed

DO NOT PROCEED UNLESS SAMPLE EXCHANGE TURBO PUMP GATE IS CLOSED

3. Vent Sample Exchange Chamber:
    a. Turn off IG1 ion gauge
    b. Turn on main N_2 supply line located on the wall opposite SEY measurement stand
    c. Slowly open green N_2 knob connected to sample exchange chamber
    d. Wait 10-20 seconds until sample exchange chamber lid is rattling
    e. Reduce N_2 to a trickle

4. Unload Sample:
    a. Remove sample puck from sample transfer arm fork using a **CLEAN** gloved hand
    b. If not loading a new sample, return empty puck to transfer fork using a **CLEAN** gloved hand
    c. Close sample exchange chamber lid
    d. Turn off main N_2 supply line located on the wall opposite SEY measurement stand
    e. Close green N_2 knob

5. Pump Down Sample Exchange Chamber:
    a. Close sample exchange turbo-backing valve
    b. Open sample exchange roughing valve
    c. Wait for sample exchange to pump down to $1x10^{-3}$ Torr (IG1 readout will go blank because the pressure drops below the convection gauge's capability)

d. Close sample exchange roughing valve
e. Open sample exchange turbo-backing valve
f. Wait 2-3 minutes
g. Open sample exchange turbo pump gate valve
h. Turn on IG1 ion gauge

+++

Vacuum Chamber Shutdown Procedures (for maintenance or long-term storage):

1. Turn Off All Gauges and Instrumentation:
    a. Ion Gauges: **OFF**
    b. Electrometers: **OFF**
    c. Electron Gun: **OFF**
    d. Sample Manipulator Thermal Controller: **OFF**
    e. Laptop/USB Camera: **OFF**
    f. Vacuum Chamber LED Light: **OFF**

2. Isolate All Vacuum Chambers:
    a. Close sample exchange/main chamber gate valve
    b. Close sample exchange turbo pump gate valve
    c. Close main chamber turbo pump gate valve
    d. Ensure sample exchange roughing valve is closed

3. Shut Down Vacuum Pumps:
    a. Unplug sample exchange turbo pump
    b. Unplug main chamber turbo pump
    c. Close sample exchange turbo-backing valve
    d. Turn off sample exchange roughing pump
    e. Close main chamber turbo-backing valve
    f. Turn off main chamber roughing pump

Appendix D. SEY Measurement Procedures

NOTE: These procedures assume that the main chamber pressure is < 1.0×10^{-8} Torr and a sample has already been loaded onto the sample manipulator and centered under the e-gun.

1. Turn on both electrometers to let them warm up. Set the electrometers to read current with auto range enabled. NOTE: ideally, both electrometers should be turned on at least 1 hour prior to data collection.
2. Turn on the electron gun (e-gun). NOTE: ideally, the e-gun power supply should be turned on at least 1 hour prior to data collection.
    a. Check all the e-gun cables, ensuring that they are connected securely to the appropriate location.
    b. Turn on the main power to the e-gun power supply (green switch).
    c. Turn on the high voltage to the e-gun power supply (red switch).
    d. Wait to program the e-gun settings.
3. Minimize the sample working distance by raising the sample to the highest possible position using the vertical micrometer on the sample manipulator.
4. Connect the sample bias battery box (see Figure 78).
    a. Test the batteries to ensure the bias is -27V. Use a 360Ω resistor connected in series between a multimeter lead and a terminal of the battery box. Connect the other multimeter lead to the other terminal on the battery box. The multimeter, set to read current in mA, should read 7.5mA for fully charged batteries.
    b. Connect the battery box terminals to the sample manipulator and the sample current electrometer.

5. Record the main chamber pressure then turn off the main chamber ion gauge to prevent it from emitting electrons that could skew the SEY measurements.
6. On the laptop, double-click the LabVIEW® file, "Keithley 6514 SEY Program" located on the desktop. This will open up the interface shown in Figure D-1. Select the I/O address for the Faraday cup and Sample Current electrometers and set the "Data Log Path" to the desired file folder location where the output text files will be saved. Then click the "Run" button at the top of the LabVIEW® window to execute the program. The program will begin by prompting the user to input the electron beam energy. Enter the e-beam energy and hit "enter." The program will then instruct the user to rotate the Faraday cup in-line with the e-beam. After ensuring the Faraday cup is rotated in-line with the e-gun tip, the user should lock the Faraday cup in position and then proceed to step 7. DO NOT hit "enter" a second time.

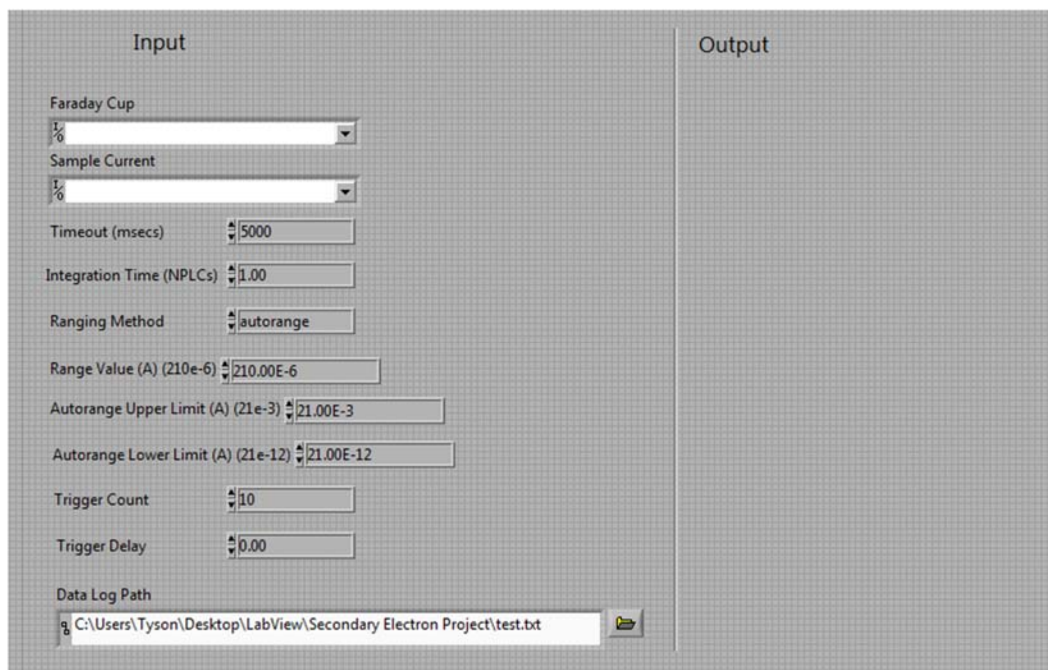

Figure D-1: Screenshot of the SEY measurement LabVIEW® data collection interface.

7. Set the remaining e-gun settings:
   a. Set the e-gun to provide low beam current.
   b. Set the e-gun "ENERGY" to 2keV
   c. Set the e-gun "GRID" to 20V, the "1st ANODE" to 200V, and the "FOCUS" to 700V (see Table 8).
   d. Set the e-gun "SOURCE" to 0.5V and observe the cathode voltage slowly rise to 0.5V. Once the cathode has reached 0.5V, set the "SOURCE" to 0.9V and observe the cathode voltage rise to 0.9V. Once the cathode has reached 0.9V, set the "SOURCE" to 0.95V and observe the Faraday cup Current on the appropriate electrometer. Adjust the "SOURCE" voltage so that the Faraday cup current is ~20nA.
   e. Record the e-gun settings and start time in the user's logbook.
8. With the e-beam on and the Faraday cup electrometer reading the e-beam current, the user should return to the LabVIEW® program and click on the button "Measure e-beam current!"
9. Once LabVIEW® has recorded the e-beam (Faraday cup) current, the program will prompt the user to rotate the Faraday cup out of the e-beam. Once completed, the user should click the LabVIEW® button "Measure sample current!"
10. Once LabVIEW® has recorded the sample current, the program will ask the user "Would you like to take another SEY measurement?" The user should quickly rotate the Faraday cup back in-line with the e-gun tip to minimize sample irradiation. The user should then click "Yes" to continue recording SEY measurements.

11. The user should now adjust the e-gun settings according to the values supplied in Table 8 and repeat the procedure for the new energy.
12. Once the measurements are complete, the Faraday cup should be rotated in-line with the e-gun tip and the user should press the button labeled "SHUTDOWN" on the e-gun power supply. Once all the display values on the e-gun power supply read zero, the user should turn off the high voltage switch and then the power switch on the e-gun power supply.
13. Record the e-gun stop time in the user's logbook.
14. Isolate the battery box by disconnecting it from the sample manipulator.
15. Turn on the main chamber vacuum ion gauge.

Appendix E. SEY Chamber Bakeout Procedures

Any time the main UHV chamber on SEY measurement system is vented, a 180-190°C bakeout becomes necessary to remove the condensates that become deposited on the inner walls of the main vacuum chamber. This bakeout should be performed continuously for 5-7 days to allow the chamber enough time to "bake out" the condensates so they can be removed by the main chamber's turbopump. This process should be performed with great care because of the fire hazard it poses when not attended (i.e. at nighttime). Additionally, the user should take precautions to ensure that the bakeout temperature does not exceed 200°C (the limit for both the sample manipulator and the e-gun). Figures E-1 through E-3 provide a photographic example of how the heater tapes can be wrapped around the chamber to provide the most

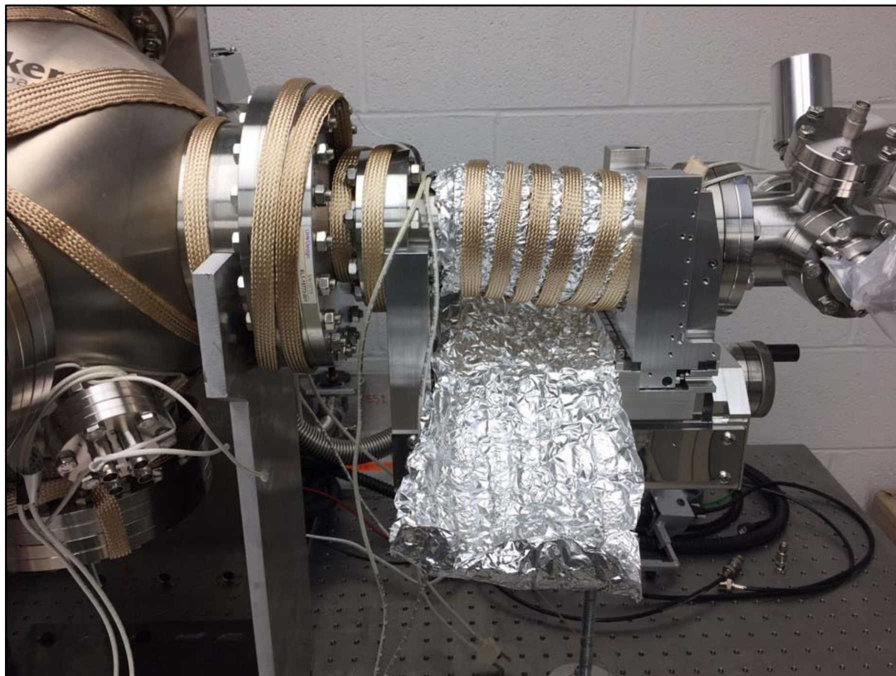

Figure E-1: Vacuum bakeout heater tape arrangement for the sample manipulator.

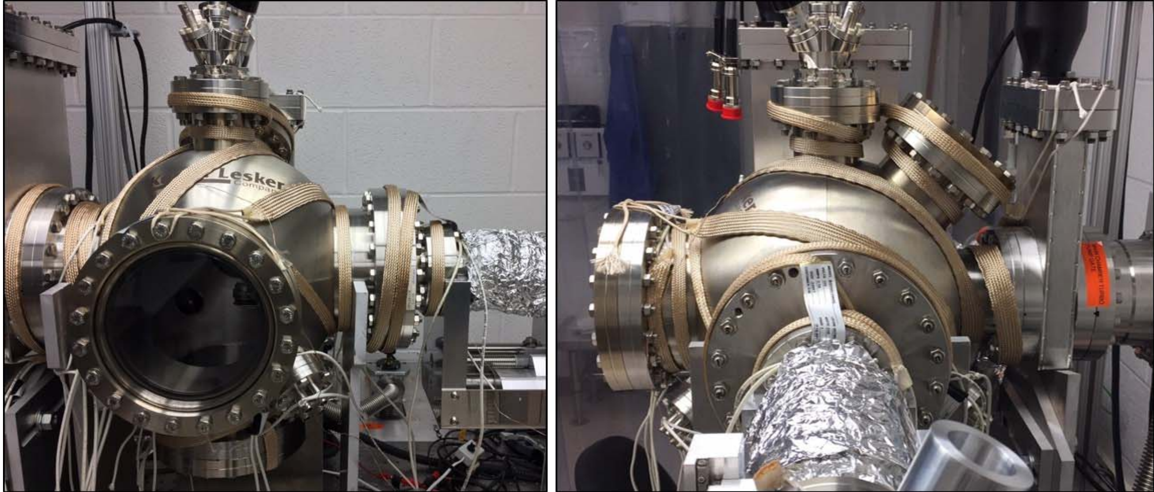

Figure E-2: Vacuum bakeout heater tape arrangement for the main UHV chamber.

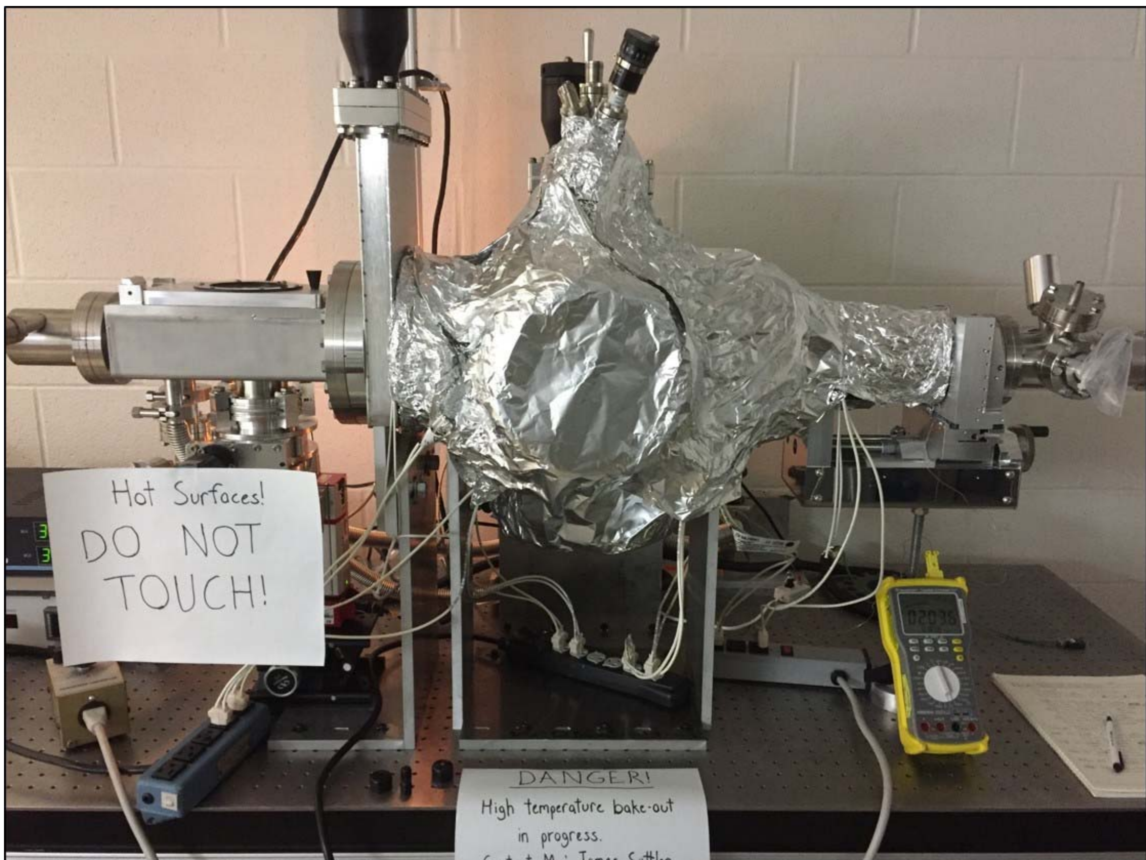

Figure E-3: Final vacuum bakeout setup using two thermocouple sensors (one on the manipulator bellows and one on the main chamber) and three voltage duty cycle controllers connected to three surge protectors.

uniform heat distribution possible with these heater tapes. Uniform heating is important because condensates that a “baked off” from a high temperature surface will tend to migrate to any local cooler surfaces where they will become redeposited and remain until that cooler surface temperature is raised (which generally will not happen during a bakeout). Uniform surface heating helps ensure that the condensates do not redeposit on an interior chamber surface before being swept out of the chamber by the main turbopump.

A total of 8 heater tapes were used in the bakeout. Because these tapes draw a large amount of current, care must be taken to avoid exceeding the current-rating of the laboratory’s outlets. The heater tapes were divided into 3 groups corresponding to the 3 voltage duty cycle controllers that limited the amount of time the heater tapes were energized. The multimeter shown in Figure E-3 was used in conjunction with two thermocouples to monitor the UHV chamber surface temperature in two locations: the sample manipulator bellows and the main chamber. The voltage duty cycle controllers were manually adjusted to maintain a chamber surface temperature of 180-190°C. Finally, the user should ensure that the sample exchange/main chamber gate valve is closed throughout the bakeout process.

During the first day of the bakeout, the user should perform frequent checks to “dial in” the voltage duty cycle controllers so that the chamber temperature reaches 180-190°C. Before allowing the bakeout setup to operate overnight, the user should have already been performing the bakeout for 8-10 hours to ensure correct operation. The user should also turn down the voltage duty cycle controllers a few percent before leaving for the evening to ensure the temperature does not “run-away” overnight.

Appendix F. SIMION® Tutorial

SIMION® is particle trajectory simulator that can incorporate electric fields. Kimball Physics, the manufacturer of the electron gun incorporated in the new AFIT SEY measurement system, has provided a SIMION® model of their ELG-2 electron gun. This model allows the user to specify the ELG-2 settings (electron energy, grid voltage, anode voltage, focus, and beam current) and the gun-sample working distance. The user can perform a single e-gun trajectory simulation or specify a series of simulations where the focus is adjusted incrementally. AFIT has purchased a single computer license of SIMION® 8.1 that was installed on the HP Elitebook® 8560w used for SEY measurement data recording (See Figure F-1).

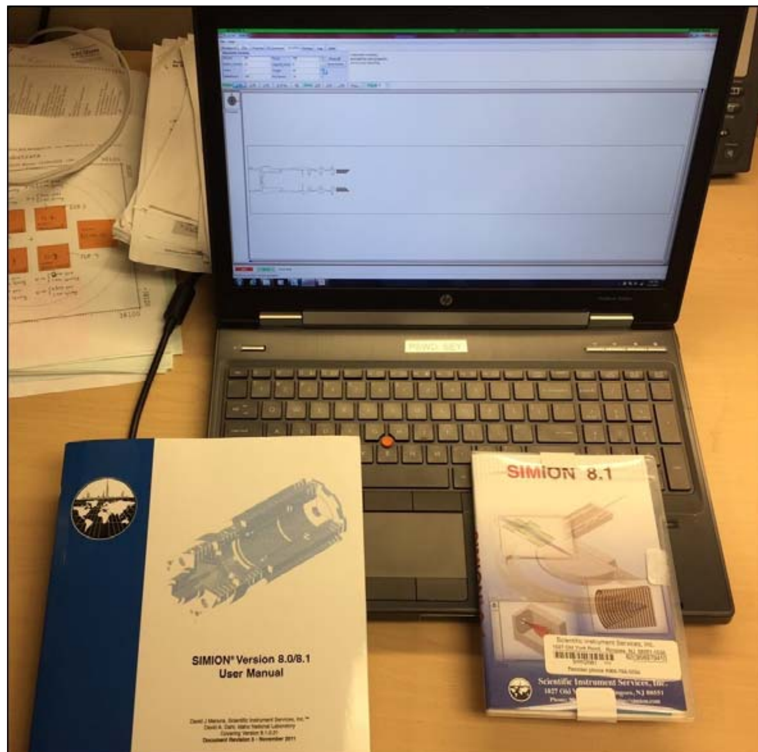

Figure F-1: Photo of SIMION® 8.1 software install disc, user manual, and laptop of installation.

The following procedure is intended to help a new user be able to perform basic simulations of the AFIT SEY measurement system electron gun using the SIMION® ELG-2 model provided by Kimball Physics.

1. Double-click the “SIMION® 8.1” icon located on the desktop of the HP laptop. This will bring up a welcome screen – click “OK”. The user should now see the SIMION® window shown in Figure F-2.

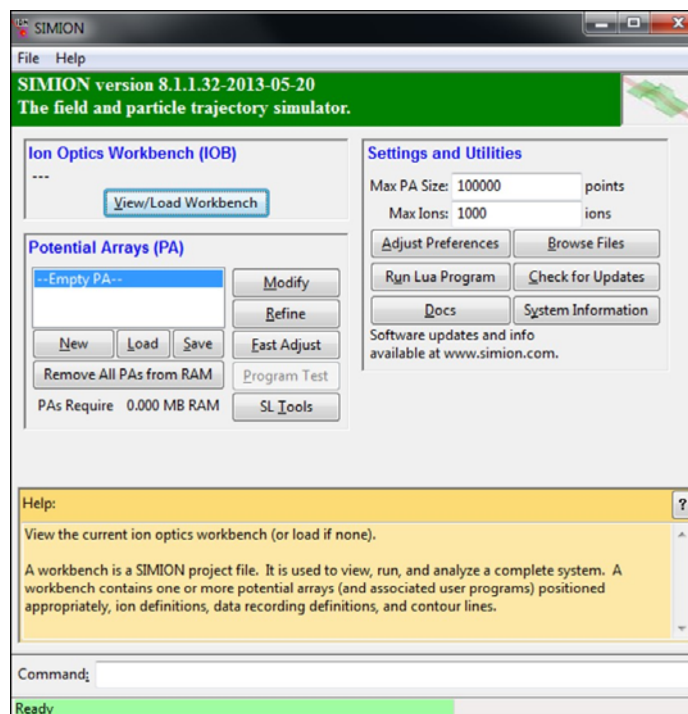

Figure F-2: Screenshot of initial SIMION® 8.1 command window.

2. In the upper left of this window under the title “Ion Optics Workbench (IOB)” click on “View/Load Workbench” and select the file “ELG2.iob” that resides in “SIMION 8.1\ELG2_SIMION” folder. The user should now see the SIMION® window shown in Figure F-3, which is a view of the e-gun model in the x-y plane where x is the horizontal axis and y is the vertical axis.

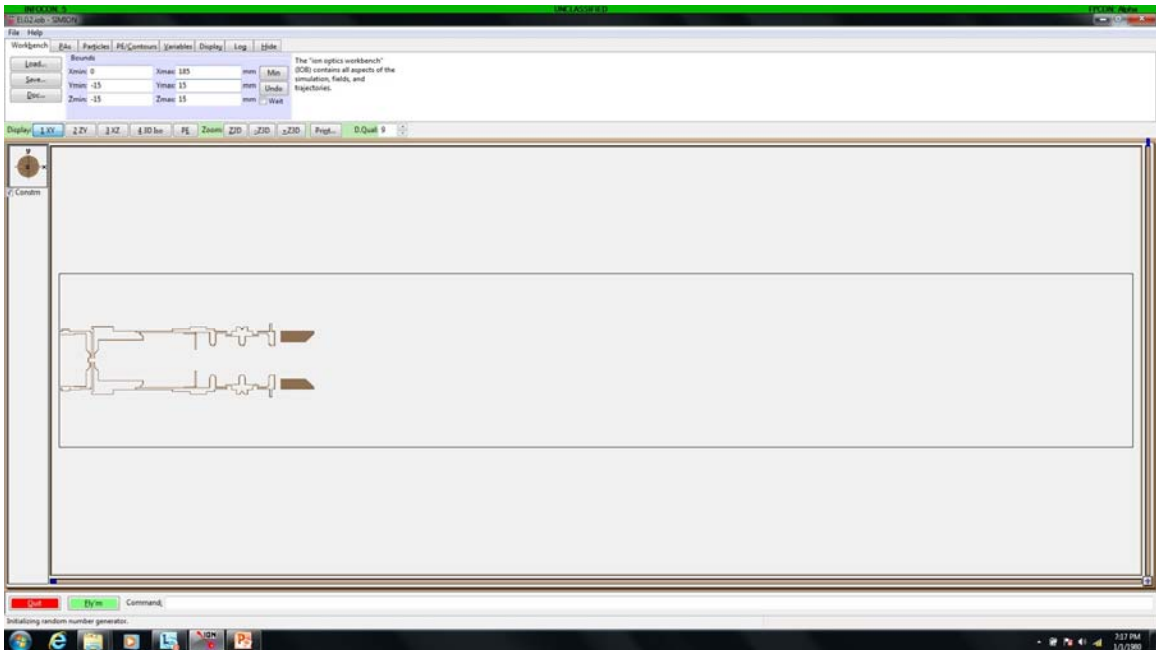

Figure F-3: Screenshot of SIMION® 8.1 window after loading the ELG2.iob file.

3. Adjust the “D.Qual” setting to 9 as shown in Figure F-4.

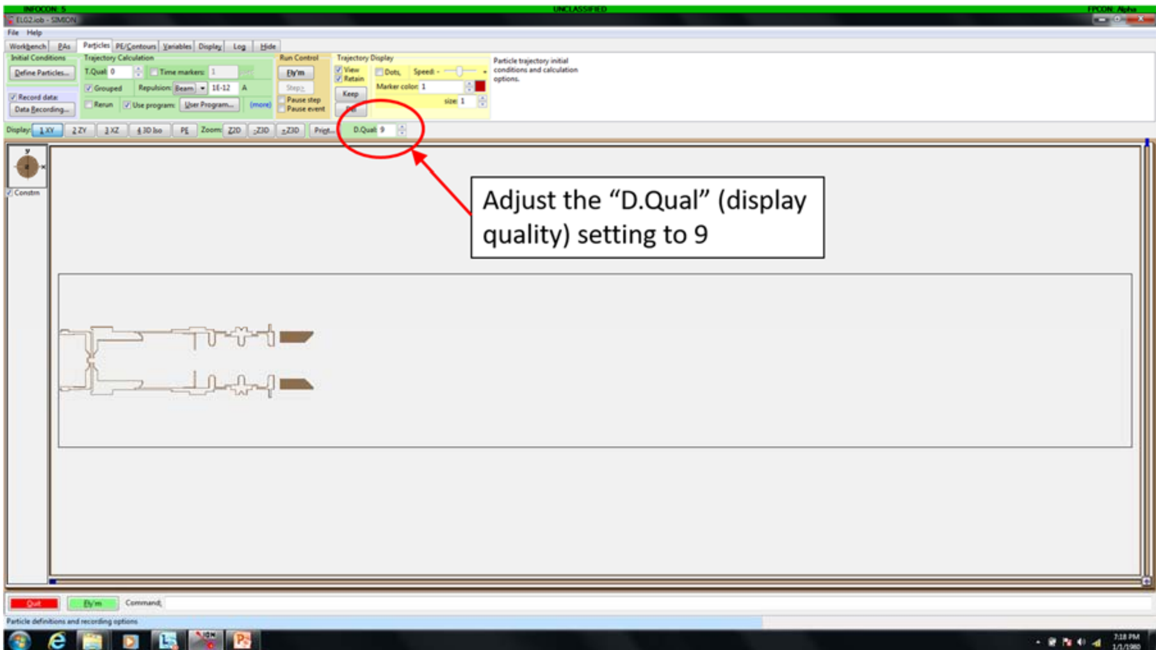

Figure F-4: Location of “D.Qual” (display quality) setting.

4. Under the “Particles” tab, check the box for “Grouped” particles and select “Beam” for the “Repulsion” setting as shown in Figure F-5.

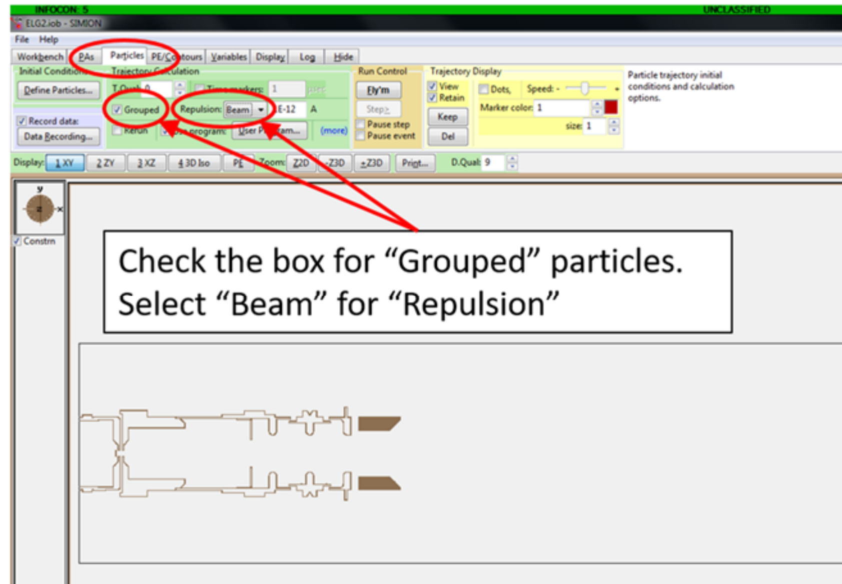

Figure F-5: Location of “Grouped” particles checkbox and “Repulsion” setting.

5. Under the “Variables” tab set the parameters for “Cathode” (electron energy), “Grid”, “Anode”, “Focus”, and “Beam Current” (see Figure F-6).

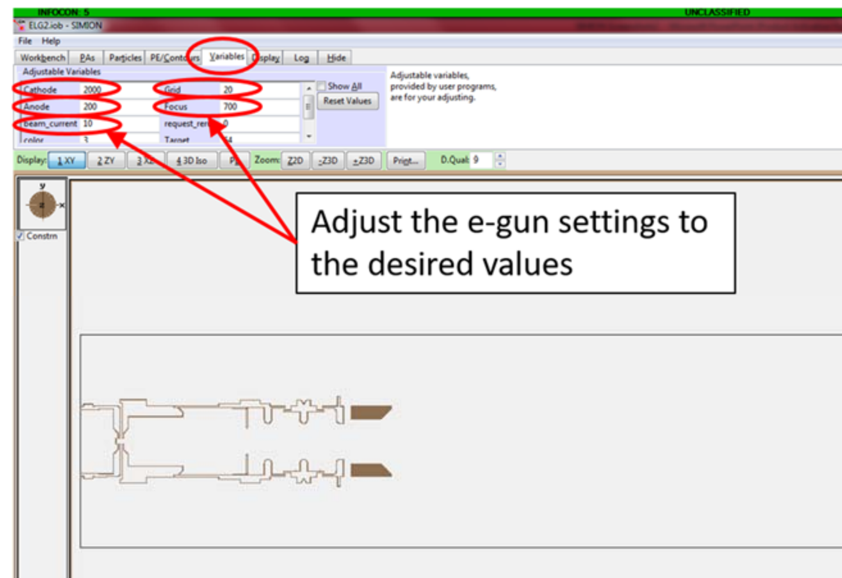

Figure F-6: Location of e-gun settings (cathode, grid, anode, focus, and beam current).

6. Note the location of the mouse curser, when it is located in the main model window, provides coordinates that are displayed at the bottom left of the SIMION® window (see Figure F-7). These coordinates are needed to determine the position of the gun-tip (i.e. the location where the electrons are free of the e-gun's influence). For this model, the position of the e-gun tip is at x = 44 mm.

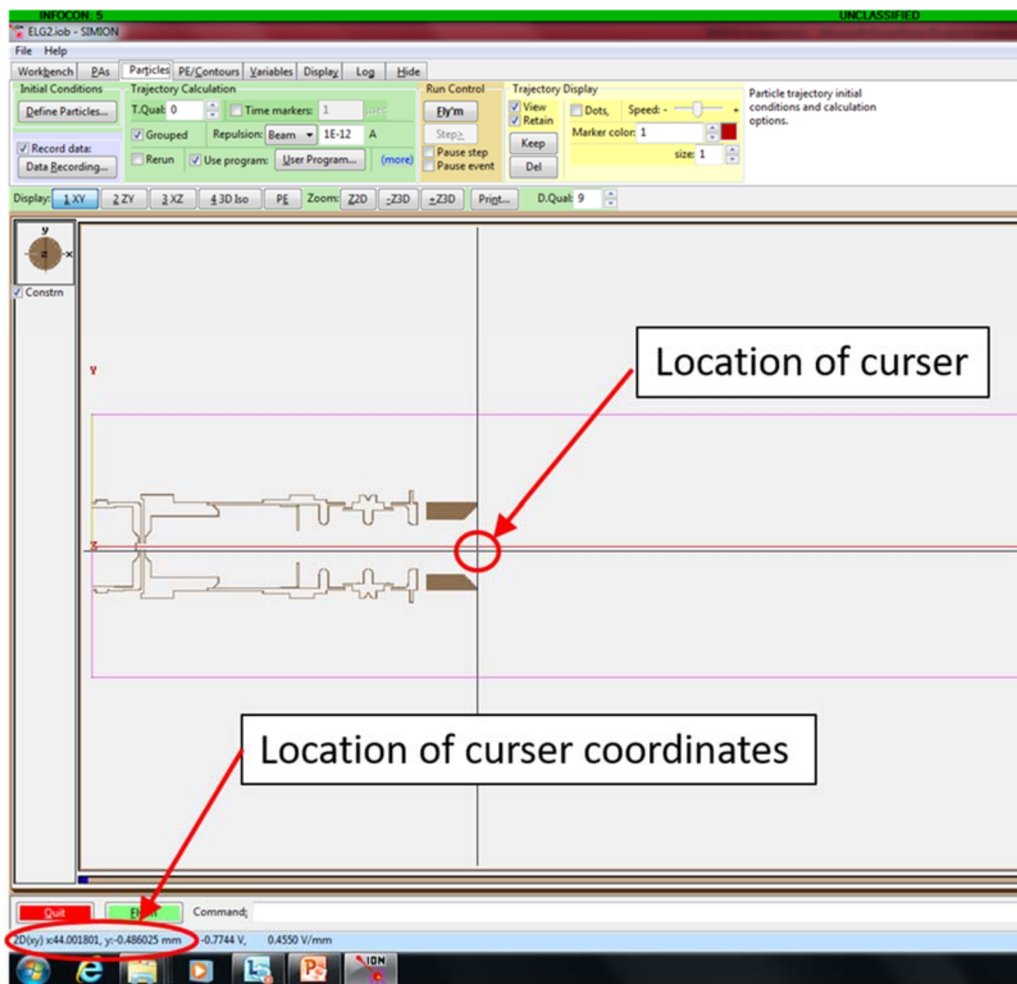

Figure F-7: Location of model coordinates based on curser position.

7. Set the working distance by setting the “Target” parameter to be the sum of the e-gun tip location (44 mm) and the desired working distance (20 mm for the AFIT SEY measurement system). Thus, for the AFIT SEY measurement system, “Target” should be set to 64 as shown in Figure F-8.

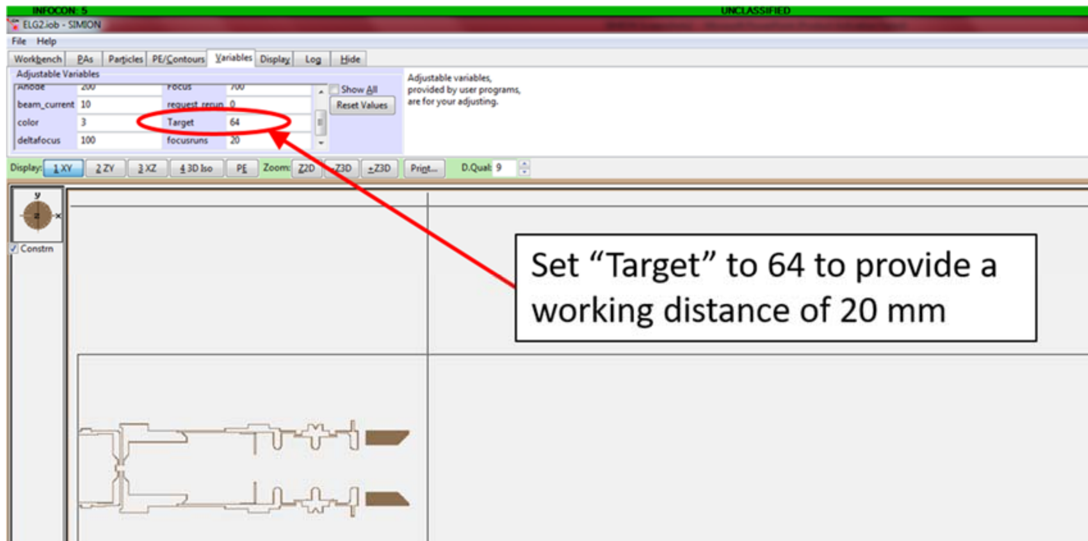

Figure F-8: Location of “Target” setting used to define the working distance.

8. Once the desired e-gun settings have been specified, click “Fly’m at the bottom left of the screen to initiate the simulation.

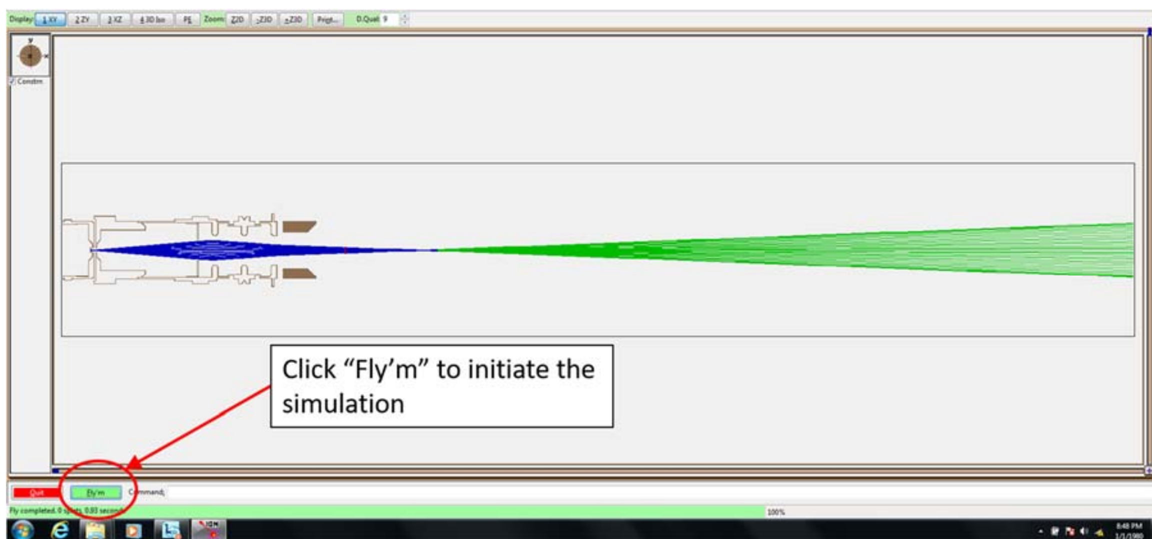

Figure F-9: Location of “Fly’m” button to initiate the simulation.

9. An output file with filename “ELG2data.txt” is generated when the simulation is completed. The file contains the e-gun settings and the beam spot diameter at the working distance specified. NOTE: a quirk with this software is that the output file is only updated after a subsequent simulation run. In other words, you have to click on “Fly’m” twice in order to see the results from the first simulation.
10. To determine optimal ELG-2 settings that minimize spot diameter, an automated series of simulations is possible for various values of beam focus. This is enabled by performing the following actions under the “Variables” tab (see Figure F-10):
    a. Setting the “request_rerun” parameter to a non-zero value.
    b. Setting the “deltafocus” parameter to the desired focus increment
    c. Setting the “focusruns” parameter to the number of simulations to perform (i.e. the number of different focus values to simulate)

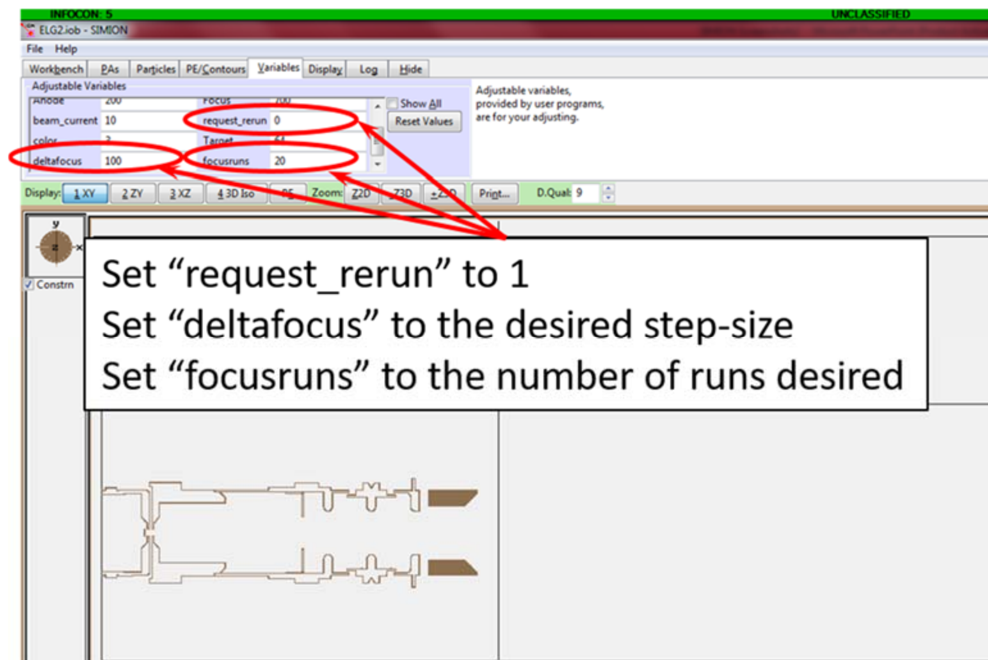

Figure F-10: Location of settings to provide an automated series of simulations over a variety of different e-gun focus values.

Appendix G. MATLAB® Code

This appendix contains the MATLAB® code that was used to study the 2D and 3D porous surface SEY models and provide the plots for Figures 26, 27, 28, and 29.

```
% Description: MATLAB scipts used to study the 2D and 3D Porous Surface
Secondary Electron Yield Models
% Author: James Sattler
% Dates: Developed over 2016 and 2017


%%%%%%%%%%%%%%%%%%%%%%%%%%%%%%%%%%%%%%%%%%%%%%%%%%%%%%%%%%%%%%%%%%%%%%%%%%
% Plot Pescape_2D vs. Porosity
clear all;
close all;
clc;

SEY_nonpore = 1.7;
SEY_porebottom = 1.6;
AR1 = 0;
AR2 = 0.1;
AR3 = 1;
AR4 = 10;
AR5 = 100;
Porosity = linspace(0,1,101); %Indpt Variable

Pescape_2D_1 = (1/2)*sin(atan(3./(4*AR1))) +
(1/2)*sin(atan(1./(4*AR1)));
Pescape_2D_2 = (1/2)*sin(atan(3./(4*AR2))) +
(1/2)*sin(atan(1./(4*AR2)));
Pescape_2D_3 = (1/2)*sin(atan(3./(4*AR3))) +
(1/2)*sin(atan(1./(4*AR3)));
Pescape_2D_4 = (1/2)*sin(atan(3./(4*AR4))) +
(1/2)*sin(atan(1./(4*AR4)));
Pescape_2D_5 = (1/2)*sin(atan(3./(4*AR5))) +
(1/2)*sin(atan(1./(4*AR5)));

SEY_surface1 = SEY_nonpore*(1-Porosity) +
SEY_porebottom*Pescape_2D_1*Porosity;
SEY_surface2 = SEY_nonpore*(1-Porosity) +
SEY_porebottom*Pescape_2D_2*Porosity;
SEY_surface3 = SEY_nonpore*(1-Porosity) +
SEY_porebottom*Pescape_2D_3*Porosity;
SEY_surface4 = SEY_nonpore*(1-Porosity) +
SEY_porebottom*Pescape_2D_4*Porosity;
SEY_surface5 = SEY_nonpore*(1-Porosity) +
SEY_porebottom*Pescape_2D_5*Porosity;
```

```
figure
plot(Porosity,SEY_surface1,'k-','LineWidth',2)
ylim([0 2])
grid on
hold on
plot(Porosity,SEY_surface2,'c-','LineWidth',2)
plot(Porosity,SEY_surface3,'g-','LineWidth',2)
plot(Porosity,SEY_surface4,'b-','LineWidth',2)
plot(Porosity,SEY_surface5,'r-','LineWidth',2)
xlabel('Porosity','fontweight','bold','FontSize',16)
set(gca,'FontWeight','bold')
ylabel('\sigma_{porous-surface}','fontweight','bold','FontSize',16)
set(gca,'FontWeight','bold')
legend('Aspect Ratio = 0','Aspect Ratio = 0.1','Aspect Ratio =
1','Aspect Ratio = 10','Aspect Ratio =
100','fontweight','bold','Location','southwest')
set(gca,'XTick',0:0.2:1)
set(gca,'YTick',0:0.5:2)


%%%%%%%%%%%%%%%%%%%%%%%%%%%%%%%%%%%%%%%%%%%%%%%%%%%%%%%%%%%%%%%%%%%%%%%%%
% Plot Pescape_2D vs. Aspect Ratio
clear all;
close all;
clc;

SEY_nonpore = 1.7;
SEY_porebottom = 1.6;
AR = linspace(0,10,101); %Indpt Variable
Porosity1 = 0;
Porosity2 = 0.1;
Porosity3 = 0.5;
Porosity4 = 0.785;

Pescape_2D = (1/2)*sin(atan(3./(4*AR))) + (1/2)*sin(atan(1./(4*AR)));

SEY_surface1 = SEY_nonpore*(1-Porosity1) +
SEY_porebottom*Pescape_2D*Porosity1;
SEY_surface2 = SEY_nonpore*(1-Porosity2) +
SEY_porebottom*Pescape_2D*Porosity2;
SEY_surface3 = SEY_nonpore*(1-Porosity3) +
SEY_porebottom*Pescape_2D*Porosity3;
SEY_surface4 = SEY_nonpore*(1-Porosity4) +
SEY_porebottom*Pescape_2D*Porosity4;

figure
plot(AR,SEY_surface1,'k-','LineWidth',2)
ylim([0 2])
grid on
hold on
plot(AR,SEY_surface2,'r-','LineWidth',2)
plot(AR,SEY_surface3,'g-','LineWidth',2)
plot(AR,SEY_surface4,'b-','LineWidth',2)
xlabel('Aspect Ratio','fontweight','bold','FontSize',16)
```

```
set(gca,'FontWeight','bold')
ylabel('\sigma_{porous-surface}','fontweight','bold','FontSize',16)
set(gca,'FontWeight','bold')
legend('Porosity = 0','Porosity = 0.1','Porosity = 0.5','Porosity =
0.785','fontweight','bold','Location','southwest')
set(gca,'XTick',0:2:10)
set(gca,'YTick',0:0.5:2)


%%%%%%%%%%%%%%%%%%%%%%%%%%%%%%%%%%%%%%%%%%%%%%%%%%%%%%%%%%%%%%%%%%%%%%
% Surface Plot of Pescape_2D vs. Porosity and Aspect Ratio
clear all;
close all;
clc;

SEY_nonpore = 1.7;
SEY_porebottom = 1.6;
NumPts = 101;
Half_Num_Pts = (NumPts-1)/2 + 1;
ARmax = 10;
AR = linspace(0.01,ARmax,NumPts); %Indpt Variable
Porosity = linspace(0,1,NumPts); %Indpt Variable

%Compute Pescape_2D
Pescape_2D = (1/2)*sin(atan(3./(4.*AR))) + (1/2)*sin(atan(1./(4.*AR)));

%Compute Pescape_2D
for i = 1:NumPts
    for j = 1:NumPts
        SEY_surface(i,j) = SEY_nonpore*(1-Porosity(j)) +
SEY_porebottom*Pescape_2D(i)*Porosity(j);
    end
end

surf(Porosity, AR, SEY_surface);
xlabel('Porosity')
ylabel('Aspect Ratio')
zlabel('\sigma_{porous-surface}','fontweight','bold','FontSize',16)
set(gca,'XLim', [0 1])
set(gca,'YLim', [0 ARmax])
set(gca,'ZLim', [0 2])
set(gca,'XTick',0:0.2:1)
set(gca,'YTick',0:2:ARmax)
set(gca,'ZTick',0:0.25:2)


%%%%%%%%%%%%%%%%%%%%%%%%%%%%%%%%%%%%%%%%%%%%%%%%%%%%%%%%%%%%%%%%%%%%%%%
% Plot the distribution of r for the 3D pore model
clear all;
close all;
clc;

R = 1;
r = linspace(0,R,101); %Indpt Variable
```

```
r_distribution = (2*r)/(R^2);

figure
plot(r,r_distribution,'k-','LineWidth',2)
set(gca,'YLim', [0 2*R])
xlabel('r')
ylabel('distribution of r')

Integral_r_distribution = (trapz(r,r_distribution))

%%%%%%%%%%%%%%%%%%%%%%%%%%%%%%%%%%%%%%%%%%%%%%%%%%%%%%%%%%%%%%%%%%%%%%%%%
% Plot Pescape_3D vs phi for a given Aspect Ratio, assume r = R/sqrt(2)
clear all;
close all;
clc;

AR = 5;
phi = linspace(0,2*pi,101); %Indpt Variable

Pescape_3D = sin(atan((sqrt(1+(cos(phi)).^2) -
cos(phi))/(2*AR*sqrt(2))));

%Compute the upper/lower bounds and average of Pescape_3D
Pescape_min = Pescape_3D(1)
Pescape_max = Pescape_3D(51)
Pescape_3D_Avg = mean(Pescape_3D)

%Compute Pescape_2D for comparison
Pescape_2D = (1/2)*sin(atan((2+sqrt(2))/(4*AR))) + (1/2)*sin(atan((2-
sqrt(2))/(4*AR)))

figure
plot(phi,Pescape_3D,'k-','LineWidth',2)
xlabel('\phi')
ylabel('Probability of Escape')
set(gca,'XLim', [0 2*pi])
set(gca,'YLim', [0 1])
set(gca,'XTick',0:pi/2:2*pi)
set(gca,'XTickLabel',{'0','p/2','p','3p/2','p'}, 'fontname','symbol')


%%%%%%%%%%%%%%%%%%%%%%%%%%%%%%%%%%%%%%%%%%%%%%%%%%%%%%%%%%%%%%%%%%%%%%%%%
% Plot Pescape vs Aspect Ratio for 2-D & 3-D models, assume r=R/sqrt(2)
% Plot Total SEY for both 2D and 3D Models, assume r = R/sqrt(2)
clear all;
close all;
clc;

NumPts = 101;
Half_Num_Pts = (NumPts-1)/2 + 1;
phi = linspace(0,2*pi,NumPts); %Indpt Variable
SEY_nonpore = 1.7;
```

```
SEY_porebottom = 1.6;
ARmax = 10;
AR = linspace(0.01,ARmax,NumPts); %Indpt Variable
P1 = 0.15;
P2 = 0.25;
P3 = 0.5;
P4 = 0.75;

%Compute Pescape_2D...for r = R/2
Pescape_2D_rmedian = (1/2)*sin(atan(1./(4.*AR))) +
(1/2)*sin(atan(3./(4.*AR)));

%Compute Pescape_3D using MATLAB mean method...for r = R/sqrt(2)
for i = 1:NumPts
    for j = 1:NumPts
        Pescape_3D_rmedian(i,j) = sin(atan((sqrt(1+(cos(phi(j))).^2) -
cos(phi(j)))/(2*AR(i)*sqrt(2))));
    end
end
Avg_Pescape_3D_rmedian_mean = mean(Pescape_3D_rmedian,2);

%Calculate the difference between the 2D and 3D models
Model_Diff = Pescape_2D_rmedian - Avg_Pescape_3D_rmedian_mean'

%Plot the 2D and 3D Pescape curves
figure;
plot(AR,Pescape_2D_rmedian,'b-','LineWidth',2)
hold on;
plot(AR,Avg_Pescape_3D_rmedian_mean,'r:','LineWidth',2)
plot(AR,Model_Diff,'k--','LineWidth',2)
set(gca,'YLim', [0 1])
set(gca,'XLim', [0 10])
xlabel('Aspect Ratio')
ylabel('Mean Probability of Escape')
legend('2D Model','3D Model','2D-3D Model
Difference','Location','Northeast')

%Determine Total Surface SEY for 2D Model
SEY_surf_2D_P1 = SEY_porebottom.*Pescape_2D_rmedian.*P1 +
SEY_nonpore.*(1-P1);
SEY_surf_2D_P2 = SEY_porebottom.*Pescape_2D_rmedian.*P2 +
SEY_nonpore.*(1-P2);
SEY_surf_2D_P3 = SEY_porebottom.*Pescape_2D_rmedian.*P3 +
SEY_nonpore.*(1-P3);
SEY_surf_2D_P4 = SEY_porebottom.*Pescape_2D_rmedian.*P4 +
SEY_nonpore.*(1-P4);

%Determine Total Surface SEY for 3D Model
SEY_surf_3D_P1 = SEY_porebottom.*Avg_Pescape_3D_rmedian_mean.*P1 +
SEY_nonpore.*(1-P1);
SEY_surf_3D_P2 = SEY_porebottom.*Avg_Pescape_3D_rmedian_mean.*P2 +
SEY_nonpore.*(1-P2);
SEY_surf_3D_P3 = SEY_porebottom.*Avg_Pescape_3D_rmedian_mean.*P3 +
SEY_nonpore.*(1-P3);
```

```
SEY_surf_3D_P4 = SEY_porebottom.*Avg_Pescape_3D_rmedian_mean.*P4 +
SEY_nonpore.*(1-P4);

figure;
plot(AR,SEY_surf_2D_P1,'g:','LineWidth',2.5)
hold on;
plot(AR,SEY_surf_3D_P1,'go-','LineWidth',2)
plot(AR,SEY_surf_2D_P2,'b--','LineWidth',2.5)
plot(AR,SEY_surf_3D_P2,'bs-','LineWidth',2)
plot(AR,SEY_surf_2D_P3,'r-.','LineWidth',2.5)
plot(AR,SEY_surf_3D_P3,'rd-','LineWidth',2)
plot(AR,SEY_surf_2D_P4,'k','LineWidth',2.5)
plot(AR,SEY_surf_3D_P4,'k^:','LineWidth',2)
hline = refline([0 1]);
set(hline,'LineStyle',':')
set(gca,'YLim', [0 SEY_nonpore])
set(gca,'XLim', [0 5])
xlabel('Aspect Ratio')
ylabel('Total Secondary Electron Yield')
legend('2D Model: Porosity = 0.2','3D Model: Porosity = 0.2','2D Model:
Porosity = 0.3','3D Model: Porosity = 0.3','2D Model: Porosity =
0.4','3D Model: Porosity = 0.4','2D Model: Porosity = 0.6','3D Model:
Porosity = 0.6','Location','Southwest')



%%%%%%%%%%%%%%%%%%%%%%%%%%%%%%%%%%%%%%%%%%%%%%%%%%%%%%%%%%%%%%%%%%%%%%%%%
% Plot Total SEY vs. Aspect Ratio for 3D Model, assume r = R/sqrt(2)
clear all;
close all;
clc;

NumPts = 101;
Half_Num_Pts = (NumPts-1)/2 + 1;
ARmax = 5.0;
AR = linspace(0,ARmax,NumPts); %Indpt Variable
phi = linspace(0,2*pi,NumPts); %Indpt Variable
SEY_nonpore = 1.7;
SEY_porebottom = 1.6;
P1 = 0.15;
P2 = 0.25;
P3 = 0.5;
P4 = 0.75;

for i = 1:NumPts
    for j = 1:NumPts
        Pescape_3D_rmedian(i,j) = sin(atan((sqrt(1+(cos(phi(j))).^2) -
cos(phi(j)))/(2*AR(i)*sqrt(2))));
    end
end
Avg_Pescape_3D_rmedian_mean = mean(Pescape_3D_rmedian,2);

SEY_surf_3D_P1 = SEY_porebottom.*Avg_Pescape_3D_rmedian_mean.*P1 +
SEY_nonpore.*(1-P1);
```

```
SEY_surf_3D_P2 = SEY_porebottom.*Avg_Pescape_3D_rmedian_mean.*P2 +
SEY_nonpore.*(1-P2);
SEY_surf_3D_P3 = SEY_porebottom.*Avg_Pescape_3D_rmedian_mean.*P3 +
SEY_nonpore.*(1-P3);
SEY_surf_3D_P4 = SEY_porebottom.*Avg_Pescape_3D_rmedian_mean.*P4 +
SEY_nonpore.*(1-P4);

figure;
plot(AR,SEY_surf_3D_P1,'k-','LineWidth',2.5)
hold on;
plot(AR,SEY_surf_3D_P2,'r-.','LineWidth',2)
plot(AR,SEY_surf_3D_P3,'g--','LineWidth',2.5)
plot(AR,SEY_surf_3D_P4,'b:','LineWidth',2)
hline = refline([0 1]);
set(hline,'LineStyle',':')
set(gca,'YLim', [0 1.8])
set(gca,'XLim', [0 ARmax])
xlabel('Aspect Ratio')
ylabel('Total Secondary Electron Yield')
legend('Porosity = 0.1','Porosity = 0.3','Porosity = 0.5','Porosity =
0.7','Location','Southwest')


%%%%%%%%%%%%%%%%%%%%%%%%%%%%%%%%%%%%%%%%%%%%%%%%%%%%%%%%%%%%%%%%%%%%%%%
% Plot Total Surface SEY vs Porosity for 3D Model, assume r = R/sqrt(2)
clear all;
close all;
clc;

NumPts = 101;
Half_Num_Pts = (NumPts-1)/2 + 1;
Pmax = 0.785;
Porosity = linspace(0.01,Pmax,NumPts); %Indpt Variable
phi = linspace(0,2*pi,NumPts); %Indpt Variable
SEY_nonpore = 1.7;
SEY_porebottom = 1.6;
AR1 = 0.1;
AR2 = 0.5;
AR3 = 1;
AR4 = 2;
AR5 = 5;

for i = 1:NumPts
    for j = 1:NumPts
        Pescape_3D_AR1_rmedian(i,j) =
sin(atan((sqrt(1+(cos(phi(j))).^2) - cos(phi(j)))/(2*AR1*sqrt(2))));
        Pescape_3D_AR2_rmedian(i,j) =
sin(atan((sqrt(1+(cos(phi(j))).^2) - cos(phi(j)))/(2*AR2*sqrt(2))));
        Pescape_3D_AR3_rmedian(i,j) =
sin(atan((sqrt(1+(cos(phi(j))).^2) - cos(phi(j)))/(2*AR3*sqrt(2))));
        Pescape_3D_AR4_rmedian(i,j) =
sin(atan((sqrt(1+(cos(phi(j))).^2) - cos(phi(j)))/(2*AR4*sqrt(2))));
        Pescape_3D_AR5_rmedian(i,j) =
sin(atan((sqrt(1+(cos(phi(j))).^2) - cos(phi(j)))/(2*AR5*sqrt(2))));
```

```
    end
end
Avg_Pescape_3D_AR1_rmedian_mean = mean(Pescape_3D_AR1_rmedian,2);
Avg_Pescape_3D_AR2_rmedian_mean = mean(Pescape_3D_AR2_rmedian,2);
Avg_Pescape_3D_AR3_rmedian_mean = mean(Pescape_3D_AR3_rmedian,2);
Avg_Pescape_3D_AR4_rmedian_mean = mean(Pescape_3D_AR4_rmedian,2);
Avg_Pescape_3D_AR5_rmedian_mean = mean(Pescape_3D_AR5_rmedian,2);

SEY_surf_3D_AR1 =
(SEY_porebottom*Avg_Pescape_3D_AR1_rmedian_mean.*Porosity')' +
SEY_nonpore*(1-Porosity);
SEY_surf_3D_AR2 =
(SEY_porebottom*Avg_Pescape_3D_AR2_rmedian_mean.*Porosity')' +
SEY_nonpore*(1-Porosity);
SEY_surf_3D_AR3 =
(SEY_porebottom*Avg_Pescape_3D_AR3_rmedian_mean.*Porosity')' +
SEY_nonpore*(1-Porosity);
SEY_surf_3D_AR4 =
(SEY_porebottom*Avg_Pescape_3D_AR4_rmedian_mean.*Porosity')' +
SEY_nonpore*(1-Porosity);
SEY_surf_3D_AR5 =
(SEY_porebottom*Avg_Pescape_3D_AR5_rmedian_mean.*Porosity')' +
SEY_nonpore*(1-Porosity);

figure;
plot(Porosity,SEY_surf_3D_AR1,'k-','LineWidth',2.5)
hold on;
plot(Porosity,SEY_surf_3D_AR2,'b--','LineWidth',2)
plot(Porosity,SEY_surf_3D_AR3,'g-.','LineWidth',2.5)
plot(Porosity,SEY_surf_3D_AR4,'r:','LineWidth',2)
plot(Porosity,SEY_surf_3D_AR5,'mo-','LineWidth',2)
hline = refline([0 1]);
set(hline,'LineStyle',':')
set(gca,'YLim', [0 2])
set(gca,'XLim', [0 1])
xlabel('Porosity')
ylabel('Total Secondary Electron Yield')
legend('Aspect Ratio = 0.1','Aspect Ratio = 0.5','Aspect Ratio =
1.0','Aspect Ratio = 2.0','Aspect Ratio = 5.0','Location','Southwest')


%%%%%%%%%%%%%%%%%%%%%%%%%%%%%%%%%%%%%%%%%%%%%%%%%%%%%%%%%%%%%%%%%%%%%%%%%%
% Surface Plot of Pescape_3D vs. r and phi
clear all;
close all;
clc;

R = 1;
H = 10;
phi = linspace(0,2*pi,101); %Indpt Variable
r = linspace(0,R,101); %Indpt Variable
Pescape = zeros(101);
```

```
for i = 1:101
    for j = 1:101
        Pescape(i,j) = sin(atan((sqrt(R^2 - (r(i)*sin(phi(j)))^2) -
r(i)*cos(phi(j)))/(H)));
    end
end

Avg_Pescape = mean(Pescape,2);
Avg_Pescape_phi = Avg_Pescape(72)

figure;
surf(phi, r, Pescape);
xlabel('\phi')
ylabel('r')
zlabel('Probability of Escape')
set(gca,'XLim', [0 2*pi])
set(gca,'YLim', [0 R])
set(gca,'ZLim', [0 1])
set(gca,'XTick',0:pi/2:2*pi)
set(gca,'XTickLabel',{'0','p/2','p','3p/2','2p'}, 'fontname','symbol')


%%%%%%%%%%%%%%%%%%%%%%%%%%%%%%%%%%%%%%%%%%%%%%%%%%%%%%%%%%%%%%%%%%%%%%%%%
% Plot D (from the 3D model) vs. phi (given r and R)
clear all;
close all;
clc;

R = 1;
r = 0.5*R;
phi = linspace(0,2*pi,101); %Indpt Variable

D = sqrt(R^2 - (r*sin(phi)).^2) - r*cos(phi);

figure
plot(phi,D,'k-','LineWidth',2)
set(gca,'YLim', [0 2*R])
set(gca,'XLim', [0 2*pi])
xlabel('Azimuthal Angle (phi)')
ylabel('Distance from Emission Site to Pore Circumference')
set(gca,'XTick',0:pi/2:2*pi)
set(gca,'XTickLabel',{'0','p/2','p','3p/2','2p'}, 'fontname','symbol')
grid ON;


%%%%%%%%%%%%%%%%%%%%%%%%%%%%%%%%%%%%%%%%%%%%%%%%%%%%%%%%%%%%%%%%%%%%%%%%%
% Find Pescape_3-D model for a given Aspect Ratio, assume r = R/sqrt(2)
clear all;
close all;
clc;

NumPts = 1001;
Half_Num_Pts = (NumPts-1)/2 + 1;
```

```
AR = 2;
phi = linspace(0,2*pi,NumPts); %Indpt Variable

%Compute Pescape_3D using MATLAB mean method r = 2R/3
for i = 1:NumPts
    Pescape_3D_rexpected(i) = sin(atan((sqrt(1+(cos(phi(i))).^2) -
cos(phi(i)))/(2*AR*sqrt(2))));
end
format long;
Avg_Pescape_3D_rexpected_mean = mean(Pescape_3D_rexpected)

% Determine SEY_porous-surface for the above Pescape_3-D given Porosity
and
%SEY_nonpore and SEY_porebottom
SEY_nonpore = 1.70;
SEY_porebottom = 1.70;
Porosity = 0.52;

SEY_surf_3D =
(SEY_porebottom*Avg_Pescape_3D_rexpected_mean.*Porosity')' +
SEY_nonpore*(1-Porosity)
```

Bibliography

[1] S. Riyopoulos, D. Chemin, and D. Dialetis, "Effect of random secondary delay times and emission velocities in electron multipactors," *IEEE Trans. Electron Devices*, vol. 44, no. 3, pp. 489–497, 1997.

[2] A. Sazontov, M. Buyanova, V. Semenov, E. Rakova, N. Vdovicheva, D. Anderson, M. Lisak, J. Puech, and L. Lapierre, "Effect of emission velocity spread of secondary electrons in two-sided multipactor," *Phys. Plasmas*, vol. 12, no. 5, pp. 1–8, 2005.

[3] S. Anza, C. Vicente, B. Gimeno, V. E. Boria, and J. Armendáriz, "Long-term multipactor discharge in multicarrier systems," *Phys. Plasmas*, vol. 14, no. 8, 2007.

[4] M. Buyanova, V. E. Semenov, D. Anderson, M. Lisak, and J. Puech, "Influence of secondary emission yield on the saturation properties of multipactor discharges between two parallel metal plates," *Phys. Plasmas*, vol. 17, no. 4, 2010.

[5] C. J. Lingwood, G. Burt, A. C. Dexter, J. D. A. Smith, P. Goudket, and P. H. Stoltz, "Phase space analysis of multipactor saturation in rectangular waveguide," *Phys. Plasmas*, vol. 19, no. 3, p. 32106, 2012.

[6] A. A. Vikharev, E. V. Ilyakov, S. V. Kuzikov, and I. S. Kulagin, "Multipactor discharge in crossed fields in a cylindrical cavity for the 3-cm wavelength band," *Radiophys. Quantum Electron.*, vol. 54, no. 12, pp. 820–827, 2012.

[7] J. R. M. Vaughan, "Multipactor," *Electron Devices, IEEE Trans.*, vol. 35, no. 7, pp. 1172–1180, 1988.

[8] R. A. Kishek, Y. Y. Lau, L. K. Ang, A. Valfells, and R. M. Gilgenbach, "Multipactor discharge on metals and dielectrics: Historical review and recent theories," *Phys. Plasmas*, vol. 5, no. 5, pp. 2120–2126, 1998.

[9] E. Sorolla and M. Mattes, "Multipactor saturation in parallel-plate waveguides," *Phys. Plasmas*, vol. 19, no. 7, p. 72304, 2012.

[10] V. Nistor, L. A. Gonzalez, L. Aguilera, I. Montero, L. Galan, U. Wochner, D. Raboso, "Multipactor suppression by micro-structured gold/silver coatings for space applications," *Appl. Surf. Sci.*, vol. 315, no. 0, pp. 445–453, Jan. 2014.

[11] E. Somersalo and D. Proch, "Analysis of multipacting in coaxial lines," in *Proceedings of the 1995 Particle Accelerator Conference*, 1995, pp. 1500–1502.

[12] F. Höhn, W. Jacob, R. Beckmann, and R. Wilhelm, "The transition of a multipactor to a low-pressure gas discharge," *Phys. Plasmas*, vol. 4, no. 4, p. 940, 1997.

[13] V. A. Ivanov, A. S. Sakharov, and M. E. Konyzhev, "Strong Local Interaction of Microwave Discharges With Solid Dielectrics in Vacuum," *IEEE Trans. Plasma Sci.*, vol. 43, no. 6, pp. 1871–1878, 2015.

[14] R. A. Kishek, "Interaction of Multipactor Discharge and RF Structures," The University of Michigan, 1997.

[15] R. Kishek and Y. Y. Lau, "Interaction of multipactor discharge and rf circuit," *Phys. Rev. Lett.*, vol. 75, no. 6, pp. 1218–1221, 1995.

[16] S. Anza, C. Vicente, J. Gil, M. Mattes, D. Wolk, U. Wochner, V. E. Boria, B. Gimeno, and D. Raboso, "Prediction of multipactor breakdown for multicarrier applications: The quasi-stationary method," *IEEE Trans. Microw. Theory Tech.*, vol. 60, no. 7, pp. 2093–2105, 2012.

[17] D. González-Iglesias, B. Gimeno, V. E. Boria, Á. Gómez, and A. Vegas, "Multipactor Effect in a Parallel-Plate Waveguide Partially Filled With Magnetized Ferrite," *IEEE Trans. Electron Devices*, vol. 61, no. 7, pp. 2552–2557, 2014.

[18] R. Hayes and D. Preist, "Research on Microwave Window Multipactor and its Inhibition," Eitel-McCullough, Inc. Final Report for U.S. Army Electronics Laboratories Contract No. DA 36-039 SC-90818, San Carlos, CA, 1965.

[19] R. A. Kishek and Y. Y. Lau, "Multipactor discharge on a dielectric," *Phys. Rev. Lett.*, vol. 80, no. 1, pp. 193–196, 1998.

[20] R. A. Kishek, Y. Y. Lau, and D. Chernin, "Steady state multipactor and dependence on material properties," *Phys. Plasmas*, vol. 4, no. 1997, pp. 863–872, 1997.

[21] M. Alfonseca, L. Conde, J. de Lara, F. Perez, and D. Raboso, "Langevin Simulation of RF Corona Discharges for Space Hardware," in *5th International Workshop on Multipactor, Corona, and Passive Intermodulation*, Noordwijk, The Netherlands, 2005.

[22] H. M. Wachowski, "Breakdown in Waveguides Due to the Multipactor Effect," Aerospace Corporation Report No. TDR-269(9990)-5, El Segundo, CA, 1964.

[23] M. Mostajeran and M. L. Rachti, "On the phase stability in two-sided multipactor," *Nucl. Instruments Methods Phys. Res. Sect. A Accel. Spectrometers, Detect. Assoc. Equip.*, vol. 615, no. 1, pp. 1–5, 2010.

[24] N. G. Rogers, *Electron multipactor: theory review, comparison and modeling of mitigation techniques in ICEPIC*. MS thesis, AFIT/GE/ENP/09-M02. School of Engineering and Management, Air Force Institute of Technology (AU), Wright-Patterson AFB OH, March 2009 (AD-A495885).

[25] Y. Y. Lau, J. P. Verboncoeur, and H. C. Kim, "Scaling laws for dielectric window breakdown in vacuum and collisional regimes," *Appl. Phys. Lett.*, vol. 89, no. 26, p. 261501, 2006.

[26] A. R. Nyaiesh, E. L. Garwin, F. K. King, and R. E. Kirby, "Properties of Thin Anti-Multipactor Coatings for Klystron Windows," Stanford Linear Accelorator Center Report No. SLAC-PUB-3760, Stanford, CA, 1985.

[27] M. Kuchnir and E. Hahn, "Coating Power RF Components with TiN," Fermi National Accelerator Laboratory Report No. FERMILAB-TM-1928, Bativa, IL, 1995.

[28] J. Tuckmantel, C. Benvenuti, D. Boussard, G. Geschonke, E. Haebel, N. Hilleret, S. Juras, H. P. Kindermann, J. Uythoven, C. Wyss and M. Stirbet, "Improvements to power couplers for the LEP2 superconducting cavities," in *Proceedings of the 1995 Particle Accelerator Conference*, 1995, vol. 3, no. 1, pp. 1642–1644.

[29] J. Lorkiewicz, A. Brinkmann, B. Dwersteg, D. Kostin, W.-D. Moeller, and M. Layalan, "Surface TiN coating of Tesla couplers at DESY as an antimultipactor remedy," in *The 10th Workshop on RF Superconductivity*, 2001, pp. 448–452.

[30] J. G. Power, W. Gai, S. H. Gold, A. K. Kinkead, R. Konecny, C. Jing, W. Liu, and Z. Yusof, "Observation of Multipactor in an Alumina-Based Dielectric-Loaded Accelerating Structure," *Phys. Rev. Lett.*, vol. 92, no. 16, p. 164801, 2004.

[31] T. P. Graves, "Standard/Handbook for Multipactor Breakdown Prevention in Spacecraft Components," Aerospace Corporation Report No. TOR-2014-02198, El Segundo, CA, 2014.

[32] J. E. Nanevicz and R. C. Adamo, "Further Development of the Multipactor Discharge Electron Source," in *Spacecraft Charging Technology*, 1978, pp. 881–886.

[33] P. T. Farnsworth, "Television by electron image scanning," *J. Franklin Inst.*, vol. 218, pp. 411–444, 1934.

[34] European Cooperation for Space Standardization, "Space engineering: Multipaction design and test," Report No. ECSS-E-20-01A Rev.1, Noordwijk, 2013.

[35] A. J. Hatch, "Suppression of Multipacting in Particle Accelerators," *Nucl. Instruments Methods*, vol. 41, pp. 261–271, 1966.

[36] F. Le Pimpec, R. E. Kirby, F. King, and M. Pivi, "Electron conditioning of technical aluminium surfaces: Effect on the secondary electron yield," *J. Vac. Sci. Technol. A Vacuum, Surfaces, Film.*, vol. 23, no. 6, p. 1610, 2005.

[37] K. G. McKay, "Secondary Electron Emission," in *Advances in Electronics and Electron Physics Volume I*, L. Marton, Ed. New York: Academic Press Inc., Publishers, 1948, pp. 65–120.

[38] Hughes Aircraft Company, "The Study of Multipactor Breakdown in Space Electronic Systems," NASA Contractor Report No. NASA CR-448, Culver City, CA, 1966.

[39] M. Mostajeran, "Simulations of the multipactor phenomenon for surfaces with semi-spherical depressions," *J. Instrum.*, vol. 6, no. 5, pp. T05002–T05002, 2011.

[40] D. González-Iglesias, A. M. Perez, S. Anza, J. V. Cardona, B. Gimeno, V. E. Boria, D. Raboso, C. Vicente, J. Gil, F. Caspers, and L. Conde, "Multipactor Mitigation in Coaxial Lines by Means of Permanent Magnets," *Electron Devices, IEEE Trans.*, vol. 61, no. 12, pp. 4224–4231, 2014.

[41] American Institute of Aeronautics and Astronautics, "Standard/Handbook for Multipactor Breakdown Prevention in Spacecraft Components," American Institute of Aeronautics and Astronautics Report No. ANSI/AIAA S-142-2016," 2016.

[42] F. Piro and Y. Brand, “PIM and Multipactor Considerations for Future High-RF Power Space Missions,” in *The 8th European Conference on Antennas and Propagation*, 2014, no. EuCAP, pp. 1643–1646.

[43] L. Arnett and W. Caven, “A Proposed Lower Bound to P20 to Avoid Electron Cloud Accumulation Oover Multiple Envelope Cycles,” in *9th International Workshop on Multipactor, Corona and Passive Intermodulation*, Noordwijk, The Netherlands, 2017.

[44] H. Bruining, J. H. de Boer, and W. G. Burgers, “Secondary Electron Emission of Soot in Valves with Oxidecathode,” *Phys. IV*, vol. 4, no. 4, pp. 267–275, 1937.

[45] H. Bruining, “Secondary Electron Emission,” *Philips Tech. Rev.*, vol. 3, pp. 80–86, 1938.

[46] J. L. H. Jonker, “Phenomena in Amplifier Valves Caused by Secondary Emission,” *Philips Tech. Rev.*, vol. 3, pp. 211–216, 1938.

[47] D. H. Preist and R. C. Talcott, “On the Heating of Output Windows of Microwave Tubes by Electron Bombardment,” *IRE Trans. Electron Devices*, vol. 8, no. 4, pp. 243–251, 1961.

[48] J. R. M. Vaughan, “Some High-Power Window Failures,” *IRE Trans. Electron Devices*, vol. 8, no. 4, pp. 302–308, 1961.

[49] D. J. Lewis and D. K. McCarty, “Multipactor effect in X-band waveguide slots,” *Proc. IEEE*, vol. 54, no. 4, pp. 713–714, 1966.

[50] J. E. Stern and K. R. Mercy, “A Study of Voltage Breakdown in Spacecraft Systems from Test and Flight Experience,” in *Proceedings of the 2nd Workshop on Voltage Breakdown in Electronic Equipment at Low Air Pressure*, 1969, pp. 3–8.

[51] G. August and J. B. Chown, “Reduction of gas-discharge breakdown thresholds in the ionisphere due to multipacting,” in *Proceedings of the Second Workshop on Voltage Breakdown in Electronic Equipment at Low Air Pressure*, 1969, pp. 193–201.

[52] H. Jahrreiss, “Secondary electron emission from thin films,” *Thin Solid Films*, vol. 12, no. 1, pp. 187–200, 1972.

[53] C. M. Lyneis, H. A. Schwettman, and J. P. Turneaure, “Elimination on electron multipacting in superconducting structures for electron accelerators,” *Appl. Phys. Lett.*, vol. 31, no. 8, pp. 541–543, 1977.

[54] W. J. Gallagher, “The multipactor effect,” *IEEE Trans. Nucl. Sci.*, vol. NS-26, no. 3, pp. 4280–4282, 1979.

[55] C. M. Lyneis, J. Sayag, H. A. Schwettman, and J. P. Turneaure, “Performance of a superconducting accelerator structure with a modified geometry,” *IEEE Trans. Nucl. Sci.*, vol. NS-26, no. 3, pp. 3755–3756, 1979.

[56] P. J. Tallerico, “A 150-kW, 450-MHz Gyrocon RF Generator,” *IEEE Trans. Nucl. Sci.*, vol. NS-30, no. 4, pp. 3420–3422, 1983.

[57] R. Boni, V. Chimenti, P. Fernandes, R. Parodi, B. Spataro, and F. Tazzioli, “Reduction of multipacting in an accelerator cavity,” *IEEE Trans. Nucl. Sci.*, vol. NS-32, no. 5, pp. 2815–2817, 1985.

[58] S. R. Farrell and W. J. Gallagher, “Further notes on the multipactor effect,” *IEEE Trans. Nucl. Sci.*, vol. NS-32, no. 5, pp. 2900–2902, 1985.

[59] W. Weingarten, “On Electrical Breakdown in Superconducting Accelerating Cavities,” *IEEE Trans. Electr. Insul.*, vol. 24, no. 6, pp. 1005–1012, 1989.

[60] W. R. Fowkes, R. S. Callin, and A. E. Vlieks, “High power RF window and waveguide component development and testing above 100 MW at x-band,” in *Linear Accelerator Conference*, 1992.

[61] D. Proch, D. Einfeld, R. Onken, and N. Steinhauser, “Measurement of multipacting currents of metal surfaces in RF fields,” in *Proceedings of the 1995 Particle Accelerator Conference*, 1995, vol. 3, pp. 1776–1778.

[62] N. Díaz, S. Castaneda, J. M. Ripalda, I. Montero, L. Galan, S. Faltham, D. Raboso, and F. Rueda, “Materials of Low Secondary Electron Emission to Prevent the Multipactor Effect in High-Power RF Devices in Space,” in *6th Spacecraft Charging Technology Conference*, 2000, pp. 205–209.

[63] S. Michizono, Y. Saito, Suharyanto, Y. Yamano, and S. Kobayashi, “Secondary electron emission of sapphire and anti-multipactor coatings at high temperature,” *Appl. Surf. Sci.*, vol. 235, no. 1–2, pp. 227–230, 2004.

[64] G. G. Fuentes, R. J. Rodríguez, M. García, L. Galán, I. Montero, and J. L. de Segovia, “Spectroscopic investigations of Cr, CrN and TiCr anti-multipactor coatings grown by cathodic-arc reactive evaporation,” *Appl. Surf. Sci.*, vol. 253, no. 18, pp. 7627–7631, 2007.

[65] I. Montero, S. H. Mohamed, M. García, L. Galán, and D. Raboso, “Effect of surface reactions of low-energy carbon ions on the secondary electron emission of TiN:O thin films,” *J. Appl. Phys.*, vol. 101, no. 11, 2007.

[66] A. Ruiz, E. Roman, P. Lozano, M. Garcia, L. Galan, I. Montero, and D. Raboso, “UHV reactive evaporation growth of titanium nitride thin films, looking for multipactor effect suppression in space applications,” *Vacuum*, vol. 81, no. 11–12, pp. 1493–1497, 2007.

[67] Suharyanto, S. Michizono, Y. Saito, Y. Yamano, and S. Kobayashi, “Secondary electron emission of TiN-coated alumina ceramics,” *Vacuum*, vol. 81, no. 6 SPEC. ISS., pp. 799–802, 2007.

[68] M. Pivi, F. K. King, R. E. Kirby, T. O. Raubenheimer, G. Stupakov, and F. Le Pimpec, “Sharp reduction of the secondary electron emission yield from grooved surfaces,” *J. Appl. Phys.*, vol. 104, no. 10, p. 104904, 2008.

[69] C. Chang, G. Liu, H. Huang, C. Chen, and J. Fang, “Suppressing high-power microwave dielectric multipactor by the sawtooth surface,” *Phys. Plasmas*, vol. 16, no. 8, p. 83501, 2009.

[70] M. Ye, Y. N. He, S. G. Hu, R. Wang, T. C. Hu, J. Yang, and W. Z. Cui, "Suppression of secondary electron yield by micro-porous array structure," *J. Appl. Phys.*, vol. 113, no. 74904, pp. 1–8, Jan. 2013.

[71] N. Balcon, D. Payan, M. Belhaj, T. Tondu, and V. Inguimbert, "Secondary electron emission on space materials: Evaluation of the total secondary electron yield from surface potential measurements," *IEEE Trans. Plasma Sci.*, vol. 40, no. 2 PART 1, pp. 282–290, 2012.

[72] M. Ye, Y. N. He, S. G. Hu, J. Yang, R. Wang, T. C. Hu, W. B. Peng, and W. Z. Cui, "Investigation into anomalous total secondary electron yield for micro-porous Ag surface under oblique incidence conditions," *J. Appl. Phys.*, vol. 114, no. 104905, pp. 1–8, 2013.

[73] R. Valizadeh, O. B. Malyshev, S. Wang, T. Sian, M. D. Cropper, and N. Sykes, "Reduction of secondary electron yield for E-cloud mitigation by laser ablation surface engineering," *Appl. Surf. Sci.*, vol. 404, pp. 370–379, 2017.

[74] R. Valizadeh, O. B. Malyshev, S. Wang, S. A. Zolotovskaya, W. A. Gillespie, and A. Abdolvand, "Low secondary electron yield engineered surface for electron cloud mitigation," *Appl. Phys. Lett.*, vol. 105, no. 23, p. 231605, 2014.

[75] L. Cai, J. Wang, G. Cheng, X. Zhu, and H. Xia, "Self-consistent simulation of radio frequency multipactor on micro-grooved dielectric surface," *J. Appl. Phys.*, vol. 117, p. 53302, 2015.

[76] A. J. Hatch and H. B. Williams, "The secondary electron resonance mechanism of low-pressure high-frequency gas breakdown," *J. Appl. Phys.*, vol. 25, no. 4, pp. 417–423, 1954.

[77] P. T. Farnsworth, "IRE News and Radio Notes - Chicago Section," in *Radio Engineers, Proceedings of the Institute of*, 1936, pp. 149–150.

[78] L. M. Myers, *Electron Optics: Theoretical and Practical*. New York: Van Nostrand, pp. 306–325, 1939.

[79] A. J. Hatch, "Electron Bunching in the Multipacting Mechanism of High-Frequency Discharge," *J. Appl. Phys.*, vol. 32, no. 6, pp. 1086–1092, 1961.

[80] E. W. B. Gill and A. von Engel, "Starting potentials of high-frequency gas discharges at low pressure," *R. Soc. Proc. A*, vol. 192, pp. 446–463, 1948.

[81] A. L. Gilardini, "Multipacting discharges: constant-k theory and simulation results," *J. Appl. Phys.*, vol. 78, no. I, pp. 783–795, 1995.

[82] A. J. Hatch and H. B. Williams, "Multipacting modes of high-frequency gaseous breakdown," *Phys. Rev.*, vol. 112, no. 3, p. 681, 1958.

[83] S. C. Brown, *Basic Data of Plasma Physics*. The Technology Press, Massachusetts Institute of Technology, 1959.

[84] H. Bruining, "Secondary Electron Emission - Part II. Absorption of Secondary Electrons," *Physica*, vol. V, no. 10, pp. 901–912, 1938.

[85] J. R. M. Vaughan, “Observations of Multipactor in Magnetrons,” *IEEE Trans. Electron Devices*, vol. ED-15, no. 11, pp. 883–889, 1968.

[86] S. Riyopoulos, D. Chernin, and D. Dialetis, “Theory of electron multipactor in crossed fields,” *Phys. Plasmas*, vol. 2, no. 1995, p. 3194, 1995.

[87] Y. Li, C. Wan-Zhao, Z. Na, W. Xin-Bo, W. Hong-Guang, L. Yong-Dong, and Z. Jian-Feng, “Three-dimensional simulation method of multipactor in microwave components for high-power space application,” *Chinese Phys. B*, vol. 23, no. 4, p. 48402, 2014.

[88] R. A. Kishek, “Ping-Pong Modes: A New Form of Multipactor,” *Phys. Rev. Lett.*, vol. 108, no. 3, p. 35003, 2012.

[89] R. A. Kishek, “Ping-pong modes and higher-periodicity multipactor,” *Phys. Plasmas*, vol. 20, no. 5, p. 56702, 2013.

[90] I. A. Kossyi, G. S. Lukyanchikov, V. E. Semenov, E. I. Rakova, D. Anderson, M. Lisak, and J. Puech, “Polyphase (non-resonant) multipactor in rectangular waveguides,” *J. Phys. D. Appl. Phys.*, vol. 41, no. 6, p. 65203, 2008.

[91] R. A. Kishek, “A Global Approach for Analyzing Multipactor,” in 8*th International Workshop on Multipactor, Corona and Passive Intermodulation*, Valencia, Spain, 2014.

[92] H. Bruining, *Physics and Applications of Secondary Electron Emission*. New York: McGraw-Hill Book Co., Inc., 1954.

[93] A. J. Dekker, “Secondary Electron Emission,” in *Solid State Physics Volume 6*, 1958, pp. 251–311.

[94] O. Hachenberg and W. Brauer, “Secondary Electron Emission from Solids,” in *Advances in Electronics and Electron Physics Volume XI*, 1959, pp. 413–499.

[95] H. Fröhlich, “Theory of Secondary Electron Emission from Solids,” *Proc. Phys. Soc. Sect. B*, vol. 68, no. 9, pp. 657–660, 1955.

[96] R. G. Lye and A. J. Dekker, “Theory of Secondary Emission,” *Phys. Rev.*, vol. 107, no. 4, pp. 977–981, 1957.

[97] C. K. Birdsall and W. B. Bridges, *Electron Dynamics of Diode Regions*. New York: Academic Press, 1966.

[98] R. E. Simon and B. F. Williams, “Secondary-Electron Emission,” *IEEE Trans. Nucl. Sci.*, vol. 15, no. 3, pp. 167–170, 1968.

[99] J. de Lara, F. Perez, M. Alfonseca, L. Galan, I. Montero, E. Roman, and D. Raboso, “Multipactor Prediction for On-Board Spacecraft RF Equipment With the MEST Software Tool,” in *IEEE Trans. Plasma Sci.,* vol. 34, no. 2, pp. 476–484, 2006.

[100] J. R. M. Vaughan, “A new formula for secondary emission yield,” *IEEE Trans. Electron Devices*, vol. 36, no. 9, pp. 1963–1967, 1989.

[101] A. Shih and C. Hor, “Secondary emission properties as a function of the electron incidence angle,” *IEEE Trans. Electron Devices*, vol. 40, no. 4, pp. 824–829, 1993.

[102] D. C. Joy, “A Database of Electron-Solid Interactions,” Revision 08-1, 2008. Available: http://studylib.net/doc/5878300/a-database-of.

[103] N. D. Zameroski, P. Kumar, C. Watts, T. Svimonishvili, M. Gilmore, E. Schamiloglu, and J. A. Gaudet, “Secondary Electron Yield Measurements from Materials with Application to Collectors of High-Power Microwave Devices,” *IEEE Trans. Plasma Sci.*, vol. 34, no. 3, pp. 642–651, 2006.

[104] D. J. Scott, D. Capista, K. L. Duel, R. M. Zwaska, S. Greenwald, W. Hartung, Y. Li, T. P. Moore, M. A. Palmer, R. Kirby, M. Pivi, and L. Wang, “Secondary Electron Yield Measurements of Fermilab’s Main Injector Vacuum Vessel,” Fermi National Accelerator Laboratory Report No. FERMILAB-CONF-12-196-AD, 2013.

[105] “USGS Earth Explorer,” 2017. [Online]. Available: https://earthexplorer.usgs.gov/.

[106] “Mapcoordinates.net,” 2017. [Online]. Available: http://www.mapcoordinates.net/en.

[107] “NOAA Magnetic Field Calculators,” 2017. [Online]. Available: https://www.ngdc.noaa.gov/geomag-web/?model=wmm#igrfwmm.

[108] UHV Design, “5-Axis Multicentre with LN2 Cooling, Resistive Heating for Phi Puck and Sample Bias.” Mechanical Drawing, East Sussex, United Kingdom, 2016.

[109] O. Kvitek, R. Hendrych, Z. Kolská, and V. Švorcik, “Grafting of gold nanoparticles on glass using sputtered gold interlayers,” *J. Chem.*, vol. 2014, no. 450413, pp. 1–6, 2014.

[110] J. W. Tringe, T. A. Uhlman, A. C. Oliver, and J. E. Houston, “A single asperity study of Au/Au electrical contacts,” *J. Appl. Phys.*, vol. 93, no. 8, pp. 4661–4669, 2003.

[111] D. Alamarguy, M. Bertoglio, N. Lecaude, S. Noel, L. Ruaut, and L. Tristani, “Corrosion behaviour of gold surfaces protected with bonded perfluoro polyethers,” *Surfcae Interface Anal.*, vol. 36, pp. 780–783, 2004.

[112] Huntington Mechanical Labs, “Standard Mini Rotary Feedthrough.” Mechanical Drawing, Grass Valley, CA, 2017.

[113] Y. Lin and D. C. Joy, “A new examination of secondary electron yield data,” *Surf. Interface Anal.*, vol. 37, no. 11, pp. 895–900, 2005.

[114] J. M. Sattler, R. A. J. Coutu, R. A. Lake, and T. Laurvick, “Engineered Surfaces to Control Secondary Electron Emission for Multipactor Suppression,” in *IEEE National Aerospace and Electronics Conference and Ohio Innovation Summit*, 2016, pp. 296–302.

[115] T. V. Laurvick, R. A. Coutu, J. M. Sattler, and R. A. Lake, "Surface feature engineering through nanosphere lithography," *J. Micro/Nanolithography, MEMS, MOEMS*, vol. 15, no. 3, p. 31602, 2016.

[116] J. M. Sattler, R. A. J. Coutu, R. A. Lake, and T. Laurvick, "Engineering and Modeling Micro-Porous Surfaces for Secondary Electron Emission Control," in *9th International Workshop on Multipactor, Corona and Passive Intermodulation*, Noordwijk, The Netherlands, 2017.

[117] J. M. Sattler, R. A. Coutu Jr, R. Lake, T. Laurvick, T. Back, and S. Fairchild, "Modeling micro-porous surfaces for secondary electron emission control to suppress multipactor," *J. Appl. Phys.*, vol. 122, no. 055304, pp. 1–9, 2017.

[118] J. M. Sattler, R. A. Lake, T. Laurvick, and K. W. Waggoner, "Predicting Total Secondary Electron Emission from Porous Surfaces Using a 3D Pore Geometry," in *IEEE National Aerospace and Electronics Conference (in press)*, 2017.

[119] T. V Laurvick, *Improvement to Micro-Contact Performance and Reliability*. Air Force Institute of Technology (AU), Wright-Patterson AFB OH, December 2016 (AD1032060).

REPORT DOCUMENTATION PAGE

Form Approved
OMB No. 074-0188

The public reporting burden for this collection of information is estimated to average 1 hour per response, including the time for reviewing instructions, searching existing data sources, gathering and maintaining the data needed, and completing and reviewing the collection of information. Send comments regarding this burden estimate or any other aspect of the collection of information, including suggestions for reducing this burden to Department of Defense, Washington Headquarters Services, Directorate for Information Operations and Reports (0704-0188), 1215 Jefferson Davis Highway, Suite 1204, Arlington, VA 22202-4302. Respondents should be aware that notwithstanding any other provision of law, no person shall be subject to an penalty for failing to comply with a collection of information if it does not display a currently valid OMB control number.
PLEASE DO NOT RETURN YOUR FORM TO THE ABOVE ADDRESS.

1. REPORT DATE *(DD-MM-YYYY)*	2. REPORT TYPE	3. DATES COVERED *(From – To)*
14-09-2017	Doctoral Dissertation	May 2015 - Sep 2017

TITLE AND SUBTITLE
Engineered Surfaces to Control Secondary Electron Yield for Multipactor Suppression

5a. CONTRACT NUMBER
5b. GRANT NUMBER
5c. PROGRAM ELEMENT NUMBER

6. AUTHOR(S)
Sattler, James, Lt Col, USAF

5d. PROJECT NUMBER
5e. TASK NUMBER
5f. WORK UNIT NUMBER

7. PERFORMING ORGANIZATION NAMES(S) AND ADDRESS(S)
Air Force Institute of Technology
Graduate School of Engineering and Management (AFIT/EN)
2950 Hobson Way, Building 640
WPAFB OH 45433-8865

8. PERFORMING ORGANIZATION REPORT NUMBER
AFIT-ENG-DS-17-S-018

9. SPONSORING/MONITORING AGENCY NAME(S) AND ADDRESS(ES)
Intentionally left blank

10. SPONSOR/MONITOR'S ACRONYM(S)

11. SPONSOR/MONITOR'S REPORT NUMBER(S)

12. DISTRIBUTION/AVAILABILITY STATEMENT
DISTRUBTION STATEMENT A. APPROVED FOR PUBLIC RELEASE; DISTRIBUTION UNLIMITED.

13. SUPPLEMENTARY NOTES
This material is declared a work of the U.S. Government and is not subject to copyright protection in the United States.

14. ABSTRACT
A significant problem for satellites, vacuum electron devices, and particle accelerators is multipactor: an avalanche of electrons caused by recurring secondary electron emission (SEE) in a time-varying electric field. The consequences of multipactor range from temporary to permanent device failure. This research studied how surface topography can be engineered to minimize SEE and suppress multipactor. Two new semi-empirical models (one based on a 2D pore, the other based on a 3D pore) were developed to predict the secondary electron yield (SEY) of a porous surface based on pore aspect ratio and porosity. The models were validated with experimental SEY measurements of microporous gold surfaces. The more accurate 3D model predicts that a porous gold surface with pore aspect ratios = 2.0 and porosity = 0.5 will control the maximum SEY to near unity, providing a multipactor-resistant surface. Both the SEY models and experimental results confirm the understanding that the ability of a porous surface to control SEY is not dependent on pore size.

15. SUBJECT TERMS
Multipactor, Secondary Electron Emission, Engineered Surfaces, Porous Surfaces

16. SECURITY CLASSIFICATION OF: a. REPORT	b. ABSTRACT	c. THIS PAGE	17. LIMITATION OF ABSTRACT	18. NUMBER OF PAGES	19a. NAME OF RESPONSIBLE PERSON / 19b. TELEPHONE NUMBER *(Include area code)*
U	U	U	UU	223	Capt Robert A. Lake (AFIT/ENG); (937) 255-3636, ext 4550; robert.lake@afit.edu

Standard Form 298 (Rev. 8-98)
Prescribed by ANSI Std. Z39-18